

The Pennsylvania State University

The Graduate School

GEOLOGIC MODELING AND DATA ASSIMILATION FOR CO₂ SEQUESTRATION IN
POINT BAR RESERVOIRS.

A Dissertation in
Energy and Mineral Engineering
by
Ismael Dawuda

© 2024 Ismael Dawuda

Submitted in Partial Fulfillment
of the Requirements
for the Degree of

Doctor of Philosophy

May 2024

The dissertation of Ismael Dawuda was reviewed and approved by the following:

Sanjay Srinivasan

Professor, Petroleum and Natural Gas Engineering

Dissertation Advisor

Chair of Committee

Arash Dahi Taleghani

Professor, Petroleum and Natural Gas Engineering

Gregory King

Professor of Practice, Petroleum and Natural Gas Engineering

Eugene Morgan

Assistant Teaching Professor, Petroleum and Natural Gas Engineering

Charles Ammon

Professor, Geosciences

Rui Zhang

Associate Professor, Geosciences

Special Member

Jeremy Gernand

Associate Professor, Environmental Health and Safety Engineering

Associate Department Head for Graduate Education

Abstract

The target reservoirs in many CO₂ sequestration projects exhibit point bar geology characterized by the presence of shale drapes that can act as barriers to prevent the leakage of CO₂. However, these shale drapes can also act as flow barriers and impede the displacement of CO₂ in such reservoirs and restrict the storage volume. Therefore, developing a framework for modeling point bars and their associated heterogeneities is important. Yet, for the point bar model to be geologically realistic and reliable for predicting the displacement of the CO₂ plume during sequestration, it should be calibrated by assimilating historical production/injection data to reduce the uncertainties associated with predictions of flow performance. Even so, due to the complex geologic heterogeneity exhibited by point bars, there is likely to be significant residual uncertainty even after assimilating historical flow performance related data. The calibrated models are further refined by assimilating timelapse seismic data in a Bayesian model selection workflow to sub-select the most-probable models that best reflect the reservoir characteristics closely. Given the interlinked nature of these modeling efforts, this dissertation proposes an integrated modeling workflow to accomplish the research objectives. The workflow begins with detailed geometric and geologic modeling of point bar reservoirs, and subsequent calibration of the models by assimilating CO₂ injection data and time-lapse seismic information.

A stochastic approach that considers the processes leading to the deposition of the point bar is proposed to model the point bar and its associated heterogeneities. The method uses geometric functions to model the areal and vertical dimensions of the point bar reservoir. Preserving the curvilinear continuity of the point bar geometry is very difficult and this has been accomplished by implementing a gridding scheme that accounts for the aerial geometry of the accretion surfaces as well as the sigmoidal geometry of the inclined heterolithic stratifications. Also, the spatial continuity of the unique heterogeneities that characterize point bar reservoirs was honored by incorporating a grid transformation scheme in the geostatistical simulation of the reservoir properties. The residual uncertainty associated with the geological modeling process was represented by generating several realizations of point bar reservoir models.

The model calibration workflow seeks to reduce the uncertainty associated with the prediction of reservoir properties over the ensemble of point bar reservoir models. The workflow developed in this research addresses two challenges common to many history matching techniques: (1) failure to account for uncertainties in reservoir geometry despite the influence that the reservoir architecture can have on reservoir response variables, (2) inability to handle the non-Gaussian relationship between the

primary state variables and secondary variables for reservoirs with complex heterogeneities (such as point bars) within current ensemble-based schemes.

These challenges were addressed in a hierarchical, two-step approach using ensemble-based data assimilation techniques. In step 1, we tackled the first challenge by implementing ensemble Kalman Filter (EnKF) to update the geometry of the point bar reservoir. For step 2, we used the updated reservoir geometry determined in step 1 to tackle the second problem by implementing a modified Indicator-based Data Assimilation (InDA) to update the permeability distribution in the point bar system. To accommodate the curvilinear geometry of the reservoir implemented while still implementing InDA in a Cartesian framework, we incorporated a grid transformation scheme.

This two-step model calibration approach reduces but does not eliminate the uncertainty associated with the models for the point bar reservoir. Further reduction in uncertainty is possible by integrating additional data in the form of time-lapse information. In this research, we implement a Bayesian model selection workflow to further reduce the uncertainty associated with the models for the point bar reservoir. The model selection algorithm is used to create a posterior set of models that reflect the time-lapse seismic information that may be available for the field site. The algorithm proceeds by: (1) computing discrete Fréchet distances to quantify the similarity in post-injection seismic responses obtained from a large prior ensemble of models, (2) combining multidimensional scaling with k-means clustering, to partition the models into subgroups based on their seismic responses, (3) performing Bayesian computations in the reduced model space to select the subgroup of models that yield response closest to the observed seismic information, and (4) iteratively sampling the posterior models, to further refine the selection of the model clusters. The applicability of the entire integrated workflow to a real field scenario is demonstrated, using the CO₂ injection and timelapse seismic dataset for the Cranfield reservoir in Mississippi. The final ensemble of selected models can be used to assess the uncertainty in predicting CO₂ storage capacity and the future displacement of CO₂ plume.

Table of Contents

List of Figures	viii
List of Tables	xiii
Acknowledgments	xiv
Chapter 1 Introduction	1
1.1 Problem Statement	8
1.2 Proposed Approach	9
Chapter 2 Stochastic Modeling of Point bars	11
2.1 Details of point bar heterogeneities and depositional trends.....	13
2.2 Modeling Steps.....	13
2.3 Channel Path Migration	19
2.4 Rendering point bar model on curvilinear grids.....	21
2.5 Geostatistical modeling on transformed grid.	27
2.6 Application to field Data	32
2.6.1 Modeling Channel Path Migration	33
2.6.2 Curvilinear Grid Generation.....	34
2.6.3 Geological Data.....	37
2.6.4 Grid transformation and Geostatistical simulation.....	38
2.6.5 Stochastic Representation of Shale drapes across interfaces	44
2.6.6 Point Bar Geometry Perturbation	46
2.7 Flow Simulation Study.....	49
2.7.1 Simulation grid.....	49
2.7.2 Simulation Parameters.....	50
2.7.3 Rock-Fluid Interaction Property.....	50
2.7.4 Fluid Property Modeling	51
2.7.5 Well and Recurrent Data	51
2.7.6 Simulation Strategy	52
2.7.7 Shale drape effects.....	52
2.7.8 Trapped CO ₂	54
2.7.9 Geometry Perturbation and its effect on bottom hole pressure and CO ₂ Plume	55
2.8 Concluding Remarks	57
Chapter 3 Reservoir Model Calibration	58
3.1 Introduction	58

3.2 History Matching within an Indicator Framework.....	61
3.3 Application to the Cranfield Reservoir	62
3.4 Reservoir Model Calibration	62
3.5 Permeability updating using InDA.....	66
3.5.1 Defining indicator thresholds for the static variable.	68
3.5.2 Indicator definition for the static variable	68
3.5.3 Indicator threshold definition for the dynamic variable	68
3.5.4 Updating the static variable using InDA Procedure	69
3.5.5 Incorporating grid transformation scheme.	69
3.6 Implementation of InDA on the Cranfield, Mississippi reservoir model.....	70
3.6.1 Generation of initial ensemble and reference model.....	70
3.6.2 Defining primary and secondary indicator thresholds.....	72
3.6.3 Updating permeability using InDA.	74
3.7 Ensemble Permeability Variance	77
3.8 Bottom-hole Pressure response after InDA.....	78
3.9 Forecast and Analyses of CO ₂ sequestration parameters.	79
3.10 Summary and Concluding remarks.	81
Chapter 4 Rock Physics Modeling.....	83
4.1 Introduction	83
4.2 Gassmann Theory.....	83
4.3 Rock and Fluid Property Modeling	84
4.3.1 Porosity.....	84
4.3.2 Density and bulk modulus of the pore fluid mixture.....	84
4.3.3 Bulk modulus of the mineral matrix.....	86
4.3.4 Frame Bulk modulus	86
4.4 Application to the Cranfield reservoir.....	87
Chapter 5 Model Selection	93
5.1 Introduction	93
5.2 Model selection workflow.....	94
5.2.1 Generation of initial ensemble of reservoir models	94
5.2.2 Generation of model responses.	94
5.2.3 Computing dissimilarity between models	95
5.2.4 Model Grouping	96

5.2.5 k-means clustering.....	98
5.2.6 Update of prior probabilities.	98
5.3 Application to the Cranfield dataset.....	99
5.3.1 Initial ensemble of models.	99
5.3.2 Model selection objective.....	100
5.3.3 Cranfield Seismic Data.....	101
5.3.4 Model selection implementation	103
5.3.5 Bayesian update of prior probabilities.....	105
5.4 Discussions.....	107
5.5 Summary and Concluding Remarks.....	111
Chapter 6 Value of Information Analyses for Monitoring CO₂ Plume During Sequestration.	113
6.1 Introduction	113
6.2 VOI Computation.....	114
6.3 Methodology	116
6.4 Results and Discussions	118
6.5 Summary and Concluding Remarks.....	121
Chapter 7 Limitations and Recommendations.....	122
Appendix A.....	124
Appendix B Implementation of Gassman’s fluid substitution procedure	126
APPENDIX C Publications.....	130
References.....	131

List of Figures

Fig. 1.1 Aerial view of a point bar. As the meandering channel migrates outwards towards the outer bend, channel sediments are eroded from the outer bend of the channel meander (i.e., the cutbank) and are deposited at the inner bend of the meander. Adopted from (Güneralp & Marston, 2012).	1
Fig. 1.2 Point bar schematic showing laterally accreting inclined heterolithic stratifications formed by lateral migration of a sinuous river. Adapted from (McMahon & Davies, 2018).	3
Fig. 2.1 Proposed flow chart for modeling the point bar reservoir.....	12
Fig. 2.2 (a) lateral accretions, (b) Cross sectional view illustrating IHS. Arrows indicate direction of fining of sediments which would be accounted for in the geostatistical simulation (Thomas, et al., 1987; Pyrcz & Deutsch, 2004b).	13
Fig. 2.3 Classification of SP log profiles for point bar and channel identification. Blocky or cylindrical shape is an indication of a channel while a bell shape is an indication of a point bar. Adapted from(Wilson & Nanz, 1959).....	14
Fig. 2.4 Well log readings for wells 28F-3, 48–2, 28–1, 31-F1 and 31F-3 at Cranfield. The first four well logs show SP reading while the last represent GR logs. Identified channel facies (blocky shape signals) are demarcated in black. Point bar facies (bell shape signals) are in red demarcations.	15
Fig. 2.5 Workflow for modeling the meander path demonstrated on a synthetic example. (a) Modeling stage 1 – marking channel path passing through channel nodes and bending to accommodate point bars on the concave side of the bends, (b) Modeling stage 2 – insertion of secondary node to define channel path while accommodating a point bar on the concave side of the bend, (c) Modeling stage 3 and (d) Modeling stage 4 – final channel path accommodating all the well data. Blue points are channel locations and red points are point bar locations.....	17
Fig. 2.6 Cross-section of a point bar deposit illustrating IHS. Adapted from (Pranter et al., 2007).	18
Fig. 2.7 Recreating initial channel path using SGF. Arrow points to the direction of backward migration	19
Fig. 2.8 Migration of asymmetric current channel path to recreate initial channel path. a) current channel path, (b) current channel path migrated back to recreate possible initial channel meander paths, (arrow indicates the direction of backward migration, i.e., migration starting from today’s channel path to the ancient path), c) area covered by the current channel path and the pre-migration path and d) current channel path and the most probable initial channel path.	21
Fig. 2.9 Workflow for gridding the lateral accretions. (a) Domain to be gridded defined by the current channel path (green) and the initial channel path (red) (b) grid nodes computed along the channel paths, (c) grid nodes computed between the channels and (d) curvilinear grid	23
Fig. 2.10 Workflow for gridding the lateral accretions for asymmetric point bar geometries. (a) Domain to be gridded defined by the current channel path (blue) and the initial channel path (red), (b) grid nodes computed along the channel paths, (c) grid nodes computed between the channels and (d) equivalent asymmetric curvilinear grid.	24
Fig. 2.11 Workflow for gridding the IHS. (a) domain to be gridded defined by the top (blue) and the bottom IHS surface (red) (b) Gridded IHS	24
Fig. 2.12 Grid generation procedure for the entire point bar, a) 3D grid for current channel b) 3D grid for initial channel gridded c) overlap of gridded surfaces showing region to be gridded d) 3D gridded point bar.	26
Fig. 2.13 Grid Transformation procedure for the HIS. (a) Domain to be transformed. Top and bottom layers are shown in blue and red, respectively. (b) IHS layers unraveled (c) Generated grid nodes for the IHS (d), rectilinear grid for the IHS.	28

Fig. 2.14 Grid Transformation procedure for the lateral accretions (a) domain to be transformed. Initial and current channel paths are shown in green and red respectively. (b) channel paths unraveled (c) generated grid nodes (d), rectilinear grid for the lateral accretions.....	29
Fig. 2.15 Transformed grid for the entire point bar. (a)Transformed grid nodes for the entire point bar, representing the computational space for geostatistical simulation, and (b) equivalent rectilinear grid for the entire point bar.	30
Fig. 2.16 Outline of property modeling. (a) Point Bar Curvilinear Grid (b) Rectilinear Grid Transformation (c) Geostatistical Simulation of porosity (d) Back Transformation, indicating the 3D distribution of porosity in the final Point Bar Model.....	31
Fig. 2.17 Channel Meander Simulation for the Cranfield dataset. (a) Point bar locations and channel locations (b) Modeling stage 1 (c) Modeling stage 2 (d) Final Modeling stage. Blue points are channel facies interpreted using well logs. Red points are point bar facies. The circled area in the final Figure is the Detailed Area of Study at the Cranfield injection site.	32
Fig. 2.18 Meander migration process focusing on the DAS region. (a) Illustration of close match between SGF prediction and the original meander path modeled using a spline function, (b) Current and initial meander path location after backward migration of channel (arrow indicates direction of backward migration i.e., migration starting from today’s channel path to the ancient path), red line shows section across the meanders, and (d) IHS revealed along section in (c).....	34
Fig. 2.19 2D gridding process for the lateral accretions. (a) Domain to be gridded, (b) grid nodes computed along the meanders, (c) Grid nodes computed between the meanders for each pair, and (d) curvilinear grid.	35
Fig. 2.20 (a) IHS domain to be gridded, (b) Gridded IHS. Grids between the top and bottom surfaces are perpendicular to the bedding orientation. (c) Computation grid from (Niu et al., 2021), grid does not conform to the beddings	36
Fig. 2.21. a) Current channel meander gridded in 3D, b) initial channel meander gridded in 3D c) Overlap of gridded surfaces showing region to be gridded d) 3D gridded point bar.....	37
Fig. 2.22 Porosity logs for wells a) 31-F1, b) 31-F2 and c) 31-F3.....	38
Fig. 2.23 Sequential Gaussian Simulation workflow. modified after (Bai & Tahmasebi, 2022).....	39
Fig. 2.24 vertical variation of mean porosity along a section containing the wells a)31-F1, b) 31-F2 and c) 31-F3.	40
Fig. 2.25 Variogram directions in (a, b, c) curvilinear grid and d) rectilinear grid. <i>hmax</i> , <i>hmed</i> and <i>hmin</i> are in the downstream direction, accretion, and dip direction, respectively. Please note: the lengths of arrows indicated here do not depict the magnitude of the ranges; they are just guiding the reader in identifying the major, minor and vertical directions of spatial continuities.	41
Fig. 2.26 Single SGSIM realization for IHS set 1. (a) realization on rectilinear grid (b) front view showing fining upward (Arrow points to the front view).....	42
Fig. 2.27 Single realization of the 3D Point bar. Downstream direction is from left to right.	43
Fig. 2.28 Fining trend captured in the geostatistical simulation,(a) bottom slice (taken at the last layer from top), (b) mid slice (taken at the 14th layer from top), and (c) top slice (taken at the 6th layer from top). Please note: the arrow indicates direction of fining in sediments from bottom to the top of the point bar.	44
Fig. 2.29 a) Sectional view showing shale simulated as a continuous layer on top of the IHS sets. Black rectangular demarcation is the continuous shale layer at the interface between two adjacent IHS sets 2 b) Variation in porosity along the continuous shale layer at the interface between the two IHS sets, and c) front view of IHS set 2, illustrating shale drapes captured as erosional surface.....	45
Fig. 2.30 Cross-section slice of the point bar across all IHS sets before (a) and after (b) modeling shale drapes.....	46

Fig. 2.31 Point bar geometry perturbed at different channel displacements. Channel displacement (and therefore sinuosity) increases from a to c, which: 1) affects the slopes of the IHS or beddings as one moves from d to f and 2) increases the areal extent of the point bar as we move from a to c or d to f. 47

Fig. 2.32 Geometry perturbation and variation in grid coordinates of wells (see red points). (a) Geometry perturbation at $\omega = 50^\circ$, and subsequent regeneration of grid. (b) Geometry perturbation at $\omega = 43^\circ$, and subsequent regeneration of grid. 48

Fig. 2.33 (a) Portion of the Cranfield point bar model used for simulation. Injection well 31-F1 is centrally located within the demarcated region. (b) Simulation grid cut from the point bar model. 50

Fig. 2.34 . CO₂-brine relative permeability curve used for simulation (Bennion and Bachu, 2005). 51

Fig. 2.35 Field injection rate schedule used for simulation. Please note, the original Cranfield injection rate was in terms of mass flow rate in kg/min – however ever in this study, it has been converted to volumetric flow rate in m³/day using a super-critical CO₂ fluid density of 576.72 kg/ m³. 52

Fig. 2.36 The effect of shale drapes on the dissolved CO₂ concentration. (a) Spatial distribution of dissolved CO₂ molality for the case when shale drape effect is ignored and (b) Dissolved CO₂ molality for case when shale drape effect is considered. When the shale drape is absent, the dissolved plume moves laterally in the injection zone before moving upwards. In the presence of shale drapes, the shale curtails lateral movement of the plume and consequently the vertical migration of the CO₂ plume is favored. 53

Fig. 2.37 The effect of shale drapes on the free gas CO₂ saturation. (a) CO₂ saturation for simulation run when shale drape effect is ignored, and (b) CO₂ saturation for simulation run when shale drape effect is considered. The shale drape causes vertical migration of the CO₂ plume. 54

Fig. 2.38 Trapped CO₂ volume as a function of time. 55

Fig. 2.39 CO₂ plume in the injection zone as the point bar geometry is altered at (a, d) $\omega=30^\circ$ deg when viewed in plan as well as cross-sectional view. (b, e) $\omega=40^\circ$ deg when viewed in plan and in section. (c, f) $\omega=50^\circ$ deg when viewed in plan as well as cross-sectional view. 56

Fig. 2.40 Sensitivity of bottom hole pressure to point bar geometry. An inverse relationship is observed as the point bar is perturbed at different angular displacements or channel sinuosities. Please note: Higher angular displacement is an indication of higher sinuosity. 56

Fig. 3.1 . Randomly selected realizations of point-bar reservoir geometries used for performing EnKF. (I) Shows the case when the angular displacement of the sine generation function was perturbed by 19.4°. Correspondingly, the slope of the beddings denoted by the sigmoidal function also change and is shown on the right. (II) The results when the angular displacement of the sine generation function is perturbed by 45°. 63

Fig. 3.2 Illustration of the gridding employed for performing the flow simulation and the location of injection well F1 within the reservoir. 64

Fig. 3.3 Cranfield injection schedule used for simulation at injection well F1. 64

Fig. 3.4 Results obtained at the end of the simulation period by applying the EnKF procedure, a) BHP before EnKF. (b) the updates to the angular displacement obtained by EnKF for various members of the initial ensemble. (c) BHP after EnKF. Red plot indicates BHP from geometry with least error (d) Updated point bar geometry with the least error to be used in the next phase of workflow. 66

Fig. 3.5 Modified InDA procedure incorporating grid transformation scheme. Color-coded sections represent modifications in InDA. Adapted from (Devesh Kumar & Srinivasan, 2018).I. 67

Fig. 3.6 One of the permeability models in the initial ensemble of models shown (a) with sections along the F1 injection well (b), and observation wells F2 and F3 (c, d). 72

Fig. 3.7 Cumulative distribution function for permeability based on a base case permeability model developed using the modeling workflow in Chapter 2. The primary indicator thresholds retrieved for permeability distribution are also shown. Note the non-Gaussian characteristics of the permeability distribution. 73

Fig. 3.8 Indicator definitions for Bottom-hole pressure (BHP) at a well location. The underlying behavior of the bottom-hole pressure is also non-Gaussian.	74
Fig. 3.9 Update of primary variable (permeability) using InDA.....	75
Fig. 3.10 Permeability distribution in the base model in the vicinity of a) injection well F1 and b) observation well F2. Ensemble average permeability distribution before InDA in the vicinity of c) injection well F1 and e) observation well F2. After InDA in the vicinity of d) injection well F1 and f) observation well F2.....	76
Fig. 3.11 Permeability variance in the vicinity of injection and observation wells before InDA (a, c, e) and after InDA (b, d, f).....	77
Fig. 3.12 History Matching Results (a) Simulated bottom-hole pressure before InDA, and (b) Simulated bottom-hole pressure after InDA. The line indicated by the black points are the field observed data.....	79
Fig. 3.13 CO ₂ sequestration responses before and after permeability updates. Moles of residual trapped gas (a) before InDA and (b) after InDA. Moles of dissolved gas (c) before InDA and (d) after InDA. Black scatter plots represent the reference.....	81
Fig. 4.1 Wireline logs from Observation well F-2 at Cranfield. a) density log, b) gamma ray log, c) S-wave velocity log (black) and P-wave velocity log (green). The black rectangular demarcation across the panels highlights the zone of interest, which is the injection zone.	89
Fig. 4.2 Post-injection p-wave velocity (V _p) at the well locations for a) injection well F-1 b) observation well F-2. Black plots are profiles from log data and red are those computed from rock-physics modeling.	90
Fig. 4.3 P-wave velocities that were determined from fluid substitution. Pre-injection P-wave velocity (red) and post-injection velocity (black) at a) injection well F-1 b) observation well F-2.....	91
Fig. 4.4 Grid locations for the conditioning wells (red) and another location away from the conditioning wells (black).....	92
Fig. 4.5 P-wave velocity profiles at a location away from the conditioning well locations computed using the ensemble of history-matched models described in Chapter 3.	92
Fig. 5.1 Discrete Fréchet distances computed for curves A(red) and B(blue)	96
Fig. 5.2 D map generated by MDS.....	97
Fig. 5.3 Ensemble permeability variance for the 3D point bar models (a) before and (b) after updates, with sections along S1 and S2 displayed in c) and d) respectively.....	100
Fig. 5.4 Seismic p-wave velocity data that will be used to constrain the model selection process. a) p-wave velocity for the entire Cranfield area b) Top view demarcating the area used for CO ₂ injection, c) Extracted seismic volume corresponding to the injection zone.....	102
Fig. 5.5 Projection of models into a 2D space after applying MDS.....	103
Fig. 5.6 Plot of Objective Function (i.e., Silhouette score) against number of clusters.	104
Fig. 5.7 Clustering of ensemble of models in the MDS projection space.....	104
Fig. 5.8 The calculation of Bayesian likelihood by assuming a Gaussian probability envelope centered on the observed response and with a variance equal to the mean squared error between the simulated and observed response corresponding to all ensemble members.....	106
Fig. 5.9 . Model Selection workflow in three stages. Top row shows the clustering and selection process at each stage. Second row shows the time-lapse velocity difference for all models within the selected cluster. Red plots in second row represent the observed time-lapse seismic velocity data.....	107
Fig. 5.10 Permeability variance computed using the ensemble of selected 3D point bar models, (a) after model calibration using injection history data and (b) after model selection using time-lapse seismic information, with sections along S ₁ and S ₂ displayed in c) and d) respectively.....	108

Fig. 5.11 Representative geologic model after implementing the model selection workflow to illustrate the porosity distribution in curvilinear space (figures (a, b, c)), and the corresponding distribution in rectilinear space (figures d, e, f). 109

Fig. 5.12 Average p-wave velocity difference for a representative section a) observed seismic data, b) before model selection (after injection data assimilation), and c) after model selection assimilating time-lapse seismic data. 110

Fig. 5.13 Bottom-hole pressure response at different iterative stages of the model selection process. 111

Fig. 6.1 Workflow for computing VOI for assimilating data into models for point bar deposits. Adapted from (Barros et al., 2016)..... 118

Fig. 6.2 VOI trends by assimilating injection data during history matching (black), and by assimilating time-lapse seismic data during model selection (red). 120

Fig. 6.3 Map of predicted CO₂ saturation after various stages of data assimilation. a) before history matching, b) after history matching, and c) difference in saturation between the two models., d) before assimilating time-lapse seismic data through model selection, e) after model selection, and f) difference in CO₂ saturation between the two models. 120

List of Tables

Table 2.1 Variogram inputs for SGSIM	42
Table 2.2 Well locations before and after geometry perturbation	49
Table 2.3 Reservoir Properties at Initial Conditions	50
Table 2.4 Injection Well Parameters and Specifications.	52
Table 3.1 Injection well parameters used for simulation.	64
Table 4.1 Procedure for the application of Gassmann's formulations.....	87
Table 4.2 Properties of minerals and fluid for the Cranfield Reservoir.....	88
Table 5.1 Model selection workflow	94

Acknowledgments

A work of this magnitude certainly cannot be accomplished by the sole effort of one individual. There are many whose tremendous contributions to this work deserve to be acknowledged. First and foremost, my deepest appreciation goes to my advisor, Dr. Sanjay Srinivasan for being a great shepherd and an excellent mentor. My overall academic development at Penn State owes so much to his exceptional guidance and enormous support, and I am thankful for working under his stewardship. As I step into the real world, Dr. Srinivasan's passion to help his students to succeed is an admirable character that I will emulate. My gratitude extends to my committee members for their immense contributions to my work. Their insights and recommendations shaped this work greatly. I also am pleased to acknowledge the funding received as a part of the John and Willie Leone family chair.

I also extend a hand of appreciation to Dr. Rui Zhang for graciously providing me with the Cranfield 3D velocity models, and for offering me time and support. Dr. Zhang was always immediately available whenever I needed his expertise.

Special thanks to my current lab mates for enriching my experience at Penn State. To my former lab mate, Dr. Kshitij Dawar, thank you for the outstanding friendship, and support.

I want to thank my wife, Mariam, for working behind the scenes to ensure that I succeed. She has been relentlessly supportive, and has been the most precious gift that life has given me. I am grateful for her love, encouragement, and the wonderful children (Irfan and Rushda) she has given me.

To my parents Aisha Ibrahim and Dawuda Adam, I thank you for the constant prayers, support, and encouragement. I pray for you to live long enough to reap the fruits of the seed you have sown in me.

I would be remiss if I did not express my most profound gratitude to the Almighty Allah for how far He has brought me. "Alhamdulillah!"

Dedication

To my late uncle, Kobina, who was my staunch supporter, and who formed part of my decision to pursue PhD studies, but did not live to see me finish this journey, it is to your memory that I dedicate this dissertation. The sacrifice, and the memories you have created in my life will never be forgotten.

Chapter 1 Introduction

Point bars (Fig. 1.1) are channel sediments that accumulate when sinuous or meandering rivers or channels migrate laterally over a geologic period. The migration is due to the erosion of channel sediments from the outer bend of the channel (cut bank), and subsequent deposition of the eroded sediments into the inner bed of the channel (Nanson and Croke, 1992; Willis & Tang, 2010). Point bars can serve as high storage capacity reservoirs. For example, the Athabasca Oil Sands deposit in the Lower Cretaceous McMurray Formation in Canada—which hosts one of the world’s largest heavy oil accumulations—is predominantly composed of point bar deposits (Austin-Adigio et al., 2018; Labrecque et al., 2011). The Widuri field (Carter, 2003) and the Little Creek Field in southwestern Mississippi (Werren et al., 1990) are other examples. Also, the Cranfield, Mississippi reservoir which is considered by several studies (e.g., Daley et al., 2014; Delshad et al., 2013; Lu et al., 2013a; Yang et al., 2013; Zhang et al., 2013) as a viable candidate for CO₂ sequestration experiments is characterized as a point bar reservoir.

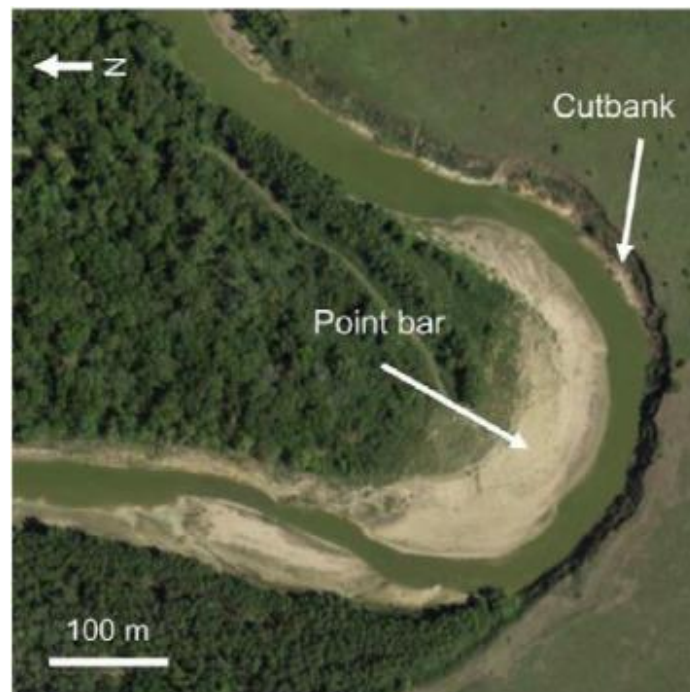


Fig. 1.1 Aerial view of a point bar. As the meandering channel migrates outwards towards the outer bend, channel sediments are eroded from the outer bend of the channel meander (i.e., the cutbank) and are deposited at the inner bend of the meander. Adopted from (Güneralp & Marston, 2012).

However, point bars exhibit complex spatial heterogeneity (Su et al., 2013) that can influence their exploitation for hydrocarbon production and CO₂ sequestration. The heterogeneity varies in different spatial directions due to the changing flow dynamics of the meandering river as it interacts with the topography. Accurate and efficient modeling of the point bar requires an understanding of the river flow dynamics and how that impacts the patterns of heterogeneities. As a sediment-charged river flows from upstream to downstream, the energy associated with the flow reduces (Leopold and Wolman, 1960; Thompson, 1986). Consequently, the coarser sediments (i.e., sand-prone sediments) are deposited first while the finer ones (i.e., mud-prone sediments) are carried in suspension until they are deposited later when the flow medium energy is low enough. This gives the point bar a fining trend in the downstream direction (Fustic et al., 2012; Labrecque et al., 2011; Thomas et al., 1987). The same difference in energy of the flow is seen if one progresses laterally across the channel meander. At the outer bank (i.e., cut bank), the energy associated with the flow medium is high while the flow weakens at the inner bank (Nanson, 1980). This encourages deposition of sediments in a manner that fines into the inner bend of the channel (Jackson, 1976). In the vertical direction, the contrasting densities in sediments causes an overall fining upward succession (Allen, 1965). Lateral migration of the channel leads to the formation of lateral accretion surfaces, the vertical component of which is the inclined heterolithic stratification (IHS) surfaces (Fig. 1.2). Within each IHS unit, grain sizes decrease in the direction perpendicular to the inclined surfaces. Shale draping occurs along the surfaces of the lateral accretions and the IHS (Pranter et al., 2007).

The impact of the shale drapes on hydrocarbon fluid flow and production can be significant (Willis and White, 2000). They are potential flow baffles (Hartkamp-Bakker and Donselaar, 1993; Richardson et al., 1978), as they interrupt reservoir connectivity and impede fluid flow (Awejori & Radonjic, 2022). This in turn affects the distribution of fluids, sweep efficiency, breakthrough time and the overall recovery efficiency of recovery schemes in point bar reservoirs (Awejori et al., 2021, 2022; Davies & Haldorsen, 1987; Jackson & Muggeridge, 2000; Pranter et al., 2007; Stephen et al., 2001). In CO₂ storage scenarios, the heterogeneities can affect the migration of the CO₂ plume and the storage capacity of the reservoir (Issautier et al., 2013, 2014).

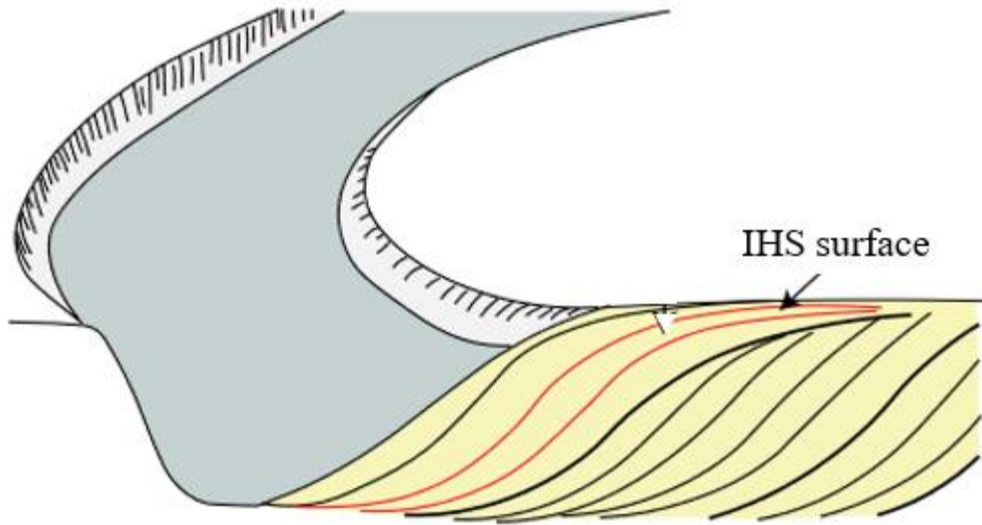


Fig. 1.2 Point bar schematic showing laterally accreting inclined heterolithic stratifications formed by lateral migration of a sinuous river. Adapted from (McMahon & Davies, 2018).

Several studies have attempted to model or characterize point bar reservoir heterogeneities. Some works have relied on outcrop analogs to model point bars (e.g., Pranter et al., 2007; Musial et al., 2013). As impactful as these works have been, it is worth mentioning that outcrop data are generally sparse and are affected by factors such as weathering. Therefore, models derived solely from outcrop observations may not accurately reflect the reservoir characteristics under subsurface conditions. This may lead to a difficulty in reconciling subsurface information with surface or outcrop observations. This observation has also been reinforced in earlier works by (Nardin et al., 2013; Li and Srinivasan, 2015; Durkin et al., 2017). Some of these prior modeling approaches are largely deterministic (e.g., Musial et al., 2013) and do not allow for the assessment of uncertainties. However, considering the high level of uncertainty associated with the precise pattern of heterogeneity exhibited by point bar features such as the shale drapes, deterministic predictions of process performance such as recovery of hydrocarbons or injection of CO₂ for subsurface sequestration may completely miss the mark. In contrast, stochastic schemes (e.g., Pyrcz and Deutsch, 2004; Pyrcz et al., 2009; Yin, 2013) account for uncertainties. Stochastic-based models used for representing fluvial bodies could be object-based models, process-based models, surface-based models, or geostatistical models.

Object-based methods (e.g., Boisvert, 2011; Deutsch & Wang, 1996; Deutsch & Tran, 2002; Yin, 2013) model fluvial reservoirs as spatial objects defined by a conceptual geometric model and stochastically embed the objects within a background matrix. The placement of these objects is driven by a probabilistic criterion such as a Poisson distribution. These methods are particularly applicable

when the geometry of the geobody is well understood and can be defined using simple parametric objects (Hassanpour et al., 2013). Some object-based methods are iterative (e.g., Deutsch & Tran, 2002), and data conditioning is realized via an objective function that accounts for the mismatch between facies proportions and the conditioning data. For the iterative object-based methods, data conditioning is difficult when there is a large dataset to be honored. Some non-iterative object-based approaches can overcome this drawback. Viseur et al., (2001) and Shmaryan and Deutsch, (1999) developed an object-based technique that efficiently generates channels such that, by construction, the well or hard data is honored non-iteratively. Well data is interpreted as channel sand or non-channel sand facies (e.g., shale, levee, splay). The algorithm works such that the objects by construction pass through the data locations. The non-iterative techniques can easily honor large datasets; they are also very fast in simulating channelized bodies. However, the non-iterative techniques can be challenged when implemented on spatially dense data such as those from horizontal wells, because then the process of conditioning while preserving the geometric description of the objects becomes difficult.

Process-based models, on the other hand, represent reservoir geology by simulating the fundamental processes that cause migration of meandering rivers (e.g., point bars). Sun et al., (1996) proposed a process-based model to study channel meander migration process. The model is based on the bend theory of river meanders by Ikeda, et al., (1981), and is similar to the work of Howard, (1983). Other process-based studies include (Pyrzcz, 2001; Pyrcz and Deutsch, 2004; Pyrcz et al., 2009; Shu et al., 2015). For all these works, channel meander migration is determined from equation 1.1 (Ikeda, et al., 1981; Sun, et al., 1996)

$$\xi = E\bar{u}_{sb} \quad (1.1)$$

where ξ is the meander migration rate, E is the erosion coefficient and \bar{u}_{sb} is the near-bank velocity which is determined from equation (1.2) (Sun, et al., 1996).

$$\bar{u}_{sb} = -bu_{so}\bar{C} + \frac{bC_f}{u_{so}} \left[\frac{u_{so}^4}{gh_o^2} + (A' + 2) \frac{u_{so}^2}{h_o} \right] \cdot \int_0^\infty \exp\left(\frac{-2C_f s'}{h_o}\right) \cdot \bar{C}(s - s') ds \quad (1.2)'$$

where b is the channel or river half width, u_{so} is the mean flow velocity, \bar{C} is the local channel curvature of the channel centerline, C_f is the frictional coefficient, g is the gravitational constant, h_o is the average depth of channel, A' is the scour factor ($A' > 0$) and s is the coordinate along the river central line.

Process-based methods can produce geologically realistic models because they account for the erosion, deposition, and sedimentation processes in fluvial reservoir formation. Due to this, they have found many applications in fluvial reservoir modeling, particularly in reproducing the geologic heterogeneity in point bar reservoirs. Pircz and Deutsch, (2004) used this method to generate IHS models by simulating the lateral migration of channels, while Willis and Tang, (2010) applied this method to develop 3D models for architectural connectivity in point bars to capture flow barriers. However, just like object-based methods, conditioning process-based models to data remains an unresolved challenge.

Surface-based methods (e.g., Niu et al., 2021; Pircz et al., 2005) model fluvial bodies using the bounding surfaces of architectural elements. The surfaces represent the transition between sedimentary events that have been preserved during the processes of erosion and deposition. The underlying principle for this method is to initiate the modeling process from a given base surface and generate a new surface from the base surface, by stacking the depositional or erosional events. The process is subsequently repeated by taking the new surface as the base surface upon which the next event is stacked (Bertoncello et al., 2013). Some of these methods (e.g., Ruiu et al, 2016; Zhang et. al, 2018) are very efficient in modeling complex geometries of fluvial reservoirs like point bars. For surface-based methods, if one does not have a good working knowledge of the surfaces, accurate delineation of the bounding surfaces of architectural elements can be elusive. Thus, aliasing can occur at the interfaces between successive fluvial bodies. Additionally, surface-based methods can be very difficult to constrain to data (Bertoncello et al., 2013). Another concern with these methods is that their implementation can be time-consuming and computationally burdensome due to the fine mesh that is required to preserve the smoothness of the surfaces.

Geostatistical methods (e.g., Sequential Indicator Simulation (Deutsch, 2006)) have also featured prominently in the modeling of point bars and are very useful particularly in the case of sparse or insufficient dataset. These methods use statistical measures such as semi-variograms or multiple point statistics (MPS) to describe the spatial continuity of reservoir rock types. As these methods increasingly become popular among researchers and modelers, so are research attempts targeted at solving the challenges in their implementation. In recent times, some studies have focused on reducing the computational burden associated with geostatistical methods using multiple point statistics (e.g., Cui et al., 2021) or hybrid MPS and machine learning based methods (e.g., Bai & Tahmasebi, 2021). Others (e.g., Yao et al., 2021) have addressed the problem of using training images as statistical analogs, which stem from the conflicts that occur between training images and sample data, especially

in the MPS method. In simulating spatial attributes, the authors use kernels to develop a learning-based algorithm for geostatistical interpolation, based on high-order spatial statistics that matches the spatial attributes of the target model. de Figueiredo et al., (2021) have also proposed the Direct Multivariate Simulation method to handle the modeling problems associated with generating multiple realizations of random fields, particularly where there is complex multivariate distribution with heteroscedastic and non-linear relations among variables.

The geostatistical methods offer the greatest advantage in terms of reproducing geological realism while representing the high degree of associated uncertainty. Yet, despite these successes, geostatistical methods are faced with a common problem regarding the preservation of heterogeneities for reservoirs with complex curvilinear architecture like point bars. Geostatistical methods rely on rectilinear grids (i.e., orthogonal grids) to model spatial properties. However, given the curvilinear architecture of point bars, modeling the properties on a rectilinear grid cannot properly represent the curvilinear continuity of the heterogeneities. Even the geostatistical simulation techniques that can be constrained to multiple point statistics (e.g., Caers and Zhang, 2005; Eskandari and Srinivasan, 2010)), cannot sufficiently capture the erosional surfaces (Li and Srinivasan, 2015), which are major discontinuity surfaces that typify point bars. And as has long been recognized (Giordano et al., 1985; Haldorsen & Chang, 1986), the continuity of channels or shale drapes controls the fluid flow in heterogeneous porous media such as point bars. For this reason, the inability of the conventional geostatistical methods to adequately preserve these salient heterogeneities may compromise flow simulation results from geostatistically generated point bar models.

Furthermore, owing to the thinness of the shale drapes, if they are modeled using an extremely fine mesh—as is typically the case—the computational cost can escalate steeply, and subsequent upscaling may also destroy the shale drape continuity. The modeling difficulties are further compounded by uncertainties stemming from multiple sources. An example is the high level of uncertainty associated with the location and proportion of shale drapes on the IHS surfaces. The location and proportion of shale drapes are difficult to infer from well data and seismic information, due to the sparsity of well data and the insufficient resolution of seismic data to adequately capture such thin features. Other sources of uncertainty are the geometry of the point bar, and the location of the channel path, which are again, difficult to infer due to the sparsity of well data.

To reduce model uncertainties, dynamic data such as production and injection data are typically assimilated into geologic models. This data assimilation process (i.e., history matching) is a model calibration procedure that adjusts the reservoir model parameters to reflect field observations. Many

of the proposed history matching methods capture prior uncertainty in models by generating initial ensemble of models using geostatistical simulation. The most commonly used ensemble-based method is the Ensemble Kalman Filter (EnKF) (Geir Evensen, 2003), in which updates are performed on the initial ensemble of models by assimilating observed secondary variables (e.g., pressure). The EnKF can assimilate multiple data and is computationally efficient. The underlying assumption of the EnKF is that the joint relationship between the primary state variables (e.g., permeability) and the secondary state variables (e.g., flow rate) is multivariate Gaussian, and therefore optimally represented using a linear update equation. However, this is a simplification that renders the EnKF incapable of performing optimal updates in cases where the state variables describing the reservoir are described by a non-Gaussian distribution and hence the optimal form of the update equation for state variables is nonlinear.

Apart from the ensemble-based methods, there are non-ensemble based data assimilation methods like the gradual deformation method (Hu, 2000), which reduces the history matching problem to a basic optimization problem. This method requires the reservoir geology to follow a Gaussian distribution; therefore, it is ill-suited for complex reservoir geologies with curvilinear architecture such as point bars that exhibit a high degree of continuity that is impossible to preserve in a Gaussian model. A more suitable history matching method for complex reservoirs is the probability perturbation method (Caers, 2003a). However, a common problem with both methods is deterioration of performance due to poor convergence. The parameterizations used in these methods limit the search space for optimization, which results in a poor convergence (Johansen & Stenby, 2005). Detailed discussions of different history matching techniques are done later in this dissertation.

Data to be assimilated in reservoir modeling workflows can come from several sources. Apart from production and injection data that are commonly integrated, timelapse seismic information is also assimilated using both ensemble-based and non-ensemble-based methods. Seismic forward models are obtained by using rock-physics modeling, commonly based on the (Gassmann, 1951) method, to derive elastic properties and seismic properties from reservoir (e.g., porosity, mineral composition) and fluid properties (e.g., saturation, pressure, density).

Time lapse seismic data integration poses some challenges to the data assimilation workflow. For one, due to the frequency of seismic surveys, time lapse seismic data can be exceptionally large volumes of data to be integrated into the data assimilation workflow. This can be computationally demanding and time consuming (Yin et al., 2019). In the case of EnKF, the degree of freedom available for data assimilation is dictated by the ensemble size, which limits the ability of the EnKF to assimilate seismic data for large reservoirs (Emerick & Reynolds, 2012). Additionally, integrating time-lapse seismic

information directly into the data assimilation workflow without prior evaluation of the data may lead to the inheritance of errors being propagated within the data assimilation workflow(Alfonzo et al., 2017). As noted by Li, (2017), data assimilation is sensitive to errors, which implies that small errors in data can cause large fluctuations in predictions. This problem can worsen with the increased size of seismic datasets (Yin et.al, 2019)

1.1 Problem Statement

Point bar reservoir geology is frequently encountered in oil and gas developments projects, and in CO₂ sequestration projects worldwide. Reliably predicting subsurface CO₂ displacement in these projects requires accurate models for the point bar reservoir geology. However, a comprehensive modeling method that adequately preserves point bar internal architecture and its associated heterogeneities is still not available. Traditional geostatistical methods cannot adequately capture the curvilinear architecture of point bars. Even geostatistical simulation techniques that can be constrained to multiple point statistics cannot capture the architecture of the point bars because they use regular grids to represent the heterogeneity. The modeling challenges are further compounded by the high level of uncertainty that characterizes models that are used to represent point bar reservoirs. These uncertainties stem from various sources. Firstly, the well data that provides reliable source of information for reservoir modeling are sparse especially in the case of CO₂ sequestration projects. Additionally, the precise pattern of heterogeneities in the subsurface reservoirs is fraught with uncertainties such as due to erosion, that are difficult to capture in subsurface reservoir models. Even 3D seismic data collected in the field may sometimes miss salient reservoir heterogeneities, especially in thin bed reservoirs like the Cranfield reservoir because the seismic resolution is not enough to capture the heterogeneities.

The data assimilation methods that are commonly used to resolve the prior geologic uncertainties are unable to properly account for the strong non-linear relationship between the highly heterogeneous point bar reservoir properties (e.g., permeability), and the reservoir flow response variables like flow rate, bottom-hole pressure etc. Also, assimilating time-lapse seismic data into history matching workflow is challenging computationally challenging due to the large volumes of seismic data that needs to be integrated within modeling workflows. Further, ensemble-based data assimilation methods like EnKF are unable to faithfully represent time-lapse seismic information because of the computational expense associated with generating a large ensemble, of rather large

reservoir models. These challenges leave significant amount of residual uncertainty in the updated reservoir models even after integrating all available data. Therefore, in addition to the need for a modeling framework that can adequately preserve the reservoir heterogeneity, a data assimilation workflow that can handle the non-linear characteristics of the reservoir while realistically representing the residual uncertainties in the updated models is necessary.

1.2 Proposed Approach

The prior discussions call for a modeling framework that can 1) accurately preserve point bar architecture and heterogeneities, 2) accomplish model calibration using dynamic injection data while preserving the non-Gaussian characteristics of the reservoir and 3) faithfully represent the time-lapse seismic information. In this dissertation, an integrated modeling framework is proposed to address these challenges in three broad steps. First, a flexible and stochastic process-based model (conditioned to well data) is proposed for representing the point bar reservoir, while honoring its typical structural characteristics and geologic heterogeneities. This is done by combining geometric modeling with geostatistical property modeling. Ensemble of models are generated to account for uncertainties. The preservation of the curvilinear architecture of the reservoir and the heterogeneities is done respectively by 1) developing a gridding scheme that generates highly representative curvilinear grids to account for the point bar curvilinear geometry, and 2) incorporating a grid transformation scheme that maps the curvilinear grid to a rectilinear grid where the geostatistical modeling can be take place. Essential element of the proposed workflow is the stochastic representation of shale drapes across interfaces between successive accretion surfaces and inclined heterolithic stratification surfaces. The dissertation also examines the geological modeling of the point bar reservoir within the context of fluid flow. The impact of point-bar reservoir model parameters on fluid flow and flow response variables (e.g., bottom-hole pressure) is investigated. The second major aim of this dissertation is to assimilate field flow response data to calibrate the ensemble of point bar models. Specifically, it focusses on reducing the uncertainties in the ensemble of models by assimilating CO₂ injection data. This is accomplished by implementing a two-step model update process. In the first step the structure of the point bar model is perturbed within the EnKF framework. That is followed by a second step where the reservoir property (permeability) is perturbed using a non-Gaussian Indicator based Data Assimilation (InDA) approach. The last important aim of this research is to assimilate time-lapse seismic information within the modeling framework. Time-lapse seismic data reveals important information about CO₂ migration paths that can further constrain the geologic models. In this research, a unique Bayesian model

selection workflow is implemented that uses a rock physics to synthesize the seismic response of the reservoir model ensemble, perform multidimensional scaling to identify clusters of models and finally, utilize a Bayesian approach to retrieve the cluster closest to the observed time-lapse seismic response model. For each stage of the data assimilation workflow, value of information analyses is conducted to evaluate whether the expected improvement in the model that is realized by assimilating additional information justifies the cost of obtaining that information.

Chapter 2 Stochastic Modeling of Point bars

The process for modeling point bars commences by first interpreting facies and categorizing them into channels and point bars based on available log data. Based on that interpretation, we developed a stochastic algorithm for modeling the channel flow path, and migrating the channel path to capture the lateral accretions and inclined heterolithic stratifications (IHS). Curvilinear grids are subsequently generated for representing these heterogeneities and then, the geometries of the lateral migrations and IHS are combined to form a 3D grid to represent the entire point bar geometry. Geostatistical simulation is then performed by first transforming the curvilinear geometry to a cartesian grid and subsequently performing geostatistics on the transformed grid to model the point bar reservoir properties. Finally, the modeled grid is mapped back to the original curvilinear grid. The proposed workflow for modeling the point bar is summarized in Fig. 2.1. This workflow will be discussed in detail in subsequent sections.

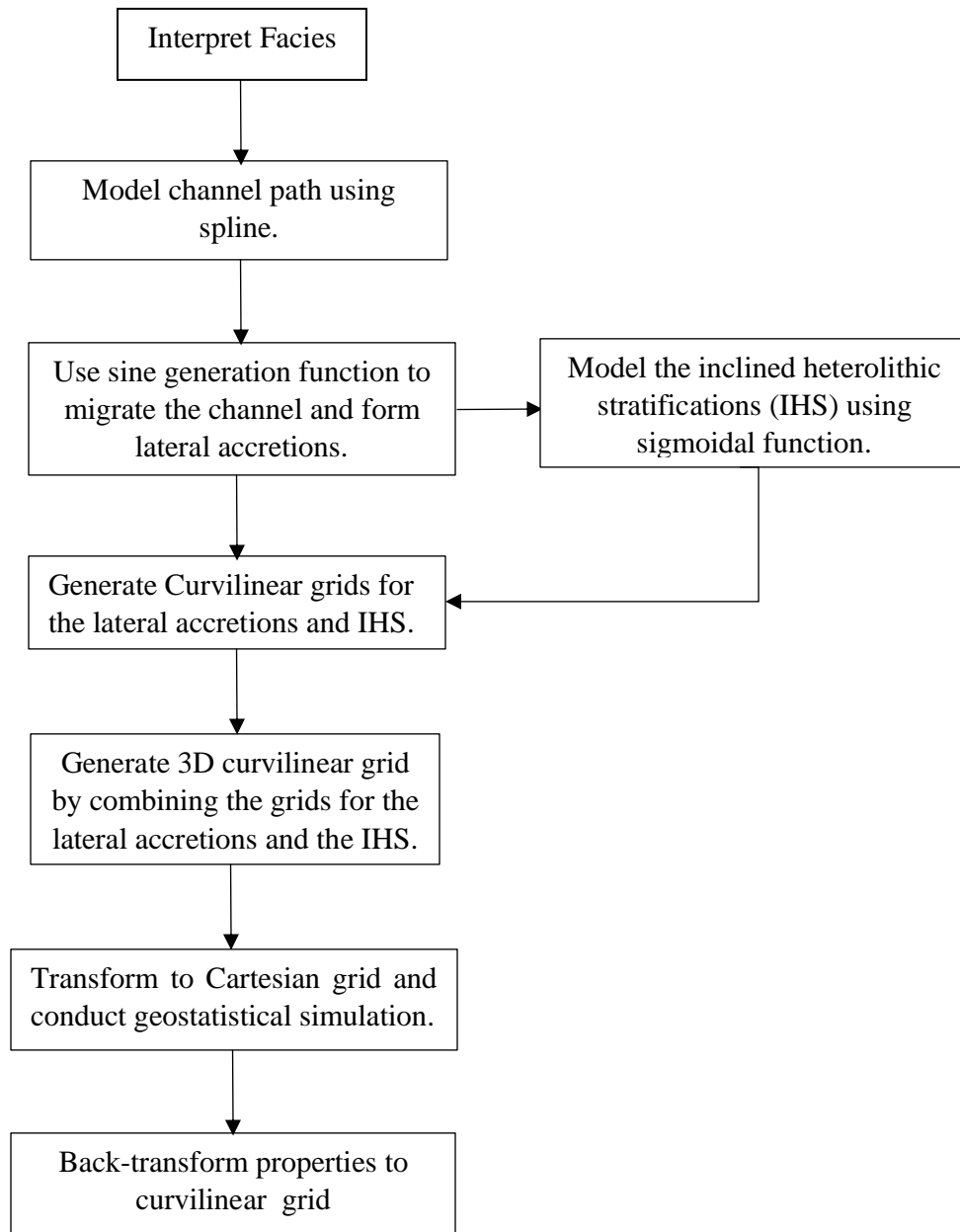


Fig. 2.1 Proposed flow chart for modeling the point bar reservoir.

2.1 Details of point bar heterogeneities and depositional trends

The main heterogeneities in point-bar systems are lateral accretions and inclined heterolithic stratifications (IHS) which are formed as a result of lateral migration of the channel. Moving along section AB in Fig. 2.2a, first the channel is encountered. As one progresses further towards B, some curvilinear features are observed. These are remnants of past channel migrations which are referred to as lateral accretions. In cross section, these accretion surfaces make up the IHS as shown in 2.2b. The channel migrations are characterized by an abrupt erosion on the convex part of the bend (closer to A in 2.2a) and a gradual deposition on the concave part (closer to B in 2.2a). The arrows in 2.2b indicate direction of depositional trends to be captured in the geostatistical modeling process. Details of these depositional trends will be discussed later.

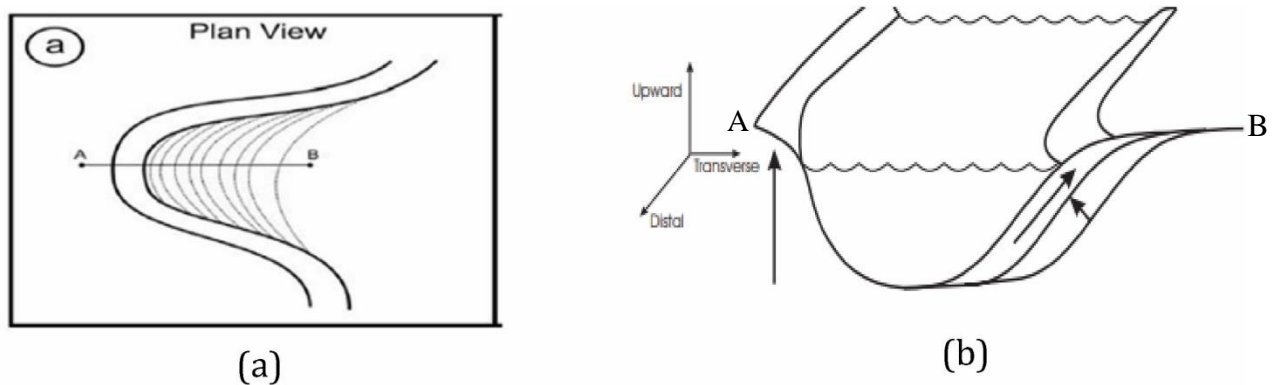


Fig. 2.2 (a) lateral accretions, (b) Cross sectional view illustrating IHS. Arrows indicate direction of fining of sediments which would be accounted for in the geostatistical simulation (Thomas, et al., 1987; Pyrcz & Deutsch, 2004b).

2.2 Modeling Steps

i. Channel and point bar identification.

Different techniques have been used to identify point bars and channels. Some of these are based on outcrop examinations (e.g., Pranter et al., (2007), and well log interpretations (e.g., Durkin et al., 2017; Nazeer et al., 2016; Odundun & Nton, 2011). In those works, it has been shown that a bell shape signature in Spontaneous Potential (SP) logs and Gamma Ray (GR) logs is an indication of point bar, while a blocky or cylindrical shape signal indicates a channel sand (Fig. 2.3). In this research, we used well logs (SP logs and GR logs) from the Cranfield, Mississippi dataset to identify the facies in the

study area. The wells from Cranfield were chosen because they are located at the site of a geologic sequestration experiment, which is of interest to this study. In addition to the well logs that provide facies information at those locations, there is CO₂ injection data available for this site and that will be used in a follow up study for a history matching/model calibration exercise. Fig. 2.4 shows some of the well logs used in this research and how the facies interpretation was done based on the signatures documented in Fig 2.3.

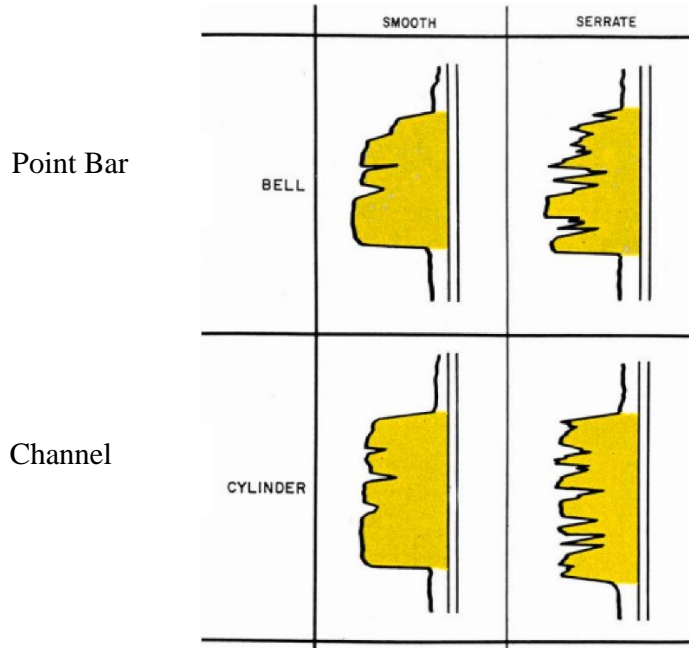


Fig. 2.3 Classification of SP log profiles for point bar and channel identification. Blocky or cylindrical shape is an indication of a channel while a bell shape is an indication of a point bar. Adapted from (Wilson & Nanz, 1959)

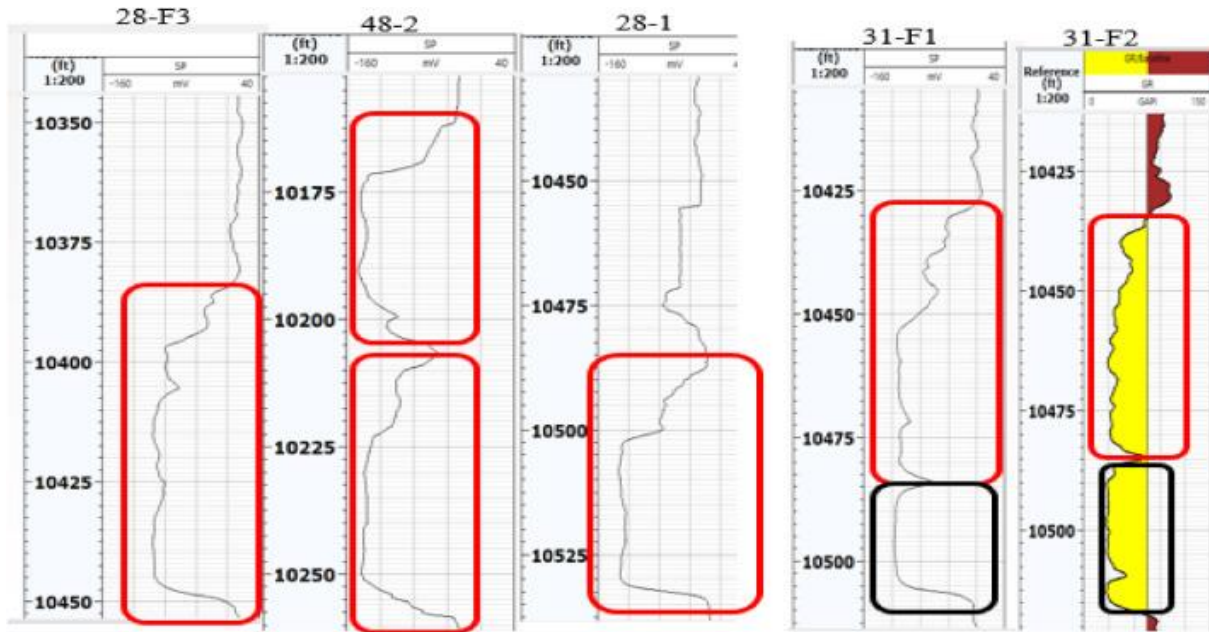


Fig. 2.4 Well log readings for wells 28F-3, 48-2, 28-1, 31-F1 and 31F-3 at Cranfield. The first four well logs show SP reading while the last represent GR logs. Identified channel facies (blocky shape signals) are demarcated in black. Point bar facies (bell shape signals) are in red demarcations.

ii. Modeling the channel flow path

To model the point bar, it is necessary to recreate the channel flow path as the point bar itself is a manifestation of the migration of that channel path. It is the migration of the channel that allows for modeling the main heterogeneities, which would be combined to form the 3D point bar model. The proposed procedure for recreating the channel path is as follows:

Identifying meander direction: Channel direction can be inferred considering the variation in channel thickness which decreases as the channel migrates from upstream to downstream (Brierley & Hickin, 1985; Pitlick & Cress, 2002). Based on well log interpretation, well coordinates can be sorted accordingly in the direction of channel progression. Fig. 2.5 illustrates the stepwise procedure for recreating the meander path; the blue points are channel nodes, and the red points are point bar nodes. The direction of channel or meander progression is in the East-West direction from channel node 1 through 13.

Conditioning meander path through channel nodes: Here, two constraints can be imposed; the primary constraint is that the meander path must go through channel nodes sequentially in the direction of channel progression. In the case of insufficient channel nodes, additional nodes (i.e., secondary nodes) are stochastically generated to guide the meander path. The secondary

constraint is that the meander path must bend around the point bar locations. As can be seen in all the modeling stages in Fig. 2.5, the meander path, while going through the channel nodes, is conditioned to bend around the point bar nodes. This secondary constraint is necessary to satisfy the geological and morphological phenomenon that point bars are formed at the bends of meandering fluvial bodies. The meander path is defined by a parametric natural cubic spline which passes through the given sequence of channel nodes.

The basic form of cubic spline, with coefficients a, b, c and d is given as:

$$P(t) = at_j^3 + bt_j^2 + ct_j + d \quad (2.1)$$

The parameter value t for the j th channel node, denoted by t_j is the cumulative sum of the square root of chord length defined according to the centripetal scheme by (Lee, 1989), expressed as:

$$t_j = \sum_{i < j} \sqrt{\|channelnodes_{i+1} - channelnodes_i\|_2} \quad (2.2)$$

The coefficients (a, b, c, d) which are weights for interpolating the channel nodes, which can be determined by following the formulations of (Bartels et al., 1995). For details, see appendix A.

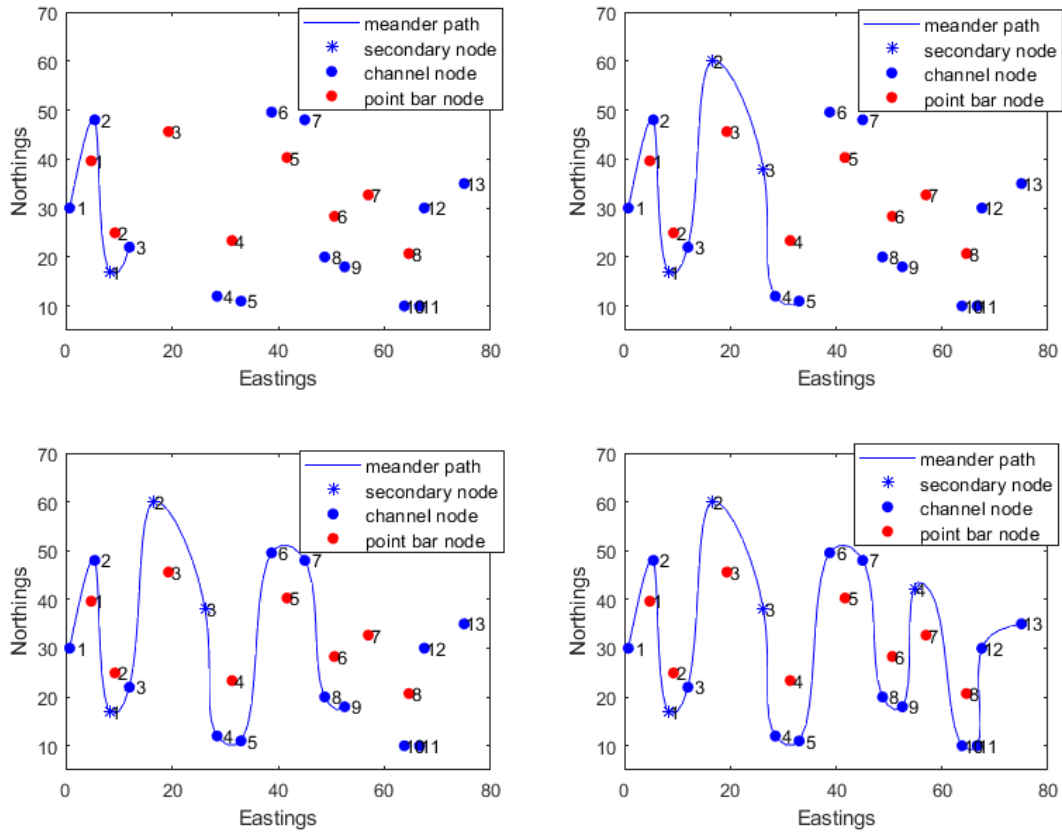


Fig. 2.5 Workflow for modeling the meander path demonstrated on a synthetic example. (a) Modeling stage 1 – marking channel path passing through channel nodes and bending to accommodate point bars on the concave side of the bends, (b) Modeling stage 2 – insertion of secondary node to define channel path while accommodating a point bar on the concave side of the bend, (c) Modeling stage 3 and (d) Modeling stage 4 – final channel path accommodating all the well data. Blue points are channel locations and red points are point bar locations.

iii. Geometric modeling of IHS and lateral accretions

The IHS were modeled using sigmoidal function as described by (Thomas et al, 1987). Suppose h is the height of the point bar, and a controls the slope of the IHS over a horizontal distance x as shown in Fig. 2.6, then the sigmoidal function (equation 2.3) can be used to define the geometry, Z_{ihs} of the IHS.

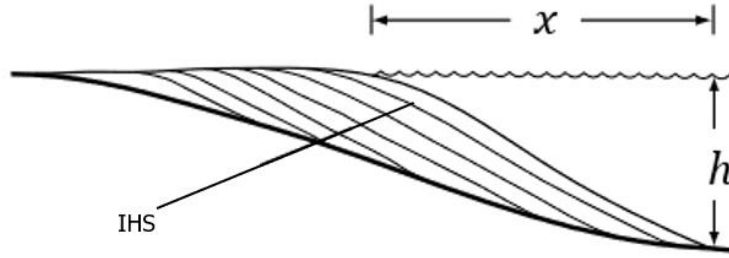


Fig. 2.6 Cross-section of a point bar deposit illustrating IHS. Adapted from (Pranter et al., 2007).

$$Z_{ihs} = \frac{h}{1 + e^{-ax}} \quad (2.3)$$

Equation 2.4 defines sine generation function (SGF) as proposed by (Langbein and Leopold, 1966). This would be used in later discussion to approximate the meander path and migrate the meander to model the geometry of the lateral accretion.

$$\theta(l) = \omega \cdot \sin\left(\frac{2\pi l}{L}\right) \quad (2.4)$$

where, for our case, L , is the total length along the channel, l is the length at any point along the channel, $\theta(l)$ defines the direction at each point along the channel and ω is the maximum angular displacement of the channel with the horizontal. The parametric forms which express the SGF in Cartesian coordinates are equations 2.5a and 2.5b (Hathout, 2015; Movshovitz-Hadar & Shmukler, 2000)

$$x(t) = \int_0^t \cos\left[\omega \cdot \sin\left(\frac{2\pi l}{L}\right)\right] dl \quad (2.5a)$$

$$y(t) = \int_0^t \sin\left[\omega \cdot \sin\left(\frac{2\pi l}{L}\right)\right] dl \quad (2.5b)$$

where t and ω satisfy the conditions $0 < t < L$ and $0^\circ < \omega < 90^\circ$, respectively.

2.3 Channel Path Migration

Migrating the current channel path back in time to recreate the initial channel path allows us to capture the geometry of lateral accretions. In doing so, channel path is approximated using the SGF. The SGF gives a close approximation of the original channel path as the channel migrates (Langbein and Leopold, 1966; Hathout, 2015). The backward migration of the channel is done by decreasing the angular placement (ω) in the SGF to recreate the initial channel path (Fig. 2.7).

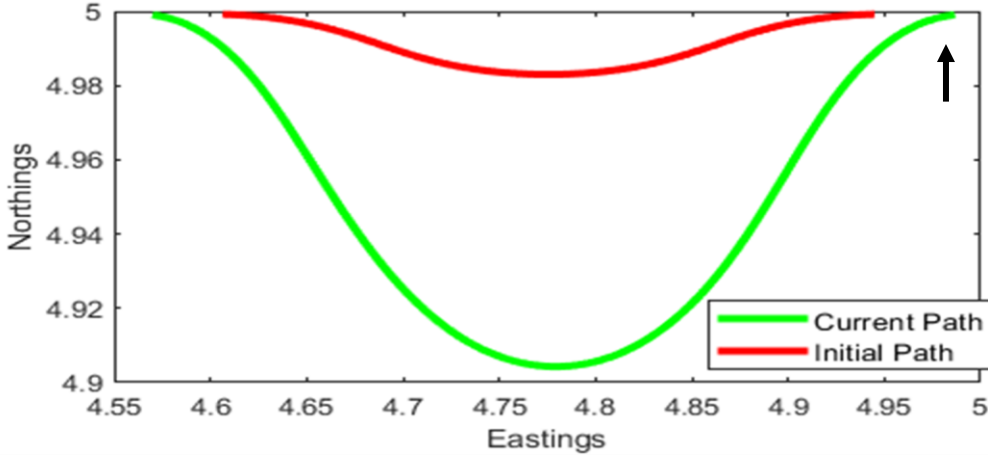


Fig. 2.7 Recreating initial channel path using SGF. Arrow points to the direction of backward migration

However, the use of SGF to migrate the current channel path to recreate the initial channel path may not yield realistic approximations for channels with asymmetric aerial geometry (Fig 2.8a). In such cases, a cubic spline function can be used. Migration of the channel path can be done by perturbing the spline coefficients. This approach is problematic because ensuring that the coefficients of the spline exhibit consistency among themselves is extremely difficult. Instead, we accomplish the migration task by defining a focal point towards which n possible channel meander paths can be migrated (Fig. 2.8b). That is, if there are p points along the current channel path with coordinates (x_i, y_i) $i = 1, 2 \dots p$, then equation 2.6 can be used to generate n possible initial channel paths between the current channel path and the focal point (x_f, y_f)

$$\left(x_{i_j}, y_{i_j} \right) = \left(x_i + (j - 1) \cdot \frac{(x_i - x_f)}{(n - 1)}, y_i + (j - 1) \cdot \frac{(y_i - y_f)}{(n - 1)} \right) \quad (2.6)$$

where $i = 1, 2, 3 \dots p$; $j = 1, 2, 3 \dots n$; x_i and y_i are respectively, the x and y coordinates of each point at node i along the current channel path, and (x_f, y_f) are defined as:

$$(x_f, y_f) = \begin{cases} \left(x|_{\frac{dy}{dx}=0}, \max(y_i, i = 1, \dots, p) \right), & \text{if channel concaves up} \\ \left(x|_{\frac{dy}{dx}=0}, \min(y_i, i = 1, \dots, p) \right), & \text{if channel concaves down} \end{cases} \quad (2.7)$$

$x|_{\frac{dy}{dx}=0}$ is the x-coordinate at the bend where the local slope of the channel path is zero.

Please note that in all our discussions, it is assumed that the channel progresses in the E-W direction. In case the channel path is oblique, then additional coordinate rotation is necessary for the formulations to work.

Applying equations 2.6 and 2.7 yields the focal point (red point) and the possible initial channel meander paths in Fig. 2.8b. To select the most probable initial meander path, we make use of the idea of erosion coefficients for each of the possible initial channel meander paths. The use of erosion coefficients is guided by the observation that before lateral migration of the channel, the channel path is linear (see Fig. 2.8c). The channel begins to bend when erosion occurs at the banks. Therefore, the extent of channel curvature is an indication of the degree of erosion. Thus, we can capture the extent of curvature or erosion coefficient (α), by using the area bounded by the curves (i.e., the channel paths), as shown in equation 2.8.

$$\alpha = 1 - \frac{A'}{A} \quad (2.8)$$

where A is the area bounded by the pre-migration channel path and the current channel path (Fig. 2.8c), and A' is that bounded by the initial meander path and the current channel path (Fig. 2.8d). If knowledge or field data about the erosion co-efficient is available, we can select the initial meander path as the one that yields the closest match to the erosion coefficient from field data, after applying equation 2.8. Otherwise, one can assume equal likelihood of occurrence for each of the paths and randomly select one of the generated initial channel meander paths. In this demonstration, we randomly sampled the initial meander path (Fig. 2.8d).

Finally, the region bounded by the initial and current channel paths, in Figs. 2.7 and 2.8d can be gridded by following the grid generation procedure that will be discussed in the ensuing sections.

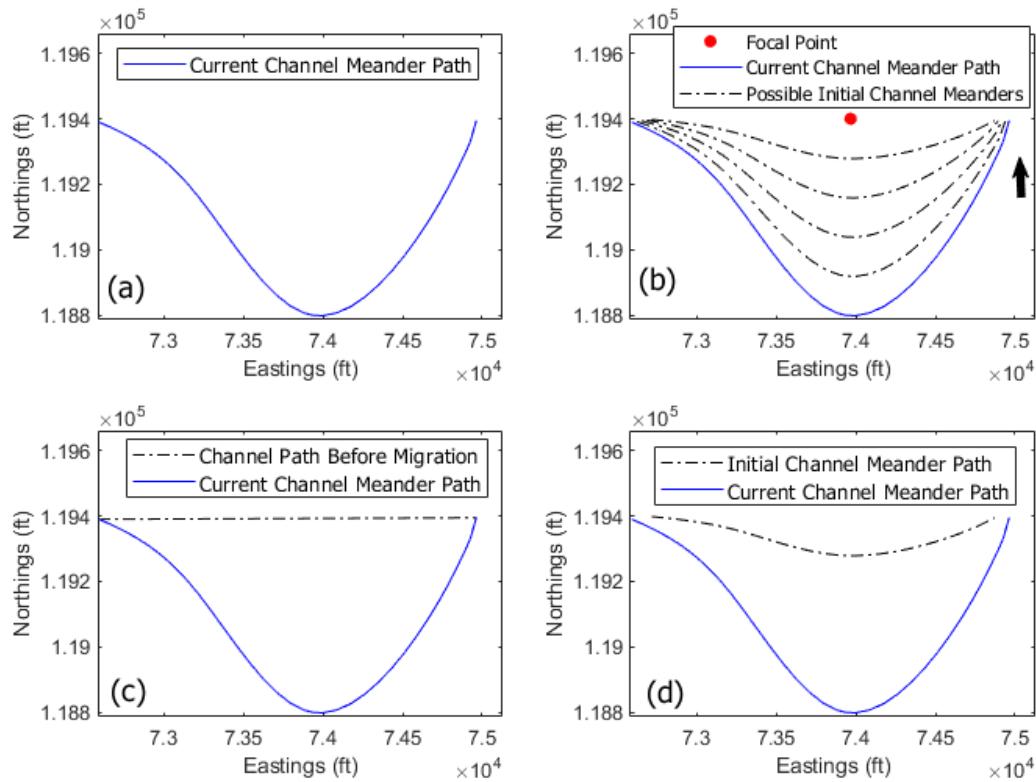


Fig. 2.8 Migration of asymmetric current channel path to recreate initial channel path. a) current channel path, (b) current channel path migrated back to recreate possible initial channel meander paths, (arrow indicates the direction of backward migration, i.e., migration starting from today's channel path to the ancient path), c) area covered by the current channel path and the pre-migration path and d) current channel path and the most probable initial channel path.

2.4 Rendering point bar model on curvilinear grids

The grid generation was implemented separately for the two main heterogeneities – the lateral accretion surfaces and the IHS. The problem was tackled sequentially, first, as a 1D problem by gridding along the meanders only, then as a 2D problem by gridding in-between the prior gridded nodes along one meander path and their corresponding pairs on the other meander. Subsequently, the gridded lateral accretions and the IHS were combined to generate 3D gridded surfaces for the current position of the channel and its initial position prior to the migration. Finally, the region bounded by the two 3D gridded surfaces is also gridded to complete the gridding of the entire point bar.

The grid generation procedure begins by defining a domain of interest. This domain is the region bounded by the initial and current position of the channel. The length, L , of meander path, m , denoted, L_m , is then determined from equation 2.9 (Hartman et al., 2014)

$$L_m = \int_s^b \sqrt{1 + \left(\frac{dy}{dx}\right)^2} dx \quad (2.9)$$

where s and b are respectively, the coordinates at the beginning and end of the channel, the subscript m can range from the initial position to the current position of the channel meander, and $\frac{dy}{dx}$ represents the local slope of the channel.

The number of grid blocks along each meander path and that between the meanders are specified as nx and ny , respectively. To compute the grid nodes along the channel meanders, the block size along the channel meanders is determined from the ratio $\frac{L}{nx}$, and the cumulative distance lx along each channel meander at grid node i becomes $\frac{L}{nx} \cdot (i - 1)$, $\forall i = 1, 2, 3, \dots, nx + 1$. Using this cumulative distance lx at node i , the grid nodes along the channel meanders are determined by revisiting equation 2.5a and 2.5b, where lx replaces l .

The grid generation procedure for the lateral accretions is summarized in Fig. 2.9. Figs. 2.9a and b, show the domain to be gridded and the grid nodes that were determined along each meander path respectively. Next, we determine the grid nodes between the meanders. In Fig. 2.9b, every grid node in any of the meanders has a corresponding pair in the other meander path, and for these corresponding pairs, we determine the Euclidean distance between them, denoted D_{ij} $\forall i = 1, 2, 3 \dots nx + 1$ and $\forall j =$

$1, 2, 3 \dots ny + 1$. Between these pairs, the grid size for each grid block is $\frac{D_{ij}}{ny}$. By computing the angles

between these pairs as α_{ij} , the grid coordinates between the pairs at node ij are determined from equations 2.10a and b as follows:

$$x_{ij} = X_{ij} \pm (j-1) \cdot \frac{D_{ij}}{ny} \cdot \cos \alpha_{ij} \quad (2.10a)$$

$$y_{ij} = Y_{ij} \pm (j-1) \cdot \frac{D_{ij}}{ny} \cdot \sin \alpha_{ij} \quad (2.10b)$$

Here, X_{ij} and Y_{ij} are the grid nodes or coordinates for either of the meanders (red points or green points in Fig. 2.9b). In computing x_{ij} and y_{ij} , one may choose X_{ij} and Y_{ij} from either the current meander only or the initial meander path only, and the signs in equations 2.7a and 2.7b is dependent on this choice.

Equations 2.10a and b complete the gridding in 2D which yields Fig. 2.9c whose equivalent grid is displayed in Fig. 2.9d.

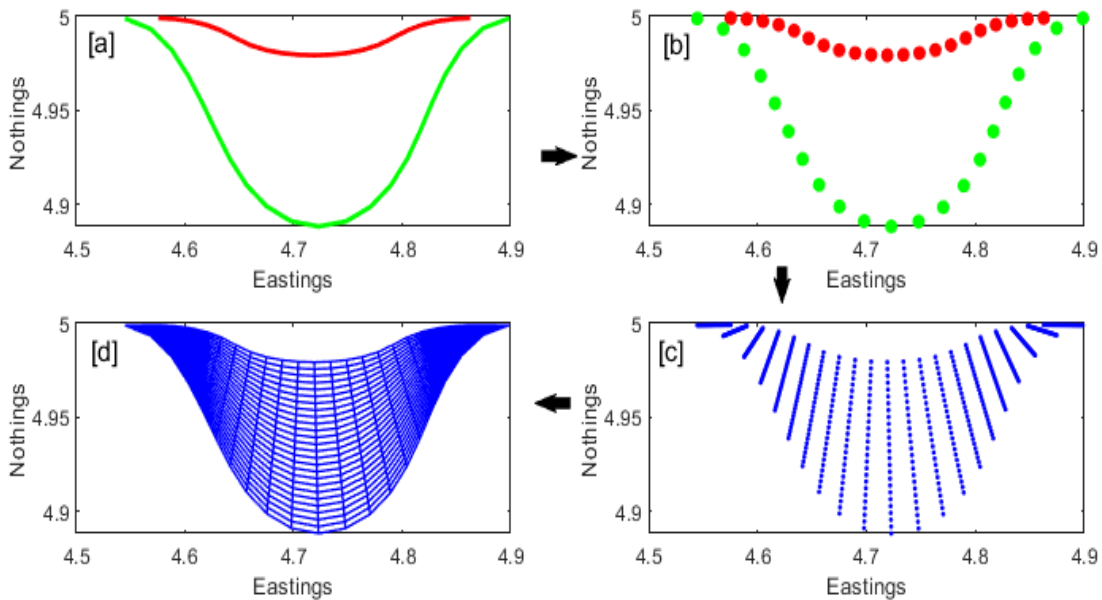


Fig. 2.9 Workflow for gridding the lateral accretions. (a) Domain to be gridded defined by the current channel path (green) and the initial channel path (red) (b) grid nodes computed along the channel paths, (c) grid nodes computed between the channels and (d) curvilinear grid

In situations where the point bar is aerially asymmetric as discussed earlier, the above procedure is still capable of generating a suitable curvilinear grid. To illustrate this, we revisit Fig. 2.8d and apply the above grid generation procedure as illustrated in Fig. 2.10. The grid nodes and the equivalent curvilinear grids are displayed in Fig 2.10c and d, respectively.

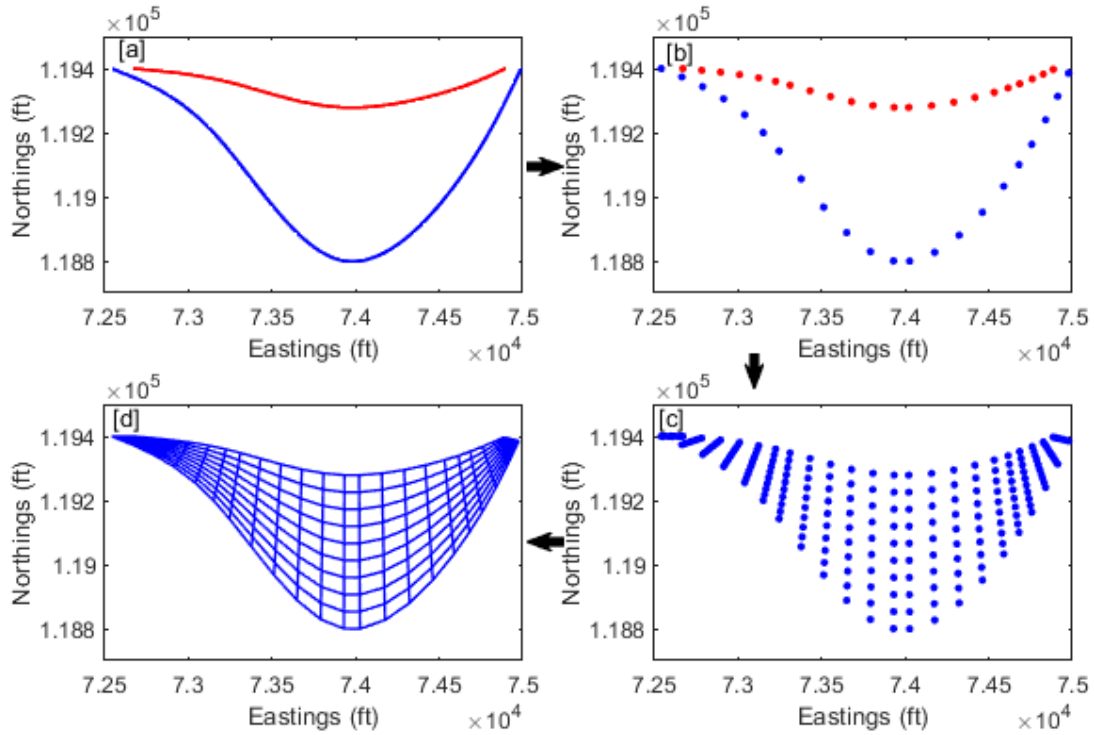


Fig. 2.10 Workflow for gridding the lateral accretions for asymmetric point bar geometries. (a) Domain to be gridded defined by the current channel path (blue) and the initial channel path (red), (b) grid nodes computed along the channel paths, (c) grid nodes computed between the channels and (d) equivalent asymmetric curvilinear grid.

The process for gridding the IHS surfaces is the same as that of the lateral accretions and requires specification of the number of grid blocks along the z-axis (Fig. 2.11).

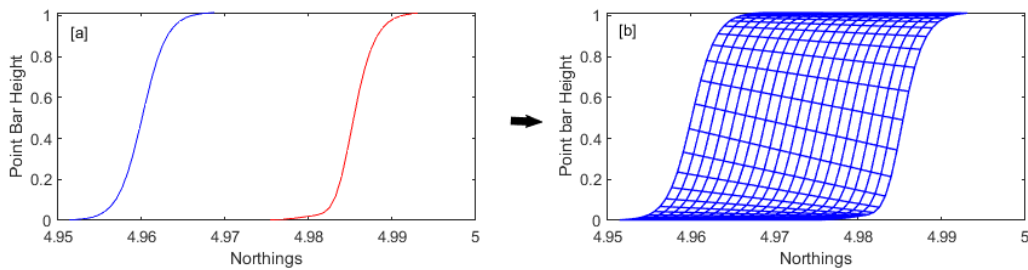


Fig. 2.11 Workflow for gridding the IHS. (a) domain to be gridded defined by the top (blue) and the bottom IHS surface (red) (b) Gridded IHS

The equivalent 3D grids for each channel path, formed by combining their respective aerial and vertical grids, are as shown in Figs 2.12a and b. The region bounded by the two gridded surfaces as illustrated in Fig. 2.12c is also gridded using equations 2.8a – c. Equations 2.8a – c show the final x, y, z grid coordinates (x^*, y^*, z^*) at node $ijk \quad \forall i = 1, 2, 3, \dots, nx+1 \quad \text{and} \quad \forall j = 1, 2, 3, \dots, ny+1, \quad \text{and} \quad \forall k = 1, 2, 3, \dots, nz+1.$

$$x_{ijk}^* = X_{ijk}^* \pm (j - 1) \cdot \frac{D_{ijk}^*}{ny} \cdot \cos \theta_{ijk}^* \quad (2.11a)$$

$$y_{ijk}^* = Y_{ijk}^* \pm (j - 1) \cdot \frac{D_{ijk}^*}{ny} \cdot \sin \theta_{ijk}^* \quad (2.11b)$$

$$z_{ijk}^* = Z_{ijk}^m \pm (j - 1) \cdot \frac{|Z_{ijk}^{current} - Z_{ijk}^{initial}|}{ny} \quad (2.11c)$$

where, θ_{ijk}^* and D_{ijk}^* are respectively, the angle and distance of separation between a grid node at location ijk in a gridded meander in Fig. 2.12c and the corresponding nodal pair in the other gridded meander also in Fig. 2.12c. X_{ijk}^* , Y_{ijk}^* and Z_{ijk}^m are the grid nodes or coordinates for either of the meanders in Fig. 2.12c. One may choose X_{ijk}^* , Y_{ijk}^* and Z_{ijk}^m from either the gridded current meander only or the initial meander path only, and this choice dictates the signs in equations 2.11a-c. $Z_{ijk}^{current}$ and $Z_{ijk}^{initial}$ are the z-coordinates at node ijk for the current and initial meanders respectively.

Applying equations 2.11a-c on Fig. 2.12c completes the gridding of the point bar in 3D with the final results shown in Fig. 2.12d.

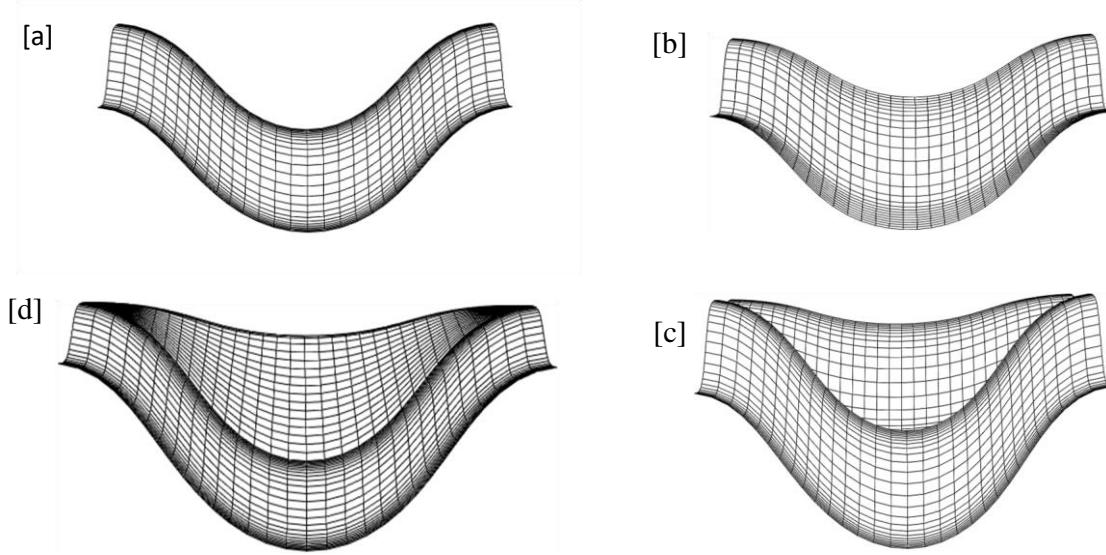


Fig. 2.12 Grid generation procedure for the entire point bar, a) 3D grid for current channel b) 3D grid for initial channel gridded c) overlap of gridded surfaces showing region to be gridded d) 3D gridded point bar.

The above grid generation procedure produces grids in a corner-point format. To allow for geostatistical computations, a conversion to a block-centered format is needed. For a 3D case (i.e., number of dimensions $n = 3$), the block centered grid coordinates at node $ijk \quad \forall i = 1, 2, 3, \dots, nx \quad \forall j = 1, 2, 3, \dots, ny$ and $\forall k = 1, 2, 3, \dots, nz$, can be computed from the corner point grid nodes, denoted as $(x_{ijk}^*, y_{ijk}^*, z_{ijk}^*) \quad \forall i = 1, 2, 3 \dots nx + 1, \quad \forall j = 1, 2, 3 \dots ny + 1, \quad \text{and} \quad \forall k = 1, 2, 3 \dots nz + 1$ using the following:

$$x_{ijk}^{center} = \frac{1}{2^n} (x_{ijk}^* + x_{i+1jk}^* + x_{i+1j+1k}^* + x_{ij+1k}^* + x_{ij+1k+1}^* + x_{ij+1k+1}^* + x_{i+1jk+1}^* + x_{i+1j+1k+1}^*) \quad (2.12a)$$

$$y_{ijk}^{center} = \frac{1}{2^n} (y_{ijk}^* + y_{i+1jk}^* + y_{i+1j+1k}^* + y_{ij+1k}^* + y_{ij+1k+1}^* + y_{ij+1k+1}^* + y_{i+1jk+1}^* + y_{i+1j+1k+1}^*) \quad (2.12b)$$

$$z_{ijk}^{center} = \frac{1}{2^n} (z_{ijk}^* + z_{i+1jk}^* + z_{i+1j+1k}^* + z_{ij+1k}^* + z_{ij+1k+1}^* + z_{ij+1k+1}^* + z_{i+1jk+1}^* + z_{i+1j+1k+1}^*) \quad (2.12c)$$

Essentially, a block centered grid node at any grid location is the average of all its immediate surrounding corner-point grid nodes.

2.5 Geostatistical modeling on transformed grid.

Petrophysical property modeling for the different IHS sets can be performed using any geostatistical modeling scheme such as Sequential Gaussian Simulation, SGSIM (Deutsch & Journel, 1998). The petrophysical data (e.g., porosity) can be obtained from wells that penetrate the point bar at different locations. Various aspects of the geostatistical modeling workflow such as the inference of semivariograms and the subsequent computation of spatial correlation values within the estimation and simulation algorithm are much more intuitive when performed in a rectilinear grid. In order to transform the curvilinear grid to a rectilinear basis, a suitable grid transformation scheme must be incorporated. Basically, in the grid transformation, the point bar is unraveled aerially and vertically. To unravel the point bar in section, (i.e., vertically), the inclined beds (IHS layers) are unraveled and stretched into a rectilinear form. This is done starting from the middle of the IHS layer either at the bottom or top of the point bar. For this discussion, we start from the bottom layer. Using few points in this section (see points indicated on the bottom layer in Fig. 2.13a), we can determine S_{ihs} , which is the slope of this bottom layer and α , the angle of inclination of this layer with respect to the horizontal. If L_{ihs} is the total length along the IHS, we can calculate the coordinates at the ends of the unraveled IHS (see round red makers on the bottom layer in Fig. 2.13b) as follows:

$$(y_{start}, z_{start}) = \left(y_{mid} - \frac{L_{ihs}}{2} \cdot \sin(90-\alpha), z_{mid} - \frac{L_{ihs}}{2} \cdot \cos(90-\alpha) \right) \quad (2.13a)$$

$$(y_{end}, z_{end}) = \left(y_{mid} + \frac{L_{ihs}}{2} \cdot \sin(90-\alpha), z_{mid} + \frac{L_{ihs}}{2} \cdot \cos(90-\alpha) \right) \quad (2.13b)$$

where (y_{start}, z_{start}) and (y_{end}, z_{end}) are respectively, the coordinates at the beginning and end of the unraveled IHS surface. (y_{mid}, z_{mid}) is the coordinate at the midpoint of the IHS. The IHS length L_{ihs} can be approximated numerically by dividing the IHS into n subintervals, to generate P points, so that $L_{ihs} = \lim_{n \rightarrow \infty} \sum_{i=1}^n |P_{i+1} - P_i|$. To unravel the top IHS surface, we combine the slope of the line orthogonal to the bottom surface, i.e., $-(S_{ihs})^{-1}$, with the perpendicular distance between the two IHS surfaces to compute coordinates perpendicular to (y_{start}, z_{start}) and (y_{end}, z_{end}) . This produces the plots shown as round blue markers in Fig. 2.13b. The grid generation process within the unraveled domain in Fig. 2.13b is same as discussed earlier. We generate grid nodes along and between the unraveled IHS surfaces to produce Fig. 2.13c, whose rectilinear grid is shown in Fig. 2.13d.

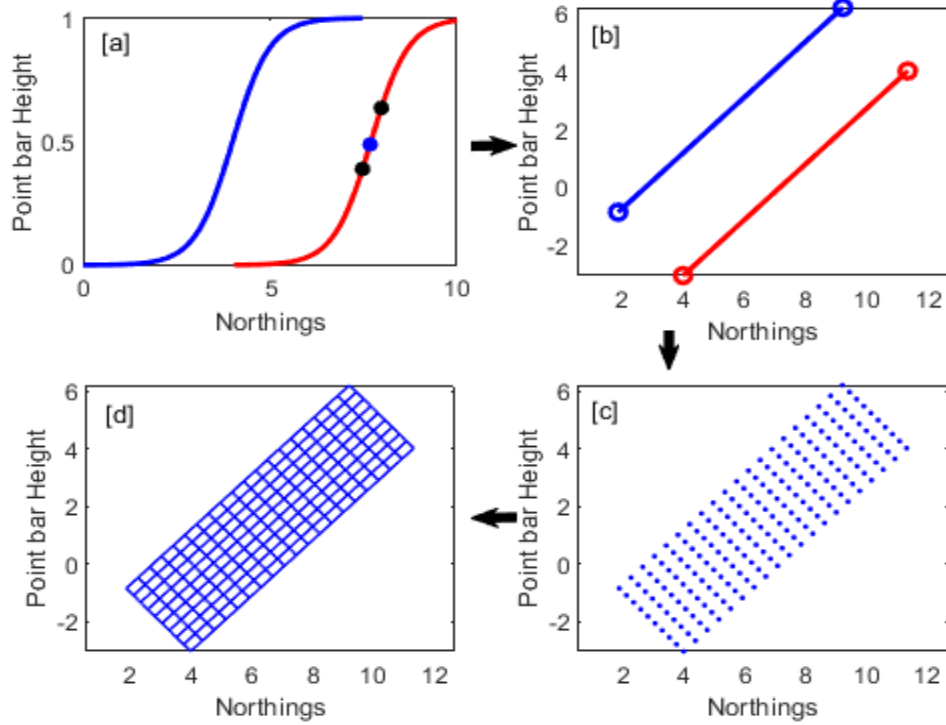


Fig. 2.13 Grid Transformation procedure for the HIS. (a) Domain to be transformed. Top and bottom layers are shown in blue and red, respectively. (b) IHS layers unraveled (c) Generated grid nodes for the IHS (d), rectilinear grid for the IHS.

In unraveling the point bar aerially, we begin from the section where there is maximum continuity, which occurs along the middle of the channels. Throughout this demonstration, it is assumed that the local axis of the channel coincides with the global x-y axis. However, if this is not the case, rotation of the coordinates is necessary for the grid transformation scheme to work well. Suppose the initial and current channel paths are respectively, the green and red curves in Fig. 2.14a. For each channel path, the coordinate at the middle of channel (x_{mid}, y_{mid}) is determined (see blue points on Fig. 2.14a). Next, the length L_{ch} , which is the length of the longest channel path is determined. Using this length (L_{ch}) and the coordinates (x_{mid}, y_{mid}) , we can determine the coordinates at the beginning and end of each channel path as:

$$(x_{start}, y_{start}) = \left(x_{mid} - \frac{L_{ch}}{2}, y_{mid}\right) \quad 2.14c$$

$$(x_{end}, y_{end}) = \left(x_{mid} + \frac{L_{ch}}{2}, y_{mid}\right) \quad 2.14d$$

Applying equations 2.14c and d yields the blue points in Fig. 2.14b. The region bounded by the coordinates at the ends of the unraveled channels represents the domain to be gridded (Fig. 2.14b). By repeating the grid generation procedure as discussed earlier, we have Fig. 2.14c, and the corresponding rectilinear grid is shown in Fig. 2.14d.

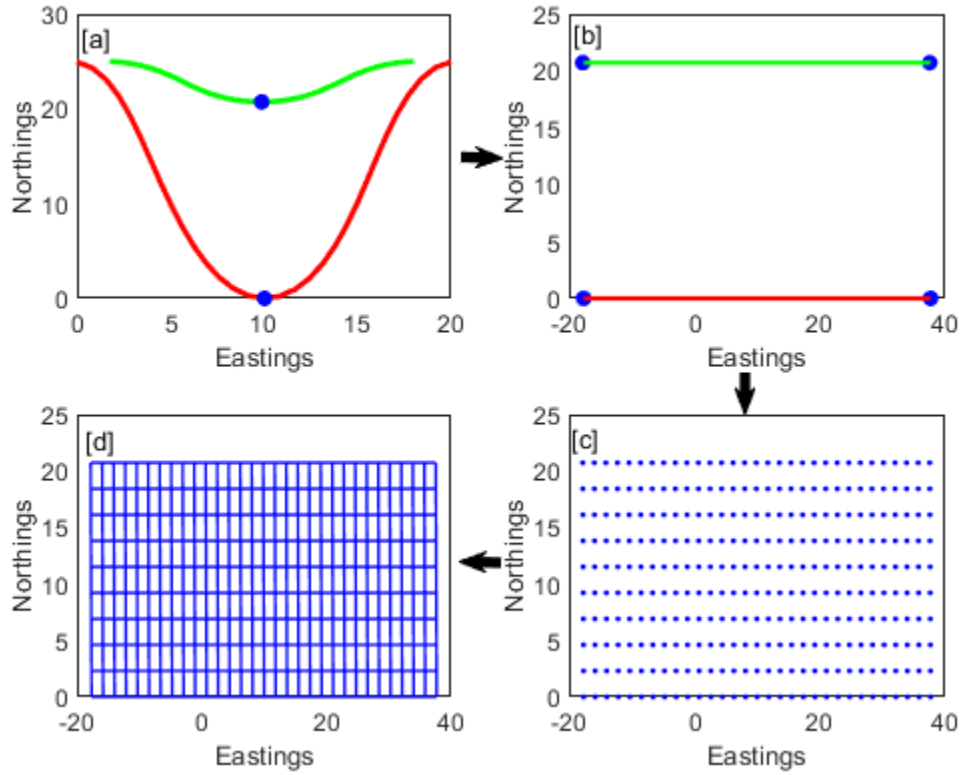


Fig. 2.14 Grid Transformation procedure for the lateral accretions (a) domain to be transformed. Initial and current channel paths are shown in green and red respectively. (b) channel paths unraveled (c) generated grid nodes (d), rectilinear grid for the lateral accretions.

For the entire point bar, the coordinates of the transformed grid (x^T, y^T, z^T) can be computed as:

$$(x^T, y^T, z^T) = \left(x_{start} + (i - 1) \cdot \frac{L_{ch}}{nx}, y_{start} + (j - 1) \cdot \frac{L_{I,C}}{ny}, z_{start} + (k - 1) \cdot \frac{L_{ihs}}{nz} \right) \quad (2.14e)$$

where L_{ch} is the length of the longest channel meander, $L_{I,C}$ is the maximum distance of separation between the initial channel meander I and current meander C , which occurs at the middle of the point bar.

Applying equation 2.14e yields Fig. 2.15a, which is the transformed grid nodes for the entire point bar. The corresponding rectilinear grid is shown in Fig. 2.15b.

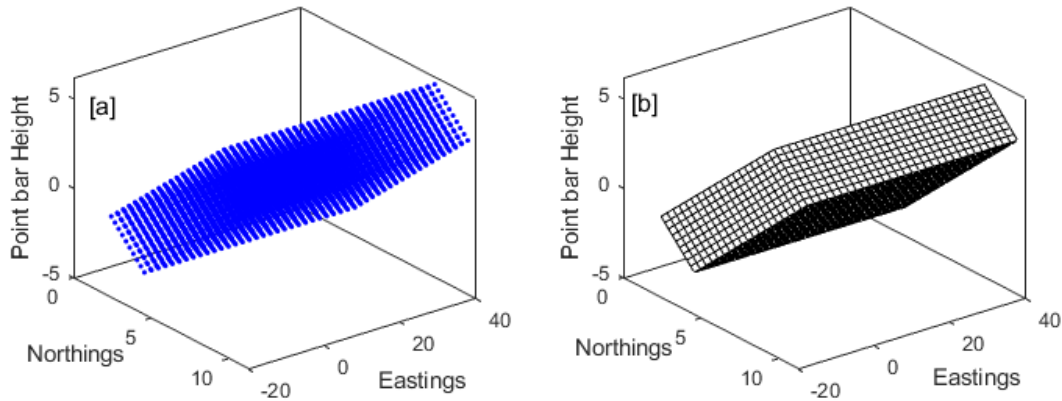


Fig. 2.15 Transformed grid for the entire point bar. (a) Transformed grid nodes for the entire point bar, representing the computational space for geostatistical simulation, and (b) equivalent rectilinear grid for the entire point bar.

The geostatistical modeling of the point bar properties for each IHS set is performed on the transformed grid where the point bar geology, guided by depositional trends, is modeled conditioned to the available well data. After simulation, each grid node is indexed to map the modeled properties in the rectilinear grid into the curvilinear grid. Fig. 2.16 illustrates the outline of the geostatistical simulation incorporating grid transformation. Details of the geostatistical modeling scheme for incorporating the depositional trends typically observed in point-bar systems are described for the field modeling scenario in the subsequent sections. A detailed description of the stochastic modeling method for representing shale drapes that have undergone erosion is also included.

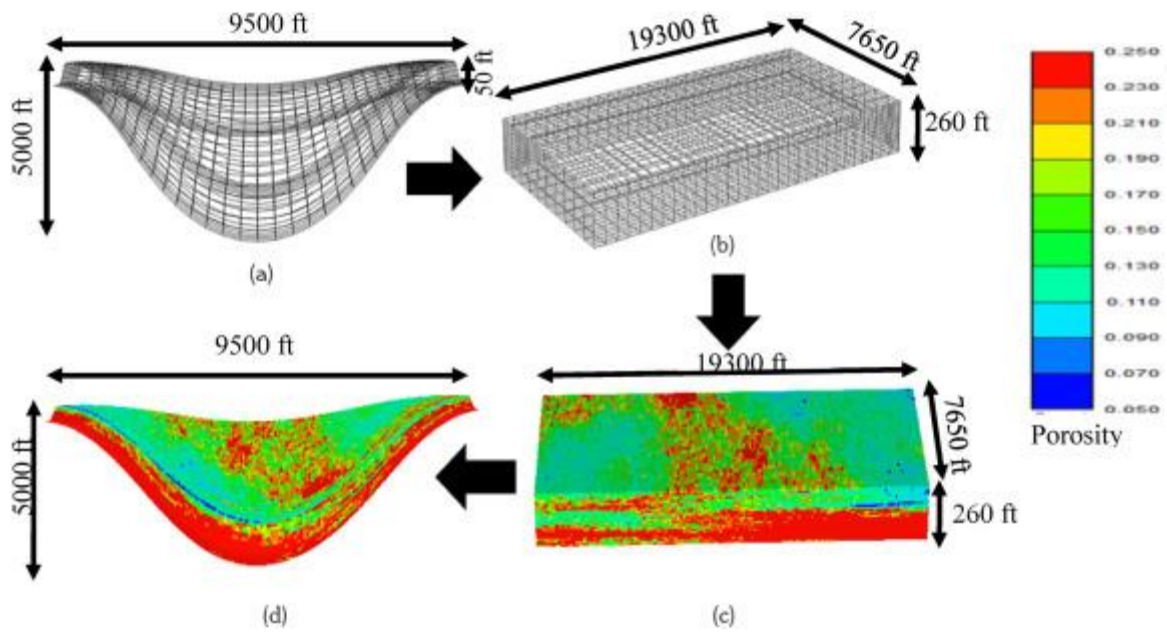


Fig. 2.16 Outline of property modeling. (a) Point Bar Curvilinear Grid (b) Rectilinear Grid Transformation (c) Geostatistical Simulation of porosity (d) Back Transformation, indicating the 3D distribution of porosity in the final Point Bar Model.

2.6 Application to field Data

The algorithm was tested on the Cranfield, Mississippi reservoir—a test site for CO₂ injection and sequestration experiment. The geology of the reservoir is a point bar formed as a result of lateral migration of fluvial channels. The reservoir is about 13.72 to 24.38 m thick and is located at a depth approximately 3000 m below sea level. The injection zone is characterized by a fining upward fluvial depositional trend where cross-bedded conglomerates occupy the bottom of the sequence, followed by sandstones, and muddy sandstones. (Hosseini et al., 2013; Lu et al., 2013b). To establish fluvial continuity, an attempt was made to correlate well logs using the channel signature. By analyzing well logs, facies were identified either as channels or point bars. Well log signatures that showed bell shapes were interpreted to be point bars while those that showed blocky signatures were inferred to be channels. Fig. 2.17 shows the application of the above workflow for modeling the channel path based on the Cranfield dataset. The encircled region in the last modeling stage (see Fig. 2.17d) is the Detailed Area of Study (DAS) which is the Cranfield injection site. This area would be selected for developing the detailed model of the point bar.

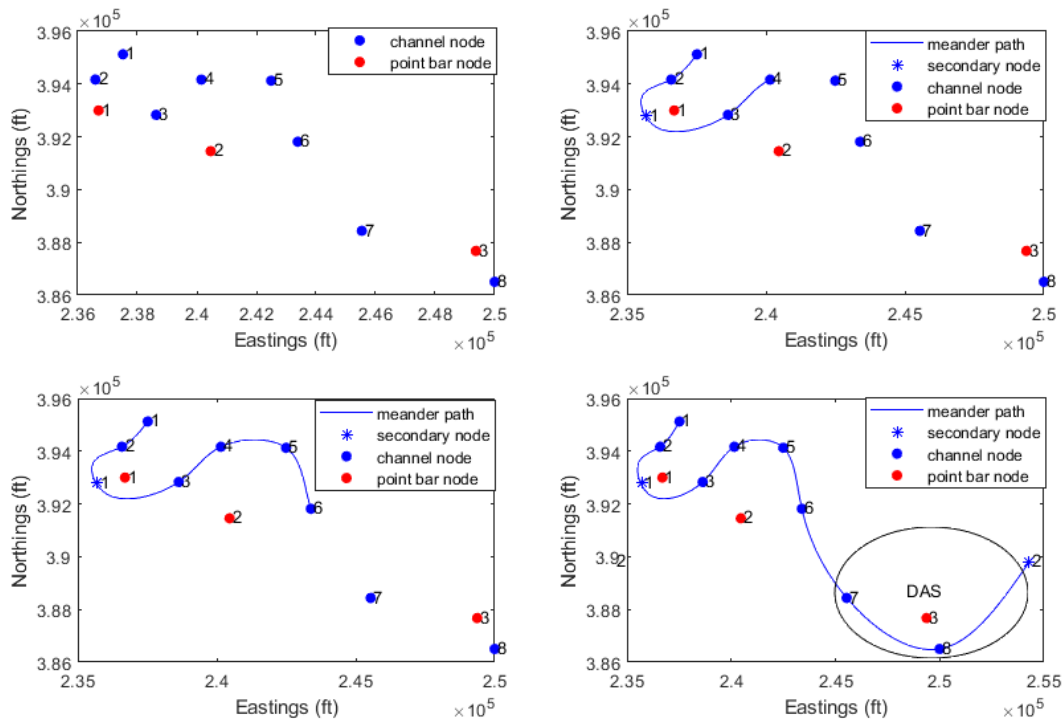


Fig. 2.17 Channel Meander Simulation for the Cranfield dataset. (a) Point bar locations and channel locations (b) Modeling stage 1 (c) Modeling stage 2 (d) Final Modeling stage. Blue points are channel facies interpreted using well logs. Red points are point bar facies. The circled area in the final Figure is the Detailed Area of Study at the Cranfield injection site.

2.6.1 Modeling Channel Path Migration

Channel meander migration is necessary to capture the main heterogeneities, which are the lateral accretions and IHS. To model the accretions, the Sine Generation Function (SGF) was used to migrate the channel for the reasons that: 1) the current channel path in the area of interest as shown in Fig.2.17d is symmetric, making SGF better suited for channel migration, and 2) as indicated in earlier section, migrating the channel using a cubic spline is extremely challenging due to the difficulty in ensuring that the coefficients of the spline exhibit consistency among themselves.

As indicated earlier, the SGF provides a convenient closed-form approximation of channel path as the channel meanders from one point to another (Hathout, 2015). To confirm that the SGF does approximate the meander generated using the cubic spline, the comparison between the meanders is illustrated in Fig. 2.18a. By stochastically varying the angular displacement in the SGF, the channel can be laterally migrated back in time to recreate the initial meander path (Fig. 2.18b). A cross-section across the initial and current position of meander (Fig.2. 18c) reveals the vertical heterogeneity of the point bar, which is the IHS as shown in Fig. 2.18d. The aerial and vertical surfaces would be gridded and combined to generate 3D surfaces for the initial and final meander.

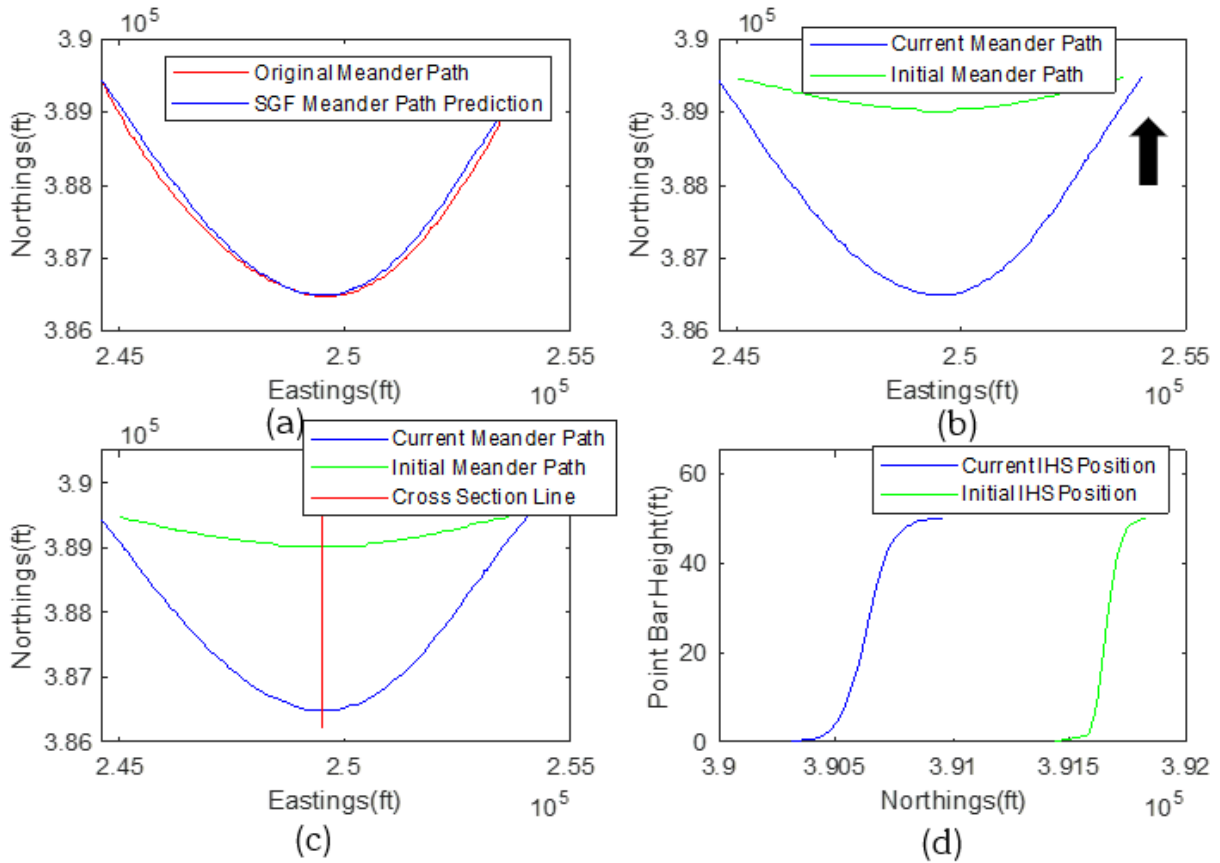


Fig. 2.18 Meander migration process focusing on the DAS region. (a) Illustration of close match between SGF prediction and the original meander path modeled using a spline function, (b) Current and initial meander path location after backward migration of channel (arrow indicates direction of backward migration i.e., migration starting from today's channel path to the ancient path), red line shows section across the meanders, and (d) IHS revealed along section in (c)

2.6.2 Curvilinear Grid Generation

i) Lateral accretions

As discussed before, the grid generation process was implemented separately for the two main heterogeneities. The workflow for gridding the lateral accretions is shown in Fig. 2.19.

The domain of interest bounded by the initial and current meander is shown in Fig. 2.19a, while Fig. 2.19b illustrates the grid nodes that were determined along each meander path. Next, we determine the grid nodes between the channel meanders. In Fig 2.19b, every grid node in any of the channel paths has a corresponding pair in the other meander path, and the grid coordinates are determined. The

corresponding location of the grid nodes are shown in Fig. 2.19c while the gridding in 2D is displayed in Fig. 2.19d.

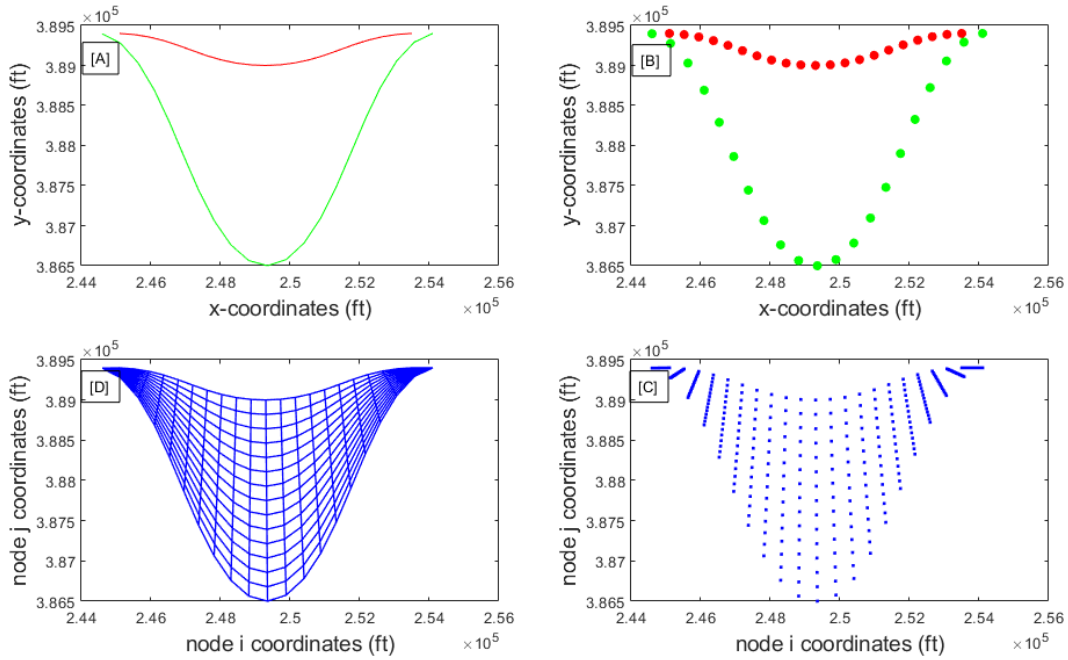


Fig. 2.19 2D gridding process for the lateral accretions. (a) Domain to be gridded, (b) grid nodes computed along the meanders, (c) Grid nodes computed between the meanders for each pair, and (d) curvilinear grid.

ii) Inclined heterolithic stratifications

By specifying the number of grid blocks along the z -axis as n_z and repeating the above procedure for the IHS, we can generate a grid for the IHS domain to be gridded (Fig. 2.19a) to generate Fig. 2.19b.

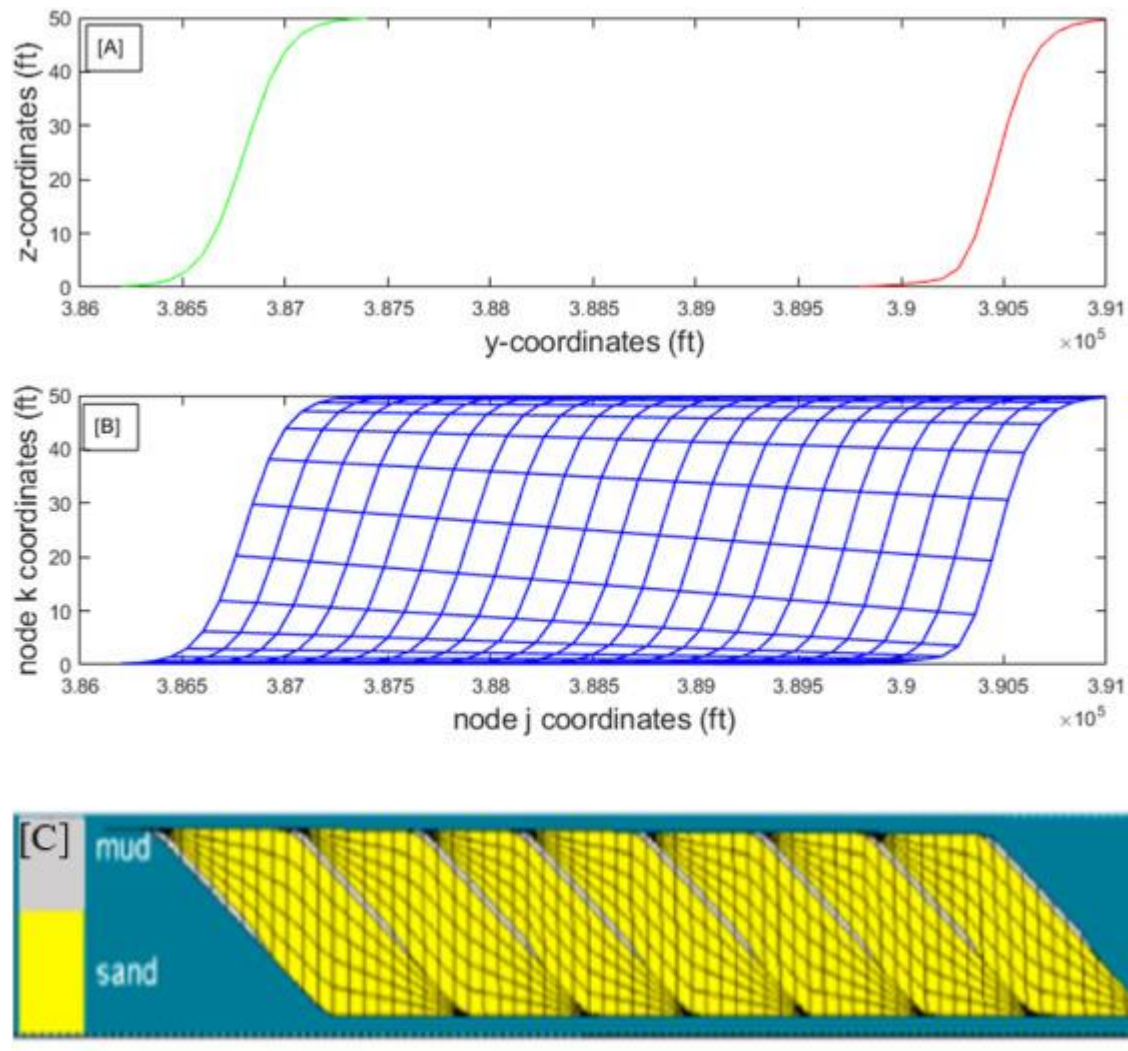


Fig. 2.20 (a) IHS domain to be gridded, (b) Gridded IHS. Grids between the top and bottom surfaces are perpendicular to the bedding orientation. (c) Computation grid from (Niu et al., 2021), grid does not conform to the beddings

As demonstrated in Fig.2.20b, the results from the grid generation conform to the geometry of the lateral IHS (bedding). Generating a grid that conforms to, for example, the bedding orientation can be challenging. Fig.2.20c shows the computational grid used in a surface-based study by (Niu et al, 2021). Comparing Fig. 2.20b and c, one can realize that Fig. 2.20c does not properly define the structure perpendicular to the bedding plane. This can affect the preservation of the heterogeneities in the geostatistical simulation because the vertical range of correlation may be improperly inferred and modeled.

The equivalent 3D grids for each meander, formed by combining their respective aerial and vertical grids, are as shown in Fig. 2.21a and b. The region bounded by the two gridded surfaces as illustrated in Fig. 2.21c is also gridded. This completes the gridding of the point bar in 3D as illustrated in Fig. 2.21d.

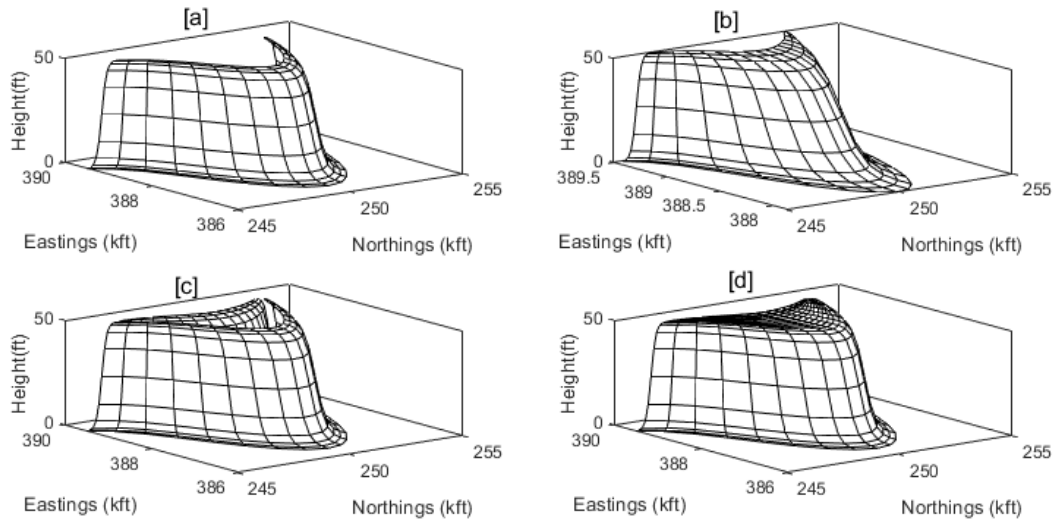


Fig. 2.21. a) Current channel meander gridded in 3D, b) initial channel meander gridded in 3D c) Overlap of gridded surfaces showing region to be gridded d) 3D gridded point bar.

2.6.3 Geological Data

The petrophysical properties (i.e., porosity for our case) that were used in the geostatistical simulation were obtained from wells that penetrated the point bar at different locations. For Cranfield, available well log data span the across the entire injection zone of the reservoir. Fig. 2.22 shows some of the porosity log data that were used to condition the geostatistical model. A common observation with these wells is the upward decrease in porosity, suggesting a fining trend in sediments.

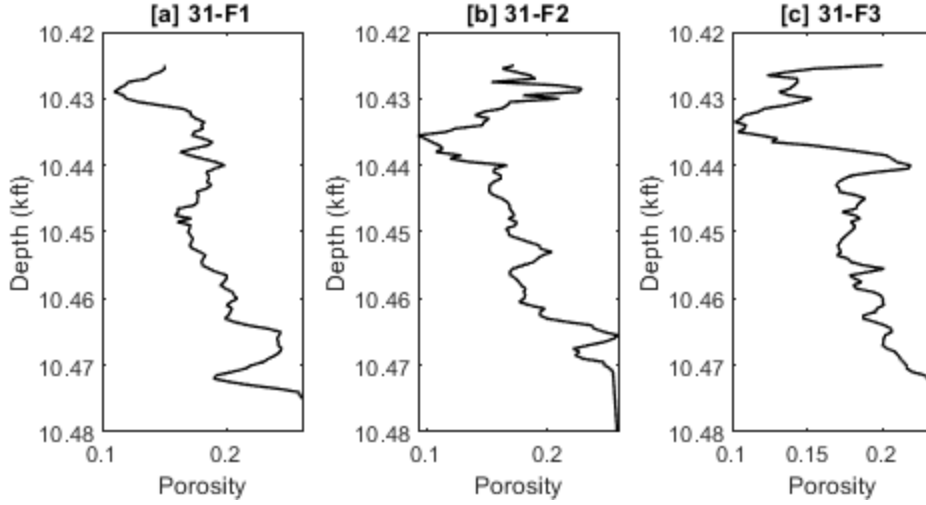


Fig. 2.22 Porosity logs for wells a) 31-F1, b) 31-F2 and c) 31-F3

2.6.4 Grid transformation and Geostatistical simulation

As indicated earlier, the geostatistical simulation method used for modeling property variations within the point bar was SGSIM. To account for spatial depositional trends, mean porosity maps were generated to reflect the spatial trends and used within the simulation procedure with locally varying mean. That is, given the porosity data z , the porosity estimate, z_o^* can be estimated as:

$$z_o^* = m_o + \sum_{\alpha=1}^n \lambda_{\alpha} (z_{\alpha} - m_{\alpha}) \quad (2.15)$$

where m_o refers to the local mean, which is in the form of the fining upward depositional trends and m_{α} refers to the mean at the data location. The weight term λ_{α} can be determined by solving the following system of equations, derived by minimizing the error variance at the estimation location:

$$\sum_{\beta=1}^n \lambda_{\beta} C(h_{\alpha\beta}) = C(h_{\alpha o}) \quad \forall \alpha = 1, \dots, n \quad (2.16)$$

The term $C(h_{\alpha o})$, which is the covariance between the data and a simulation node, accounts for the information in the data towards the quantity to be estimated/simulated, such that data at locations that are structurally closer to the estimation/simulation location exhibit higher correlation. $C(h_{\alpha\beta})$ accounts for the redundancy between the data themselves.

Equation 2.15 is incorporated during the kriging stage in the SGSIM workflow. The SGSIM algorithm used to model the reservoir properties as detailed by (Deutsch & Journel, 1998; Remy, 2004) is summarized in Fig. 2.23.

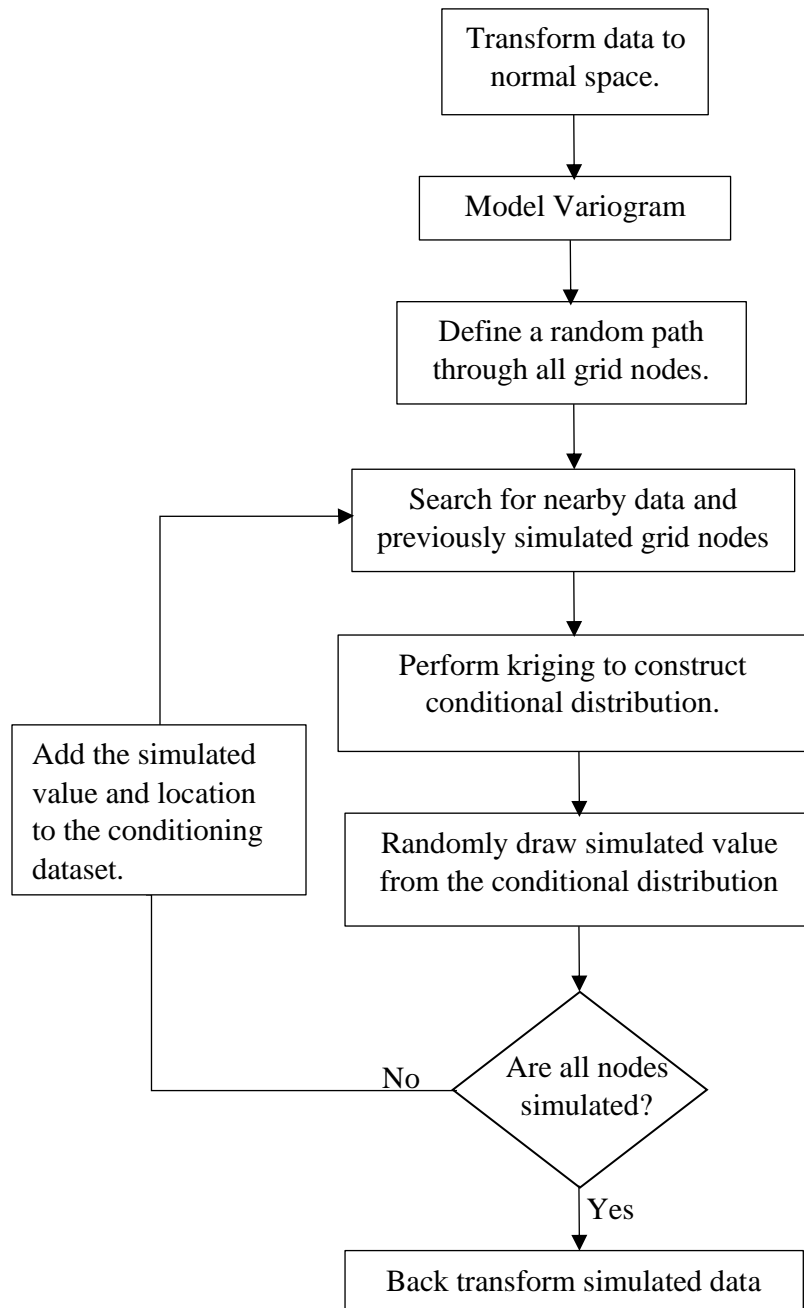


Fig. 2.23 Sequential Gaussian Simulation workflow. modified after (Bai & Tahmasebi, 2022)

To condition the reservoir model to the fining upward trend, a soft input for m_o is incorporated in the geostatistical simulation. That input is basically in the form of mean porosity maps that could be based on the proportion of high to low porosity facies at a grid location as one moves from the bottom to the top of the reservoir. In this research, the mean porosity in a grid cell at a particular depth is determined by averaging the porosity data for all the wells at that depth. The result of this is a map showing locally varying mean of porosities with depth. Fig. 2.24 shows sections taken from this mean porosity volume. The wells 31-F1, 31-F2 and 31-F3 are contained within these sections. The maps show a decreasing porosity trend from the bottom to the top of the reservoir. From this map, the stratigraphic succession of the reservoir can be inferred. That is, the high porosity sedimentary rocks like conglomerates, sandstones or sand-prone sediments dominate the bottom of the point bar, and this transitions into low porosity rocks like the fine-grained shales, siltstones, or mud-dominated sediments as one moves to the top of the reservoir.

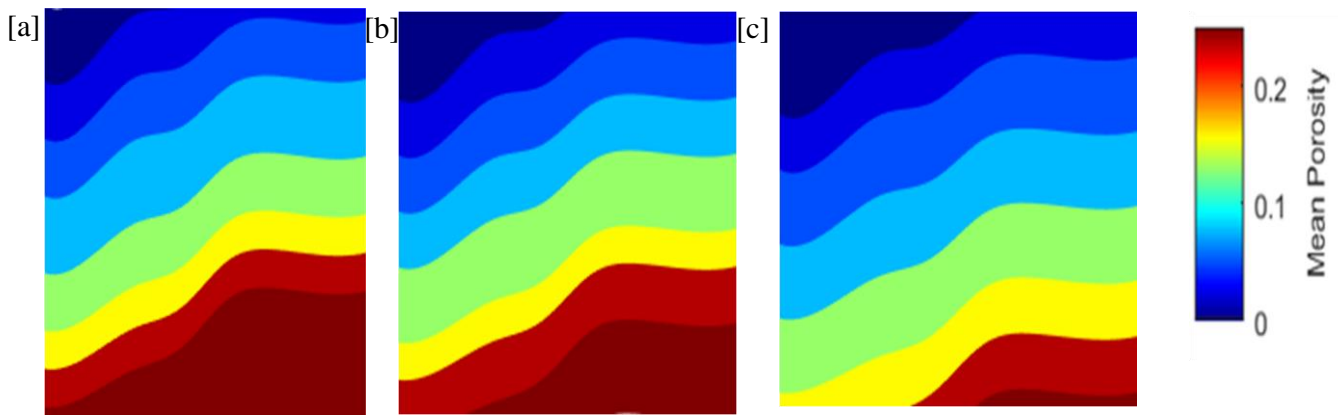


Fig. 2.24 vertical variation of mean porosity along a section containing the wells a)31-F1, b) 31-F2 and c) 31-F3.

The SGSIM algorithm is variogram-based and it is difficult to infer and model the variogram in a curvilinear geometry. To overcome this problem, a grid transformation scheme is employed. Essentially, the grid transformation straightens the point bar curvilinear geometry into an equivalent rectilinear form as discussed previously. Variogram modeling was guided by depositional trends or continuities that are typical of point bars. Point bars are laterally extensive compared to the vertical, this results in maximum continuity in the downstream flow direction while the least continuity is in the perpendicular direction between successive IHS (i.e., accretion direction). Between these limits, we have the medium continuity which occurs in the dip direction. Fining trends are observed along

these directions (Hickin, 1986; Thomas, et. al., 1987). In accordance with these trends, the maximum range (h_{max}), medium range (h_{med}) and minimum range (h_{min}) were chosen to be in the direction of continuity along the downstream flow direction, dip direction and accretion direction, respectively. These assumptions were necessary given the sparse data available to infer the semi-variogram. Fig. 2.25 shows the directions along which the variogram ranges are inferred as depicted in the curvilinear and the equivalent rectilinear space for the point bar.

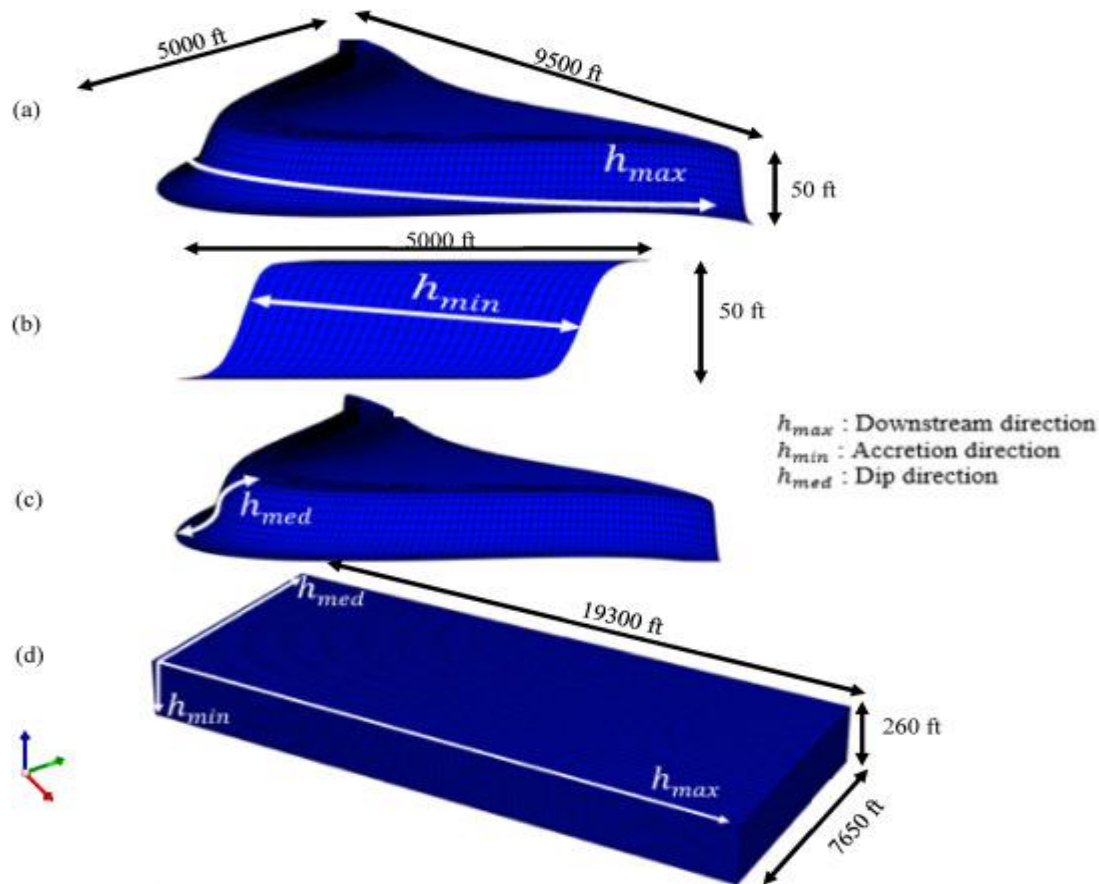


Fig. 2.25 Variogram directions in (a, b, c) curvilinear grid and d) rectilinear grid. h_{max} , h_{med} and h_{min} are in the downstream direction, accretion, and dip direction, respectively. Please note: the lengths of arrows indicated here do not depict the magnitude of the ranges; they are just guiding the reader in identifying the major, minor and vertical directions of spatial continuities.

The h_{max} , h_{med} and h_{min} used as the major, medium, and minor axis of anisotropy, respectively, for the variogram model. Six migration episodes, totaling 5 IHS sets were modeled. These IHS sets are the inclined layers that make up the point bar. The IHS sets were modeled separately on a rectilinear grid with dimensions $150 \times 30 \times 25$. Table 2.1 shows some of the variogram inputs for each IHS set.

Table 2.1 Variogram inputs for SGSIM

IHS Set	Nugget	Sill	h_{\max} (ft)	h_{med} (ft)	h_{\min} (ft)
1	0.1	1	1734	120	80
2	0.1	1	1592	120	80
3	0.1	1	1262	120	80
4	0.1	1	1074	120	80
5	0.1	1	1566	120	80

Fig. 2.26a shows an arbitrary realization in rectilinear grid for IHS set 1 after incorporating these probability maps in the SGSIM implementation. The arrow points to the front view, which shows a fining upward trend (see Fig. 2.26b) The complete 3D point bar model was obtained by stacking the IHS sets in an orderly fashion from set 1 to 5 and mapping their properties into the point bar curvilinear grid of dimensions $150 \times 150 \times 25$ (Fig. 2.27).

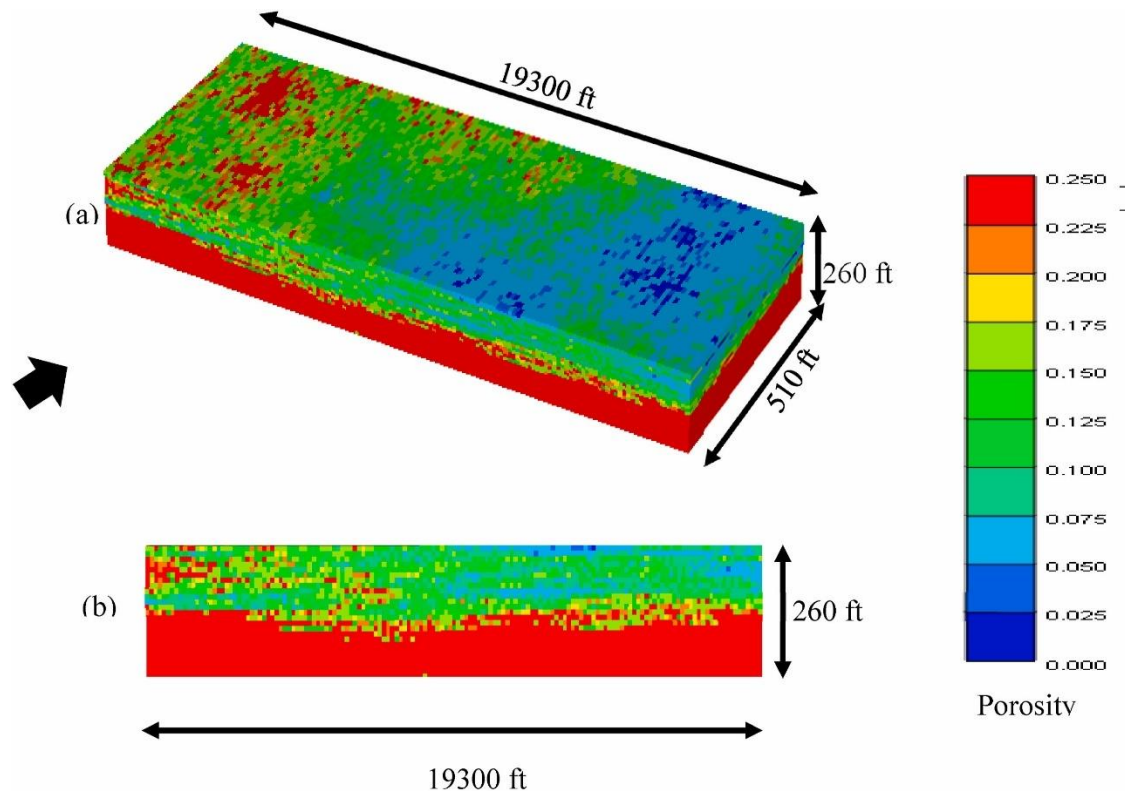


Fig. 2.26 Single SGSIM realization for IHS set 1. (a) realization on rectilinear grid (b) front view showing fining upward (Arrow points to the front view)

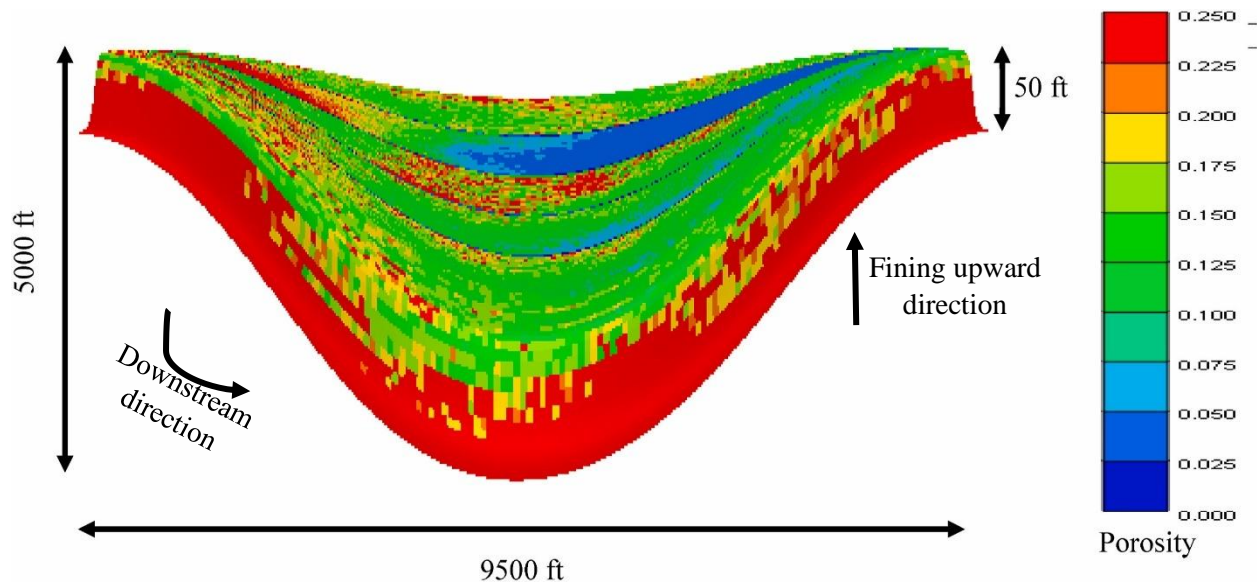


Fig. 2.27 Single realization of the 3D Point bar. Downstream direction is from left to right.

The point bar property model displayed here is one of the several realizations that were generated for the point bar. The reservoir response computed over the suite of realizations would provide an assessment of uncertainty associated with response predictions. In the ensuing chapter we will discuss the process for further conditioning the reservoir models to the observed injection data in order to minimize the uncertainties in the model.

In order to confirm that the fining upward trend is preserved as the reservoir properties are mapped from the rectilinear grid into the original curvilinear grid, horizontal slices are taken across the point bar at the different depths. Fig. 2.28 shows horizontal slices taken at the bottom, middle and top of the reservoir. The horizontal arrow shows the bottom to top direction. As can be seen, as one moves from the bottom (Fig.2.28a) to the top (Fig. 2.28c), porosity decreases, indicating that the fining upward trend is honored in the geostatistical simulation workflow and preserved during grid transformation. This trend reflects the stratigraphic succession at the Cranfield, Mississippi. At Cranfield, the coarser and heavier sediments (e.g., conglomerates) that have high porosity tend to settle at the bottom of the sequence followed by relatively lower porosity sediments like finer and lighter granular materials like muddy sandstones, and mudstone.

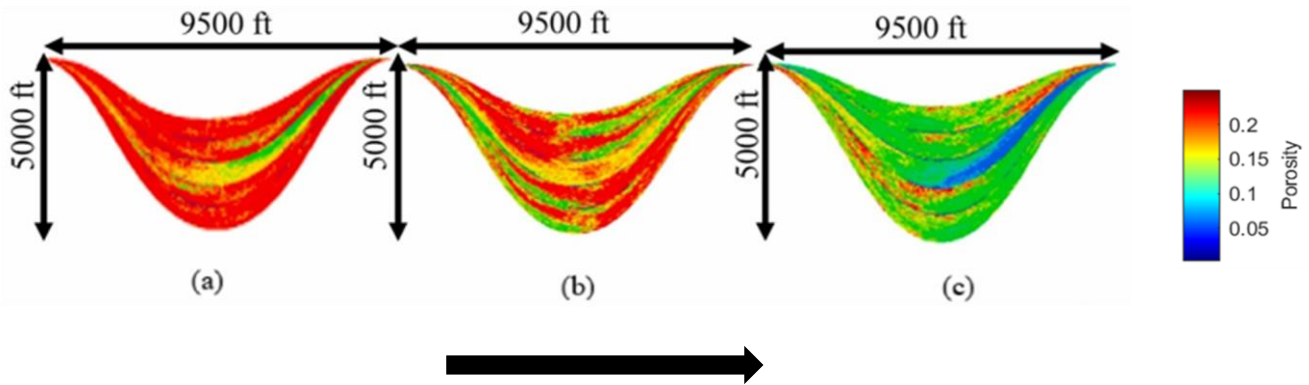


Fig. 2.28 Fining trend captured in the geostatistical simulation, (a) bottom slice (taken at the last layer from top), (b) mid slice (taken at the 14th layer from top), and (c) top slice (taken at the 6th layer from top). Please note: the arrow indicates direction of fining in sediments from bottom to the top of the point bar.

2.6.5 Stochastic Representation of Shale drapes across interfaces

The interfaces between successive accretion surfaces are erosional surfaces that mark a flooding event in the depositional history of the point bar reservoir. These surfaces form internal heterogeneities that are characterized by the existence of shale drapes on the IHS and accretion surfaces. These shale drapes could act as flow baffles, which could impact hydrocarbon recovery and CO₂ storage potential in the case of sequestration, hence the need to model them. The continuity of the shale may be interrupted due to erosional processes (Weber, 1982; Hartkamp-Bakker and Donselaar, 1993; Jackson and Muggeridge, 2000; Barton et al., 2010; Ayawah et al., 2022).

Before capturing the erosional surfaces, shale was first simulated as a continuous layer lying at the interfaces between successive IHS sets. Fig. 2.29a shows the sectional view of the simulated shale layers at the interface between two successive IHS sets. The variation in porosity along the continuous shale layer observed in front view is shown in Fig. 2.29b. For modeling the shale drape, the GSLIB program called ELLIPSIM (Deutsch & Journel, 1998) was used to simulate Boolean objects of 1s (ones) and 0s (zeros), with 1 indicating a location lying within the ellipsoid and 0 indicating a location outside the ellipsoid. These ellipsoids were dropped at random in the border region near the top surfaces of the internal IHS sets until a target proportion of ellipses was reached. The shale within the ellipsoids were assumed to be eroded (see Fig. 2.29c). We simulate shale drape properties, as has been reported by earlier researchers, (e.g., Stewart et al., 2008; Eikeland and Hansen, 2009; Alpak and Van Der Vlugt, 2014; Kadingdi et al., 2022) as very low permeability and zero-porosity facies. Porosity values between 2.05% and 5.87% has been reported by (Chen et al., 2019), while others (e.g., Goral et al., 2020) have reported typical values less than 5%. In simulating shale, we simulated values between 2.05% and

5.87%. Fig. 2.30 shows a cross-section through the point bar structure before and after modeling the eroded shale drapes.

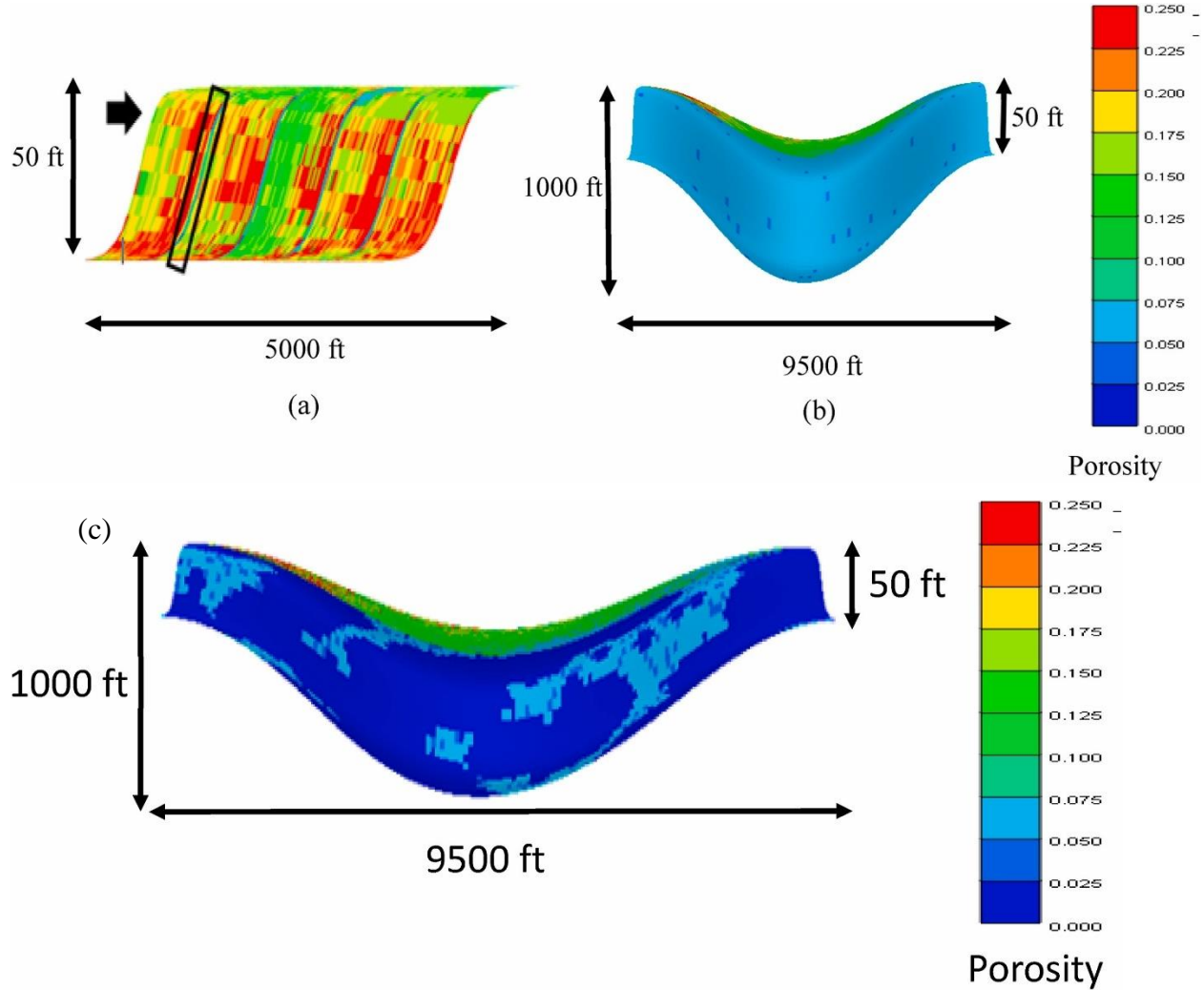


Fig. 2.29 a) Sectional view showing shale simulated as a continuous layer on top of the IHS sets. Black rectangular demarcation is the continuous shale layer at the interface between two adjacent IHS sets 2 b) Variation in porosity along the continuous shale layer at the interface between the two IHS sets, and c) front view of IHS set 2, illustrating shale drapes captured as erosional surface.

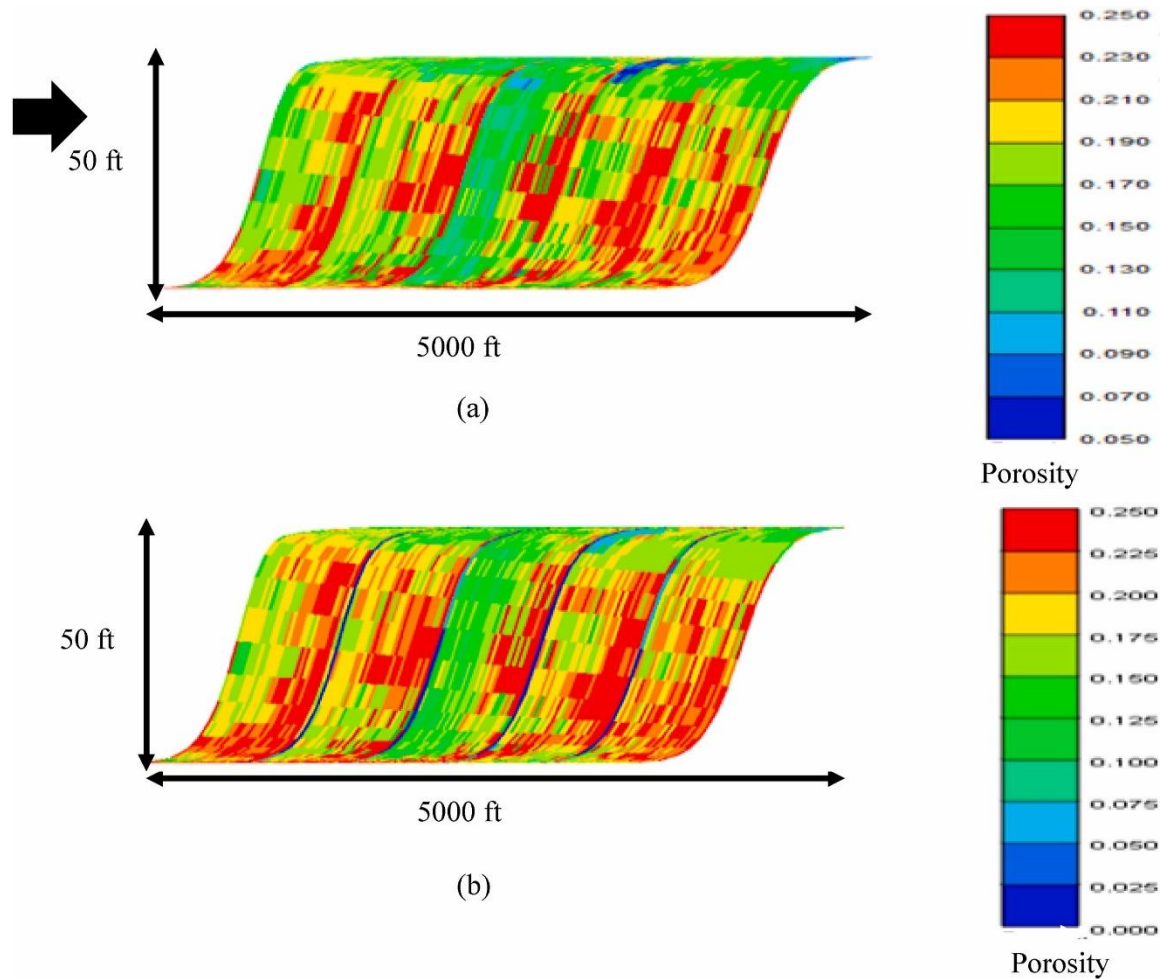


Fig. 2.30 Cross-section slice of the point bar across all IHS sets before (a) and after (b) modeling shale drapes.

2.6.6 Point Bar Geometry Perturbation

The point bar modeling algorithm is stochastic in that it is possible to alter the point bar geometry and thereby represent the uncertainty in reservoir geometry. Geometry perturbation is done by altering the angular displacement (ω) in the SGF equation, and the uncertainty in the point bar geometry is defined by drawing samples of ω from a predefined probability distribution. In this study, a Gaussian distribution is assumed. 50 samples of ω were drawn from $N(35,10)$ to generate ensembles of point bar geometries using SGF. In the perturbation process, any alteration in the channel sinuosity (by changing ω in the SGF) reflects in the bedding orientation, and therefore, the IHS orientation. Fig. 2.31 is a demonstration of some perturbations. The minimum and maximum heights of the IHS surfaces can be used to constrain the distribution of ω . Potentially, perturbation of the ω value can change the

thickness of the point bar at a well location. Consequently, non-local perturbation scheme for the ω value may be necessary to preserve the thickness of the point bar at a well location. These concepts will be explored in the next chapter, where injection data at the Cranfield site will be used to calibrate the initial set of geologic models for the point bar.

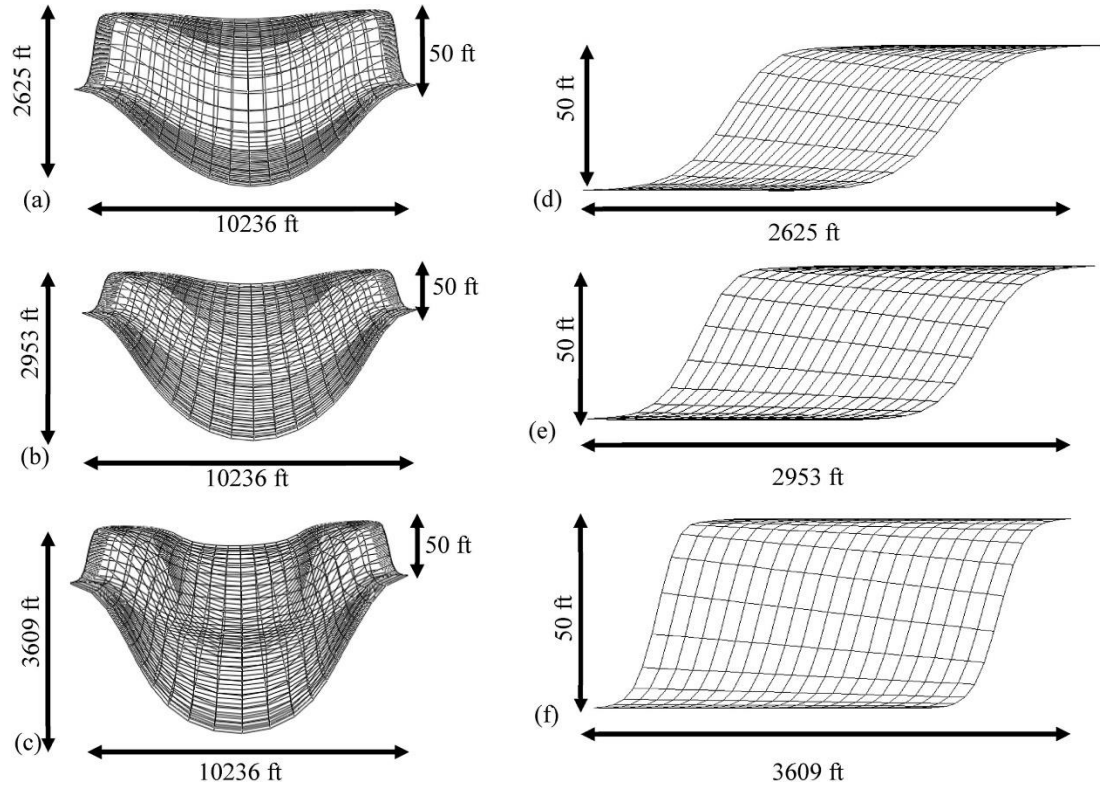


Fig. 2.31 Point bar geometry perturbed at different channel displacements. Channel displacement (and therefore sinuosity) increases from a to c, which: 1) affects the slopes of the IHS or beddings as one moves from d to f and 2) increases the areal extent of the point bar as we move from a to c or d to f.

It is important to point out that, once the point bar geometry is altered, the position of the well within the grid representing the point bar, will change and that will lead to perturbations in the flow response. The point bar reservoir algorithm in this dissertation can perturb the meander or point bar geometry—spanning from low to high angular sinuosity channels—and recreate the grids accordingly. The new grid location of wells within the reservoir is determined and reported during the geometry perturbation. As an example, the well locations before and after perturbation are shown in Fig. 2.32, and the reported grid locations are presented in Table 2.2.

The point bar perturbation also accounts for the deformation process that the point bar undergoes over a geologic period. In previous works, the Thin Plate Spline method (D. W. Thompson, 1917) has been used

to capture perturbations in the subsurface. For example, based on this method, (Tahmasebi, 2017) used some interpolation functions to perturb the geologic model to match point data. Similarly, in this dissertation, perturbation of the point bar geometry is done by altering the ω in the SGF.

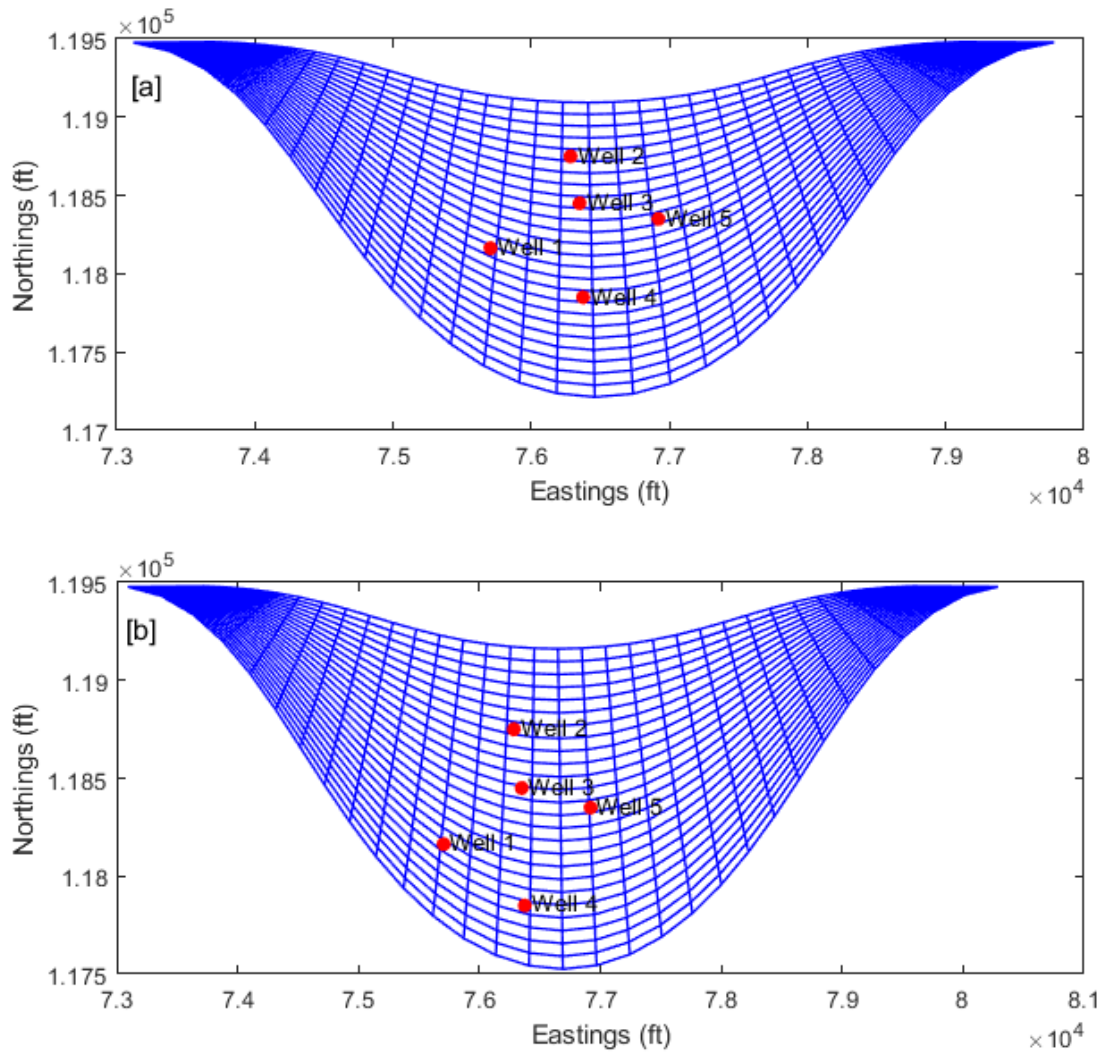


Fig. 2.32 Geometry perturbation and variation in grid coordinates of wells (see red points). (a) Geometry perturbation at $\omega = 50^\circ$, and subsequent regeneration of grid. (b) Geometry perturbation at $\omega = 43^\circ$, and subsequent regeneration of grid.

Table 2.2 Well locations before and after geometry perturbation

Well Name	Grid block indices			
	Before		After	
	i-index	j-index	i-index	j-index
Well 1	12	11	12	7
Well 2	15	21	14	19
Well 3	15	17	14	14
Well 4	15	9	14	5
Well 5	18	15	18	13

2.7 Flow Simulation Study

A CO₂ flow simulation study was conducted using the GEM reservoir simulation package from the Computer Modeling Group (CMG-GEM, 2019)—an advanced Equation of State (EOS) compositional and unconventional reservoir simulator. The objective of conducting flow simulation study using the point bar models was to gain an insight into how the migration and storage of reservoir fluids (in our case CO₂ migration and storage) are affected by the shale drapes. This is an important step to demonstrate the need to model the internal heterogeneity in point-bars especially the shale drapes on the IHS surfaces. In addition, we seek to investigate the sensitivity of flow response variables (in this case, bottom hole pressure) to the point bar reservoir geometry. In a subsequent discussion, we will incorporate the knowledge gained in this study to design and implement a scheme for sub-selecting a subset of reservoir models that best represent the injection data observed at a field site.

2.7.1 Simulation grid

It was realized that given the areal extent of the point bar reservoir, flow simulation would be computationally expensive and time consuming if the whole reservoir is used for simulation. Moreover, the CO₂ injection period at the Cranfield site (based on the available data) is relatively short, and thus the CO₂ plume will most likely affect the immediate surroundings of the injection well and not the regions far from the injection zone. The simulation grid was therefore defined as a sub-section of the detailed area of study (DAS) at the Cranfield site. The selected region does reflect the shale drape related heterogeneity and the depositional trends observed in the reservoir. The sub-section of the grid to be used for this simulation is the region bounded by the dark rectangular box shown in Fig. 2.33a. The simulation grid dimensions used are 20 × 20 × 25 making up 10000 grid bocks. The

injection well (31 F1) is in the middle of the demarcated section in Fig. 2.33. Table 2.3 presents the reservoir properties at initial conditions.

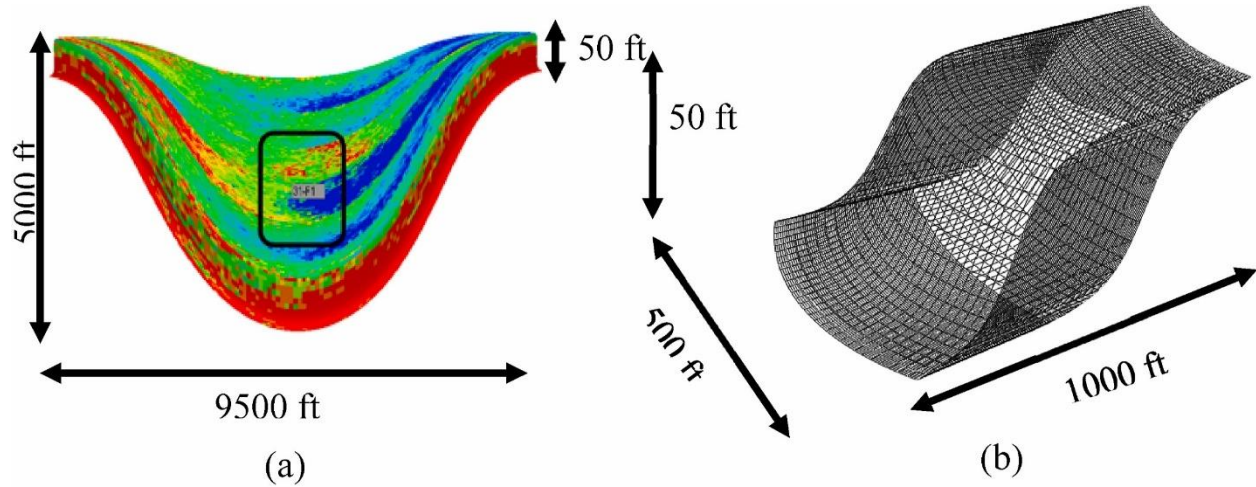


Fig. 2.33 (a) Portion of the Cranfield point bar model used for simulation. Injection well 31-F1 is centrally located within the demarcated region. (b) Simulation grid cut from the point bar model.

2.7.2 Simulation Parameters

The simulation parameters are detailed in Table 2.3.

Table 2.3 Reservoir Properties at Initial Conditions

Reservoir Property	Value	Source (if applicable)
Approximate Reservoir Depth	3000 m	(Hovorka et al., 2013)
Average Reservoir Thickness	15 m	(Hosseini et al., 2013)
Rock Compressibility	$7.3 \times 10^{-7} \text{kPa}^{-1}$	
Initial Reservoir Temperature	125 °C	(Delshad et al., 2013b)
Initial Reservoir Pressure	3200 kPa	(Delshad et al., 2013b)
Salinity	155752 ppm	(Lu et al., 2013b)
Boundary Condition	Open	

2.7.3 Rock-Fluid Interaction Property

The relative permeability curves used in this study were obtained from experimental data presented by Bennion and Bachu, (2005) for supercritical CO₂ displacing brine system. The water relative permeability curve has an end point of 1.0 at a residual CO₂ saturation of zero. For the CO₂ relative permeability curve, it has an end point of 0.54 at an irreducible gas saturation of 0.45 (Fig. 2.34).

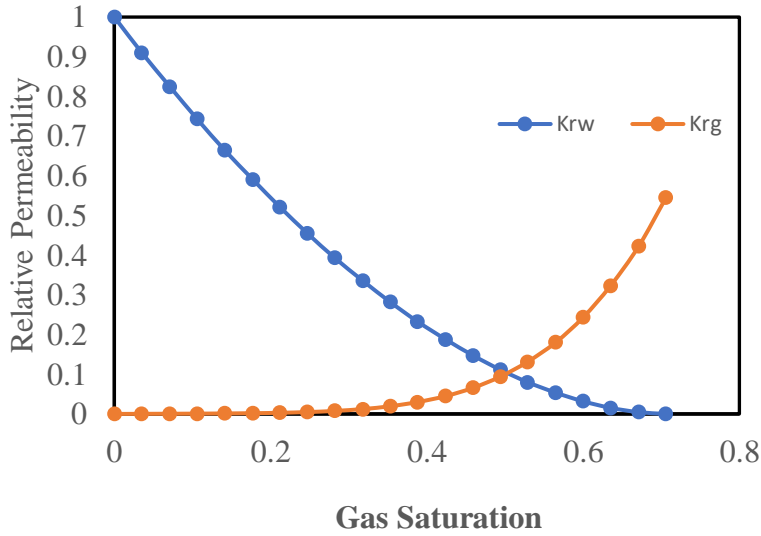


Fig. 2.34 . CO₂-brine relative permeability curve used for simulation (Bennion and Bachu, 2005).

2.7.4 Fluid Property Modeling

CMG-WinProp was used to model the phase behavior and the reservoir fluids properties (CMG-Winprop, 2019). The Peng and Robinson, (1976) EOS was used to model phase-equilibrium compositions and derive EOS parameters characteristic of supercritical CO₂. CO₂ solubility was modelled with Henry's law as discussed in Li and Nghiem, (1986) for brine at a brine salinity consistent with what has been reported for the Cranfield reservoir. A salinity of 155752 ppm as reported by Lu et al., (2013a) was used. The brine phase viscosity and density were respectively estimated using the correlations in Rowe and Chou, (1970) and Kestin et al (1981).

2.7.5 Well and Recurrent Data

The Cranfield injection well, which is centrally located in the domain of interest and exhibits point bar facies, was perforated in two layers located at the lower half of the injection zone. The injection well was set under two operating constraints: a primary constraint operating at a daily injection rate obtained from the Cranfield injection dataset (Fig. 2.35), and a secondary constraint operating at a maximum bottom-hole pressure 38000 kPa. (See Table 2.4 for details).

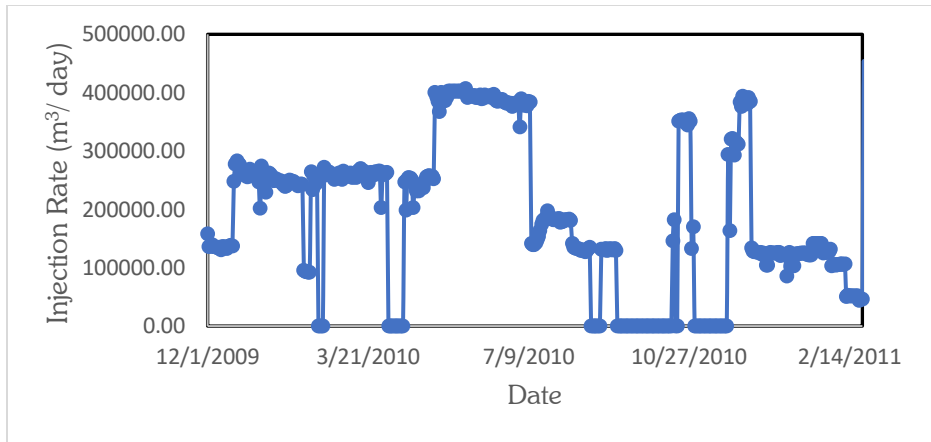


Fig. 2.35 Field injection rate schedule used for simulation. Please note, the original Cranfield injection rate was in terms of mass flow rate in $kgmin^{-1}$ however ever in this study, it has been converted to volumetric flow rate in m^3/day using a super-critical CO_2 fluid density of $576.72 kg/m^3$.

Table 2.4 Injection Well Parameters and Specifications.

Injection Well Parameter	Specification
Well Perforation Address (i, j, k)	10, 12, 8
Injection Period	Dec 1, 2009 – Feb 25, 2011
Well Radius	0.0762m
Skin	0
CO_2 Mole Fraction	1
Injection Rates	See Fig. 2.23
Maximum Bottom-hole Pressure	38000 kPa

These injection conditions mimic the actual field injection strategy adopted at Cranfield.

2.7.6 Simulation Strategy

The numerical simulation model was developed for two cases: reservoir model accounting for the effect of shale drapes and that without considering shale drape effects—all evaluated for structural, residual and dissolution trapping mechanisms. The injection well was run such that the total amount of supercritical CO_2 injected was the same for both cases under consideration. Additionally, we also simulated the effect of reservoir geometry perturbation on injection well response (bottom-hole pressure).

2.7.7 Shale drape effects

To understand the impact of shale drapes on CO_2 plume migration and storage, two simulation cases were run. The first simulation run ignored the effect of shale drapes demarcating accretion episodes and on inclined heterolithic stratification surfaces. As could be observed in Figs. 2.36a and 2.37a, the

CO₂ plume preferentially migrates laterally within the lower layers before rising upwards towards shallower depths due to buoyancy. This resulted in a CO₂ plume with a broader base (see encircled regions in Figs. 2.36a and 2.37a) and an overall relatively larger contact area with the reservoir rock. In the second simulation run, the effect of shale drapes was considered. Contrary to the first simulation run, the lateral migration of the CO₂ plume is restricted, forcing more of the gas to flow in the sandstone facies bounded by the IHS and the plume rises upwards towards shallower layers (see Figs. 2.36b and 2.37b). CO₂ plume had a relatively narrower base within the lower layers in the injection zone (see encircled region in Figs. 2.36b and 2.37b) and had a relatively smaller contact area with the reservoir rock. The shale drapes clearly serve as barriers to CO₂ displacement. The relatively rapid upward movement of gas observed in the second simulation run could lead to a situation where an excess volume of CO₂ accumulates below an overlying seal and increases the risk of seal failure and potential CO₂ leakage. This has been reported by (Hovorka et al., 2004).

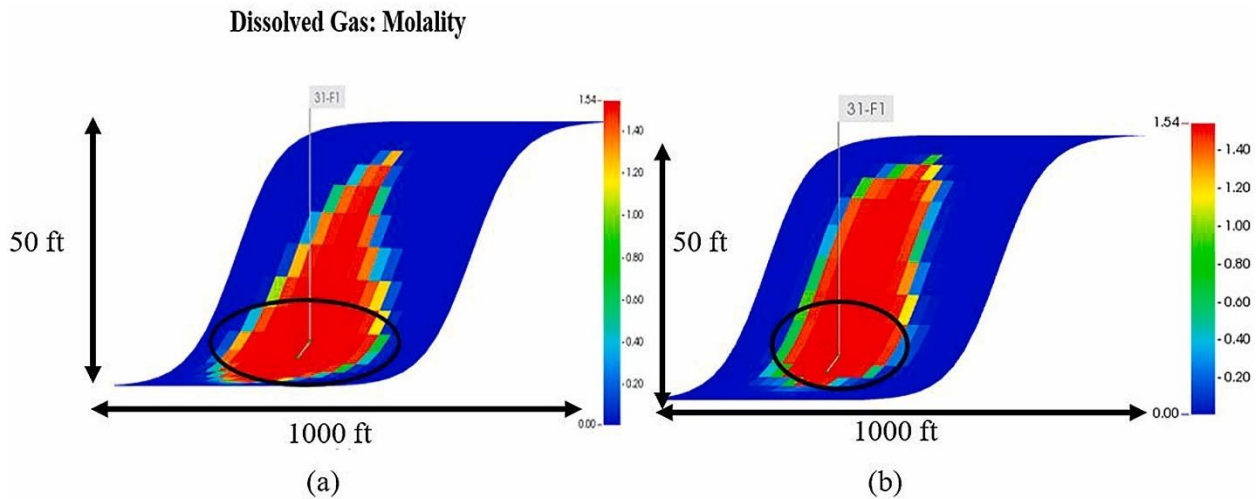


Fig. 2.36 The effect of shale drapes on the dissolved CO₂ concentration. (a) Spatial distribution of dissolved CO₂ molality for the case when shale drape effect is ignored and (b) Dissolved CO₂ molality for case when shale drape effect is considered. When the shale drape is absent, the dissolved plume moves laterally in the injection zone before moving upwards. In the presence of shale drapes, the shale curtails lateral movement of the plume and consequently the vertical migration of the CO₂ plume is favored.

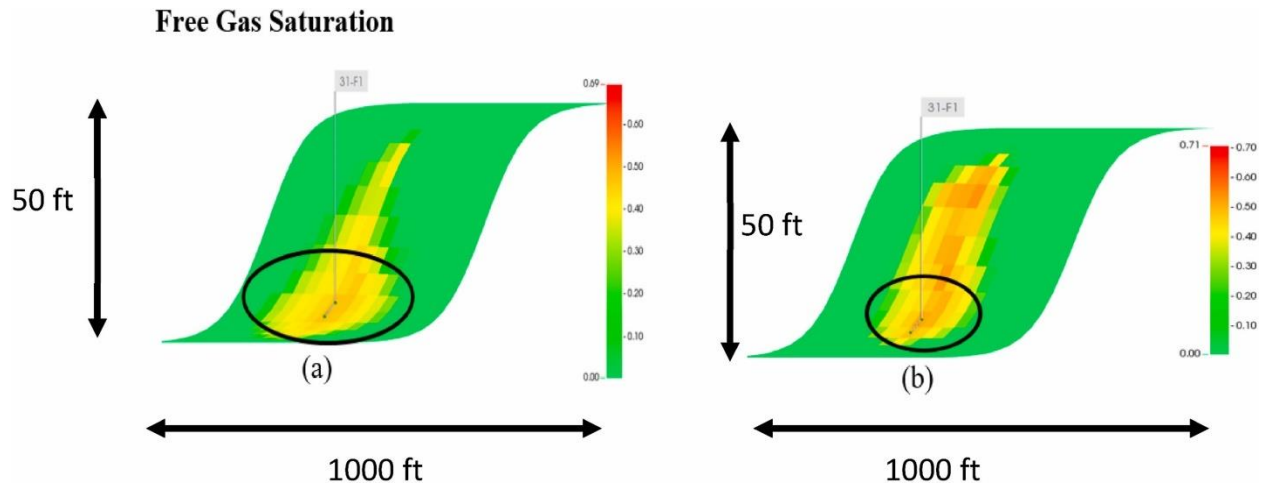


Fig. 2.37 The effect of shale drapes on the free gas CO₂ saturation. (a) CO₂ saturation for simulation run when shale drape effect is ignored, and (b) CO₂ saturation for simulation run when shale drape effect is considered. The shale drape causes vertical migration of the CO₂ plume.

2.7.8 Trapped CO₂

CO₂ trapping occurs after drainage of formation water brine when injection has ended and that is followed by imbibition of water to into the injected zone. The water re-occupies the pores and displaces the injected gas. However, not all of the gas is displaced from the pores. Consequently some residual amount of gas is left in the pores as trapped gas (Delshad et al., 2013b). Fig. 2.38 shows the trapped gas saturation in the two simulation runs. It can be observed that more gas is trapped in the simulation case where shale drape effects were not considered. In that case, the CO₂ flow paths are more dispersed, implying that CO₂ contacts larger area of the rock and that increases trapping capacity (Hovorka *et al.*, 2004). It can be argued that the relative permeability characteristics primarily affects trapped CO₂ saturation. However, in this study, the relative permeability input data is same for all the simulation cases, and therefore its influence on trapped CO₂ saturation is the same in all cases.

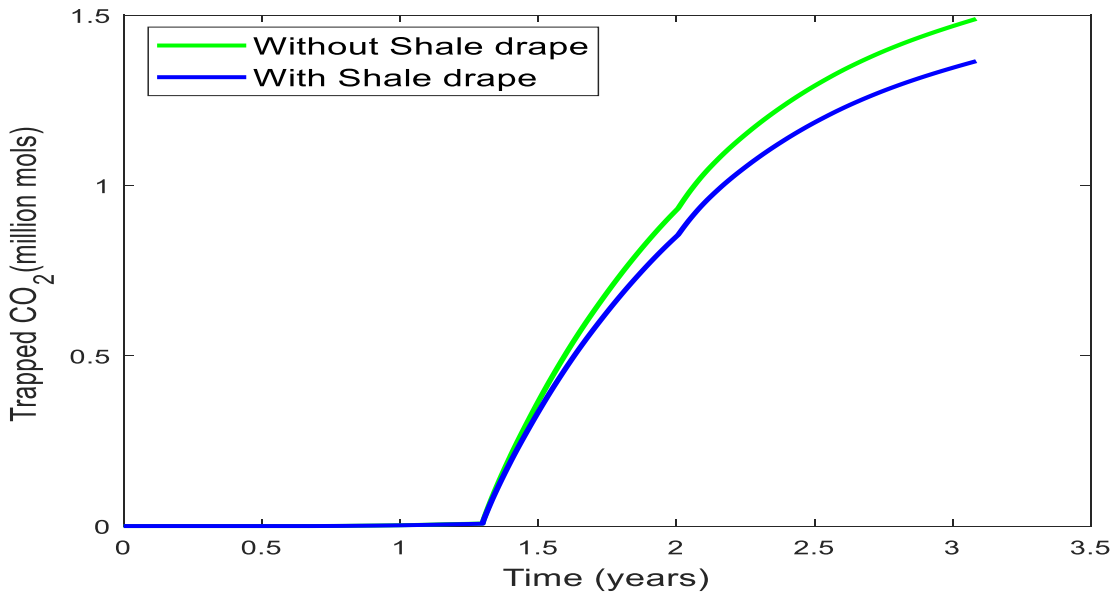


Fig. 2.38 Trapped CO₂ volume as a function of time.

2.7.9 Geometry Perturbation and its effect on bottom hole pressure and CO₂ Plume

As the geometry is perturbed from low to high angular channel displacements, the size of the reservoir is also increased, and the CO₂ plume spreads over a relatively larger area. The CO₂ plume contact area with the reservoir is correspondingly higher (Fig. 2.39). It can also be observed in that figure that the amount of dissolved CO₂ (i.e., CO₂ molality) decreased at the highest angle. This is because dissolution is pressure driven (Duan & Sun, 2003; Portier & Rochelle, 2005; Ayawah, 2014), therefore, an increase in point bar size will result in a decline in pressure at the fringes of the plume and result in less dissolution.

Bottom-hole pressure also declines with increasing angular displacement (Fig. 2.40). The behavior observed in Fig. 2.40 is because pressure has an inverse relationship with the volume that the CO₂ plume occupies. Therefore, as the point bar size increases, bottom-hole pressure is expected to drop.

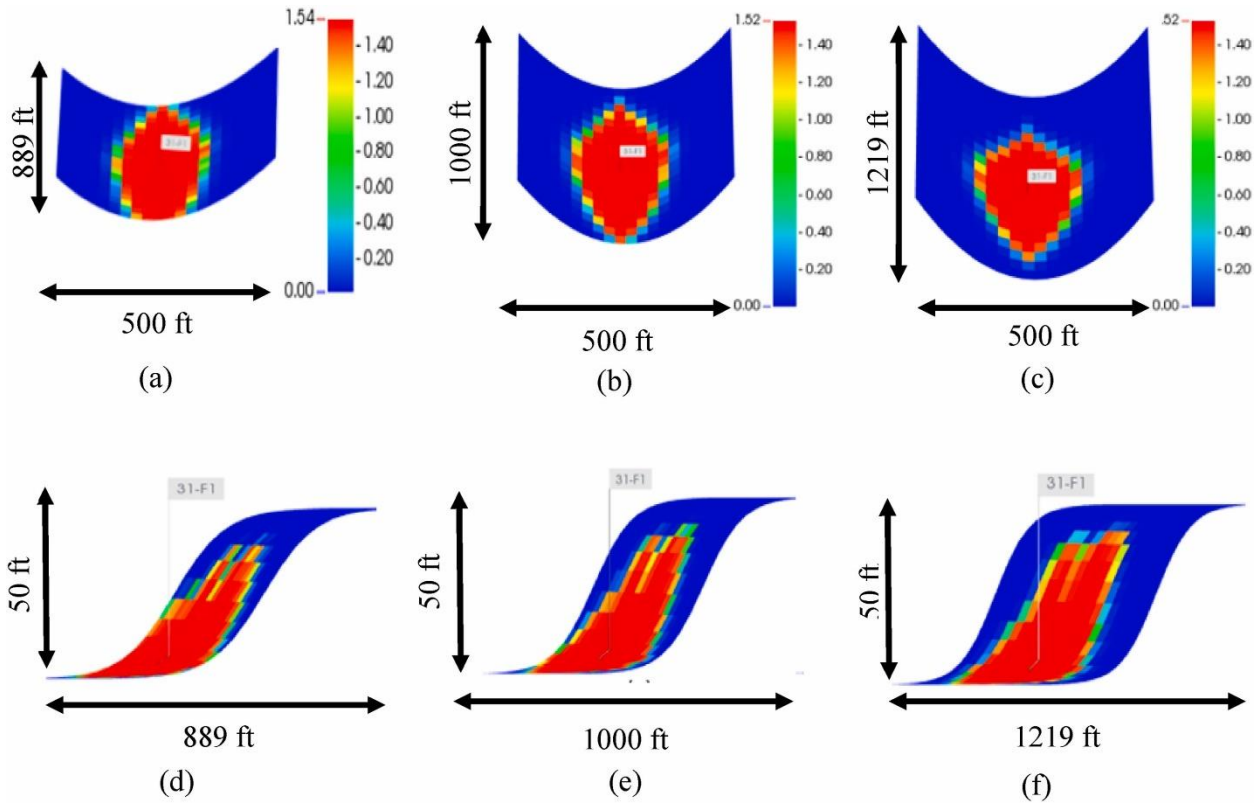


Fig. 2.39 CO₂ plume in the injection zone as the point bar geometry is altered at (a, d) $\omega=30$ deg when viewed in plan as well as cross-sectional view. (b, e) $\omega=40$ deg when viewed in plan and in section. (c, f) $\omega=50$ deg when viewed in plan as well as cross-sectional view.

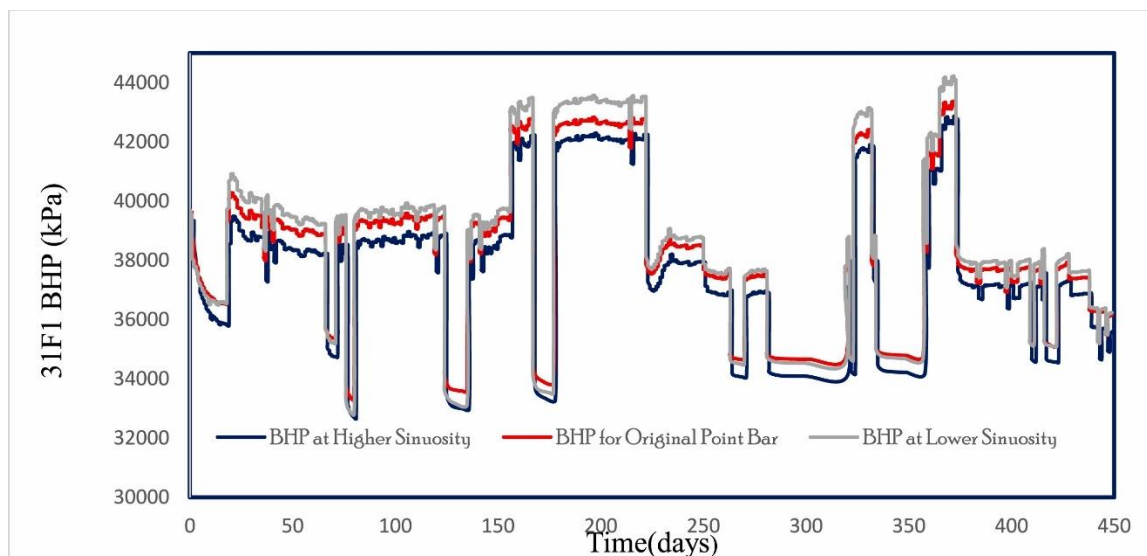


Fig. 2.40 Sensitivity of bottom hole pressure to point bar geometry. An inverse relationship is observed as the point bar is perturbed at different angular displacements or channel sinuosities. Please note: Higher angular displacement is an indication of higher sinuosity.

2.8 Concluding Remarks

A framework for modeling point bar heterogeneities using a stochastic process-based approach has been presented. The method uses geometric functions to model the areal and vertical heterogeneities. Modeling point bar properties is difficult due to its complex geometry, but this was overcome by first developing a gridding scheme that accounts for the aerial shape of the accretion surfaces as well as sigmoidal shape of the inclined heterolithic stratifications. Subsequently, a grid transformation scheme was implemented to allow for optimal geostatistical simulation of the point bar properties. The application of the workflow to the Cranfield, Mississippi dataset has been demonstrated. A novel stochastic scheme for modeling eroded shale drapes on the surface separating successive accretions is also presented. Subsequently, a flow simulation study was conducted to study the effect of point bar geometry and heterogeneities, not only on well response variables like bottom-hole pressure, but also, reservoir fluid flow and storage (i.e., CO₂ flow and storage in our case). In the next chapter, the point bar models will be conditioned to the CO₂ injection data available for the Cranfield in an effort to calibrate the geologic models to reduce the uncertainty in the models. The sensitivities observed by performing flow simulations on the point bar models will provide important insights into how the calibration process can be implemented.

Overall, the modeling approach in this dissertation assumes that the geometry of the point bar can be parametrized using smooth interpolation functions such as cubic splines as mentioned earlier. However, the issue of calibrating the parameters of the interpolation scheme is a challenge, especially when only sparse data is available to guide the inference of the parameters. The presented approach is also subject to the interpretation of channel flow path, which is always difficult based on indirect information available along wells.

Chapter 3 Reservoir Model Calibration

3.1 Introduction

A geologically realistic description of the heterogeneities associated with point bars is essential for field development planning of the reservoir. One way to assess the accuracy of the geologic model and to calibrate it is to assess if it accurately reflects historical injection data. Because the prior models developed are characterized by high uncertainties, the predictive accuracy using any one model is usually poor. This leads to inaccurate forecast of the reservoir performance. Model calibration or history matching is typically performed to address this issue. History matching is premised on the fact that spatial distribution of static or primary reservoir properties (e.g., porosity, permeability, etc.), influence the dynamic or secondary response of the reservoir (e.g., bottom-hole pressure, CO₂ saturation, CO₂ injectivity etc.). Accordingly, history matching involves a systematic adjustment of the static reservoir variables to ensure that simulated dynamic variables acceptably agree with observed dynamic variables. Assuming that the reservoir properties do influence the dynamic response, it is then reasonable to expect that the uncertainty associated with the prediction of spatial variations of reservoir properties reduces as the models are calibrated to reflect the dynamic response. Traditional history matching, e.g. Agarwal *et al.*, (2000), usually relies on engineering expertise and experience to manually adjust the static reservoir variables (Oliver and Chen, 2011). This can be frustrating, time-consuming and expensive (Cancelliere et al., 2011). That has stimulated a growing body of research in automated history matching methods like gradual deformation methods, probability perturbation methods and ensemble-based methods. Some details on these methods are presented in the following section.

Hu, (2000) introduced the gradual deformation method (GDM) for calibrating realizations of Gaussian reservoir models using dynamic data. This method uses a weighted linear combination of independent Gaussian random functions to gradually deform realizations in a stochastic process while preserving their spatial variability. Deformation parameters are used as weights for each independent realization and are adjusted to minimize the mismatch between observed and simulated flow responses. At the end of the process, a realization that maintains the target spatial variability of the reservoir as well as yields a flow response close to the observed response is obtained. GDM has been extended to handle dependent realizations by (Hu, 2002). Other modifications have been made to include elements of sequential simulation (Hu et al., 2001). GDM is simple and easy to implement; however, it guarantees

optimality only within a Gaussian framework. This makes GDM unsuitable for complex reservoirs exhibiting complex connectivity, and where the relationship between the primary state variables and the secondary variables is non-Gaussian. GDM is also computationally expensive and slow to converge, however, these were improved through the incorporation of gradient information by Hu and Le Ravalec-Dupin, (2004), and partitioning of the reservoir into sub-regions by (Le Ravalec-Dupin and Nøtinger, 2002).

A closely related technique to GDM is the probability perturbation method which was introduced by Caers, (2003), applied to large data set by Hoffman and Caers, (2004), and efficiently used to integrate production data into reservoir models by (Kashib and Srinivasan, 2006; Kashib and Srinivasan, 2003; Barrera and Srinivasan, 2009). Like the GDM, updates are realized via the optimization of locally varying deformation parameters. However, instead of using the deformation parameter to merge two Gaussian realizations, the deformation parameter is used to morph the conditional cdf for permeability at a location into a posterior distribution. Subsequently, an updated permeability value is obtained by drawing from the updated conditional distribution. Fundamentally, these methods exploit the algorithmic structure of sequential simulation by updating the conditional probability of the static variables upon the availability of dynamic data. Because the probability perturbation method works directly on the conditional distributions regardless of their shape or other characteristics, it is not restricted to Gaussian models. The probability perturbation method, though elegant, exhibits slow convergence. Some avenues to speed up the convergence are discussed in (Barrera and Srinivasan, 2009).

The use of ensemble Kalman filters (EnKF) for history matching subsurface models has also generated a vast literature, starting with the pioneering contributions of (Evensen, 1994; Burgers et al., 1998; Evensen, 2003), and on to the application of the method for data assimilation (Evensen and van Leeuwen, 1996). Other contributions particularly to reservoir characterization and hydrocarbon production include (Gu and Oliver, 2005; Haugen et al., 2008; Mantilla, Srinivasan and Nguyen, 2011; Thomas et al., 2011; Gharamti et al., 2014; Katterbauer et al., 2015; Tavakoli, Srinivasan and Wheeler, 2014; Kumar and Srinivasan, 2019; Awejori et al., 2022), and several other researchers as well. This method uses the ensemble mean and covariance between the state variables to perform updates on an ensemble of models with spatial distribution of rock properties. The mismatch between the observed and predicted reservoir response is used to update the state variable values at all locations within the reservoir using the Kalman gain, that primarily depends on the covariance between the state variable and the observed dynamic response. As advantageous as EnKF is in terms of computational efficiency

and ability to perform updates on a suite of models, it works optimally under the assumptions that: (1) the joint distribution of the static reservoir variable (e.g., porosity and permeability) as well as that between the state variables and the mismatch error between the observed and predicted dynamic response is multivariate Gaussian; (2) the mismatch between the simulated and observed responses can be linearly related to updates of the state variables. Unfortunately, these assumptions may not hold for several hydrocarbon reservoirs given that the relationship between the static and dynamic characteristics is highly non-linear. Hence the applicability of EnKF may be limited. In an effort to improve EnKF in this context, Schniger et al, (2012) developed a technique to handle non-Gaussian distributions. Their method applies univariate transformation to the state variables (i.e., the static reservoir variables), rendering them univariate Gaussian. This same strategy was also adopted by (Zhou et al., 2011) However, the transformations implemented may not be efficient as ensuring univariate Gaussianity does not imply multivariate Gaussianity, a condition necessary for optimal performance of EnKF. Other ensemble-based techniques and EnKF variants abound, e.g., Ensemble Kalman Smother, (EnKS) (Evensen & van Leeuwen, 2000). Van Leeuwen and Evensen (1996) provide a comprehensive discussion of these ensemble-based methods.

The techniques discussed earlier have been used in history matching studies using injection data from CO₂ sequestration projects (Mantilla et al., 2009; Mantilla et al., 2009 Bhowmik, Srinivasan and Bryant, 2011) . Since the workflow in this study is being implemented for the Cranfield reservoir which is a site for a field CO₂ sequestration experiment, the history matching techniques discussed in previous CO₂ sequestration studies are of interest. In the history matching approach implemented by Delshad et al., (2013) and Hosseini et al., (2013), they observed a decrease in the rate of bottom-hole pressure increase as the injection rate is increased. At an injection rate of 175 kg/min, the change in pressure was about 6.29MPa; upon increasing this rate to about 330 kg/min, the change in pressure was expected to be larger, however, it was surprisingly as low as 0.35MPa, and another rise in injection rate (500 kg/min) yielded only 0.35MPa. The authors explained that this decreasing trend in injection pressure increase may be because the increase in injection rate must have induced fractures around the injection well that serve to divert the injected fluid to regions away from the well. Consequently, they introduced permeability modifiers to match the bottom-hole pressure. However, just as many other reservoirs, the Cranfield reservoir has a complex geology; therefore, introducing permeability modifiers though may guarantee a history-matched model, the predictive accuracy of the matched model may be

compromised. The reservoir model may give a completely misleading picture of future performance even though it may show an impressive match to historical data.

3.2 History Matching within an Indicator Framework

A common drawback with the history matching techniques discussed thus far is their inability to handle complex reservoirs exhibiting non-Gaussian characteristics. The point bar geology characterizing the Cranfield reservoir is likely non-Gaussian given the complex connectivity exhibited by the reservoir facies and the depositional trends observed within such a reservoir. Working within an indicator formalism of reservoir properties (Journel, 1983; Zhu and Journel, 1993) can help us address this challenge. In order for the indicator transformation, the static reservoir variables have to be transformed into binary variables of 1s and 0s by specifying a suitable threshold. In the binary space, the expected indicator outcome at a location conditioned to the available data is directly the conditional cumulative distribution function (ccdf). Hence, subsequent to the development of the *ccdf*, outcomes can be sampled from this *ccdf*. This method is free from Gaussian assumptions as there is no assumption made regarding the form of the *ccdf*. In this dissertation, we implemented an ensemble-based history-matching method using indicator transformation called Indicator-based Data Assimilation (InDA) developed by (Kumar and Srinivasan, 2018, 2019), to history match the data for the Cranfield reservoir. Directly deploying InDA that has been developed for linear geometries to a reservoir exhibiting curvilinear characteristics would yield sub-optimal results. Consequently, we implemented InDA to accommodate such reservoirs by incorporating the reversible grid transformation scheme.

Another common drawback in most of the previous studies is that history matching techniques exclusively focus on perturbation of static reservoir variables and ignore uncertainty related to the reservoir geometry. Yet, flow simulation studies in previous works (e.g. Deveugle et al., 2011; Pranter et al., 2007; Willis and White, 2000) have shown that geometry of the reservoir exerts important controls on reservoir fluid flow. In this chapter, it would be seen that the reservoir geometry and associated uncertainty, and their potential influence on dynamic variables (e.g., bottom-hole pressure) are too significant to be ignored. We therefore propose that geometry calibration should be done even before proceeding to update the static reservoir variables. We assume that the state space describing the geometry follows a Gaussian distribution and would accordingly be calibrated using EnKF.

This results on the following two-step model calibration or history matching process:

- 1) Implement EnKF on ensemble of reservoir model geometries to update the geometry. Pick the model that yields the closest match to the observed injection data.

- 2) Perform InDA updates on ensemble of spatially distributed permeabilities within the optimal reservoir geometry determined in step 1.

3.3 Application to the Cranfield Reservoir

As evidenced by the description in the previous chapter, the Cranfield reservoir exhibits several geologic patterns that would typically suggest non-Gaussian characteristics. The reservoir exhibits porosity and permeability trends (Kim & Hosseini, 2014) and complex depositional patterns (Tao et al., 2013) that vary from core to field scale. The reservoir unit consists of fluvial sandstones with conglomerates in fluvial point-bar and channel deposits (Lu et al., 2012), with shale intercalations and erosional surfaces. The depositional trends show a fining upward sequence, where cross-bedded conglomerates occupy the bottom of the sequence, followed by sandstones, and muddy sandstones. This fluvial depositional setting imparts a high level of heterogeneity, and non-Gaussian characteristics to the Cranfield reservoir. Chlorite is an important authigenic mineral in the sandstones because it preserves porosity by forming a grain coating, which inhibits formation of quartz cementation (Hosseini et al., 2013). For an extensive description of the Cranfield, Mississippi reservoir, readers may refer to (Doetsch et al., 2013; Hosseini et al., 2013; Zhang et al., 2013; Alfi & Hosseini, 2016).

3.4 Reservoir Model Calibration

With the limited coverage of wells in the CO₂ injection area, there is likely to be significant uncertainty associated with the prediction of reservoir geometry. Therefore, the first step towards constraining the reservoir model is to use dynamic data to update initial models of the reservoir geometry using EnKF. The geometry of the reservoir under study (i.e. the Cranfield, Mississippi reservoir), as indicated earlier, is that of a point bar reservoir that has been modeled using a Sine Generation Function (SGF) to represent the lateral aggradation of the channel (Langbein and Leopold, 1966), and a sigmoidal function as described by Thomas, *et al.*, (1987) to model the inclined heterolithic stratifications. The aerial and vertical geometries were combined to form a 3D point bar geometric model. Details of the procedure for modeling the structure of the point-bars are presented in chapter 2. In this framework, the geometry of the point bar is jointly controlled by the angular displacement parameter specified in the SGF and the slope parameter of the sigmoidal function. These parameters were perturbed to generate ensembles of equally likely reservoir geometries. The perturbation was done such that any change in the angular displacement of the SGF automatically reflects in the slope of the sigmoidal

function, leading to a joint perturbation of the aerial and vertical dimension of the reservoir (Fig. 3.1). This joint perturbation was necessary to accurately represent the geometry-related uncertainty.

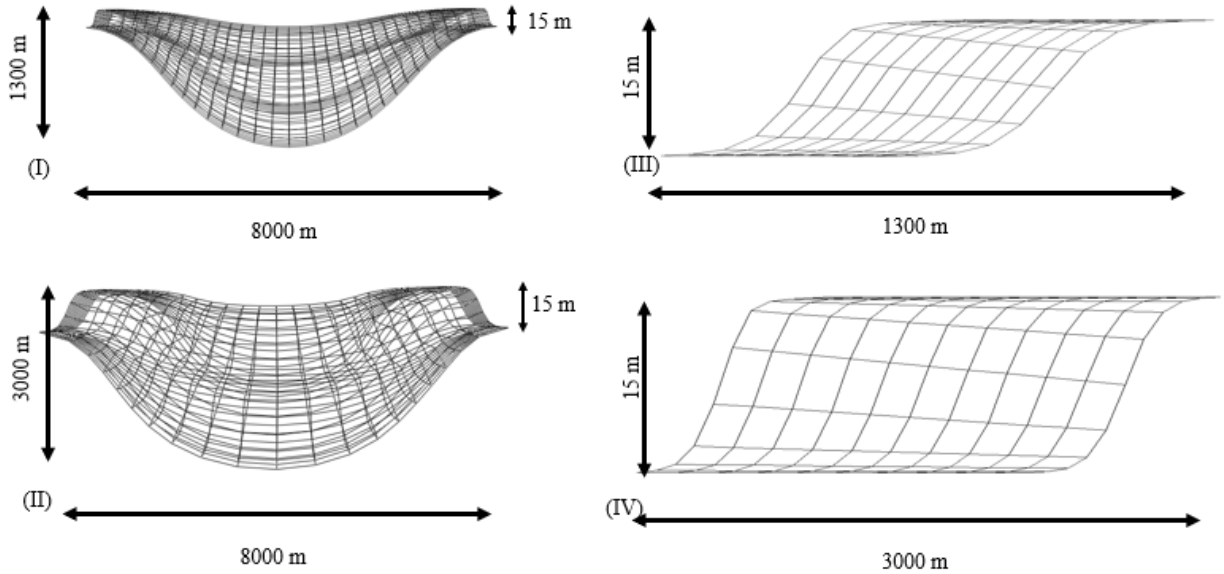


Fig. 3.1 . Randomly selected realizations of point-bar reservoir geometries used for performing EnKF. (I) Shows the case when the angular displacement of the sine generation function was perturbed by 19.4° . Correspondingly, the slope of the beddings denoted by the sigmoidal function also change and is shown on the right. (II) The results when the angular displacement of the sine generation function is perturbed by 45° .

In total, 50 angular displacements were drawn from a normal distribution with mean 35 and standard deviation 10 to generate ensembles of point bar reservoir geometries. This ensemble of geometries represents the initial or prior uncertainties that would be updated upon the availability of a secondary variable (e.g., bottom-hole pressure, reservoir pressure, injection rate). Using CMG-GEM simulator (CMG-GEM, 2019), a flow simulation was run on the ensembles for a period of 450 days. The simulation was run on a curvilinear grid with dimensions $150 \times 150 \times 25$, making up 562500 grid blocks in total. Reservoir properties like porosity and permeability for each model in the ensemble were the same and set according to a base case porosity and permeability distribution. The location of the injection well F1 within the reservoir, the injection schedule and the well parameters used for simulation are shown in Figs. 3.2, 3.3, and Table 3.1, respectively.



Fig. 3.2 Illustration of the gridding employed for performing the flow simulation and the location of injection well F1 within the reservoir.

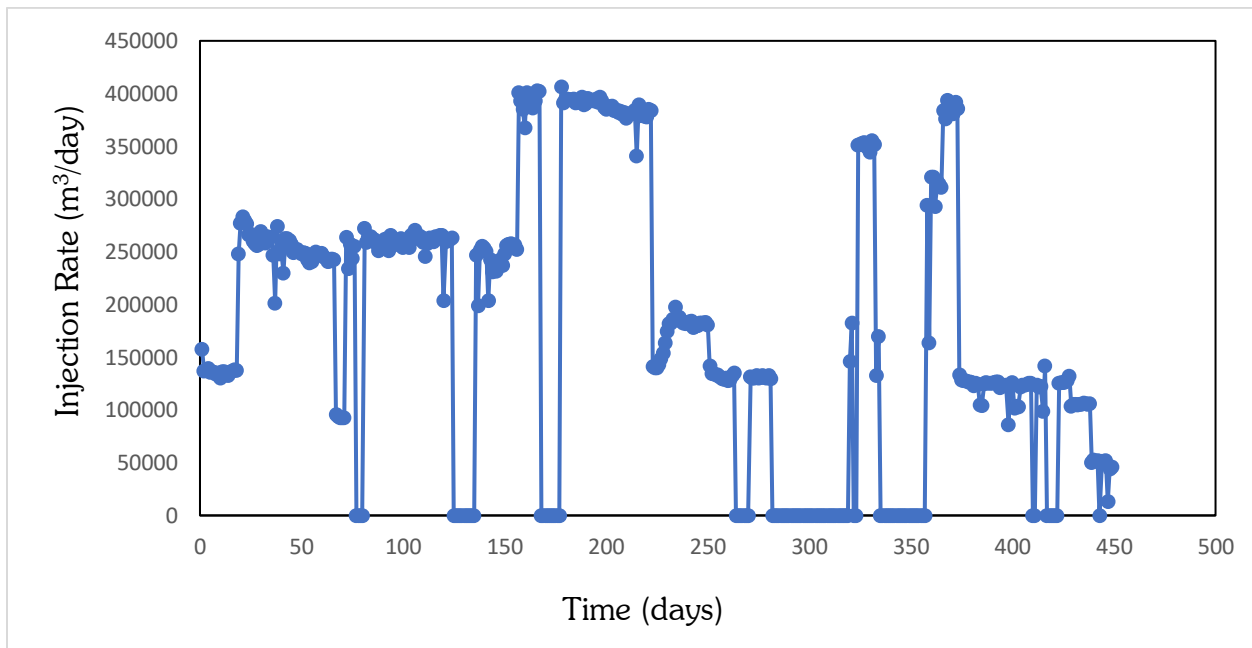


Fig. 3.3 Cranfield injection schedule used for simulation at injection well F1.

Table 3.1 Injection well parameters used for simulation.

Injection Well Parameter	Specification
Well Perforation Address (i, j, k)	75,77,9
Injection Period	Dec 1, 2009 – Feb 25, 2011
Well Radius	0.0762 m
Skin	0
CO ₂ Mole Fraction	1
Injection Rates	See Fig. 3.3
Maximum Bottom-hole Pressure	3800 kPa

Flow simulation was performed on the ensemble to obtain the corresponding simulated dynamic bottom-hole pressures that can be used to estimate errors and infer the required covariance between state parameters, and subsequently update the initial ensemble. Updates were performed on the reservoir geometries using the EnKF formulation in equation 3.1 (Kumar and Srinivasan, 2019).

$$z_o^a = z_o^f + [C_{pz}(h_{jo})]_{1 \times n} \left[[C_p(h_{ij})]_{n \times n} + \text{diag}[C_{\epsilon\epsilon}(h_{ij})]_{n \times n} \right]^{-1} [P_{obs} - P_{sim}]_{n \times 1} \quad (3.1)$$

In Equation 3.1, $C_{pz}(h_{jo})$ terms are the covariance between the state variables and the mismatch, the matrix containing the $C_p(h_{ij})$ terms are the covariance between the state variables. Equation 3.1 yields the updates z_o for the ensemble member index $o = 1, 2, 3 \dots n$; z_o^f is the initial value of the primary variable, which is angular displacement at this stage. z_o^a represents the updated value of the primary variable. P_{obs} and P_{sim} are respectively, the observed and simulated secondary variable, which is bottom-hole pressure in our case. ϵ is a vector of uncorrelated observation errors, $C_{\epsilon\epsilon}$ is therefore a diagonal matrix. To account for possible errors in the observations, samples drawn from the distribution $N(0, C_{\epsilon\epsilon})$ are added to the observed data.

The update (or error) term constitutes all the terms after the first term in equation 3.1. Fig. 3.4b illustrates the updates realized after EnKF implementation. It can be observed that the updates at higher angles are higher than those at lower angles. After performing EnKF updates and running flow simulation on the updated ensemble, a reduction in the spread (i.e., uncertainty) in the simulated bottom-hole pressures is observed (see comparison between Fig. 3.4A and C). The reservoir geometry with the least uncertainty (i.e., error) has an approximate angular displacement of 19.4° , illustrated as the black point in Fig. 3.4b. The figure also indicates that as the algorithm progresses (from right to left) the updates become smaller indicating that the updates using the injection data have stabilized. The simulated bottom-hole pressure after EnKF updates is shown in Fig. 3.4c. The BHP response after the final update corresponding to the lowest error is shown in red in Fig. 3.4c and the updated geometry is shown in Fig. 3.4d. This reservoir geometry was selected for the next phase of the history matching process.

Fig. 3.4 also suggests that geometry alone does not fully explain the dynamic response characteristics of the reservoir under study. A further confirmation is seen after running flow simulation on the updated reservoir geometry ensemble. As shown in Fig. 3.4c, after EnKF updates, the simulated bottom-hole pressures still exhibit considerable spread, indicating appreciable albeit reduced residual

uncertainty. In addition, the model with the least error still does not show much consistency with the observed bottom-hole pressure data. Even so, this calibration step is important as it allows us to select a reservoir geometry and a grid that will ensure a more successful history match of static reservoir properties.

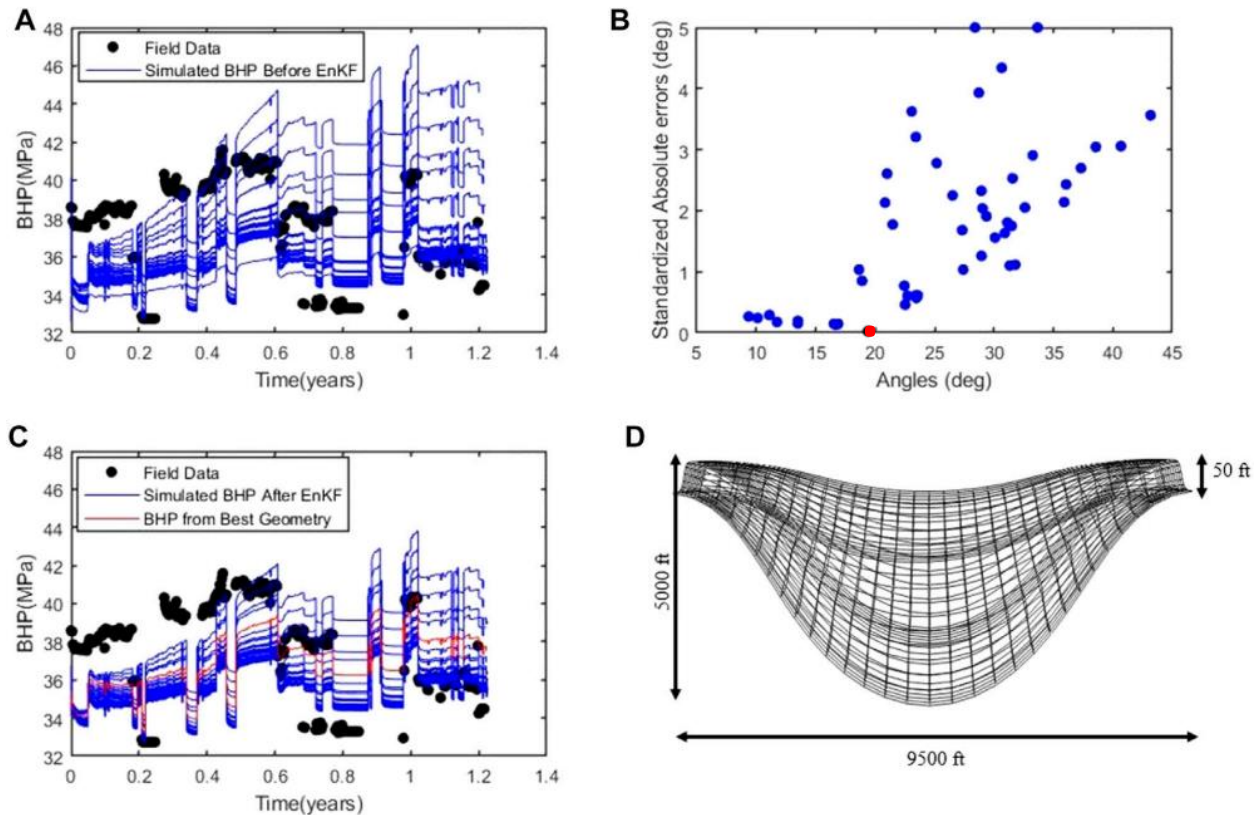


Fig. 3.4 Results obtained at the end of the simulation period by applying the EnKF procedure, a) BHP before EnKF. (b) the updates to the angular displacement obtained by EnKF for various members of the initial ensemble. (c) BHP after EnKF. Red plot indicates BHP from geometry with least error (d) Updated point bar geometry with the least error to be used in the next phase of workflow.

3.5 Permeability updating using InDA

The InDA procedure is discussed extensively in Kumar and Srinivasan (2019) and is summarized in a flow chart as shown in Fig. 3.5. A grid transformation scheme has been incorporated to accommodate the curvilinear geometry of the reservoir under study. The colored boxes are the updated portions of the InDA workflow to allow for curvilinear grid accommodation.

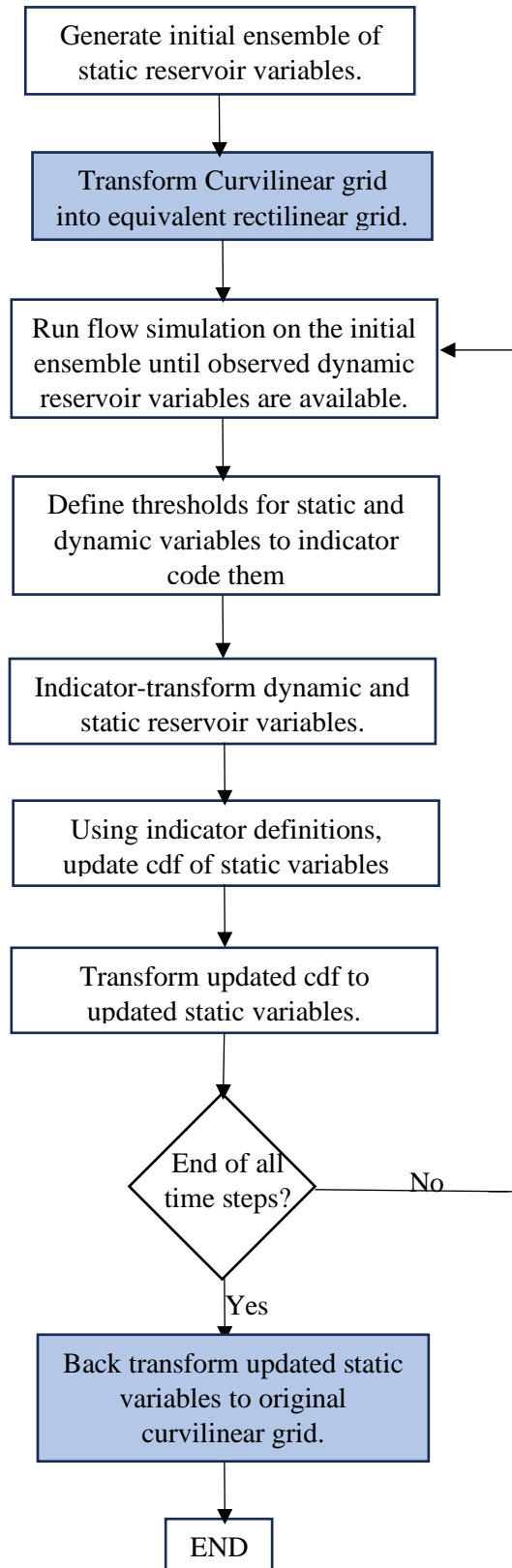


Fig. 3.5 Modified InDA procedure incorporating grid transformation scheme. Color-coded sections represent modifications in InDA. Adapted from (Devesh Kumar & Srinivasan, 2018).I

3.5.1 Defining indicator thresholds for the static variable.

In order to perform indicator transformation of static variables, thresholds(z_k) need to be applied. These thresholds are retrieved as quantiles of the *cdf* of the static variable. One strategy for defining the thresholds would be to use relatively a greater number of quantiles for the portions of the *cdf* exhibiting major variations.

3.5.2 Indicator definition for the static variable

Consider a static variable Z to be transformed into binary variables of 1s and 0s; the corresponding indicator definition for the static variable at location \mathbf{u} for K thresholds $z_1, z_2 \dots z_K$, denoted $I(Z_\alpha^f(\mathbf{u}), z_k)$, is given as:

$$I(Z_\alpha^f(\mathbf{u}), z_k) = \begin{cases} 1 & \text{if } Z_\alpha^f \leq z_k \\ 0 & \text{otherwise} \end{cases} \quad k = 1, 2, 3 \dots K \quad (3.2)$$

In equation 3.2, the superscript f represents the z value before update during EnKF, the subscript $\alpha = 1, 2, 3 \dots n$ corresponds to the realization index in the ensemble.

3.5.3 Indicator threshold definition for the dynamic variable

By running flow simulations on n ensemble of models, we can output the corresponding ensemble of simulated dynamic data ($P_{sim_\alpha}^f$), $\alpha = 1, 2, 3 \dots n$. If $P_{obs_\alpha}^f$ is the observed dynamic data, we can perform updates using the mismatch between the observed and simulated dynamic data. This mismatch, denoted $|\Delta P|$, is defined as:

$$|\Delta P| = |P_{obs_\alpha}^f - P_{sim_\alpha}^f| \quad \alpha = 1, 2, 3 \dots n \quad (3.3)$$

The indicator definition for $|\Delta P|$ at a given threshold $|\Delta P|_p$, denoted Y_p is therefore given as:

$$Y_p = Y_p(|\Delta P_\alpha^f|, |\Delta P|_p) = \begin{cases} 1 & \forall |\Delta P_\alpha^f| \leq |\Delta P|_p \\ 0 & \text{otherwise} \end{cases} \quad p = 1, 2, 3 \dots n \quad (3.4)$$

The theory behind InDA, and the procedure for coming up with the thresholds for the indicator variable based on the data mismatch is presented in (Kumar and Srinivasan, 2019). The key idea is that the thresholds are chosen such that the updated conditional *cdf* of pressure does not change significantly when the threshold for the data mismatch is perturbed around the optimum.

3.5.4 Updating the static variable using InDA Procedure

The indicator-based data assimilation (InDA) is used to estimate the spatial distribution of permeability by assimilating the bottom-hole pressure data available at wells. After the static variable (Z) and dynamic variable (Y) are transformed into binary indicator values of 1s and 0s, updates are performed to the conditional cumulative density function (cdf) describing the distribution of permeability. The updated cdf for n ensemble of models and K thresholds at location \mathbf{u} , expressed as a conditional expectation of the indicator variables is shown in equation 3.5.

$$F(Z_\alpha^f(u) \leq z_k | Y_\alpha) = E(I(Z_\alpha^f(u), z_k)) + \sum_{i=1}^{i=m} \lambda_i (Y_\alpha - E(Y_i)) \quad (3.5)$$

where $Z_\alpha^f(u)$ is the InDA update of the primary variable at a given location \mathbf{u} , the realization index $\alpha = 1, 2, 3, \dots, n$; z_k is the threshold value for the primary variable and there are K such thresholds or cutoffs; Y_α is the indicator variable corresponding to the mismatch between the observed and simulated bottom hole pressures $\forall p = 1, 2, 3, \dots, n$; λ_i is the Kalman Gain, $I(Z_\alpha^f(u), z_k)$ is the binary indicator variable corresponding to the threshold z_k . Like the EnKF update equations discussed previously, λ_i are the Kalman gain computed on the basis of the indicator cross-covariance between the primary indicator data I (corresponding to the variable Z) and the secondary indicator data Y .

As mentioned earlier, InDA is immune to non-linear transformations because of the binary nature of the indicator variable. The indicator variable is immune to any non-linear operations performed with it. In addition, working within the indicator space renders the algorithm free of any Gaussian assumptions, as applying equation 3.5 directly generates the conditional cdf without making any parametric assumptions.

3.5.5 Incorporating grid transformation scheme.

The original indicator-based data assimilation method performs updates within a rectilinear grid system. However, rectilinear grids cannot preserve the curvilinear continuity of point bar reservoirs. To ensure realistic estimates of the spatial continuity of the point bar properties, incorporating a grid transformation scheme is necessary. The grid transformation scheme unravels the point bar curvilinear layers into an equivalent rectilinear form, so that the update can proceed in a manner that preserves the point bar heterogeneity. After updates, the results are transformed back into the original curvilinear grid. Details of the grid transformation algorithm are discussed in chapter 2.

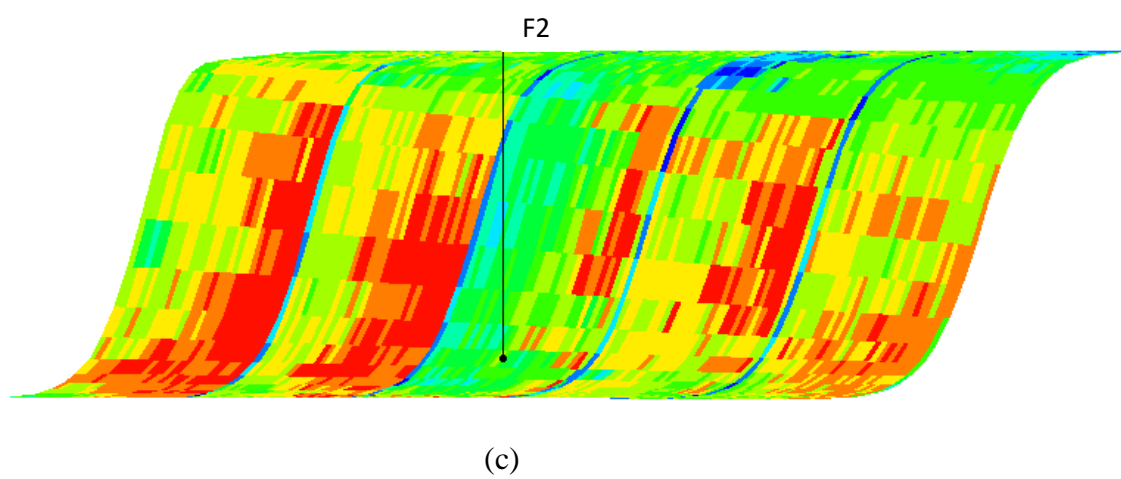
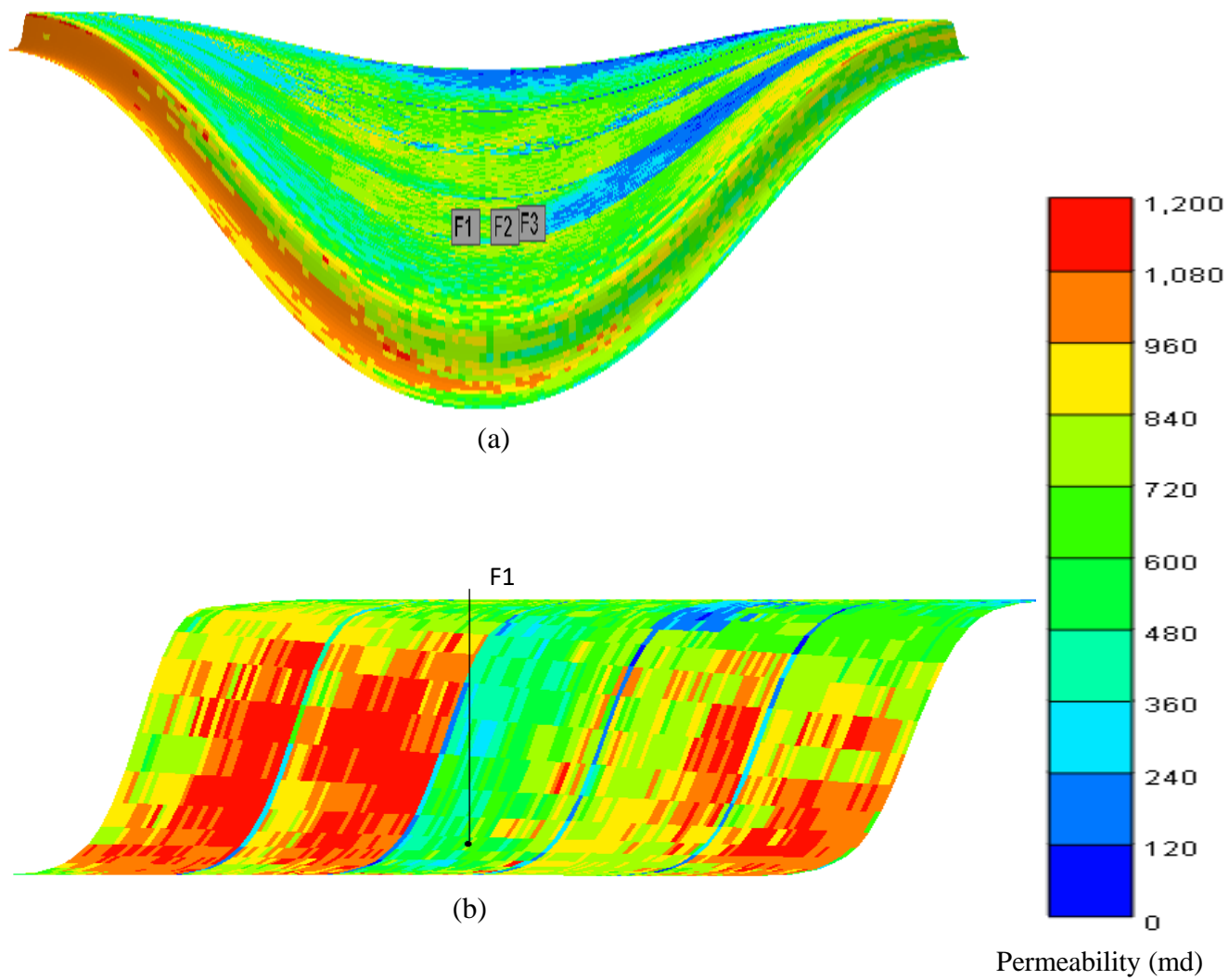
3.6 Implementation of InDA on the Cranfield, Mississippi reservoir model

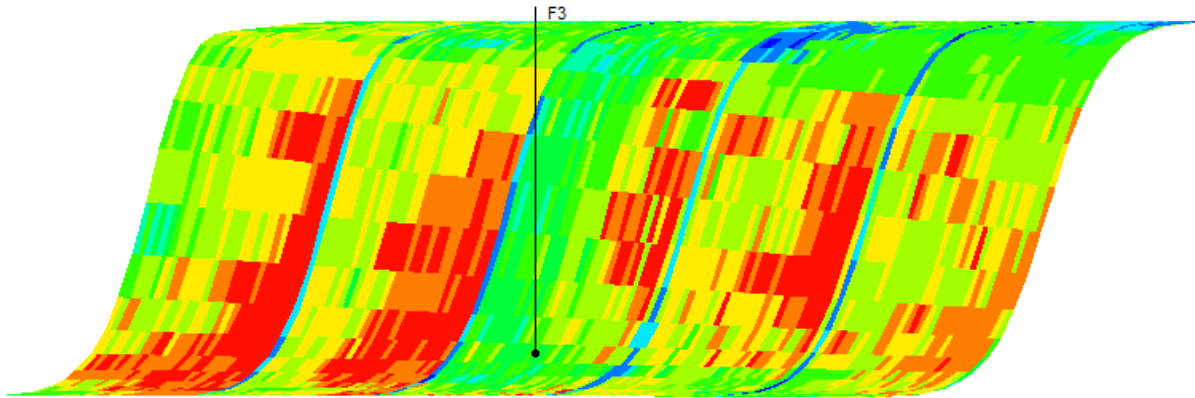
3.6.1 Generation of initial ensemble and reference model

The details of the geologic and geostatistical modeling procedure for generating the initial ensemble of models for the point bar reservoir are detailed in chapter 2. We first modeled the porosity distribution for each layer separately, and subsequently stacked them to obtain a 3D point bar model. Since the hard data for permeability for the Cranfield injection area was not available, we modeled the permeability k from the porosity ϕ models determined in chapter 2, using equation 3.6 (Boisvert et al., 2012), which was derived from micro-modeling for developing an enhanced small scale porosity-permeability relationship.

$$\ln(k) = 4121.2 \cdot \phi^4 + 3963.6 \cdot \phi^3 - 1353.3 \cdot \phi^2 + 202.05 \cdot \phi - 4.3571 \quad (3.6)$$

For point bar reservoirs like Cranfield, key geologic attributes in flow simulation models include the existence of shale drapes, overall fining up trend, and fining trend in the direction perpendicular to each inclined layer. The conditioning data used for generating the initial ensemble was obtained for the F1 injection well, and the observation wells F2 and F3 whose location are shown in Fig. 3.6a. The grid geometry used in InDA corresponds to the best base geometry from the previous EnKF step.





(d)

Fig. 3.6 One of the permeability models in the initial ensemble of models shown (a) with sections along the F1 injection well (b), and observation wells F2 and F3 (c, d).

3.6.2 Defining primary and secondary indicator thresholds.

The use of equation 6 for performing updates is contingent upon defining appropriate indicator thresholds for the primary and secondary variables. These thresholds are quantiles retrieved from the cumulative probability distribution computed on the basis of the available data such that they can adequately describe the cdf of the variable under consideration. Because the data available for modeling the Cranfield reservoir are sparse and moreover, there are trends that the reservoir properties such as porosity and permeability exhibit, a base case model exhibiting realistic property variations in the reservoir was assumed and Fig. 3.7 shows the cdf of this base case permeability model. The figure also shows the thresholds that were identified.

The secondary data thresholds were defined using the mismatch between the simulated and observed bottom-hole pressure data from the Cranfield injection well (Fig. 3.8). Were these based on the ensemble of models or based on the base case model only?

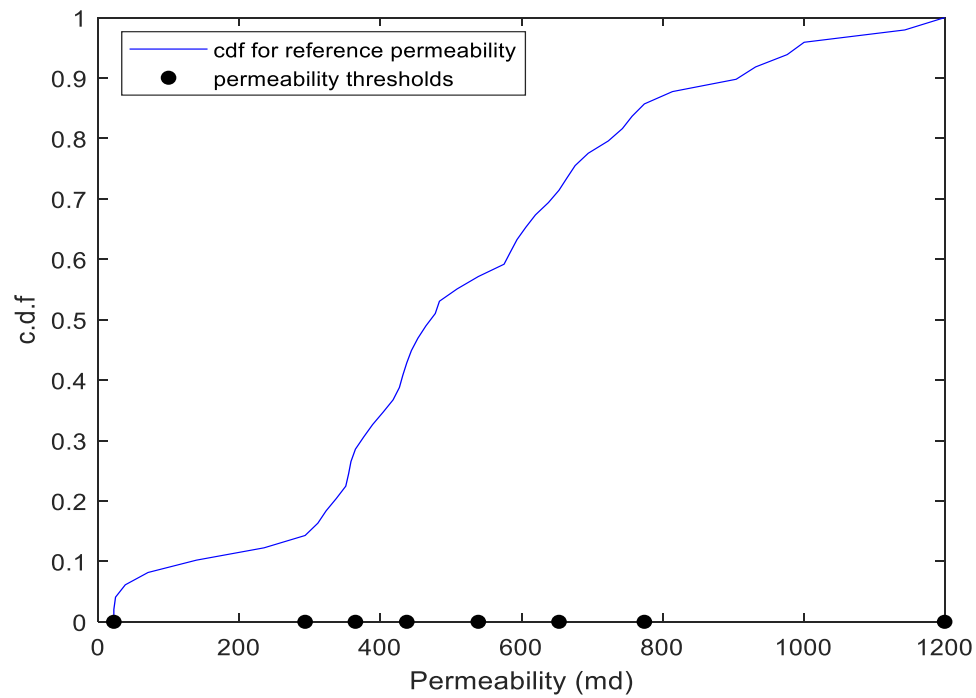


Fig. 3.7 Cumulative distribution function for permeability based on a base case permeability model developed using the modeling workflow in Chapter 2. The primary indicator thresholds retrieved for permeability distribution are also shown. Note the non-Gaussian characteristics of the permeability distribution.

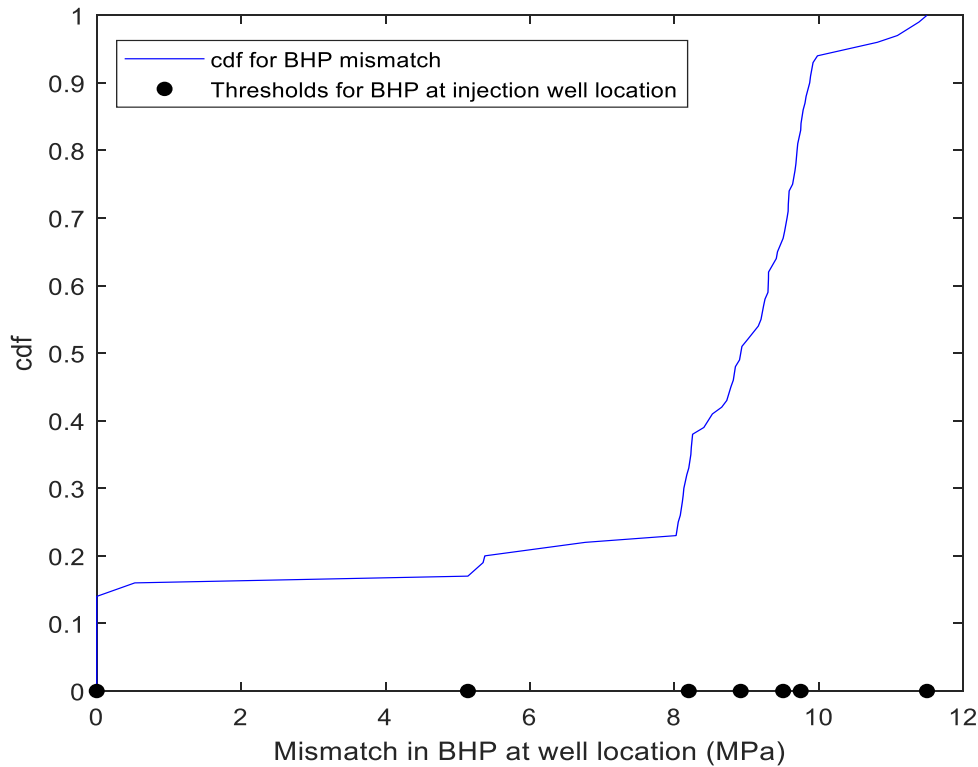


Fig. 3.8 Indicator definitions for Bottom-hole pressure (BHP) at a well location. The underlying behavior of the bottom-hole pressure is also non-Gaussian.

3.6.3 Updating permeability using InDA.

Once the thresholds were defined, flow simulations were run on the entire ensemble of models for one time step of data assimilation. The mismatch between observed and simulated bottom-hole pressure is calculated according to equation 3.3. Fig. 3.9 shows the initial and InDA updated cdf at each location. To determine an updated permeability value at a particular location, the probability corresponding to the old value of permeability is retrieved. Then using this probability, the updated permeability value is sampled from the updated cdf. This procedure is summarized in Fig. 3.9 as starting from 1 and following the arrow direction to 4. The spatial distribution of the initial and updated ensemble average of permeability is seen in Fig. 3.10. As could be observed in Fig. 3.10 and f, the depositional trends that characterize the base model are captured in the updated models. In contrast, these important trends are not apparent in the initial models. The ability of the updated models to capture the underlying geologic structure of the reference model reflects in the low variance in the spatial distribution of the permeability variance after the updates (see Fig. 3.11).

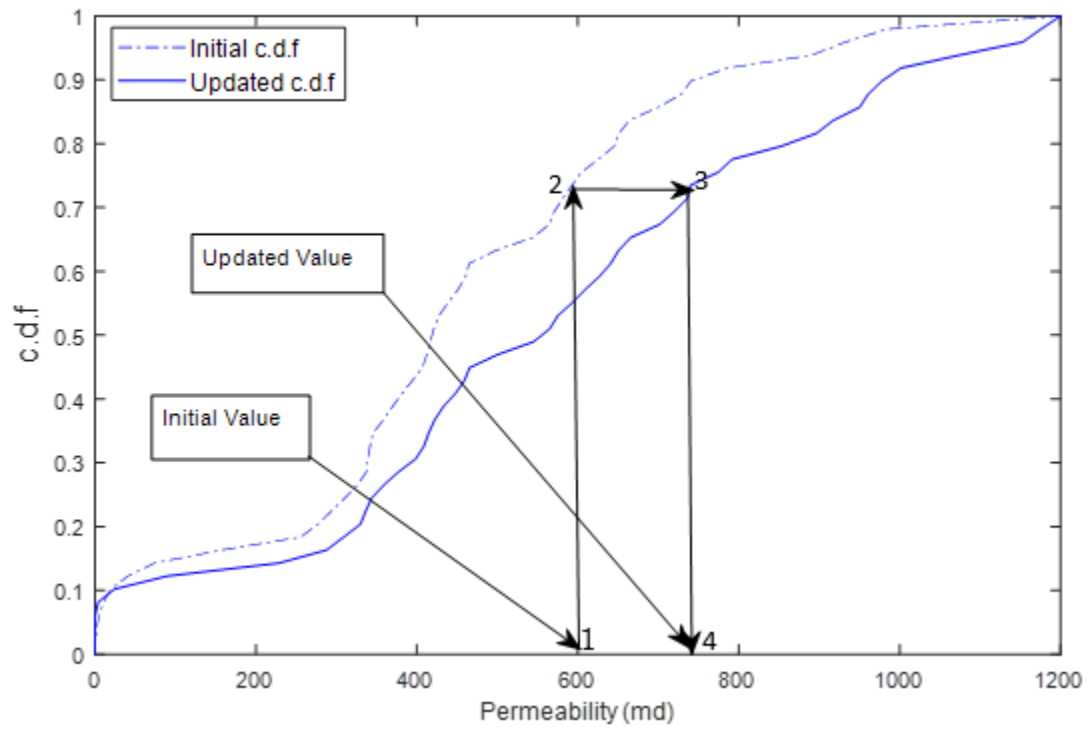


Fig. 3.9 Update of primary variable (permeability) using InDA.

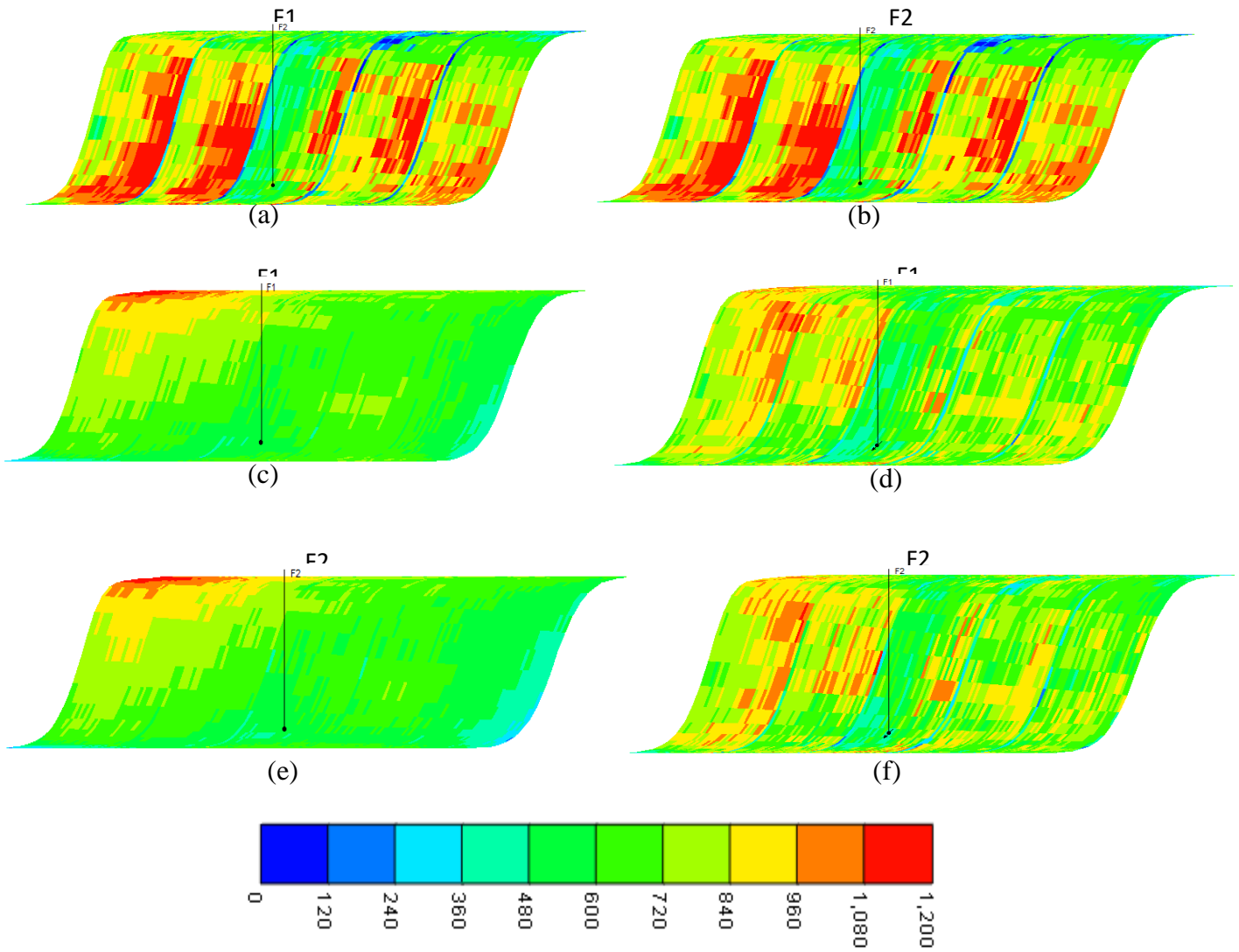


Fig. 3.10 Permeability distribution in the base model in the vicinity of a) injection well F1 and b) observation well F2. Ensemble average permeability distribution before InDA in the vicinity of c) injection well F1 and e) observation well F2. After InDA in the vicinity of d) injection well F1 and f) observation well F2.

3.7 Ensemble Permeability Variance

The uncertainty represented by the reservoir models prior to and after the data assimilation can be assessed by looking at the ensemble variance of permeability. Figure 3.11 shows the ensemble variance of permeability at each grid location.

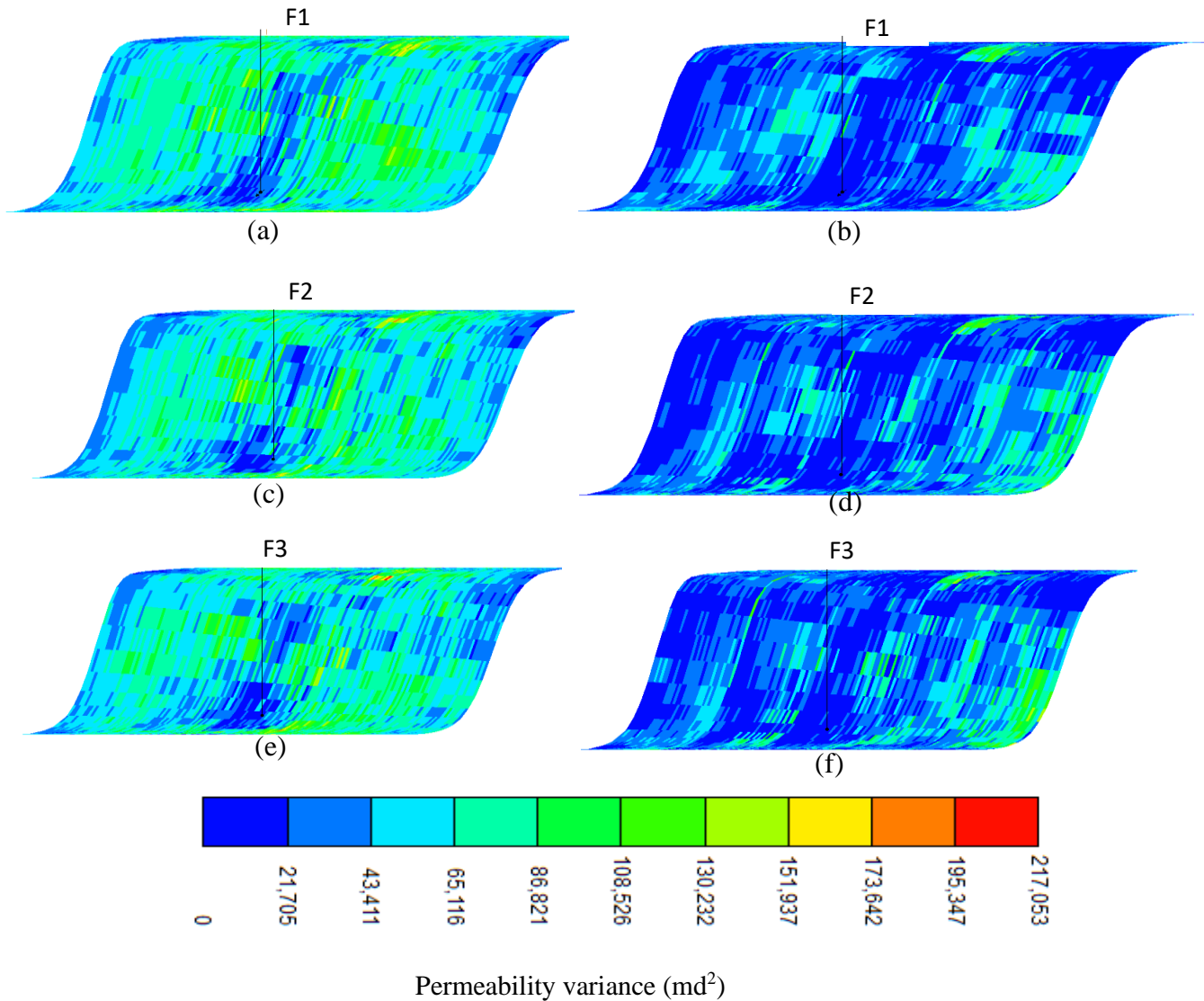
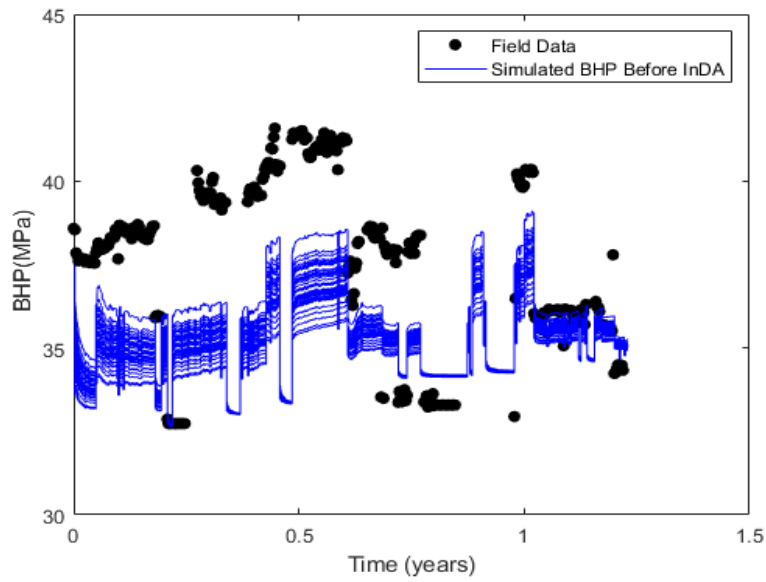


Fig. 3.11 Permeability variance in the vicinity of injection and observation wells before InDA (a, c, e) and after InDA (b, d, f).

3.8 Bottom-hole Pressure response after InDA

Just as in the case of the EnKF results, another simulation was run on the updated permeability models to assess the extent to which the simulated dynamic data (i.e., simulated bottom-hole pressure) matches observed dynamic data (i.e., observed bottom-hole pressure).

We observed an improvement in the match of the updated simulated BHP ensemble to field BHP data (see Fig. 3.12). This can be attributed to the more accurate spatial distribution of permeability obtained using InDA. The small spread, and therefore the small variance in the simulation results is due to the overall low variance of permeability realized after performing updates. Additionally, history matching within an indicator framework allows relatively big updates to be made to the static properties, which speeds up convergence as well.



(a)

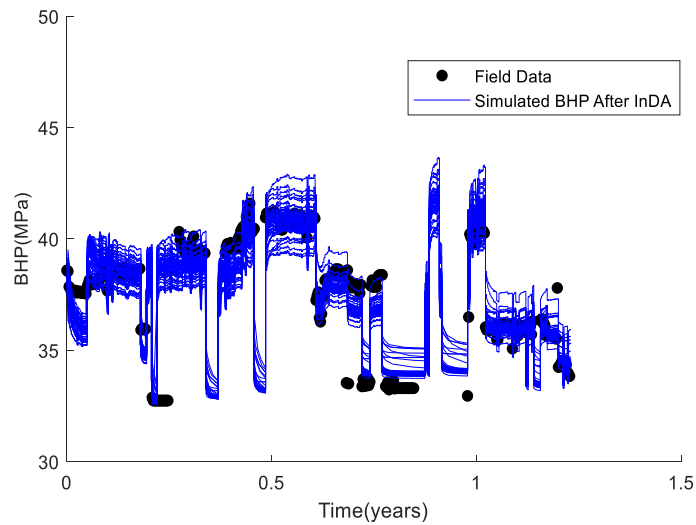


Fig. 3.12 History Matching Results (a) Simulated bottom-hole pressure before InDA, and (b) Simulated bottom-hole pressure after InDA. The line indicated by the black points are the field observed data

3.9 Forecast and Analyses of CO₂ sequestration parameters.

Using the updated models, CO₂ injection simulation was run for about 1.25 years after which the injection well was shut in; the simulation was then run in a forecast mode for the next 50 years, and the uncertain evolution of the CO₂ plume was analyzed. Fig. 3.13 shows the uncertainty in the flow

responses before and after ensemble permeability updates using InDA. As observed in this figure, the simulation results show a reasonable match with the reference results (black points). In addition, there is a reduction in the variance associated with the predictions and therefore, with the uncertainty in the prediction of CO₂ displacement after performing InDA updates. The trapped CO₂ (also called residual trapped CO₂) in millions of moles saw the most significant reduction in uncertainty as illustrated in Fig. 3.13a and b. The reduction in uncertainty is due to more accurate representation of the reservoir architecture and spatial distribution of rock properties. Point bar reservoirs (including the reservoir under study) exhibit unique depositional trends. For example, shale drapes that are found on the surfaces of the inclined beds in the point bar act as flow barriers due to their low permeability. These shale drapes are better captured after the hierarchical EnKF and InDA updates and could even be seen in the overall ensemble permeability average as shown in Fig.3.10. Because the low permeability barriers favor trapping tendencies, updating permeability to capture them would significantly affect the uncertainty in the trapped CO₂. Unlike residual trapped CO₂, pressure and temperature drive dissolved CO₂ (Duan and Sun, 2003; Portier and Rochelle, 2005). Because the temperature is held constant and the pressure response is diffused, the updating process would not significantly reduce the uncertainty associated with pressure and temperature as much as it does to the volume of residual trapped CO₂.

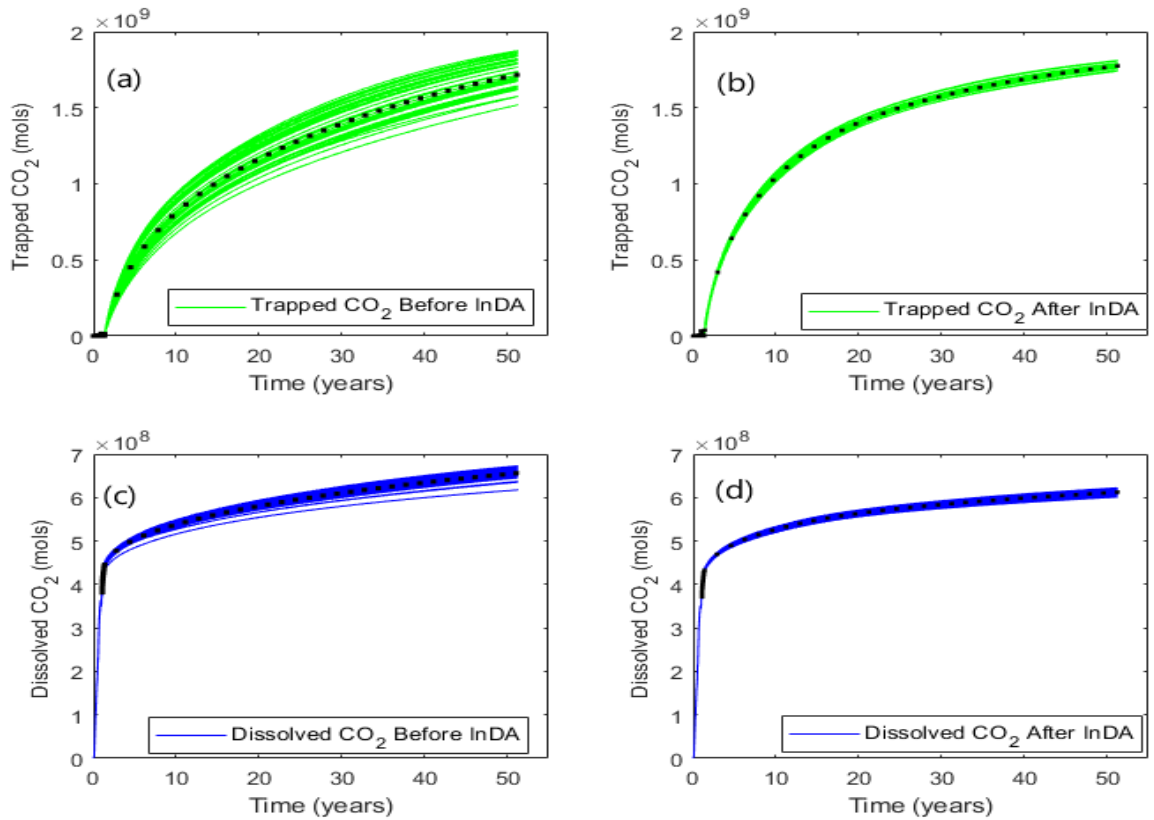


Fig. 3.13 CO₂ sequestration responses before and after permeability updates. Moles of residual trapped gas (a) before InDA and (b) after InDA. Moles of dissolved gas (c) before InDA and (d) after InDA. Black scatter plots represent the reference.

3.10 Summary and Concluding remarks.

A two-step ensemble-based history-matching procedure for calibrating heterogeneous geological formations exhibiting complex connectivity and non-Gaussian characteristics was implemented using EnKF and InDA. These ensemble-based techniques were modified to handle curvilinear grids. We emphasize the importance of considering uncertainties in the reservoir geometry and argue that the calibration of geometry must be done before perturbing the static variables. The study used data from the Cranfield, Mississippi CO₂ injection reservoir to assess the uncertainty in CO₂ sequestration potential in the long-term, after updating permeability.

The following points are important:

- 1 Uncertainty in the reservoir geometry can have an appreciable impact on the history-matching results and must therefore not be overlooked.

- 2 InDA is a robust technique for updating complex reservoirs with non-Gaussian characteristics as it can predict the underlying non-Gaussian spatial distribution of the static variables of such reservoirs. As permeability distribution in reservoir such as the point bar system in Cranfield significantly affect CO₂ flow migration and storage, InDA's ability to history-match these variables makes it a promising technique for probabilistic assessment of reservoir response and uncertainty quantification.
- 3 Despite the assertions made in point 2, it is important to note that direct implementation of InDA on reservoirs with curvilinear geometry (e.g., point bars) may not be successful unless a suitable grid transformation scheme is implemented to allow InDA to handle the curvilinear geometry of such reservoirs.

Chapter 4 Rock Physics Modeling

4.1 Introduction

In the previous chapter, we presented a method to calibrate the point bar model using dynamic data. The practicality of the method was demonstrated using the Cranfield, Mississippi injection data. The injected supercritical CO₂ introduces changes in fluid saturation within the point bar reservoir. This potentially affects the elastic properties, and consequently, the seismic velocity propagation within the reservoir. The exploration of this relationship between the distribution of CO₂ in the reservoir and the corresponding seismic response is the focus of this chapter.

4.2 Gassmann Theory

To further increase the reliability in monitoring and characterizing the test site for CO₂ sequestration, the seismic response of the point bar model that is subjected to CO₂ injection must be investigated and compared to any available seismic data. In doing this, rock physics modeling is critical as it links the reservoir rock properties, typically porosity and fluid saturations, to the seismic velocity propagation across the reservoir. Many studies (e.g., Willie *et al.*, 1956; 1958; Raymer *et al.*, 1980; Han *et al.*, 1986; Eberhart-Phillips *et al.*, 1989) have made attempts to establish empirical relationships between seismic velocity and porosity from measurements and analyses of core and log data. However, these empirical correlations are not based on physical principles. Therefore, the use of these empirical correlations usually renders an unsatisfactory modeling of the rock physics (Smith *et al.*, 2003). An alternative approach, that has risen to prominence is the fluid substitution method proposed by (Gassmann, 1951). This approach relates the elastic properties (e.g., bulk modulus) of the formation to its pore space, the fluid occupying the pore space, and matrix (or stiffness of the rock material). Specifically, Gassmann's equation relates the porosity of the reservoir rock to bulk moduli of the dry rock, the saturated rock, the mineral grains, and the pore fluid as:

$$K_{sat} = K_{dry} + \frac{\left(1 - \frac{K_{dry}}{K_{gr}}\right)^2}{\frac{\phi}{K_{fl}} + \frac{1 - \phi}{K_{gr}} - \frac{K_{dry}}{K_{gr}^2}} \quad 4.1$$

where K_{sat} is the bulk modulus of the saturated (or wet) rock; K_{dry} is the bulk modulus of the dry (or unsaturated) rock; K_{gr} is the bulk modulus of the mineral grain; K_{fl} is the bulk modulus of the pore

fluid; ϕ is the porosity of the reservoir rock. In Gassmann's formulation, the shear modulus is constant and is not a function of the presence of pore fluids in the reservoir rock (Biot, 1956a, 1956b; Berryman and Milton, 1991). A mathematical proof of this constant shear modulus behavior has been provided by Berryman, (1999).

The velocity of the compressional wave in a saturated rock, V_p^{sat} , is calculated from equation 4.2 (Aki & Richards, 1980)

$$V_p^{sat} = \sqrt{\frac{K_{sat} + \frac{4}{3}\mu_{sat}}{\rho_{sat}}} \quad 4.2$$

where μ_{sat} is the shear wave velocity across the reservoir rock. As stated earlier, in Gassmann's formulation; shear wave velocity at saturated and unsaturated conditions are the same ($\mu = \mu_{sat}$); ρ_{sat} is the density of the reservoir rock and it is calculated from equation 4.3.

$$\rho_{sat} = \phi\rho_{fl} + (1 - \phi)\rho_{gr} \quad 4.3$$

At in-situ conditions, bulk modulus for the saturated rock K_{sat} could be calculated using log data (density and velocity logs) as:

$$K_{sat} = \rho_b \left(V_p^2 - \frac{4}{3}V_s^2 \right) \quad 4.4$$

ρ_b is the bulk density of the rock, V_p and V_s are respectively, the primary wave velocity (i.e., p-wave velocity) and shear wave velocity at in-situ conditions.

4.3 Rock and Fluid Property Modeling

4.3.1 Porosity

Porosity of the reservoir could be determined from laboratory experiments on core samples, wireline logs etc. The available observed data can be interpolated to all other locations in the reservoir using geostatistical techniques as discussed in the previous chapter.

4.3.2 Density and bulk modulus of the pore fluid mixture

The fluid density, ρ_{fl} is a mixture density of all the fluid components in the reservoir. Using the saturation of each pure fluid component as weight, the mixture density of the fluid could be calculated by a weighted sum as shown in equation 4.5.

$$\rho_{fl} = \sum_{i=1}^n S_i \rho_i \quad 4.5$$

where n is the total number of pure fluid components in the reservoir; ρ_i and S_i are respectively, the density and saturation for a pure fluid component i .

The bulk modulus of the fluid mixture could be determined based on factors such as fluid saturation (Smith, *et al.*, 2003) and the direction of stress propagation with reference to the component stratification (Vasco et al., 2019). For a uniform saturation, or for a case where the stress propagation is in the direction perpendicular to the component stratification, the Reuss (1929) harmonic average can be used (see equation 4.6). Alternatively, if the saturation is non-uniform or patchy, the arithmetic average developed by Voigt, (1928) is suitable (see equation 4.7). Equation 4.7 also works for a situation where the propagation is parallel to the stratification of components in the reservoir. Hill, (1952) discovered that the bulk modulus lies between the Reuss and Voigt limits, and proposed an arithmetic average of the Reuss and Voigt approximations (See equation 4.8).

$$K_{fl} = K_{fl}^{Reuss} = \left[\sum_{i=1}^n \frac{S_i}{K_i} \right]^{-1} \quad 4.6$$

$$K_{fl} = K_{fl}^{Voigt} = \sum_{i=1}^n K_i S_i \quad 4.7$$

$$K_{fl} = K_{fl}^{Hill} = \frac{(K_{fl}^{Voigt} + K_{fl}^{Reuss})}{2} \quad 4.8$$

The properties of the pure components such as fluid bulk modulus K_i and density ρ_i are calculated using the empirical correlations of Batzle and Wang, (1992) or by applying an equation of state (as in McCain, 1990; Danesh, 1998).

The saturation of the fluid components could be obtained from field measurements (e.g., reservoir saturation tool (RST) data) or from compositional flow simulations.

When working with results from compositional flow simulation, densities and saturations for brine and CO₂ could be imported from the flow simulation into the rock physics modeling workflow.

4.3.3 Bulk modulus of the mineral matrix

To find the bulk modulus of the mineral matrix K_{gr} it is essential to determine the mineral composition of the reservoir rock. This can be obtained in different ways such as clay volume estimation from wireline logs (gamma ray logs), laboratory examination of core samples e.g., X-ray diffraction (Lu *et al.*, 2011), or by assuming that the only dominant minerals are clay and quartz (Smith *et al.*, 2003; Kumar, 2006). Upon determining the mineral abundance, the bulk modulus of the mineral matrix can be calculated either by the Reuss (1929) method using a harmonic averaging scheme (Equation. 4.9) or by the Voigt, (1928) approach using a weighted mean scheme (Equation 4.10).

$$K_{gr}^{Reuss} = \left[\sum_{i=1}^m \frac{F_i}{K_{gr,i}} \right]^{-1} \quad 4.9$$

and

$$K_{gr}^{Voigt} = \sum_{i=1}^m K_{gr,i} F_i \quad 4.10$$

m is the number of minerals making up the rock matrix, F_i is the fraction of mineral i in the rock mass; and $K_{gr,i}$ is the bulk modulus of mineral i .

(Hill, 1952) combined these two formulations as seen in equation 4.11.

$$K_{gr} = K_{gr}^{Hill} = \frac{(K_{gr}^{Voigt} + K_{gr}^{Reuss})}{2} \quad 4.11$$

4.3.4 Frame Bulk modulus

The bulk modulus of the frame represents the bulk modulus of the reservoir when all pore fluids are drained. It can be obtained from laboratory measurements, empirical correlations, or wireline log data (Budiansky and O'connell, 1976; Gregory, 1976; Zhu and McMechan, 1990; Murphy *et al.*, 1993; Spencer *et al.*, 1994). If wireline log data is available, equation 4.1 could be re-expressed to determine the bulk modulus of the frame as equation 4.12 (Zhu & McMechan, 1990)

$$K_{frame} = K_{dry} = \frac{K_{sat} \left(\frac{\phi K_{gr}}{K_{fl}} + 1 - \phi \right) - K_{gr}}{\frac{\phi K_{gr}}{K_{fl}} + \frac{K_{sat}}{K_{gr}} - 1 - \phi} \quad 4.12$$

The procedure for calculating the bulk modulus of the frame, and the post-injection seismic velocity is detailed in Table 4.1.

Table 4.1 Procedure for the application of Gassmann’s formulations

Step	Action
1	Analyze data from wireline logs (sonic, velocity logs, and porosity logs)
2	Estimate the bulk modulus of the mineral grain K_{gr} using eq. 4.9 – 4.11
3	Estimate the bulk modulus and density of brine from (Wang, 2001). With the results from step 2, estimate the fluid bulk modulus K_{fl} (use eq. 4.6 -4.8) and density $\rho_{sat} = \rho_b$ (use eq. 4.3) at in-situ conditions
4	Calculate the bulk modulus at in-situ conditions K_{sat} (use eq. 4.4)
5	Calculate the bulk modulus of the frame $K_{dry} = K_{frame}$ (use eq. 4.12)
6	Estimate the bulk modulus K_{fl} (use eq. 4.6 - 4.8) and density ρ_{fl} (use eq. 4.5) of the fluid mixture after CO ₂ injection. Density of the saturated rock after CO ₂ injection is calculated using eq. 4.3
7	With the bulk modulus from step 6, estimate the post-injection bulk modulus of the saturated rock using eq. 4.1.
8	Estimate the post-injection seismic velocity of the saturated rock V_p^{sat} use eq. 4.11

4.4 Application to the Cranfield reservoir

In this section, the Gassmann formulation described earlier will be applied to model the post-injection seismic velocity of the Cranfield reservoir rock. We begin by computing the bulk modulus of the rock matrix. As discussed previously, the mineral composition of the reservoir must be known for doing this calculation. Lu et al., (2012) presented X-ray diffraction test on core samples that were retrieved from the Cranfield well F-2 within a depth range of about 3178 – 3200 m. It was shown that the reservoir is mainly composed of quartz (79.4%), chlorite (11.8%), kaolinite (3.1%) and illite (1.3%). The less dominant minerals were calcite, albite, and dolomite. Of these three minerals, calcite is the most abundant (1.1%). In this study, the mineral compositions have been standardized to sum up to 1 as shown in Table 4.2. The elastic properties of quartz, calcite and the other minerals were obtained from (Carmichael, 1989), (Mavko *et al.*, 1998) and (Wang *et al.*, 2001), respectively. Details of the elastic properties of the minerals and fluids are shown in Table 4.2.

In order to calculate the saturated bulk modulus at in situ conditions K_{sat} and the dry bulk modulus K_{dry} , some other inputs are needed and for that purpose, the rock physics model is conditioned to well data for the detailed area of study in the Cranfield test site. The density, GR, V_p and V_s logs used for data conditioning in the rock physics modeling are shown in Fig. 4.1. The saturation and density of CO₂ and brine were imported from the compositional flow simulation conducted in chapter 3. Also, the reservoir porosity was obtained from the ensemble of geologic models that were calibrated in chapter 3. The bulk modulus of the brine and the injected CO₂ were estimated from (M. L. Batzle & Wang, 1992; Wang, 2001). The procedure described in Table 4.1 was followed to model the rock physics over all the updated ensemble of models. For a practical demonstration of how to calculate the p-wave velocities, please refer to appendix B, which implements the Gassmann's fluid substitution procedure on one of the ensemble realizations. Continuing these calculations for all depths, the post-injection seismic velocity profiles for the F-1 and F-2 wells can be obtained and shown in Fig. 4.2. A close match between the log data and the modeled velocity is expected because the conditioning data along the F-1 and F-2 wells were used to model the post-injection velocities.

A reduction in the seismic velocity is observed after CO₂ is injected (see Fig. 4.3). The introduction of CO₂ reduces the bulk density of the reservoir fluids. The reduction in seismic velocity as the fluid bulk density reduces is directly attributable to equation 4.2. Similar observation has been reported earlier in (Daley *et al.*, 2014).

Table 4.2 Properties of minerals and fluid for the Cranfield Reservoir.

Mineral/Fluid	Standardized Fractions	Density (g/cm ³)	Bulk Modulus (GPa)	Shear Modulus (GPa)
Quartz	0.8211	2.650	38	44
Chlorite	0.1220	2.681	127	81.9
Kaolinite	0.0321	2.444	47.9	19.7
Illite	0.0134	2.706	60.1	25.3
Calcite	0.0114	2.710	76.8	32
CO ₂		0.577	0.128	
Brine		1.11	2.21	

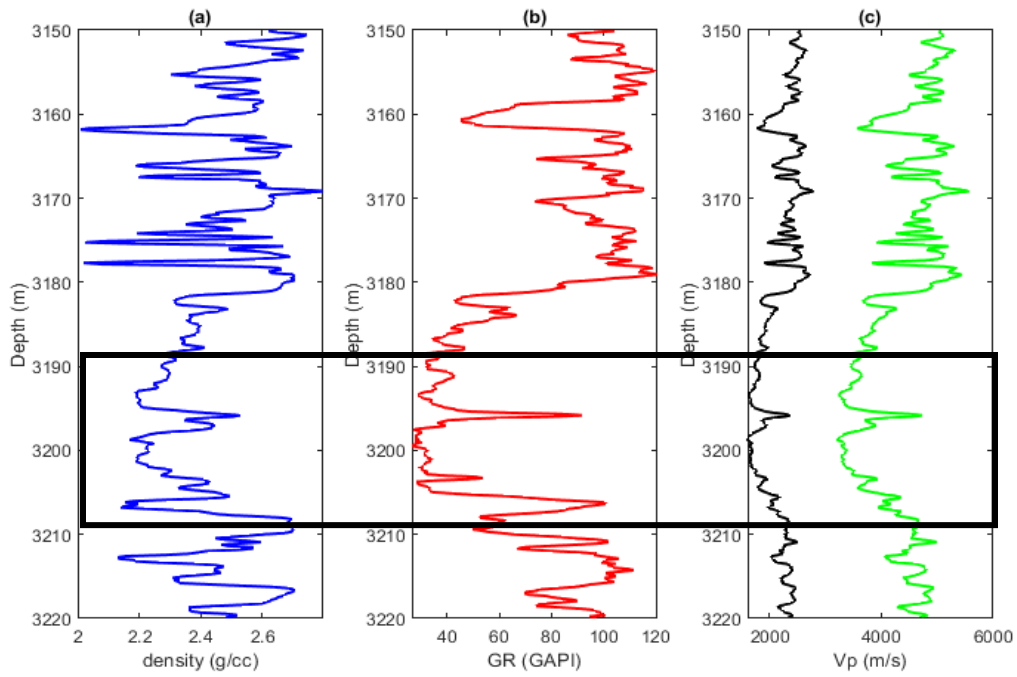


Fig. 4.1 Wireline logs from Observation well F-2 at Cranfield. a) density log, b) gamma ray log, c) S-wave velocity log (black) and P-wave velocity log (green). The black rectangular demarcation across the panels highlights the zone of interest, which is the injection zone.

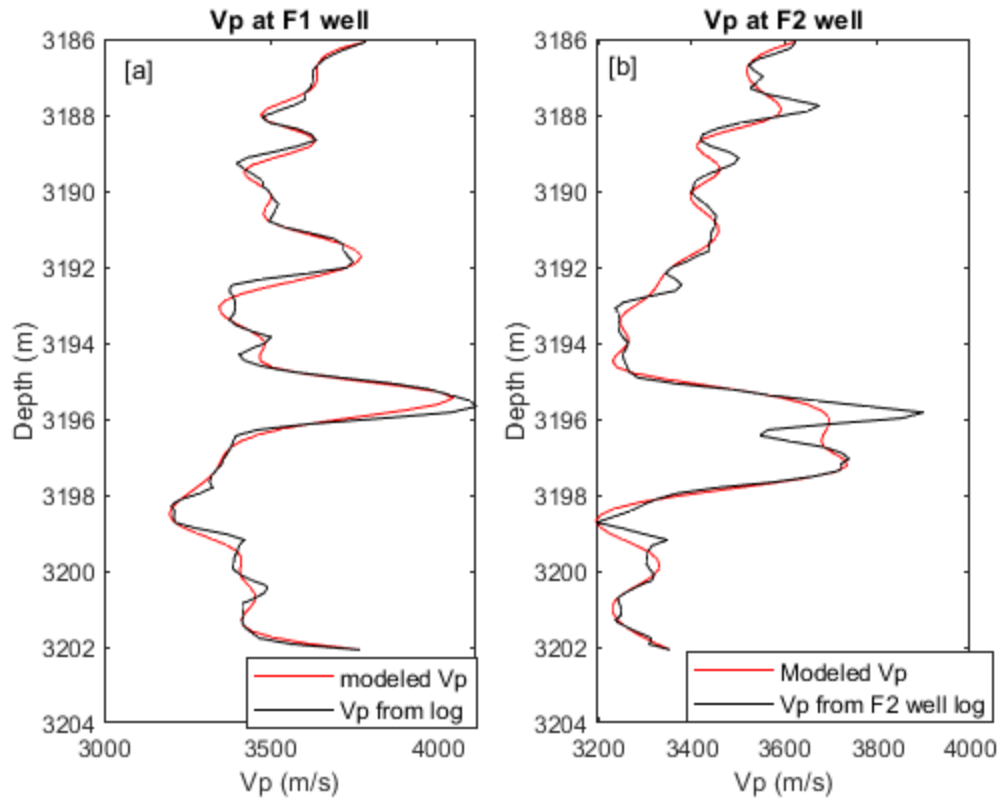


Fig. 4.2 Post-injection p-wave velocity (V_p) at the well locations for a) injection well F-1 b) observation well F-2. Black plots are profiles from log data and red are those computed from rock-physics modeling.

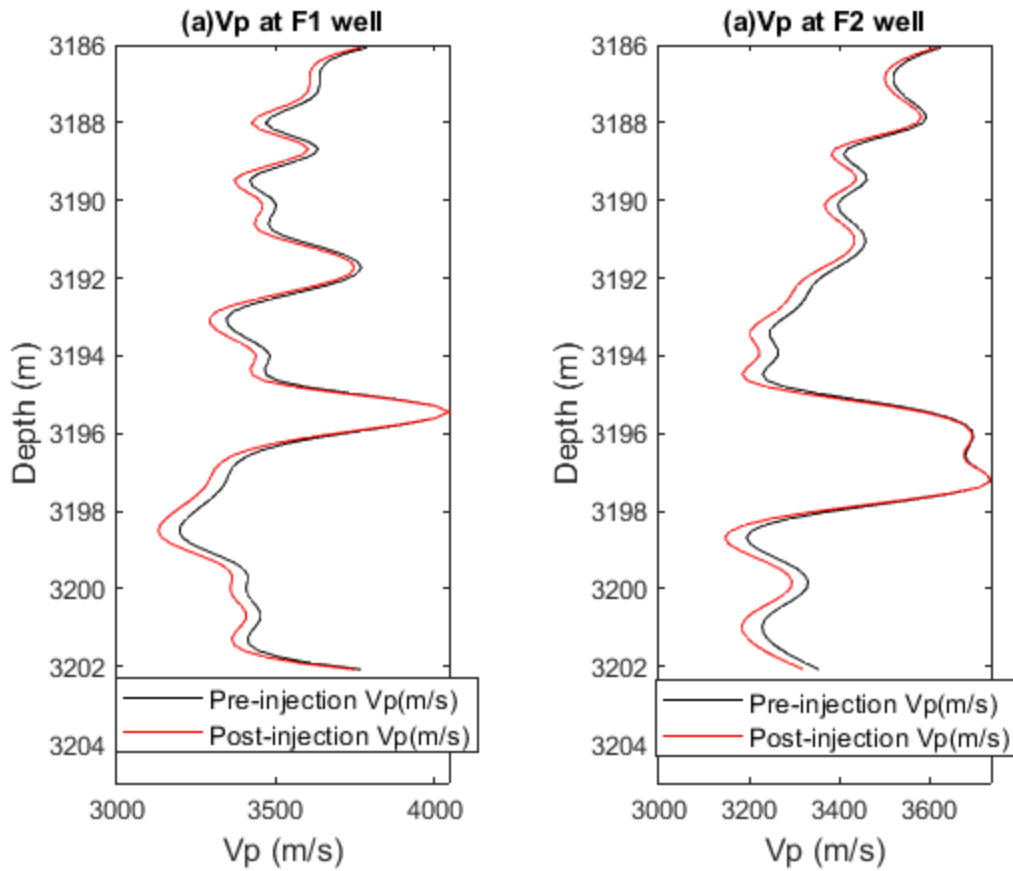


Fig. 4.3 P-wave velocities that were determined from fluid substitution. Pre-injection P-wave velocity (red) and post-injection velocity (black) at a) injection well F-1 b) observation well F-2.

The post-injection seismic velocity profiles at F-1 and F-2 wells closely follow the velocity signature from logs (see Figs 4.2a and b). This is expected because the modeling process was conditioned data along the F1 and F2 wells. However, there is a great difference in the velocities at locations other than the F-1 and F-2 well locations. Fig. 4.4 shows the grid location for the conditioning wells F-1 and F-2 (red), and another grid location away from the conditioning wells (black). The modeled velocity profiles over the entire ensemble of realizations at the grid location away from the conditioning wells are shown in Fig. 4.5. As can be seen, there is considerable uncertainty associated with the prediction of seismic velocities at locations away from the conditioning wells. In order to refine this uncertainty, we would like to use the available 3D seismic information to sub-select a set of models that mimic the seismic signature observed in the field. The next chapter develops a model selection workflow to accomplish this. Fig. 4.5 also shows the velocity profile at the location away from the conditioning wells based on the field 3D seismic survey data.

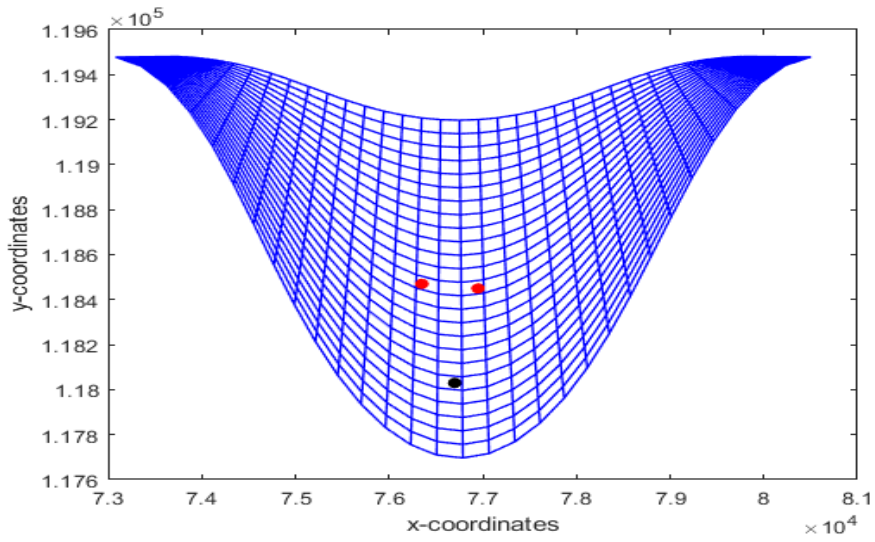


Fig. 4.4 Grid locations for the conditioning wells (red) and another location away from the conditioning wells (black)

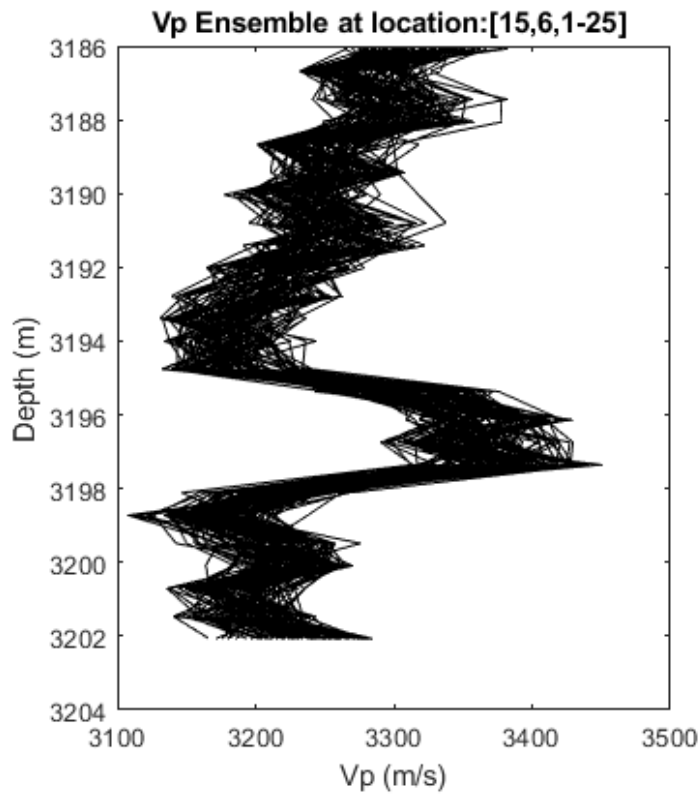


Fig. 4.5 P-wave velocity profiles at a location away from the conditioning well locations computed using the ensemble of history-matched models described in Chapter 3.

Chapter 5 Model Selection

5.1 Introduction

It has been demonstrated in previous chapters that model calibration methods that are implemented are generally capable of producing models that are geologically consistent with field data. However, the results in the previous chapter demonstrate that there can still be significant residual uncertainties even after integrating all available injection data. One reason for the residual uncertainty is the sparsity of data available for modeling subsurface reservoirs, particularly when it comes to modeling CO₂ injection and storage in reservoirs. Further, the dynamic data that is integrated into the model calibration/history-matching workflow is more prone to be influenced by the overall reservoir connectivity characteristics, rather than the individual permeability values at a grid location that is updated during the model calibration process. This can affect the predictive accuracy of the updated models. Therefore, for better management of the geologic storage of CO₂, a framework for further reducing the residual uncertainty associated with the reservoir models is necessary. This study proposes a Bayesian model selection workflow to accomplish this task. In principle, the model selection workflow sub-selects a prior ensemble of models to create a posterior set of models that reflect the time-lapse seismic information collected in the field. The model selection workflow is especially vital within the context of CO₂ injection and storage, as it allows regulators and operators to probabilistically quantify the uncertainty and risk associated with the CO₂ injection process.

The idea of using model selection to sub-select reservoir models that honor data from various sources has been pursued in the seminal works of Srinivasan and Cesar, (2012), Bhowmik et al., (2013), and Bhowmik, (2014;). Subsequently, there have been various derivative works and applications of this concept. Min et al., (2016) applied this idea to select reservoir models by accounting for the flow and geomechanical responses of the reservoir, and demonstrated its applicability to a real field CO₂ sequestration scenario using the gas storage site at Salah, Algeria. In another study, Nwachukwu et al., (2017) developed a model selection workflow that utilizes a particle tracking algorithm to mimic flow paths of injected CO₂ within reservoir models. Singh, (2019) also demonstrated the possibility of using model selection to extract information from microseismic data regarding natural fracture network.

In this dissertation, the model selection workflow is implemented to sub-select history-matched reservoir models on the basis of observed timelapse seismic data for the Cranfield reservoir. The model selection technique delivers a unique workflow that allows: 1) assessment of reservoir connectivity

paths, and delineation of the dominant heterogeneities that drive CO₂ migration, and 2) sub-selection of more representative reservoir models that can be used to predict the CO₂ plume displacement more accurately.

5.2 Model selection workflow

Table 5.1 summarizes the model selection workflow that is implemented in this research. Details of each stage in the workflow are discussed in subsequent sections.

Table 5.1 Model selection workflow

Step	Action
1	Generate initial ensemble of reservoir models.
2	Generate model responses for the ensembles of reservoir models Obtain a dissimilarity matrix of simulated waveforms between various members of the ensemble
3	Partition models into cluster on the basis of the dissimilarity matrix. Retrieve a representative model for each cluster
4	Calculate the prior probability of each cluster
5	Update the prior probabilities to posterior probabilities by comparing the response of the representative models to the observed time-lapse seismic data
6	Select cluster with the highest updated posterior probability
7	Sequentially repeat steps 3 to 6 until a reasonable match to the observed data is obtained

5.2.1 Generation of initial ensemble of reservoir models

As discussed previously, there is a high level of uncertainty associated with modeling the precise pattern of heterogeneity exhibited by the point bar system. Some level of uncertainty persists even after calibrating the models using observed injection data. This uncertainty can be represented using the ensemble of history-matched models.

5.2.2 Generation of model responses.

Generating model responses (e.g., bottom-hole pressure) allows us to compare the flow or injection response behavior of all the models, and group them accordingly. A traditional way of obtaining model responses is by running full-physics flow simulations on the ensemble of models. This can be

computationally expensive and time-consuming especially when there is a large ensemble of models. Instead, fast approximation proxies have been developed to replace the conventional reservoir flow simulators. Examples are: 1) the fast-marching method (e.g., Sharifi et al., 2014) for efficiently computing time for pressure propagation time in heterogeneous geological formations, 2) Graph theory algorithm adopted by Jeong and Srinivasan (2016), Hirsch and Schuette (1999) for assessing the connectivity of multidimensional geologic models. In this method, the edges that connect grid blocks within the reservoir are weighted based on the properties that control fluid transmissibility such as permeability. The magnitude of the weights reflects the degree of connectivity. Particle tracking proxies have also been developed (e.g., Bhowmik, 2014) to mimic the physics of CO₂ displacement in reservoir models.

5.2.3 Computing dissimilarity between models

The Fréchet distance measures the shape similarity between signals or curves by considering the location and ordering along the curves. The Fréchet distance between two signals or curves $f: [a, b]$ and $g: [a', b']$ can be defined as equation 5.1 (Eiter and Mannila, 1994) :

$$\delta_F(f, g) = \min \left[\max_{t \in [0,1]} \left\{ d \left(f(\alpha(t)), g(\beta(t)) \right) \right\} \right] \quad (5.1)$$

where $d(\cdot)$ is the distance between the curves; α and β are reparametrized non-decreasing functions mapping from $[0,1]$ onto $[a, b]$ and $[a', b']$, respectively. In our model selection workflow, a variation called the discrete Fréchet distance would be used to determine the similarity between the model responses.

Fig. 5.1 is a demonstration of how the discrete Fréchet distance is computed between curves A (blue) and B (red) assuming that there are only two possible combinations of $\alpha(t)$ and $\beta(t)$. In the first case (Fig. 5.1a), the maximum distance is $d \left(f(\alpha(t_3)), g(\beta(t_3)) \right)$, while in the second case (Fig. 5.1b) the maximum distance is $d \left(f(\alpha(t_2)), g(\beta(t_2)) \right)$. The discrete Fréchet distance then becomes the maximum of these two distances assuming $\alpha(t)$ and $\beta(t)$ have only two possible combinations.

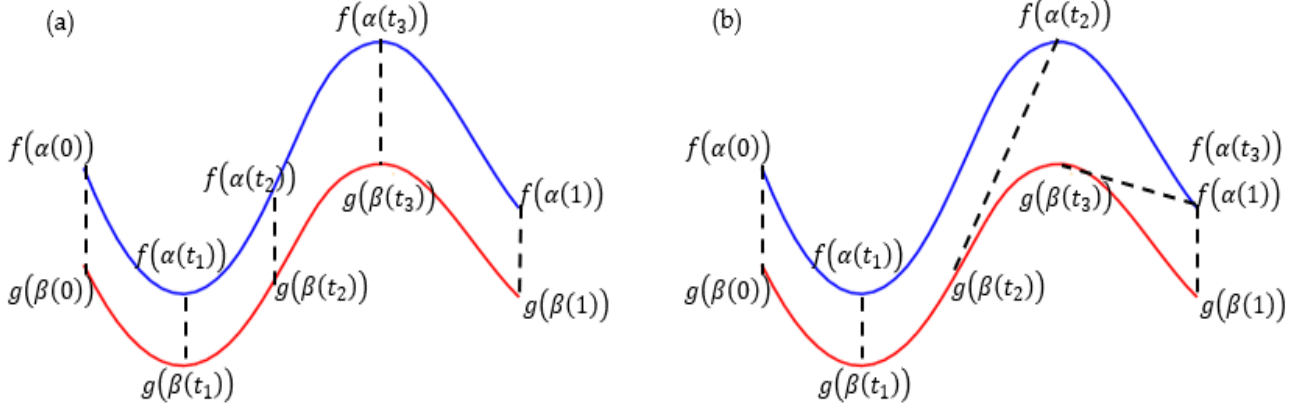


Fig. 5.1 Discrete Fréchet distances computed for curves A (red) and B (blue)

The discrete Fréchet distances between M model responses can be computed and a dissimilarity matrix D is obtained as:

$$D = \begin{bmatrix} 0 & d_{1,2} & \dots & d_{1,M-1} & d_{1,M} \\ d_{2,1} & 0 & \dots & \dots & d_{2,M} \\ \dots & \dots & \dots & \dots & \dots \\ d_{M-1,1} & \dots & \dots & 0 & d_{M-1,M} \\ d_{M,1} & d_{M,2} & \dots & d_{M,M-1} & 0 \end{bmatrix} \quad (5.2)$$

5.2.4 Model Grouping

After obtaining the dissimilarity matrix D , the next task is to project the elements in matrix D into a lower dimensional space so that the dissimilarity between the observations could be visualized and grouped. This can be accomplished by using a dimensionality reduction technique such as Principal Component Analysis (PCA) (Pearson, 1901) or Multidimensional Scaling (MDS), (Boyden & Noble, 1933; Torgerson, 1958). In this dissertation, MDS was implemented. Fundamentally, MDS uses an optimization algorithm to minimize the error between the pairwise dissimilarities in the original dimensional space $d_{i,j}$, by projecting it into a lower dimensional space $\delta_{i,j}$. That is, given the matrix D , we want to find M vectors $x_i = \{x_1, x_2, \dots, x_M\}$ in a 2D space such that: $\|x_i - x_j\| \approx d_{i,j} \quad \forall i, j = 1, \dots, M$. The normalized stress criterion, which is expressed as equation 5.3 (Kruskal, 1964) can be used to accomplish this.

$$stress = \left[\frac{\sum_{i,j} (d_{i,j} - \delta_{i,j})^2}{\sum_{i,j} d_{i,j}^2} \right]^{\frac{1}{2}} \quad (5.3)$$

To give practical meaning to this, let us assume that there are four models, P, Q, R and S. The pairwise dissimilarities between these models can be computed to obtain a dissimilarity matrix, D^* as seen in Eq. 5.2*. Then MDS can be performed on matrix D^* to project it into a lower dimensional space using the stress function given above to group the models based on their proximity. Fig. 5.2 illustrates the models in a lower dimensional space. Model responses Q and R have the least dissimilarity and are in the closest proximity to each other in space. P and S have the highest dissimilarity; therefore, they are furthest from each other. Simply put, closer points in the transformed space indicate similar response behaviors, and that in turn may suggest similar geological structures.

$$D^* = \begin{bmatrix} 0 & 2.028 & 1.748 & 4.312 \\ 2.028 & 0 & 0.400 & 4.400 \\ 1.748 & 0.400 & 0 & 3.544 \\ 4.312 & 4.400 & 3.544 & 0 \end{bmatrix} \quad (5.2^*)$$

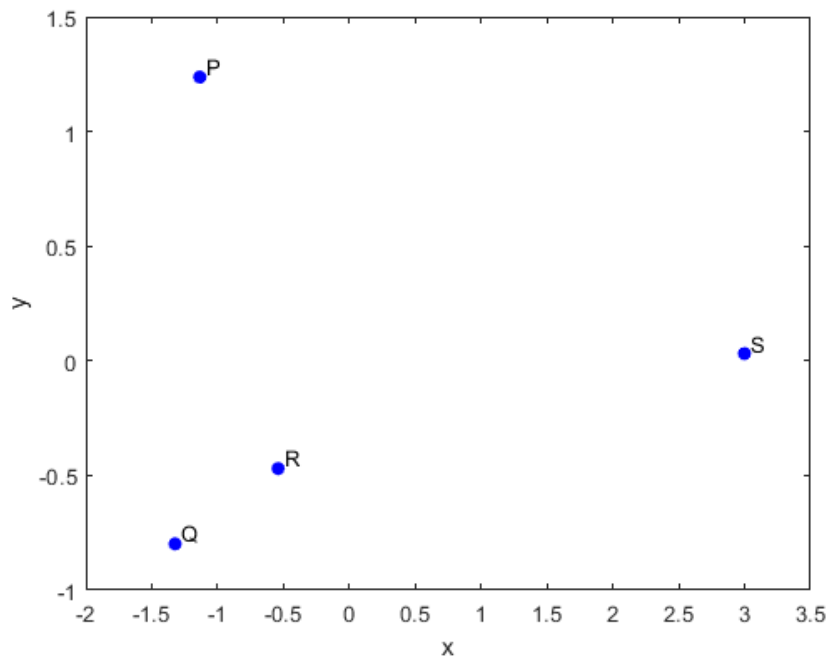


Fig. 5.2 D map generated by MDS.

The drawback of MDS is that its performance deteriorates as the ensemble size becomes larger. This is because MDS requires higher dimensions in order to properly transform the dissimilarity matrix D , and the associated computational cost for computing the corresponding basis vectors can be very high. Nonetheless, if ensemble size is relatively small, MDS is very useful for visualizing the relationship between models.

5.2.5 k-means clustering

The models that are projected into a lower dimensional space are partitioned into clusters based on their common characteristics. A data-partitioning algorithm, *k-means clustering*, is used to group the models into clusters. The *k-means clustering* procedure based on the algorithm by (Lloyd, 1982) proceeds iteratively as follows:

- Choose n initial cluster centroids at random.
- Compute point-to-cluster-centroid distances for all models
- Assign each observation to the cluster with the closest centroid.
- Compute the average of the observations in each cluster to obtain n new centroid locations.
- Repeat steps 2 through 4 until cluster assignments do not change, or the maximum number of iterations is reached.

The implementation of the above procedure is dependent on a predefined number of clusters. An appropriate predefined cluster number can be arrived at by minimizing the silhouette function (Rousseeuw, 1987). This function is given as the ratio of the intra-cluster distances of all models from a cluster centroid to the inter-cluster distances between the cluster centroids. This is shown as equation 5.4.

$$silhouette = \frac{\sum_{\beta=1}^n \sum_{\alpha \in \beta} d_{\alpha \rightarrow \beta}}{\sum_{\gamma=1}^n \sum_{\substack{\beta=1 \\ \beta \neq \gamma}}^n d_{\beta\gamma}} \quad (5.4)$$

β and γ are the cluster indices; α is index of a model within a cluster; $d_{\alpha \rightarrow \beta}$ is the distance between model α in cluster β from the centroid, and $d_{\beta\gamma}$ is the distance between centroids of cluster β and γ .

5.2.6 Update of prior probabilities.

Initially, all the models in the ensemble have equal probability of occurrence since they have been conditioned to the same data. Suppose there are N clusters where each cluster has m_n models ($n = 1, 2, \dots, N$). We denote the representative (closest to centroid) model for each cluster as z_n . If the clusters were all similarly populated, then the prior probability of each cluster $P(z_n)$ could be written as:

$$P(z_n) = \frac{1}{N} \quad (5.5)$$

However, due to the limited size of the ensemble and the conditioning influence of the available data, the clusters may have unequal number of models and in that case, the prior probability can be expressed

as the ratio of the number of sub-models (m_n) in a cluster to the total number of ensemble of models (M), i.e., $P(z_n) = \frac{m_n}{M}$.

Given the observed response data S_R , the posterior probability (i.e., updated probability) for each cluster can be obtained by applying Bayes' rule:

$$P(z_n|S_R) = \frac{P(S_R|z_n)}{P(S_R)} \times P(z_n) \quad (5.6)$$

The likelihood $P(S_R|z_n)$ can be approximated by drawing a probability envelope around the observed response S_R and computing iso-probability intervals corresponding to a prescribed probability distribution. In this dissertation, a Gaussian distribution is assumed whose mean is the observed response S_R and variance δ^2 . δ^2 is assumed to be the mean squared error between the simulated seismic response S_R^{sim} and the observed seismic response, S_R computed over the entire ensemble. In order to ensure closure, the prior probability of the observed response data $P(S_R)$, is computed from:

$$P(S_R) = \sum_{n=1}^N P(S_R|z_n) \times P(z_n) \quad (5.7)$$

The cluster whose representative has the highest posterior probability is chosen for further refinement in the next level of iteration. As the process continues, a smaller set of models that are more consistent with the observed data remains. A situation can arise where we run out of models to reliably compute the probabilities and to assess the posterior uncertainty. To avoid this, a stopping criterion can be imposed. The process can be terminated when i) a predefined minimum number of remaining models is reached or ii) the updated probabilities do not show any additional improvement based on the available data. Alternatively, the selection of models at every step of the process can be augmented using a sampling scheme. One approach would be to sample additional conditioning data that are common to all the models in the selected cluster and use that to create an additional set of models. This would create a set of models that reflect features common to models within the clusters.

5.3 Application to the Cranfield dataset

5.3.1 Initial ensemble of models.

In chapter 2, an ensemble of geologic models was generated using the process for representing the spatial heterogeneity in a point bar system. That ensemble of models was conditioned to the well log data available for the Cranfield site. A follow up study was presented in chapter 3, where the models were updated to reduce the uncertainty by integrating CO₂ injection data. For implementing the model

selection procedure, these injection-history matched models constitute the initial ensemble. To demonstrate the need to further improve the initial ensemble of models, the average ensemble uncertainties before and after applying the injection history-match process are compared. Fig. 5.3 compares the uncertainty, expressed as permeability variance for the ensemble of point bar models before (Fig. 5.3a) and after updates (Fig. 5.3b) using the injection history. Figs. 5.3 c and d show the distribution of variance along sections S_1 and S_2 , respectively. As can be seen, even though the uncertainty is greatly reduced after updating using the injection data, there is still considerable residual uncertainty.

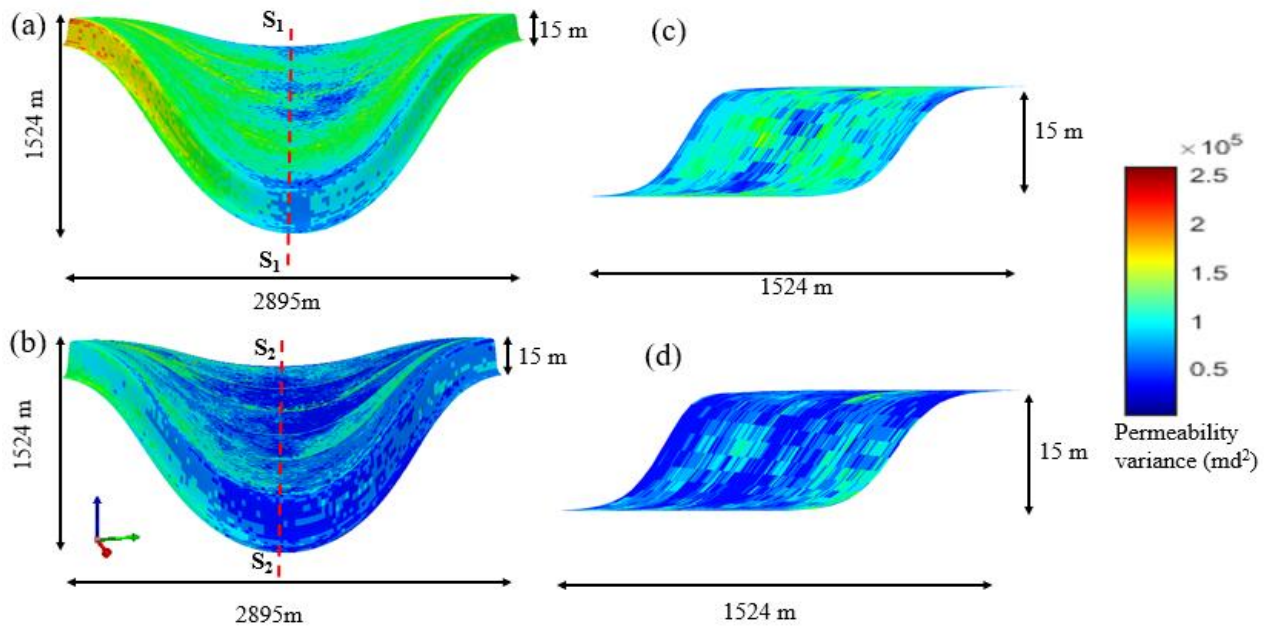


Fig. 5.3 Ensemble permeability variance for the 3D point bar models (a) before and (b) after updates, with sections along S_1 and S_2 displayed in c) and d) respectively.

5.3.2 Model selection objective

The objective of implementing model selection is to further refine the suite of calibrated models to create a posterior set of models that best reflect the reservoir characteristics most closely. This will be accomplished by:

- Incorporating the fluid saturation and pressure distribution at the end of the history matching into rock physics models to compute seismic responses that can be compared to 3D seismic data recorded in the field.
- Implementing the Bayesian model selection workflow to sub-select a set of reservoir models that are closest to the observed seismic responses.

5.3.3 Cranfield Seismic Data

A description of the Cranfield seismic datasets and the processing of the data to obtain various elastic properties such as p-wave velocity, and acoustic impedance have been discussed in the original works of Zhang et al. (2014); Zhang, et al. (2013) and Zhang et al. (2013). In the following, a summary of the available data is presented and the processing steps to derive the 3D p-wave velocity model used in this dissertation are described.

The CO₂ injection project in the Cranfield, Mississippi reservoir commenced in July 2008. Prior to injection, 3D seismic data was acquired in 2007. There were 23 pre-existing wells at the time of the 3D survey. Following this, post-injection 3D seismic data was acquired in September 2010. A key anomaly in the seismic data is the misalignment in time shift in the time-lapse post stack and pre-stack seismic datasets. This anomaly is generally considered as an artifact induced by data acquisition or data processing or both (Zhang et al., 2013). To correct this anomaly, Zhang et al. (2013) applied registration to the time-lapse pre-stack datasets by warping the post- to the pre-injection datasets based on the local correlation between them in order to isolate the time shift effect from the amplitude changes. After registration, pre-stack seismic inversion (Basis Pursuit Inversion) was applied on the original pre-stack time-lapse data and the registered post-injection data to derive estimates for the 3D p-wave velocity model that was used in this dissertation. The 3D p-wave velocity model (Fig. 5.4) is what will be used to guide the model selection process.

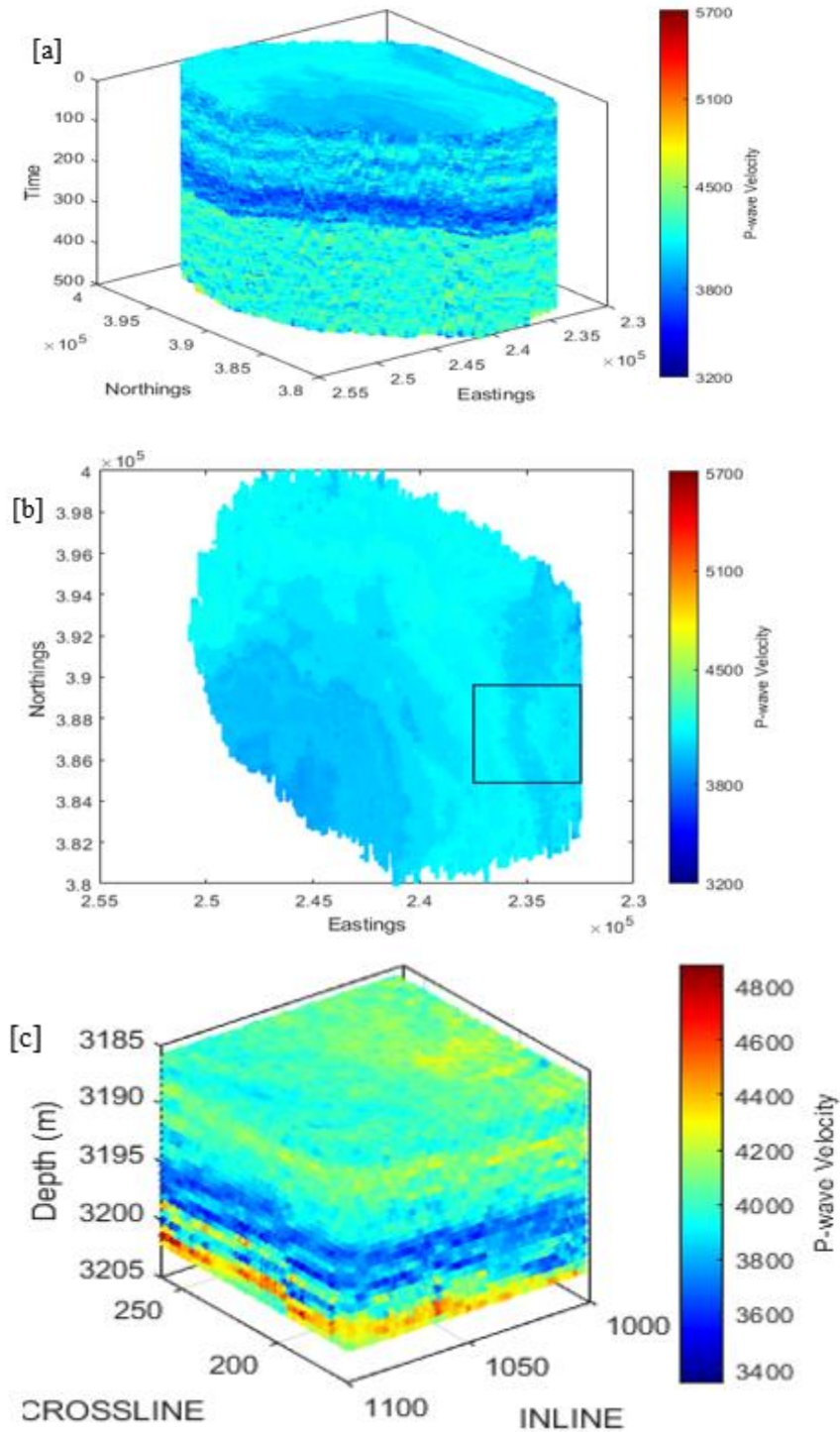


Fig. 5.4 Seismic p-wave velocity data that will be used to constrain the model selection process. a) p-wave velocity for the entire Cranfield area b) Top view demarcating the area used for CO₂ injection, c) Extracted seismic volume corresponding to the injection zone.

5.3.4 Model selection implementation

The model selection workflow is implemented by initially applying the rock physics modeling procedure described in chapter 4 to compute p-wave velocity (v_p) responses for the models. The updated geologic models and their corresponding fluid saturations and densities at the end of the injection history matching process were taken into consideration for computing the seismic response. Since the density of CO₂ is a function of pressure, incorporating fluid density into the rock fluid computations indirectly takes care of pressure changes induced by CO₂ injection. To account for the CO₂ displacement through the reservoir, the model response is expressed as the difference between the pre- and post-injection p-wave velocities. That difference is computed for each member of the ensemble of models. The Fréchet distances between these model responses are subsequently computed. Finally, the Fréchet distances are projected into a lower dimensional space using multidimensional scaling as shown in Fig. 5.5. Each point in that plot corresponds to the response of a single model in the ensemble.

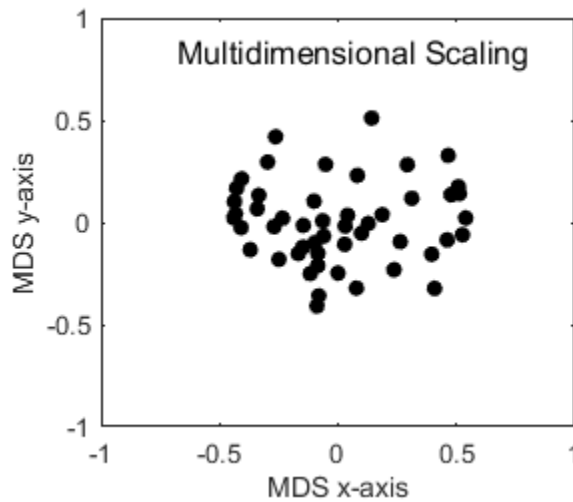


Fig. 5.5 Projection of models into a 2D space after applying MDS.

Next is to determine the optimum number of clusters to be used to partition the projected set of models. This is done by applying equation 5.4 to compute the silhouette distance corresponding to a range of possible cluster numbers (Fig 5.6). Based on this, the models were partitioned into three clusters P, Q and R (Fig. 5.7).

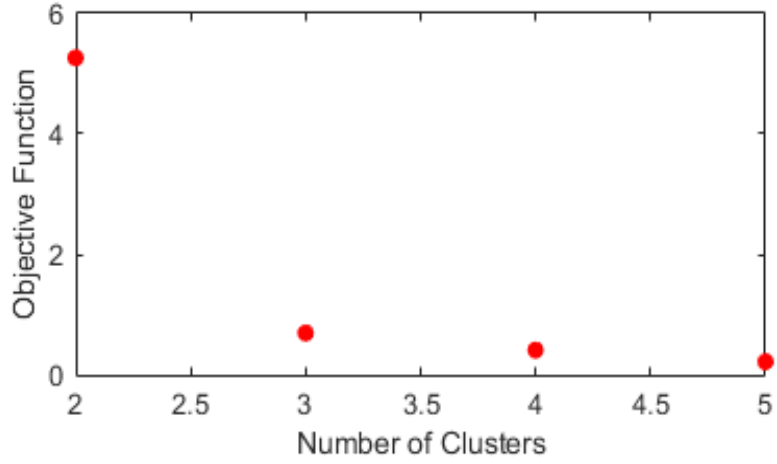


Fig. 5.6 Plot of Objective Function (i.e., Silhouette score) against number of clusters.

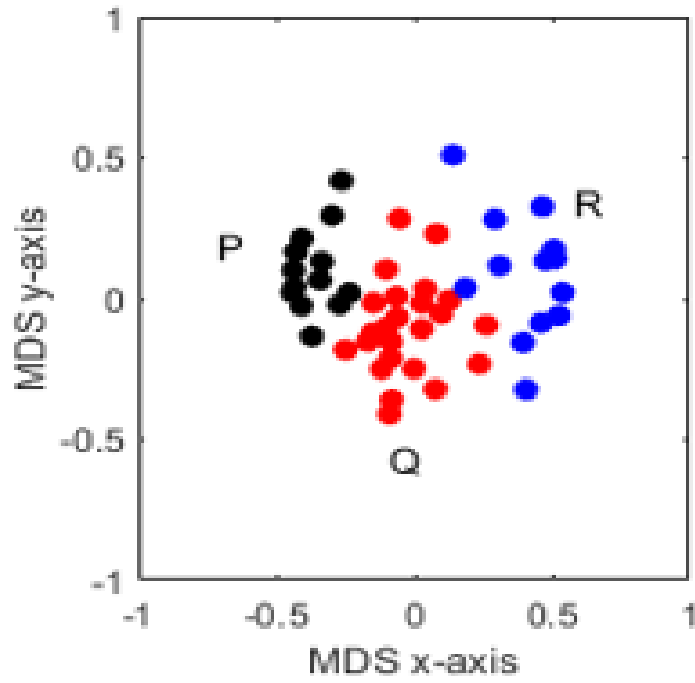


Fig. 5.7 Clustering of ensemble of models in the MDS projection space.

5.3.5 Bayesian update of prior probabilities.

The probability update begins with calculating the prior probability $P(z_n)$ for each cluster. Each cluster is equally likely; therefore, the prior probability is $\frac{1}{3}$. The likelihood $P(S_R|z_n)$ is determined from a probability envelope that is constructed by assuming a Gaussian distribution as shown in Fig. 5.8. The mean of the Gaussian is assumed equal to the observed seismic response and deviation is calculated on the basis of the mean square mismatch between the observed and simulated responses. The model responses for each cluster are plotted within this envelope, and the probability is read from the point in the envelope where there is maximum deviation from the observed response (See Point A in Fig. 5.8). After performing Bayesian updates, the posterior probabilities for the cluster representatives for cluster P, Q, and R, are respectively 0.33, 0.47, and 0.20. The cluster that has the highest updated probability is selected for the next stage of model selection, and the above procedure is repeated. Fig. 5.9 summarizes the entire iterative model selection workflow. In stage 1 (Fig. 5.9 a), cluster Q (red) was selected for the next stage because it had the highest updated probability. This cluster was further partitioned in stages 2 (Fig. 5.9b), and 3 (Fig. 5.9c). The corresponding seismic profiles for models in the selected clusters at each stage of the model selection are shown in (Figs. 5.9 d – f). As can be observed, the model responses converge towards the observed response as the model selection process advances.

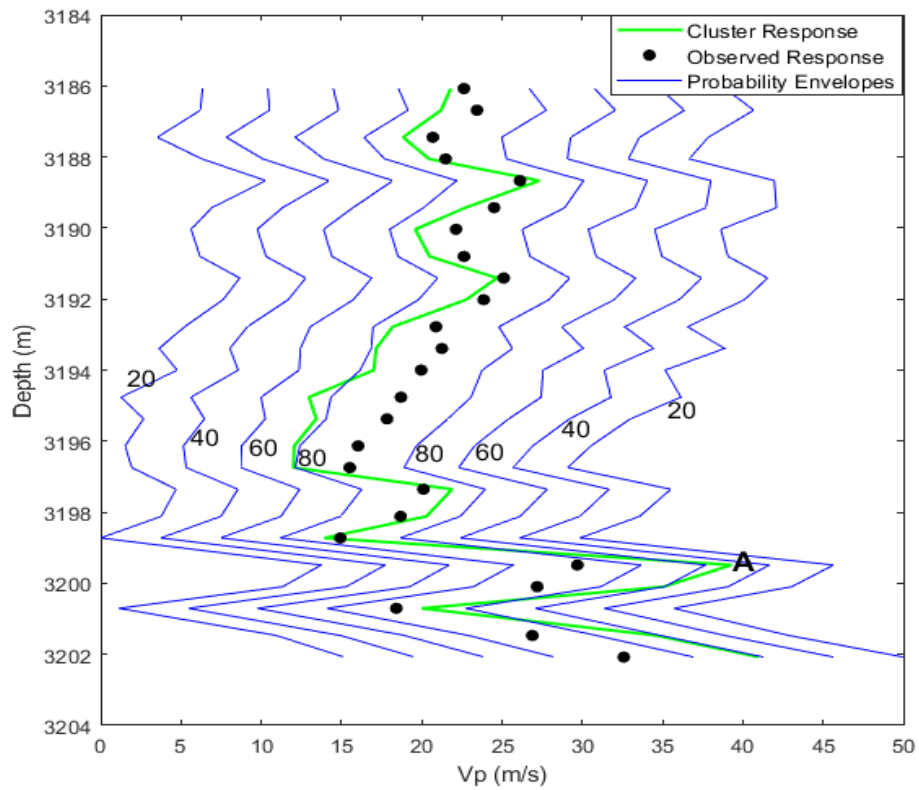


Fig. 5.8 The calculation of Bayesian likelihood by assuming a Gaussian probability envelope centered on the observed response and with a variance equal to the mean squared error between the simulated and observed response corresponding to all ensemble members.

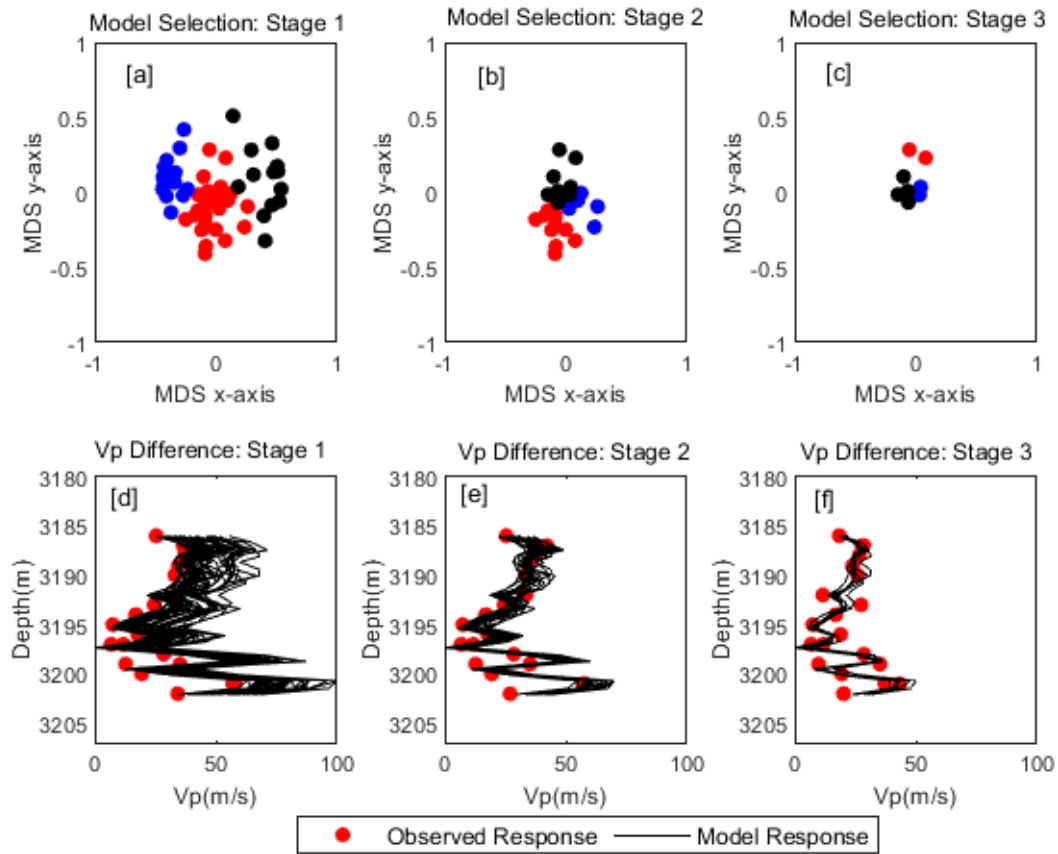


Fig. 5.9 . Model Selection workflow in three stages. Top row shows the clustering and selection process at each stage. Second row shows the time-lapse velocity difference for all models within the selected cluster. Red plots in second row represent the observed time-lapse seismic velocity data.

5.4 Discussions.

The model selection workflow discussed herein can refine an ensemble of geologic models by using the time-lapse seismic data to constrain the uncertainty. The maps in Fig. 5.10 show a reduction in the variance of the permeability distribution after model selection.

The refinement of the models allows us to delineate the dominant depositional trends and heterogeneities that drive fluid flow. Figs. 5.11 a, b, and c show sections of the cluster representatives during the final stage of the model selection workflow. Figs. 5.11 d, e, and f are a representation of these models in a rectilinear grid to allow us to properly visualize the key geologic patterns that control CO₂ flow.

For all the models, we observe an overall trend of decreasing porosity as we move from the bottom to the top of the reservoir, suggesting a fining upward depositional trend. This trend has been documented in earlier literature (e.g., Hosseini et al., 2013) as a key depositional trend that characterizes the Cranfield reservoir.

Again, a close observation of the models shows five distinct inclined units, called inclined heterolithic stratifications (IHS). At the interfaces between two successive IHS are thin layers with very low porosity. These thin layers are shale drapes that act as baffles to CO₂ migration.

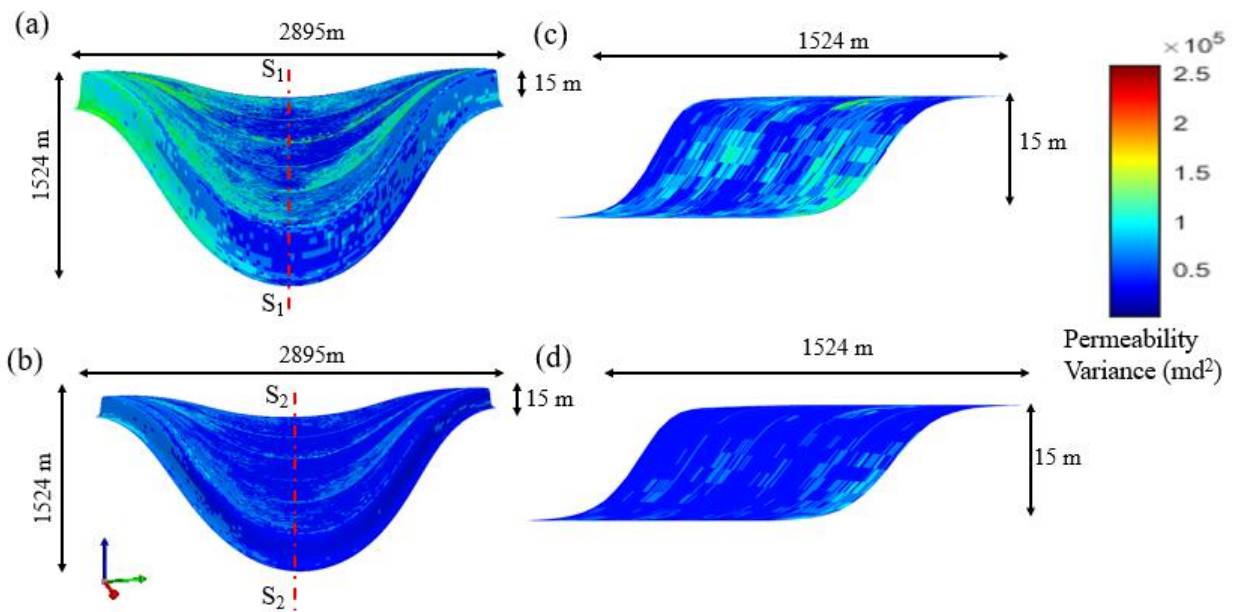


Fig. 5.10 Permeability variance computed using the ensemble of selected 3D point bar models, (a) after model calibration using injection history data and (b) after model selection using time-lapse seismic information, with sections along S₁ and S₂ displayed in c) and d) respectively.

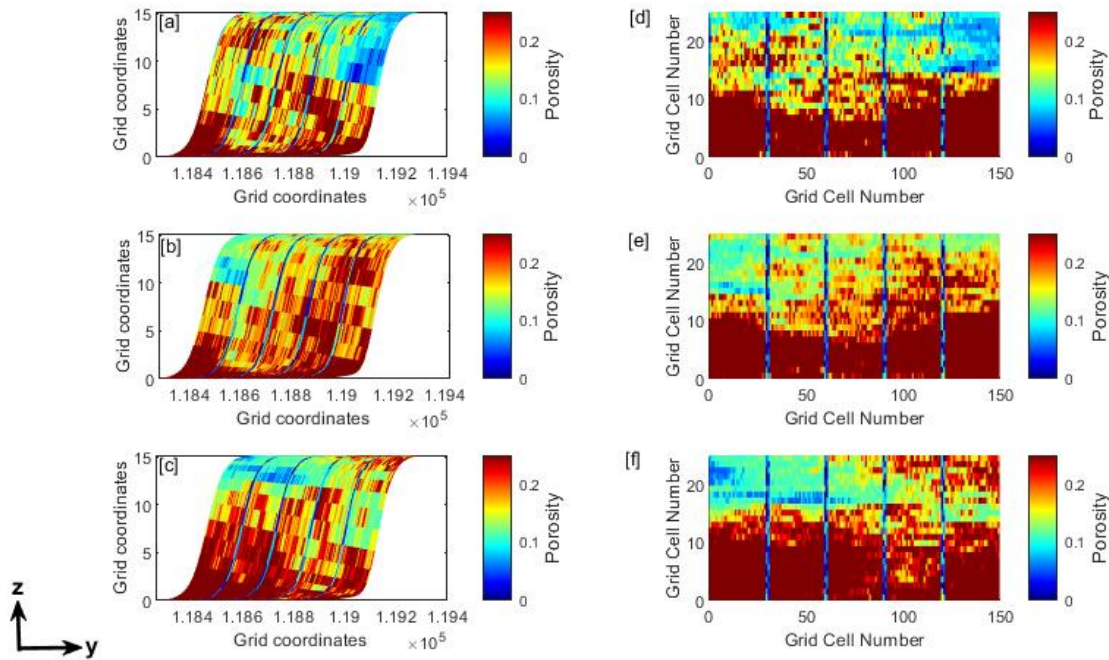


Fig. 5.11 Representative geologic model after implementing the model selection workflow to illustrate the porosity distribution in curvilinear space (figures (a, b, c)), and the corresponding distribution in rectilinear space (figures d, e, f).

Fig. 5.12 is an ensemble average of p-wave velocity difference that shows the mapped CO₂ plume locations before and after model selection. The difference maps are compared to the observed response, and those computed using models obtained after assimilating the injection data as well as those obtained after assimilating the time-lapse seismic data. The observed response based on the field acquired seismic data shows CO₂ plume at shallower depths. This CO₂ plume migration to shallower depth is better captured after model selection, and the plume connectivity or migration path is better delineated.

Finally, we compare the simulated bottom-hole pressures at all iterative stages of the model selection workflow to assess the evolution of uncertainty in injection response (Fig. 5.13). We observed a reduction in uncertainty (in terms of scatter around the observed pressure profile) and a better prediction of the field data as model selection proceeds.

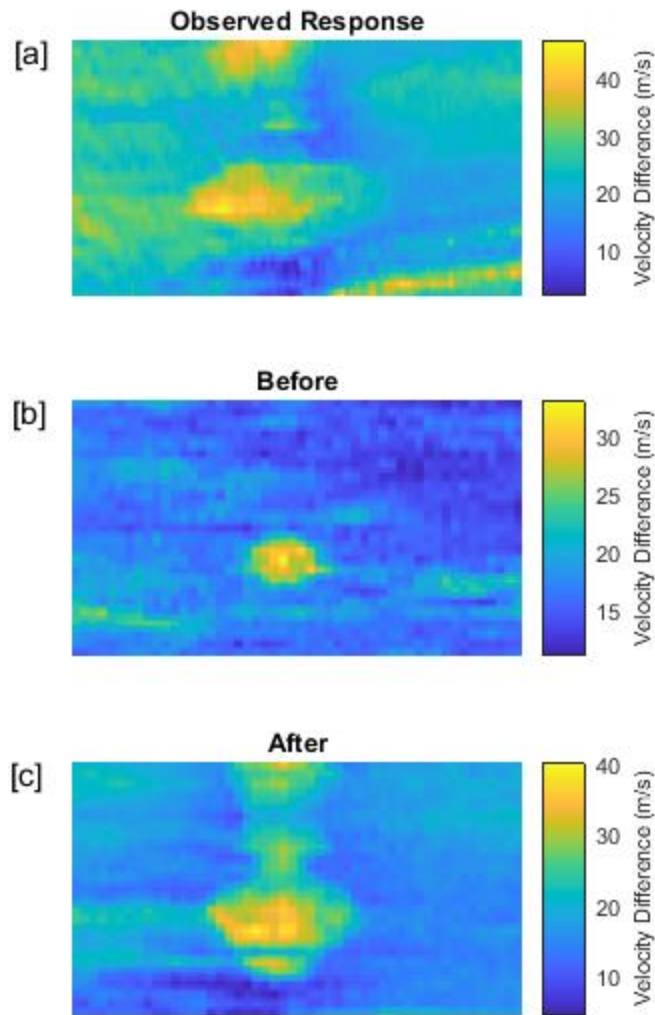


Fig. 5.12 Average p-wave velocity difference for a representative section a) observed seismic data, b) before model selection (after injection data assimilation), and c) after model selection assimilating time-lapse seismic data.

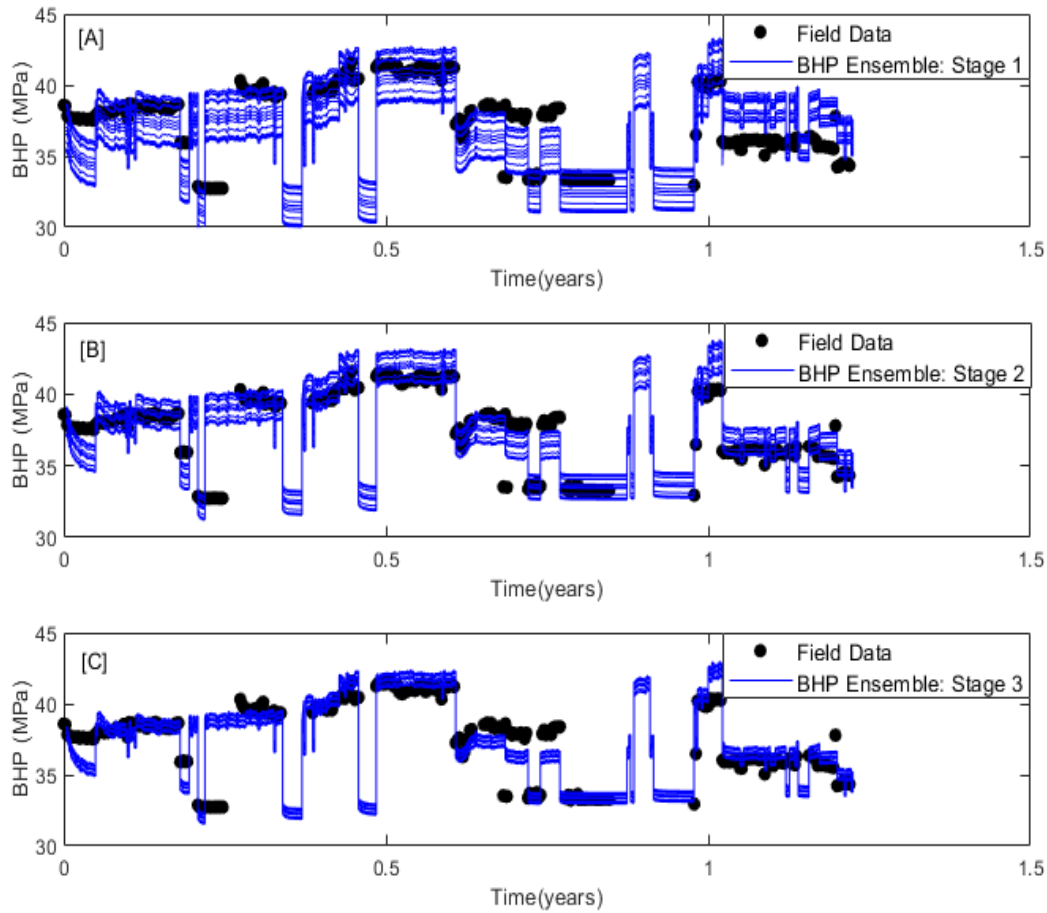


Fig. 5.13 Bottom-hole pressure response at different iterative stages of the model selection process.

5.5 Summary and Concluding Remarks.

This chapter proposes a Bayesian model selection method that uses time-lapse seismic data for refining a suite of point bar models that have been calibrated using CO₂ injection data. The process updates the uncertainty associated with reservoir geology using time-lapse seismic information. The model selection algorithm offers an efficient way for selecting an optimum set of models conditioned to seismic data that reflect the observed injection characteristics. Rock physics models provide a proxy model for the effect of CO₂ on seismic velocity in the point bar reservoir in a manner that is effective for discriminating the connectivity characteristics exhibited by different models. Bayesian probability updates are performed by considering the deviation of the simulated response of representative models from the observed data.

Application of the workflow to a suite of models that have been calibrated using injection data from the Cranfield yielded: 1) an assessment of the reservoir connectivity paths, and delineation of the dominant heterogeneities that drive fluid migration, and 2) a sub-selection of more representative reservoir models that can be used for more accurate forecasts.

The next chapter will more formally explore the value of information from each source of information: injection data and time-lapse seismic data.

Chapter 6 Value of Information Analyses for Monitoring CO₂ Plume During Sequestration

6.1 Introduction

The prediction of CO₂ plume displacement during sequestration in subsurface geological formations is associated with high uncertainties and potential risks. A key aspect of subsurface CO₂ sequestration is our ability to monitor the storage reservoir and the injection wells to ensure that the injected fluid permanently remains in the subsurface (Trainor-Guitton et al., 2013). Several techniques have been employed to monitor the CO₂ injected in the subsurface. Gasperikova & Hoversten, (2008) modeled the gravity anomaly associated with density changes due to CO₂ injection in deep brine aquifers and coal formations, while others have used seismic wave velocities (e.g., Mito & Xue, 2011), and electrical resistivity measurements (e.g., Dafflon et al., 2012; Ramirez et al., 2003; Schmidt-Hattenberger et al., 2011) to explain the physical changes induced by the injected CO₂ and thereby monitor the displacement of CO₂ in the subsurface. With regards to the Cranfield injection project, the monitoring techniques range from the use of timelapse seismic data (e.g., Zhang et al., 2013; Daley et al., 2014; Zhang et al., 2013; Ajo-Franklin et al., 2013; Alfi et al., 2015) to the deployment of rock physics models (e.g., Ghosh et al., 2012).

In order to build robust reservoir models that can be used for monitoring and assessing the storage of CO₂, information from various sources are integrated into data assimilation workflows to calibrate the models to reduce uncertainties (e.g., Alfi & Hosseini, 2016; Dawuda & Srinivasan, 2022; Delshad et al., 2013; Hosseini et al., 2013). These data assimilation techniques only assess the impact of additional information on model predictions, and do not explicitly account for how the additional information can be deployed to make better decisions. That is, it is assumed that the improved models automatically lead to better decisions, which is not necessarily the case. To adequately design a robust CO₂ monitoring program, we must account for the value of information (VOI) in the data that is assimilated. This allows us to evaluate whether the improvement in the reservoir model that is achieved by assimilating additional data justifies the cost of gathering that data, given the uncertainty associated with the fate of the injected CO₂ plume.

An early work (Howard, 1966) considered VOI in a bidding framework, and formalized the idea that information could be valued within the context of decision making under uncertainty. Since then, VOI analyses have found applications in many fields including health sciences (e.g., Welton et al. 2008;

Yokota and Thompson, 2004), and earth sciences, particularly, in the petroleum industry, where it is used in decision-making during reservoir management (e.g., Begg et al., 2002; Cunningham and Begg, 2008). Bhattacharjya et al, 2010) introduced a VOI methodology to capture the spatial dependence of reservoir sands and shales using Markov random field and estimated the value of seismic information to guide drilling decisions. Gaussian models have also been used to estimate the value of information for seismic attributes (Bickel et al., 2006), and spatially correlated continuous variables such as oil saturation and porosity (Eidsvik et al., 2008). Nakayasu et al. (2016) presented an algorithm that evaluates the value of measuring one physical property (e.g., porosity) at different locations using reservoir simulation, Gaussian random field models, Monte Carlo integration and an expectation maximization algorithm. This approach is fraught with many assumptions. An example is the assumption that the physical parameters, except the heterogenous spatial distributions of reservoir permeability and porosity, are known exactly. In well completions optimization, valuing future measurements to maximize production has also been investigated (Bailey, et al., 2011).

Within the realm of carbon capture and storage (CCS) operations, applications of VOI studies have not gained much visibility. Attempts at VOI studies in CCS have focused on methods to monitor the CO₂ stored in the subsurface. The applicability of the proposed methods has been tested on synthetic cases (e.g., Sato 2011; Trainor-guitton et al. 2013). In this study, we will apply our method to the updated simulation results which were obtained for the CO₂ injection dataset for the Cranfield reservoir.

6.2 VOI Computation

The concept of VOI can be traced to the field of decision analysis (Howard, 1966; Raiffa, 1968), and it quantifies the expected utility or monetary value gained by gathering information under uncertainty. Assuming risk neutrality, i.e., if one is neither risk-averse nor risk-prone (Pratt, et al., 1995), VOI can be defined as equation. 6.1 (Bratvold et al., 2009; Trainor-Guitton et al., 2013).

$$VOI = V_{post} - V_{prior} \quad (6.1)$$

where V_{prior} is the expected value if a decision is made without additional information, and V_{post} is the expected value after additional information. If the information assimilated in the workflow is relevant and reliable, V_{post} will be greater than V_{prior} , and VOI will be positive.

The literature is replete with a variety of methods for computing expected value (e.g., Nakayasu et al. 2016; Sato 2011). In some works (e.g., Raiffa, 1968), the expected value (i.e., expected monetary value) is computed as the probability weighted sum of all monetary outcomes. To illustrate this, let us follow the exposition of Nakayasu et al. (2016). Suppose a is a single option among a set of A options

under uncertainty X , where X is a random variable defined on Ω . For every option $a \in A$, a monetary value function $f_a: \Omega \rightarrow \mathbb{R}$ is assigned. If risk neutrality is assumed, then optimality lies in maximizing this expected monetary value function as:

$$V^{\mathcal{M}} = \int_{\Omega} f_a(x) P_X(x) dx \quad (6.2)$$

where $P_X: \Omega \rightarrow \mathbb{R}$ is the probability density function for the continuous random variable X . The expected monetary value without additional information is therefore:

$$V_{prior} = \max_{a \in A} V^{\mathcal{M}} \quad (6.3)$$

If there is an information Y to be assimilated, then the probability term P_X in equation 6.2 becomes a conditional probability as:

$$P_{X|Y}(x|y) = \frac{P_{Y|X}(y|x)p_X(x)}{p_Y(y)}$$

where $p_Y(y) = \int_{\Omega} P_{Y|X}(y|x)P_X(x)dx \quad \forall X = x$ and $\forall Y = y$

A Gaussian likelihood is commonly used for $P_{Y|X}(y|x)$ (Goda et al., 2017).

The conditional expected monetary value, given $Y = y$ becomes:

$$V^{\ell}(y) = \max_{a \in A} \int_{\Omega} f_a(x) P_{X|Y}(x|y) dx \quad (6.4)$$

Since we want to determine the value of additional information Y defined on Ω' , the function V^{ℓ} must be integrated over the domain Ω' with its probability density function P_Y as:

$$V_{post} = \int_{\Omega'} V^{\ell}(y) P_Y(y) dy \quad (6.5)$$

The new domain Ω' represents a collection of samples that are drawn from P_Y

Finally, the value of information can be computed by substituting equations 6.5 and 6.3 into equation 6.1.

In this dissertation, our approach to the computation of expected value is based on the work of Barros et al., (2016), that uses N ensembles of models $\{m_1, m_2, m_3 \dots, m_N\}$ to account for uncertainties in order to determine the optimum production/injection strategy that maximizes a given objective function over the ensemble.

The objective function is defined as the ensemble mean (i.e., expected value) of the monetary values of all the individual realizations, v_i (equation 6.6).

$$V = \frac{1}{N} \sum_{i=1}^N v_i \quad (6.6)$$

For a single realization, the objective function can be defined as:

$$v_i = \int_{t=0}^T q_{CO_2}(t, m_i) \cdot C dt \quad (6.7)$$

where t is time, T is the total CO₂ injection period, q_{CO_2} is the variable of interest (it can be CO₂ injection rate, dissolved CO₂, residual CO₂ etc.), C is the cost term. If r_{CO_2} is the cost of the variable of interest, b is the discount factor, and τ is the discounting time, then C can be defined according to (Barros et al., 2016), as:

$$C = \frac{r_{CO_2}}{(1 + b)^{t/\tau}} \quad (6.8)$$

Throughout this chapter, the term q_{CO_2} defined in equation 6.7 will denote the amount of CO₂ that is trapped in the form of dissolution. Also, since cost information is not available for the Cranfield, equation 6.7 will be re-expressed in terms of the amount of CO₂ dissolved per unit cost of gas injected (equation 6.9). This allows us to focus only on the amount of dissolved gas, which is a known quantity that can be obtained from running flow simulation.

$$\frac{v_i}{C} = \int_{t=0}^T q_{CO_2}(t, m_i) dt \quad (6.9)$$

Equation 6.9 is applied for each realization before and after data integration, and the expected value is computed using equation 6.6.

6.3 Methodology

The workflow for implementing VOI analyses within the context of data assimilation begins by generating an initial ensemble of N realizations to capture the prior uncertainty in the reservoir model parameters. Next, reservoir response or flow variables are generated from reservoir simulation or rock physics models. These response variables are then compared to the observed injections and/or time lapse seismic response within a data assimilation workflow to perform updates in order to obtain a posterior ensemble of models. The economic outcomes before, V_{prior} and after data assimilation V_{post} are then evaluated, and the difference between these outcomes is computed. The above procedure is

repeated over all the ensemble of models, and the average of the difference in monetary outcomes becomes the expected VOI, which in our case is simply the VOI.

The complete workflow used in this study for computing VOI is shown in Fig. 6.1. Most of the steps in the workflow have been covered in previous chapters. Therefore, the portion of the workflow demarcated in dashed box is what will be the focus of our attention.

The two main datasets that were assimilated in this study (i.e., CO₂ injection data and time-lapse seismic data) only cover the injection period. Within this period, pressure builds up as the CO₂ is injected, hence, trapping of CO₂ will be primarily driven by pressure. As dissolution is pressure driven, our VOI discussions will only focus on the CO₂ that is trapped by dissolution.

By starting with history matching, the flow simulation results before and after assimilating injection data are imported into the VOI workflow, and the portion of the workflow demarcated in dashed box in Fig. 6.1 is implemented, to compute the VOIs. This procedure is repeated for the model selection workflow as well.

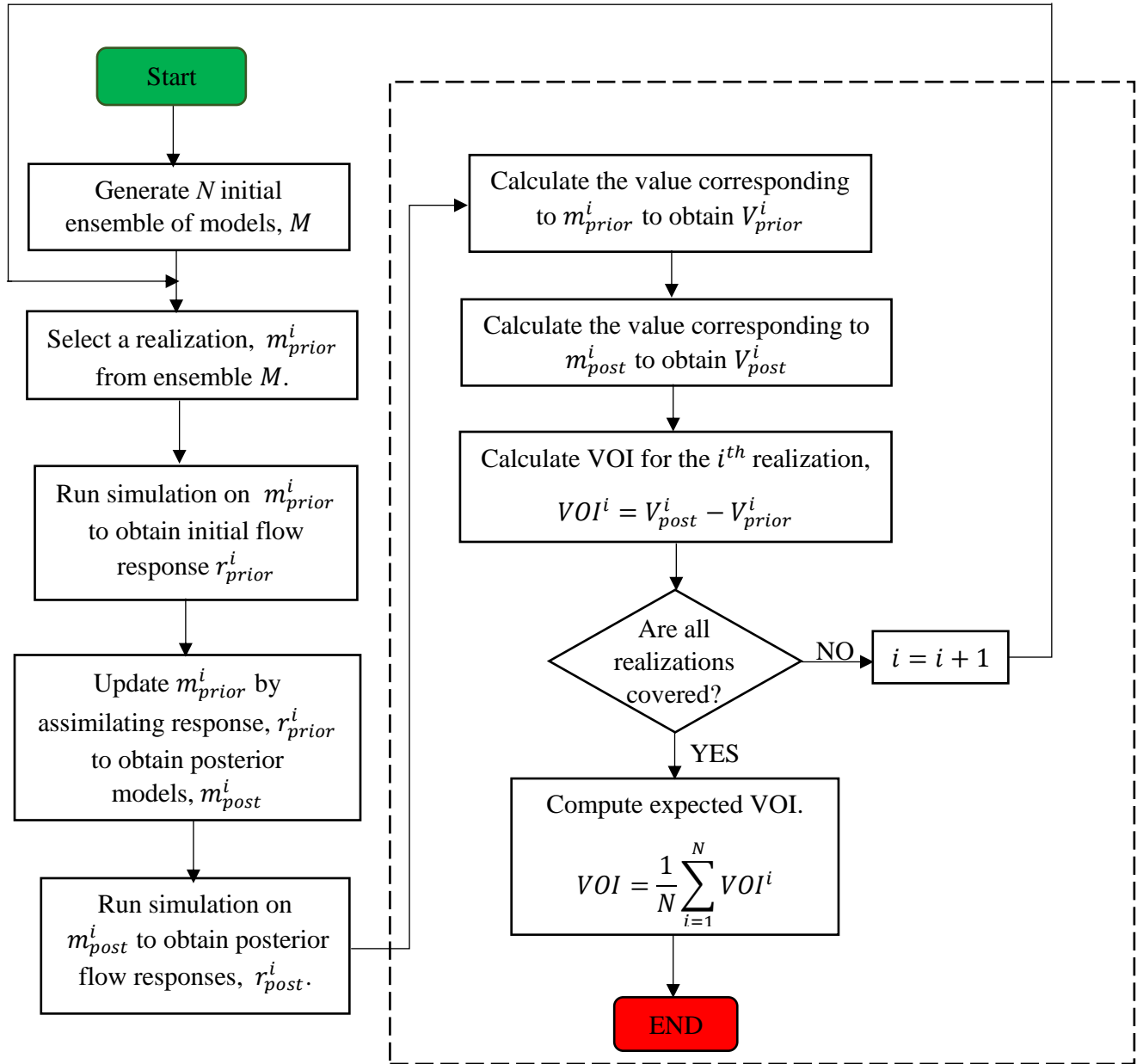


Fig. 6.1 Workflow for computing VOI for assimilating data into models for point bar deposits. Adapted from (Barros et al., 2016).

6.4 Results and Discussions

One criterion that can be used to assess the value of any information could be that it must hold the potential to change our understanding, or reveal very important information about the reservoir that can possibly change our decisions regarding reservoir management. It is also reasonable to expect the cost of obtaining that information to be less than the value it generates. To summarize, the information

must be relevant, observable, material and economical (Bratvold et al., 2009; Pickering & Bickel, 2006). As noted by Abbas et al., (2013), these criteria can be summed up as the expected utility increase after assimilating a new information. This expected gain in utility is captured in equation 6.1, which forms the basis upon which the VOIs were computed in this study.

Fig. 6.2 shows the VOI results obtained by assimilating injection data during history matching as detailed in Chapter 3 and time-lapse seismic data following the Bayesian model selection procedure detailed in Chapter 5. The figure reflects the amount of CO₂ trapped as dissolved gas per unit cost of gas injected over all the observation times. The VOI plots for the injection data (black plot) and time-lapse seismic data (red plot) show upward trends that are greater than zero over all the injection period. According to Trainor-Guitton et al., (2013), this trend suggests that the posterior data that were assimilated (i.e., injection data and time-lapse seismic data) are valuable and act as reliable sources of information. It can be further deduced that these data contain valuable information that can constrain models for subsurface heterogeneity, which is very important for CO₂ monitoring and storage.

The fluctuations in the VOI trends are due to the unsteady injection schedule used for the Cranfield.

Observing the figures also shows that maximum VOI occurs at 450 days. This is perhaps due to the fact that as injection proceeds, more of the reservoir volume is contacted and the corresponding reservoir models are constrained to more information (Barros et al., 2016). Sato, (2011) argues that over time, the VOI can reduce due to the injection-induced pressure buildup that causes geomechanical degradation of seals and faults to cause leakage of CO₂. This further suggests that the injection schedule that was adopted for the Cranfield leads to a pressure buildup that is within the sustainable pressure threshold that does not compromise the geomechanical integrity of any seals or faults. It is also interesting to note the difference in the rate at which the VOI profile increases at early times. It suggests that the injection data has more information about the near wellbore heterogeneities that cause the VOI plot to rise steeply at early times. However, as injection proceeds, the reservoir far from the injection well is informed and that causes the VOI corresponding to the time-lapse seismic to rise more steeply at later times.

In addition, after assimilating time-lapse seismic information during model selection, the VOI is more than that revealed by assimilating injection data. This can be explained by the fact that the model selection allows us to determine which of the history-matched models best reflect the observed reservoir characteristics. Thus, the models are more refined to represent prior uncertainty while revealing additional details about key geologic patterns that drive CO₂ plume migration and storage. After assimilating time-lapse seismic data within the model selection procedure, we find that the CO₂ plume is larger than what was earlier predicted from the history matching. This is clearly shown in Fig.

6.3, where the saturation map of the CO₂ plume is larger after model selection, and the difference map (Fig. 6.3d) highlights the regions of the reservoir where the displacement of the CO₂ plume was not captured during the history matching step (Fig. 6.3c). All these factors explain why the VOI is more after assimilating time-lapse seismic information using the model selection procedure.

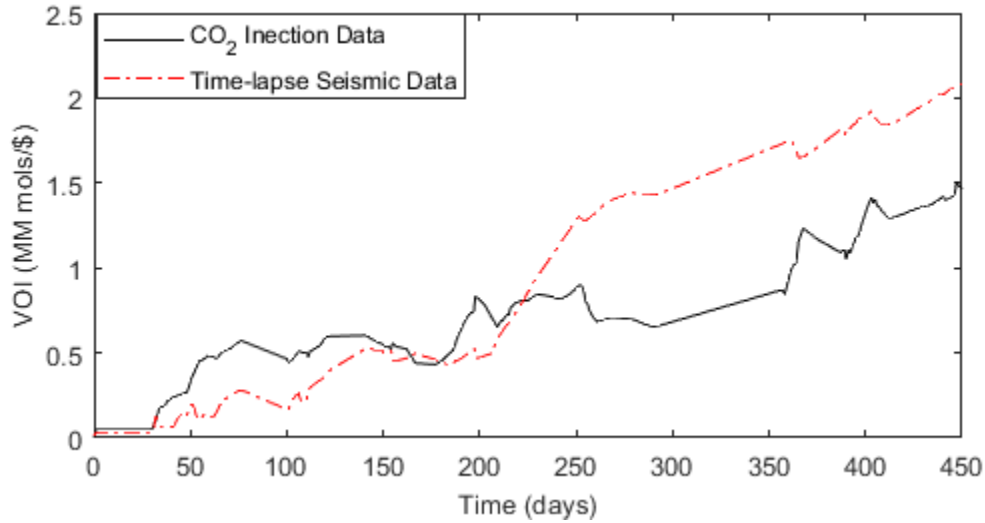


Fig. 6.2 VOI trends by assimilating injection data during history matching (black), and by assimilating time-lapse seismic data during model selection (red).

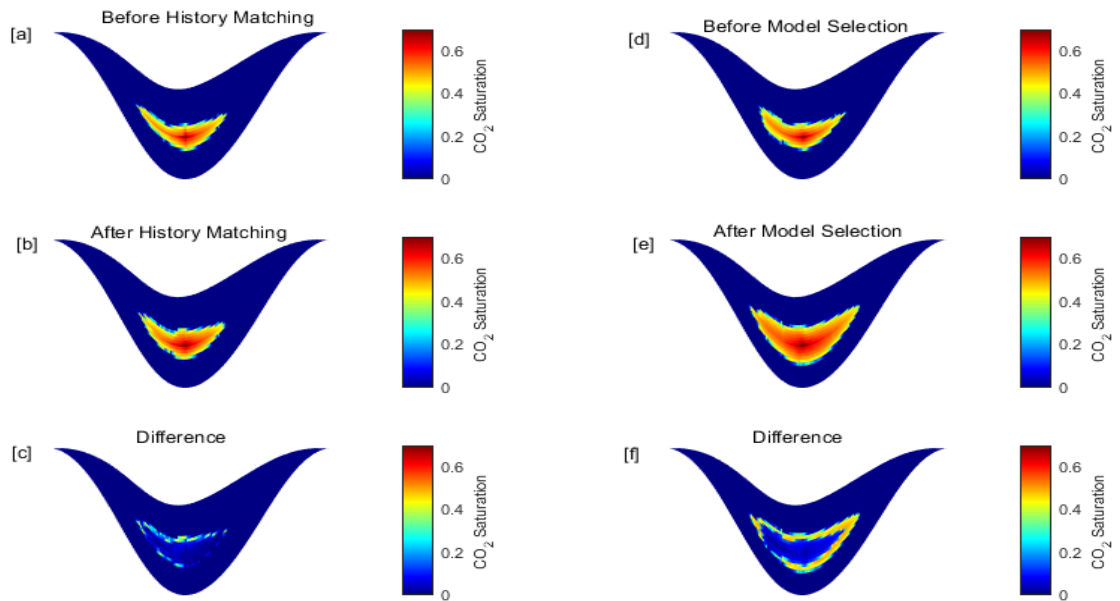


Fig. 6.3 Map of predicted CO₂ saturation after various stages of data assimilation. a) before history matching, b) after history matching, and c) difference in saturation between the two models., d) before assimilating time-lapse seismic data through model selection, e) after model selection, and f) difference in CO₂ saturation between the two models.

6.5 Summary and Concluding Remarks

The VOI analysis is introduced to assess the impact or value of data that were assimilated in the history matching and model selection workflows in this dissertation. The VOI formulation in this chapter is based on ideas adapted from (Barros et al., 2016) that demonstrates the concept in the context of production or injection optimization and history matching under uncertainty.

The CO₂ injection data and the time-lapse seismic information that were assimilated are valuable information that allow us to better characterize the point bar reservoir, and understand the CO₂ plume behavior after injection. The results reveal that the integration of time lapse seismic data serves to identify spatial features away from the well that facilitate the lateral migration of the CO₂ plume thereby resulting in additional value.

There are also unresolved issues with regards to developing a detailed VOI workflow that can provide a comprehensive knowledge for designing an appropriate CO₂ monitoring and storage program. For example, there are other non-technical factors (e.g., legal regulations, public acceptance) that affect the success of CO₂ monitoring and storage programs. Yet, till date, there is no definitive means of converting these factors into monetary values so that they can be incorporated into the VOI workflow. A more complete framework for VOI analysis that addresses these concerns is therefore necessary.

Chapter 7 Limitations and Recommendations

A versatile workflow for modeling geologic point bars and subsequently conditioning the models to injection and time-lapse seismic data has been presented in the previous chapters of this dissertation. The presented methods are flexible and yield realistic descriptions of the spatial heterogeneity associated with point bar methods. However, as with any modeling approach, the presented methods have assumptions and data requirements that may pose challenges. In this chapter, these challenges in the reservoir modeling, the model calibration, and the model selection workflows in this dissertation are presented. Possible recommendations have also been given to address these challenges.

In the geological modeling framework, it is assumed that the geometry of the point bar can be parametrized using smooth interpolation functions such as cubic splines. However, the calibration of the parameters of the interpolation scheme is a challenge, especially when only sparse data is available to guide the inference of the parameters. The interpretation of the channel flow path, and its subsequent migration, is central to the modeling approach. That is always prone to uncertainty based on indirect information available along wells. The workflow could also be extended to accommodate the possible existence of discontinuities such as faults and fractures, which influence CO₂ sequestration in the subsurface. The modeling will proceed with the simulation of point bars as if the faults were absent and subsequently applying vertical displacements consistent with those observed along faults.

In the model calibration scheme, the reservoir geometry could change depending on the petrophysical properties such as porosity and permeability used in step 1 of the model calibration. A possible solution to this problem is to sequentially update both the geometry and the spatial distribution of the petrophysical variables, so that at convergence there are stable updates of both the geometry and the primary variables. However, this approach may quickly become intractable. This is because when the geometry is perturbed, the interpreted spatial correlation length of the petrophysical properties will change, and so the ensemble of models for the reservoir property will also change and that may result in a non-convergent history matching process.

Also, the conditioning data used in the model calibration were either limited or unavailable. For example, there were only few wells available for the CO₂ injection area, and therefore, the hard data used as conditioning information for generating the initial ensemble of models were limited. This is likely in most carbon sequestration projects. The proposed method tries to address this by emphasizing the calibration of models using injection and time-lapse seismic data.

With regards to the model selection workflow, two drawbacks are noteworthy. For one, there is the possibility of model collapse. This is a situation where we run out of models due to the fewer models that remain as the model selection process advances. To avoid this challenge, one can pursue strategies to augment the model suite using the common characteristics of models in a cluster. Others (Srinivasan & Mantilla, 2012) have also proposed imposing a stopping criterion, where the process can be stopped when a predefined minimum number of remaining models is reached, or the updated probability distribution does not show any preference for any cluster.

During the Bayesian posterior probability calculation process, the resultant posterior probabilities may come out to be flat or equal for the various clusters. This would then suggest that the prior set of models may not be rich enough and consequently, the prior uncertainties may not be wide enough to represent the observed data. As a result, the posterior distribution is unable to discriminate between the models. A potential solution could be to enrich the prior ensemble of models by simply increasing the ensemble size or by adding more scenarios. Admittedly, the flatness in these probability updates could also be a procedural artifact created by the assumptions made in the model selection workflow. For example, in constructing the probability envelope that was used to perform Bayesian updates, a Gaussian likelihood was assumed. This assumption could be flawed. To avoid the limitations posed by the Gaussian assumptions, a more data-driven approach for inferring the likelihood may be considered.

Appendix A

The coefficients (a, b, c, d) which are weights for interpolating the channel nodes, can be determined by following the exposition of (Bartels et al., 1995) to represent the j^{th} spline with $n+1$ set of points (p_0, p_1, \dots, p_n) as:

$$P_j(t) = d_j t^3 + c_j t^2 + b_j t + a_j \quad (A1)$$

where $t \in [0,1]$, and $j = 0,1 \dots n - 1$, then, it follows that:

$$P_j(0) = a_j = p_j \quad (A2)$$

$$\text{and } P_j(1) = p_{j+1} = d_j + c_j + b_j + a_j \quad (A3)$$

Taking the derivative of $p_j(t)$ at $t = 0$ and $t = 1$ yields:

$$P'_j(0) = D_j = b_j \quad (A4)$$

$$P'_j(1) = D_{j+1} = 3d_j + 2c_j + b_j \quad (A5)$$

Solving equations (A2) – (A5) for d_j, c_j, b_j and a_j gives:

$$a_j = p_j \quad (A6)$$

$$b_j = D_j \quad (A7)$$

$$c_j = 3(p_{j+1} - p_j) - 2D_j - D_{j+1} \quad (A8)$$

$$d_j = 2(p_j - p_{j+1}) + D_j + D_{j+1} \quad (A9)$$

Since the second derivative must also pass through the same points, we have:

$$P_{j-1}(1) = p_j \quad (A10)$$

$$P'_{j-1}(1) = P'_j(0) \quad (A11)$$

$$P_i(0) = p_i \quad (A12)$$

$$P''_{j-1}(1) = P''_j(0)$$

$$(A13)$$

Also, the interior points and the end points must satisfy the following conditions:

$$P_j(0) = p_0 \tag{A14}$$

$$P_{n-1}(1) = p_n \tag{A15}$$

For natural cubic spline, the second derivative at the end points must be zeros, therefore:

$$P_0''(0) = 0 \tag{A16}$$

$$P_{n-1}''(1) = 0 \tag{A17}$$

Rearranging the above equations leads to a system of equations as:

$$\begin{bmatrix} 2 & 1 & 0 & 0 & 0 & 0 & 0 \\ 1 & 4 & 1 & 0 & 0 & 0 & 0 \\ 0 & 1 & 4 & 1 & 0 & 0 & 0 \\ 0 & 0 & 1 & 4 & 1 & 0 & 0 \\ \vdots & \ddots & \ddots & \ddots & \ddots & \ddots & 0 \\ 0 & 0 & 0 & 0 & 1 & 4 & 1 \\ 0 & 0 & 0 & 0 & 0 & 1 & 2 \end{bmatrix} \begin{bmatrix} D_0 \\ D_1 \\ D_2 \\ D_3 \\ \vdots \\ D_{n-1} \\ D_n \end{bmatrix} = \begin{bmatrix} 3(p_1 - p_0) \\ 3(p_2 - p_0) \\ 3(p_3 - p_1) \\ \vdots \\ 3(p_{n-1} - p_{n-3}) \\ 3(p_n - p_{n-2}) \\ 3(p_n - p_{n-1}) \end{bmatrix} \tag{A18}$$

Upon solving these system equations for the D_j ($j = 0, 1, \dots, n$) terms, we can obtain the spline coefficients by revisiting equations A6-A9

Appendix B Implementation of Gassman's fluid substitution procedure

Step 1: Compute Bulk modulus of the mineral grains and the rock matrix

$$K_{gr}^{Reuss} = \left[\frac{F_{qtz}}{K_{qtz}} + \frac{F_{chl}}{K_{chl}} + \frac{F_{kao}}{K_{kao}} + \frac{F_{ill}}{K_{ill}} + \frac{F_{cal}}{K_{cal}} \right]^{-1}$$

$$K_{gr}^{Reuss} = \left[\frac{0.8211}{2.6500} + \frac{0.1220}{2.6810} + \frac{0.0321}{2.4440} + \frac{0.0134}{2.7060} + \frac{0.0114}{2.7100} \right]^{-1} = 42.3548 \text{ GPa}$$

$$K_{gr}^{Voigt} = K_{qtz} \times F_{qtz} + K_{chl} \times F_{chl} + K_{kao} \times F_{kao} + K_{ill} \times F_{ill} + K_{cal} \times F_{cal}$$

$$K_{gr}^{Voigt} = 2.650 \times 0.8211 + 2.6810 \times 0.1220 + 2.4440 \times 0.0321 + 2.7060 \times 0.0134 + 2.7100 \times 0.0114 = 49.9143 \text{ GPa}$$

$$K_{matrix} = K_{gr}^{Hill} = \frac{(K_{gr}^{Voigt} + K_{gr}^{Reuss})}{2} = \frac{(49.9143 + 42.3548)}{2} = 46.1345 \text{ GPa}$$

Step 2: Calculate the water and brine properties at in-situ conditions.

Compute the p-wave velocity through pure water using the following equation (M. Batzle & Wang, 1992):

$$v_w = \sum_{i=1}^5 \sum_{j=1}^4 w_{ij} T^{i-1} P^{j-1}$$

where T and P are respectively, in-situ temperature and pressures w_{ij} are the coefficients w for computing water properties at row i and column j as shown in Table A1.

Table A1 Coefficients for computing p-wave velocity in water (M. Batzle & Wang, 1992)

1403.9	1.524	0.0034	-1.2×10^{-5}
4.871	-0.0111	1.74×10^{-4}	-1.63×10^{-6}
-.0478	2.747×10^{-4}	-2.14×10^{-6}	1.24×10^{-8}
1.487×10^{-4}	-6.503×10^{-7}	-1.46×10^{-8}	1.33×10^{-10}
-2.197×10^{-7}	7.99×10^{-10}	5.23×10^{-11}	-4.61×10^{-13}

For the Cranfield, the in-situ temperature, pressure, and salinity are as shown in Table A2

Table A2 In-situ conditions at the Cranfield, Mississippi injection reservoir (J. Lu et al., 2013b)

In-situ Conditions	Value
Temperature	125°C
Pressure	32MPa
Brine density	1.11 g/cm ³
Salinity	155752 ppm

Using the coefficients in Table A1, and the pressure and temperature in Table A2, p-wave velocity through water, can be computed as: $v_w = 1588 \text{ m/s}$

The p-wave velocity through brine, v_{brine} is computed using the following correlation (M. Batzle & Wang, 1992):

$$v_{brine} = v_w + S(1170 - 9.6T + 0.055T^2 - 8.5 \times 10^{-5}T^3 + 2.6P - 0.0029TP - 0.0476P^2) + S^{1.5}(780 - 10P + 0.16P^2) - 1820S^2$$

where P , T and S are respectively, the in-situ conditions for pressure (MPa), temperature ($^{\circ}\text{C}$) and salinity (fraction) as detailed in Tabled A2. Substituting the values computed for p-wave velocity in water, and the in-situ conditions in Table A2, we have $v_{brine} = 1689.1 \text{ m/s}$

Bulk modulus of brine:

$$k_{brine} = \rho_{brine} \cdot v_{brine}^2 \cdot 10^{-6} = 3.4807 \text{ GPa}$$

Step 3: Determine fluid bulk modulus at in-situ conditions.

The reservoir at initial conditions is assumed to be fully saturated with brine, therefore, the initial water saturation s_{wi} used in running simulation is about $0.9999 \cong 1$. From Table 4.2, bulk modulus of CO_2 is 0.128, therefore the bulk modulus of the fluid becomes:

$$k_{fl} = \left(\frac{s_{wi}}{k_{brine}} + \frac{1 - s_{wi}}{k_*} \right)^{-1} = 0.5579 \text{ GPa}$$

Step 4: Determine the in-situ elastic moduli when the reservoir is fully saturated with brine.

From Fig. 4.1 the p-wave velocity (v_p), s-wave velocity (v_s) and formation density (ρ) at a depth of 3200m are:

$$v_p = 3.750 \text{ km/s}$$

$$v_s = 1.250 \text{ km/s}$$

$$\rho = 2.232 \text{ g/cm}^3$$

The bulk modulus k_{sat} and the shear modulus of the saturated rock μ_{sat} are computed as:

$$k_{sat} = \rho \left(v_p^2 - \frac{4}{3} v_s^2 \right) = 26.7375 \text{ GPa}$$

$$\mu_{sat} = \mu = \rho v_s^2 = 3.4875 \text{ GPa}$$

Step 5: Calculate the bulk modulus of the dry rock, k_{dry} using the equation:

$$k_{dry} = \frac{k_{sat} \left(\frac{\phi k_{matrix}}{k_{fl}} + 1 - \phi \right) - k_{matrix}}{\frac{\phi k_{matrix}}{k_{fl}} + \frac{k_{sat}}{k_{matrix}} - 1 - \phi}$$

At a depth of 3200m, the porosity ϕ is 0.25. All input parameters have been calculated earlier; by substitution, we have: $k_{dry} = 20.5373 \text{ GPa}$

Step 6: Calculate the density of the fluid ρ_{fl} and the saturated rock ρ_{sat} . After CO_2 injection, recalculate the bulk modulus of the fluid, k_{fl} , density of the fluid ρ_{fl} and that of the rock ρ_{sat} .

Input parameters obtained from flow simulation:

Brine saturation: $s_{brine} = 0.897$

CO_2 saturation: $s_{\text{CO}_2} = 0.103$

Brine density: $\rho_{brine} = 0.988 \text{ kgm}^{-3}$

CO_2 density: $\rho_{\text{CO}_2} = 0.6 \text{ kgm}^{-3}$

$$k_{fl} = \left(\frac{s_{brine}}{k_{brine}} + \frac{s_{\text{CO}_2}}{k_{\text{CO}_2}} \right)^{-1}$$

k_{brine} has been computed earlier as 3.4807 GPa, and k_{CO_2} is 0.128 GPa (from Table 4.2). By substituting, we have:

$$k_{fl} = \left(\frac{0.897}{3.4807} + \frac{0.103}{0.128} \right)^{-1} = 0.9192 \text{ GPa}$$

$$\rho_{fl} = s_{brine} \cdot \rho_{brine} + s_{\text{CO}_2} \cdot \rho_{\text{CO}_2} = 0.897 \times 0.988 + 0.103 \times 0.6 = 0.9480 \text{ kgm}^{-3}$$

$$\rho_{sat} = \phi \cdot \rho_{fl} + (1 - \phi) \cdot \rho_{matrix} = 0.25 \times 0.948 + (1 - 0.25) \times 2.6451 = 2.22 \text{ kgm}^{-3}$$

Step 7: Compute the bulk modulus of the saturated rock after CO_2 injection.

$$k_{sat} = k_{dry} + \frac{\left(1 - \frac{k_{dry}}{k_{matrix}}\right)^2}{\frac{\phi}{k_{fl}} + \frac{(1 - \phi)}{k_{matrix}} - \frac{k_{dry}}{k_{matrix}^2}}$$

$$k_{sat} = 20.5373 + \frac{\left(1 - \frac{20.5373}{46.1345}\right)^2}{\frac{0.25}{0.9192} + \frac{(1 - 0.25)}{46.1345} - \frac{20.5373}{46.1345^2}} = 21.6423 \text{ GPa}$$

Step 8: Compute the p-wave velocity after CO_2 injection.

$$V_p^{sat} = \sqrt{\frac{K_{sat} + \frac{4}{3}\mu_{sat}}{\rho_{sat}}}$$

$$V_p^{sat} = \sqrt{\frac{21.6423 + \frac{4}{3}(3.4875)}{2.22}} = 3.4414 \text{ km/s}$$

APPENDIX C Publications

Portions of this dissertation had been published in earlier works as follows:

- Dawuda, I., & Srinivasan, S. (2022). A hierarchical stochastic modeling approach for representing point bar geometries and petrophysical property variations. *Computers & Geosciences*, *164*, 105127.
- Dawuda, I., & Srinivasan, S. (2021, July). Geometric and Geostatistical Modeling of Point Bars. In *International Geostatistics Congress* (pp. 63-79). Cham: Springer International Publishing.
- Dawuda, I., & Srinivasan, S. (2022). Geologic Modeling and Ensemble-Based History Matching for Evaluating CO₂ Sequestration Potential in Point Bar Reservoirs. *Frontiers in Energy Research*, *10*, 867083.
- Dawuda, I., and Srinivasan, S. (2022). A hierarchical ensemble-based data assimilation technique for improving prediction of CO₂ plume displacement during sequestration: Computational Geosciences (Under Review)
- Joon, S., Dawuda, I., Morgan, E., & Srinivasan, S. (2022). Rock Physics-Based Data Assimilation of Integrated Continuous Active-Source Seismic and Pressure Monitoring Data during Geological Carbon Storage. *SPE Journal*, *27*(04), 2510-2524.

References

- Abbas, A. ., Bakir, N. ., Klutke, G. A., & Sun, Z. (2013). Effects of risk aversion on the value of information in two-action decision problems. *Decis. Anal*, 10(3), 257–275.
- Agarwal, B., Hermansen, H., Sylte, J. E., & Thomas, L. K. (2000). Reservoir characterization of Ekofisk field: a giant, frac-tured chalk reservoir in the Norwegian North sea — historymatch. *SPE Reserv. Evalu. Eng*, 3(6), 534–543.
- Ajo-Franklin, J. B., Peterson, J., Doetsch, J., & Daley, T. . (2013). High-resolution characterization of a CO₂ plume using crosswell seismic tomography: Cranfield, MS, USA. *International Journal of Greenhouse Gas Control*, 18, 497–509.
- Aki, K. I., & Richards, P. G. (1980). *Quantitative seismology*. W. H. Freeman and Co.
- Alfi, M., & Hosseini, S. A. (2016). Integration of reservoir simulation, history matching, and 4D seismic for CO₂-EOR and storage at Cranfield, Mississippi, USA. *Fuel*, 175, 116–128. <https://doi.org/10.1016/j.fuel.2016.02.032>
- Alfi, M., Hosseini, S. A., Alfi, M., & Shakiba, M. (2015). Effectiveness of 4D Seismic Data to Monitor CO₂ Plume in Cranfield CO₂-EOR Project. *Carbon Management Technology Conference*. <https://doi.org/10.7122/439559-MS>
- Alfonzo, M., Oliver, D. S., & Macbeth, C. (2017). Analysis and calibration of 4D seismic data prior to 4D seismic inversion and history matching–Norne field case. *79th EAGE Conference and Exhibition 2017-Workshops. European Association of Geoscientists & Engineers*, 519.
- Allen, J. R. . (1965). The sedimentation and palaeogeography of the Old Red Sandstone of Anglesey, north Wales. *Proceedings of the Yorkshire Geological Society*, 35(2), 139–185.
- Alpak, F. O., & Van Der Vlugt, F. (2014). Shale-drape modeling for the geologically consistent simulation of clastic reservoirs. *SPE Journal*, 19(5), 832–844. <https://doi.org/10.2118/169820-PA>
- Austin-Adigio, M. E., Wang, J., Alvarez, J. M., & Gates, I. D. (2018). Novel insights on the impact of top water on Steam-Assisted Gravity Drainage in a point bar reservoir. *International Journal of Energy Research*, 42(2), 616–632. <https://doi.org/10.1002/er.3844>
- Awejori, G. A., & Radonjic, M. (2022). Review of Geochemical and Geo-Mechanical Impact of Clay-Fluid Interactions Relevant to Hydraulic Fracturing. *Emerging Technologies in Hydraulic Fracturing and Gas Flow Modelling*, 113.
- Awejori, Gabriel Adua, Doughty, C., Spycher, N., Xiong, F., Paronish, T., & Radonjic, M. (2022). Integrated Experimental and Modeling Study of Geochemical Reactions of Simple Fracturing Fluids with Caney Shale. *Energy and Fuels*.
- Awejori, Gabriel Adua, Luo, G., Katende, A., Radonjic, M., Doughty, C., Spencer, N., Paronish, T., O’Connell, L., & Rihn, A. (2021). Fracturing Fluid-Induced Mineralogy Changes and Impact on Elastic Properties for the Caney Shale, Oklahoma. *55th US Rock Mechanics/Geomechanics Symposium*.
- Ayawah, A. E. P. (2014). Evaluation of Oil Recovery Efficiency of Water-Flooding, Gas-Flooding and Wag Injection in a Turbidite Reservoir. *Dissertation*.
- Ayawah, P. E., Sebbeh-Newton, S., Azure, J. W., Kaba, A. G., Anani, A., Bansah, S., & Zabidi, H. (2022). A review and case study of Artificial intelligence and Machine learning methods used for

- ground condition prediction ahead of tunnel boring Machines. *Tunnelling and Underground Space Technology*, 125, 104497.
- Bai, T., & Tahmasebi, P. (2021). Accelerating geostatistical modeling using geostatistics-informed machine Learning. *Computers and Geosciences*, 146(July 2020), 104663. <https://doi.org/10.1016/j.cageo.2020.104663>
- Bai, T., & Tahmasebi, P. (2022). Sequential Gaussian simulation for geosystems modeling: a machine learning approach. *Geoscience Frontiers*, 13(1).
- Bailey, W. J., Couët, B., & Prange, M. (2011). Forecast optimization and value of information under uncertainty. In *Uncertainty analysis and reservoir modeling. AAPG Memoir*, 96, 217–233.
- Barrera, A., & Srinivasan, S. (2009). History matching by simultaneous calibration of reservoir geological models at pore-level and field scales. *Proceedings - SPE Annual Technical Conference and Exhibition*, 6, 3840–3852. <https://doi.org/10.2118/124939-ms>
- Barros, E. G. D., Van den Hof, P. M. ., & Jansen, J. D. (2016). Value of information in closed-loop reservoir management. *Computational Geosciences*, 737–749. <https://doi.org/10.1007/s10596-015-9509-4>
- Bartels, R. H., Beatty, J. C., & Barsky, B. A. (1995). *An introduction to splines for use in computer graphics and geometric modeling*. Morgan Kaufmann.
- Batzle, M. L., & Wang, Z. (1992). Seismic properties of pore fluids. *Geophysics*, 64, 1396–1408.
- Batzle, M., & Wang, Z. (1992). Seismic properties of pore fluids. *Geophysics*, 57(11), 1396–1408.
- Begg, S., Bratvold, R., & Campbell, J. (2002). The value of flexibility in managing uncertainty in oil and gas investments. *SPE Annual Technical Conference and Exhibition. OnePetro*.
- Bennion, B., & Bachu, S. (2005). Relative permeability characteristics for supercritical CO₂ displacing water in a variety of potential sequestration zones in the Western Canada sedimentary basin. *SPE Annual Technical Conference Proceedings*.
- Berryman, J. G. (1999). Origin of Gassmann's equations. *Geophysics*, 64, 1627–1629.
- Berryman, J. G., & Milton, G. W. (1991). Exact results for generalized Gassmann's equation in composite porous media with two constituents. *Geophysics*, 56, 1950–1960.
- Bertoncello, A., Sun, T., Li, H., Mariethoz, G., & Caers, J. (2013). Conditioning Surface-Based Geological Models to Well and Thickness Data. *Mathematical Geosciences*, 45(7), 873–893. <https://doi.org/10.1007/s11004-013-9455-4>
- Bhattacharjya, D., Eidsvik, J., & Mukerji, T. (2010). *The Value of Information in Spatial Decision Making*. 141–163. <https://doi.org/10.1007/s11004-009-9256-y>
- Bhowmik, S. (2014). *Particle tracking proxies for prediction of CO₂ plume migration within a model selection framework*. University of Texas at Austin.
- Bhowmik, S., Srinivasan, S., & Bryant, S. L. (2011). Inferring migration of CO₂ plume using injection data and a probabilistic history matching approach. *Energy Procedia*, 4, 3841–3848. <https://doi.org/10.1016/j.egypro.2011.02.320>
- Bhowmik, S., Srinivasan, S., & Bryant, S. L. (2013). Prediction of plume migration using injection data and a model selection approach. *Energy Procedia*, 37, 3672–3679.

- Bickel, J. E., Gibson, R. L., Mcvay, D. A., Texas, A., Pickering, S., & Waggoner, J. (2006). *Quantifying 3D Land Seismic Reliability and Value*.
- Biot, M. A. (1956a). Theory of Propagation of Elastic Waves in a Fluid-Saturated Porous Solid. I. Low frequency range. *Journal of the Acoustical Society of America*, 28(2), 168–178. <https://doi.org/10.1121/1.1908239>
- Biot, M. A. (1956b). Theory of Propagation of Elastic Waves in a Fluid-Saturated Porous Solid II. Higher Frequency Range. *Journal of the Acoustical Society of America*, 28(2), 179–191. <https://doi.org/10.1121/1.1908241>
- Boisvert, J. B, Manchuk, J. G., Neufeld, C., Niven, E. B., & Deutsch, C. V. (2012). Boisvert, J. B Manchuk, J. G Neufeld, C. Niven, E. B Deutsch, C. V. In P. Abrahamsen, R. Hauge, & O. Kolbjørnsen (Eds.), *Micro-modeling for enhanced small scale porosity-permeability relationships. In Geostatistics Oslo*. Springer, Dordrecht.
- Boisvert, Jeffery B. (2011). *Conditioning Object Based Models with Gradient Based Optimization. 2011(1)*. <http://www.ccgaberta.com>
- Boyden, A., & Noble, G. K. (1933). The relationships of some common Amphibia as determined by serological study. *American Museum Novitates*, 606.
- Bratvold, R.B, Bickel, J. ., & Lohne, H. . (2009). Value of information in the oil and gas industry: past, present, and future. *SPE Reserv. Eval. Eng*, 12(4), 630–638. <https://doi.org/http://dx.doi.org/10.2118/110378-PA>
- Bratvold, Reidar B, Bickel, J. E., Risk, A., & Lohne, H. P. (2009). *Value of Information in the Oil and Gas Industry : Past , Present , and Future. August*, 11–14.
- Brierley, G. J., & Hickin, E. J. (1985). The downstream gradation of particle sizes in the Squamish River, British Columbia. *Earth Surface Processes and Landforms*, 10(6), 597-606.
- Budiansky, B., & O'connell, R. J. (1976). Elastic moduli of a cracked solid. *International Journal of Solids and Structures*, 12(2), 81–97. [https://doi.org/10.1016/0020-7683\(76\)90044-5](https://doi.org/10.1016/0020-7683(76)90044-5)
- Burgers, G., van Leeuwen, P. J., & Evensen, G. (1998). Analysis scheme in the ensemble Kalman filter. *Monthly Weather Review*, 126, 1719–1724.
- Caers, J. (2003a). Efficient gradual deformation using a streamline-based proxy method. *Journal of Petroleum Science and Engineering*, 39(1–2), 57–83. [https://doi.org/10.1016/S0920-4105\(03\)00040-8](https://doi.org/10.1016/S0920-4105(03)00040-8)
- Caers, J. (2003b). History Matching Under Training-Image-Based Geological Model Constraints. *Society of Petroleum Engineers*, 74716, 218–226.
- Caers, J., & Zhang, T. (2005). Multiple-point geostatistics: A quantitative vehicle for integrating geologic analogs into multiple reservoir models. *AAPG Memoir*, 80, 383–394.
- Cancelliere, M., Verga, F., & Viberti, D. (2011). Benefits and limitations of assisted history matching. *Society of Petroleum Engineers - Offshore Europe Oil and Gas Conference and Exhibition 2011, OE 2011*, 2(September), 935–943. <https://doi.org/10.2118/146278-ms>
- Carmichael, R. S. (1989). *Practical handbook of physical properties of rocks and minerals*. CRC Press.
- Carter, D. C. (2003). 3-D seismic geomorphology: insights into fluvial reservoir deposition and performance, Widuri field, Java Sea. *AAPG Bull.*, 87, 909–934.

- Chen, F., Lu, S., Ding, X., Zhao, H., & Ju, Y. (2019). Total porosity measured for shale gas reservoir samples: A case from the lower Silurian Longmaxi formation in southeast Chongqing, China. *Minerals*, 9(1). <https://doi.org/10.3390/min9010005>
- CMG-GEM. (2019). *Compositional and Unconventional Simulator. Version 2019.10 User's Guide*. Computer Modeling Group Ltd., Calgary, Alberta. (2019.10).
- CMG-Winprop. (2019). *Fluid Property Characterization Tool. Version 2019.10 User's Guide*. Computer Modeling Group Ltd., Calgary, Alberta.
- Cui, Z., Chen, Q., Liu, G., Mariethoz, G., & Ma, X. (2021). Hybrid parallel framework for multiple-point geostatistics on Tianhe-2: A robust solution for large-scale simulation. *Computers and Geosciences*, 157(August), 104923. <https://doi.org/10.1016/j.cageo.2021.104923>
- Cunningham, P., & Begg, S. (2008). Using the value of information to determine optimal well order in a sequential drilling program. *AAPG Bulletin*, 92 (10), 1393–1402. <https://doi.org/https://doi.org/10.1306/06040808071>
- Dafflon, B., Wu, Y., Hubbard, S., Birkholzer, J., Daley, T., Pugh, J., Peterson, J., & Trautz, R. (2012). Monitoring CO₂ intrusion and associated geochemical transformations in a shallow groundwater system using complex electrical methods. *Journal of Environmental Science & Technology*. <https://doi.org/http://dx.doi.org/10.1021/es301260e>.
- Daley, T. M., Hendrickson, J., & Queen, J. H. (2014). Monitoring CO₂ Storage at Cranfield, Mississippi with time-lapse offset VSP - Using integration and modeling to reduce uncertainty. *Energy Procedia*, 63, 4240–4248. <https://doi.org/10.1016/j.egypro.2014.11.459>
- Danesh, A. (1998). *PVT and phase behaviour of petroleum reservoir fluids*. Elsevier.
- Davies, B. J., & Haldorsen, H. H. (1987). Pseudofunctions in Formations Containing Discontinuous Shales: a Numerical Study. *Society of Petroleum Engineers of AIME, (Paper) SPE*, 221–229. <https://doi.org/10.2118/16012-ms>
- Dawuda, I., & Srinivasan, S. (2022). Geologic Modeling and Ensemble-Based History Matching for Evaluating CO₂ Sequestration Potential in Point bar Reservoirs. *Front. Energy Res.*, 10. <https://doi.org/10.3389/fenrg.2022.867083>
- de Figueiredo, L. P., Schmitz, T., Lunelli, R., Roisenberg, M., Santana de Freitas, D., & Grana, D. (2021). Direct Multivariate Simulation - A stepwise conditional transformation for multivariate geostatistical simulation. *Computers and Geosciences*, 147(October 2020), 104659. <https://doi.org/10.1016/j.cageo.2020.104659>
- Delshad, M., Kong, X., Tavakoli, R., Hosseini, S. A., & Wheeler, M. F. (2013a). Modeling and simulation of carbon sequestration at Cranfield incorporating new physical models. *International Journal of Greenhouse Gas Control*, 18, 463–473. <https://doi.org/10.1016/j.ijggc.2013.03.019>
- Delshad, M., Kong, X., Tavakoli, R., Hosseini, S. A., & Wheeler, M. F. (2013b). Modeling and simulation of carbon sequestration at Cranfield incorporating new physical models. *International Journal of Greenhouse Gas Control*, 18, 463–473. <https://doi.org/10.1016/j.ijggc.2013.03.019>
- Deschamps, R., Guy, N., Preux, C., & Lerat, O. (2011). *SPE 147035 Impact of Upscaling on 3-D Modelling of SAGD in a Meander Belt*. November.
- Deutsch, Clayton V. (2006). A sequential indicator simulation program for categorical variables with point and block data: BlockSIS. *Computers and Geosciences*, 32(10), 1669–1681. <https://doi.org/10.1016/j.cageo.2006.03.005>

- Deutsch, Clayton V., & Wang, L. (1996). Hierarchical object-based stochastic modeling of fluvial reservoirs. *Mathematical Geology*, 28(7), 857–880. <https://doi.org/10.1007/BF02066005>
- Deutsch, C V, & Tran, T. T. (2002). *FLUVSIM: a program for object-based stochastic modeling of fluvial depositional systems* \$. 28, 525–535.
- Deutsch, Clayton V, & Journel, A. G. (1998). *GSLIB: Geostatistical Software Library* (2nd ed). Oxford University Press, New York.
- Deveugle, P. E. K., Jackson, M. D., Hampson, G. J., Farrell, M. E., Sprague, A. R., Stewart, J., & Calvert, C. S. (2011). Characterization of stratigraphic architecture and its impact on fluid flow in a fluvial-dominated deltaic reservoir analog: Upper Cretaceous Ferron Sandstone Member, Utah. *AAPG Bulletin*, 95, 693–727.
- Doetsch, J., Kowalsky, M. B., Doughty, C., Finsterle, S., Ajo-Franklin, J. B., Carrigan, C. R., Yang, X., Hovorka, S. D., & Daley, T. M. (2013). Constraining CO₂ simulations by coupled modeling and inversion of electrical resistance and gas composition data. *International Journal of Greenhouse Gas Control*, 18, 510–522. <https://doi.org/10.1016/j.ijggc.2013.04.011>
- Duan, Z., & Sun, R. (2003). An improved model calculating CO₂ solubility in pure water and aqueous NaCl solutions from 273 to 533 K and from 0 to 2000 bar. *Chemical Geology*, 193(3–4), 257–271.
- Durkin, P. R., Boyd, R. L., Hubbard, S. M., Shultz, A. W., & Blum, M. D. (2017). Three-Dimensional Reconstruction of Meander-Belt Evolution, Cretaceous McMurray Formation, Alberta Foreland Basin, Canada. *Journal of Sedimentary Research*, 87(10), 1075–1099. <https://doi.org/10.2110/jsr.2017.59>
- Eberhart-Phillips, D., Han, D.-H., & Zoback, M. D. (1989). Empirical relationships among seismic velocity, effective pressure, porosity, and clay content in sandstone. *Geophysics*, 54, 82–89.
- Eidsvik, J., Bhattacharjya, D., & Mukerji, T. (2008). Value of information of seismic amplitude and CSEM resistivity. *Geophysics*, 73(4), R59–R69. <https://doi.org/https://doi.org/10.1190/1.2938084>
- Eikeland, K. M., & Hansen, H. (2009). Dry gas reinjection in a strong waterdrive gas/condensate field increases condensate recovery—case study: The sleipner Øst ty field, South Viking Graben, Norwegian North Sea. *SPE Reservoir Evaluation and Engineering*, 12(2), 281–296. <https://doi.org/10.2118/110309-PA>
- Eiter, T., & Mannila, H. (1994). Computing discrete Fréchet distance. *Notes*, 94, 64. <http://citeseerx.ist.psu.edu/viewdoc/download?doi=10.1.1.90.937&rep=rep1&type=pdf>
- Eskandari, K., & Srinivasan, S. (2010). Reservoir modelling of complex geological systems—A multiple point perspective. *Canadian International Petroleum Conference 2008*, 59–68. <https://doi.org/10.2118/2008-176>
- Evensen, G. (1994). Sequential data assimilation with a nonlinear quasi-geostrophic model using Monte Carlo methods to forecast error statistics. In *Journal of Geophysical Research* (Vol. 99, Issue C5). <https://doi.org/10.1029/94jc00572>
- Evensen, Geir. (2003). The Ensemble Kalman Filter: Theoretical formulation and practical implementation. *Ocean Dynamics*, 53(4), 343–367. <https://doi.org/10.1007/s10236-003-0036-9>
- Evensen, Geir, & van Leeuwen, P. J. (1996). Assimilation of Geosat altimeter data for the Agulhas Current using the Ensemble Kalman Filter with a quasi-geostrophic model. *Monthly Weather Review*, 124, 85–96. <http://library1.nida.ac.th/termpaper6/sd/2554/19755.pdf>

- Evensen, Geir, & van Leeuwen, P. J. (2000). An Ensemble Kalman Smoother for Nonlinear Dynamics. *Monthly Weather Review*, *128*(6), 1852–1867. [https://doi.org/10.1175/1520-0493\(2000\)128%3C1852:AEKSFN%3E2.0.CO;2](https://doi.org/10.1175/1520-0493(2000)128%3C1852:AEKSFN%3E2.0.CO;2)
- Fustic, M., Hubbard, S. M., Spencer, R., Smith, D. ., Leckie, D. A., Bennett, B., & Larter, S. (2012). *Recognition of down-Valley Translation in Tidally influenced Meandering Fluvial Deposits, Athabasca Oil Sands (Cretaceous), Alberta, Canada. Marine and Petroleum Geology*. *29*, 219–232.
- Gasperikova, E., & Hoversten, G. . (2008). Gravity monitoring of CO₂ movement during sequestration: model studies. *Geophysics*, *73*(6), WA105–WA112.
- Gassmann, F. (1951). *Über die Elastizität poröser Medien: Vier. der Natur. Gesellschaft in Zürich*. *96*, 1–23.
- Ghosh, R., Zhang, R., Sen, M. K., & Srinivasan, S. (2012). Monitoring CO₂ movement by interpreting time-lapse seismic data using rock physics modeling in the Tuscaloosa formation, Cranfield, MS Valley. *SEG International Exposition and Annual Meeting*. <https://doi.org/10.1190/segam2012-0917.1>
- Giordano, R. M., Salter, S. J., & Mohanty, K. K. (1985). The effects of permeability variations on flow in porous media. *SPE Annual Technical Conference and Exhibition*.
- Goda, T., Katsuta, O., & Sato, K. (2017). Value of information in optimizing reservoir development under geological uncertainty. *Journal of the Japan Petroleum Institute*, *60*(1), 41–52.
- Goral, J., Panja, P., Deo, M., Andrew, M., Linden, S., Schwarz, J. O., & Wiegmann, A. (2020). Confinement Effect on Porosity and Permeability of Shales. *Scientific Reports*, *10*(1), 1–11. <https://doi.org/10.1038/s41598-019-56885-y>
- Gregory, A. R. (1976). Fluid saturation effects on dynamic elastic properties of sedimentary rocks. *Geophysics*, *41*, 895–921.
- Gu, Y., & Oliver, D. S. (2005). History matching of the PUNQ-S3 reservoir model using the ensemble Kalman filter. *SPE Journal*, *10*(2), 217–224. <https://doi.org/10.2118/89942-PA>
- Güneralp, İ., & Marston, R. A. (2012). Process–form linkages in meander morphodynamics: Bridging theoretical modeling and real world complexity. *Progress in Physical Geography*, *36*(6), 718–746.
- Haldorsen, H. H., & Chang, D. W. (1986). Notes on stochastic shales: from outcrop to simulation model. In L. Lake & H. B. Carroll (Eds.), *Reservoir Characterization* (pp. 445–485). London Academic Press. <https://doi.org/10.1016/B978-0-12-434065-7.X5001-1>
- Han, D.-H., Nur, A., & Morgan, D. (1986). Effects of porosity and clay content on wave velocities in sandstones. *Geophysics*, *51*, 2093– 2107.
- Hartkamp-Bakker, C. ., & Donselaar, M. . (1993). Permeability patterns in point bar deposits: Tertiary Loranca Basin, central Spain, in S. S. Flint and I. D. Bryant, eds., *The geological modelling of hydrocarbon reservoirs and outcrop analogs: International Association of Sedimentologists Special Publication 15*, 157–168.
- Hartman, G., Heinold, B., Troy, S., & Chalishajar, D. (2014). *Apex Calculus II* (J. Bowen (ed.); 2nd ed.). CreateSpace Independent Publishing Platform.
- Hassanpour, M. M., Pyrcz, M. J., & Deutsch, C. V. (2013). Improved geostatistical models of inclined heterolithic strata for McMurray Formation, Alberta, Canada. *AAPG Bulletin*, *97*(7), 1209–1224. <https://doi.org/10.1306/01021312054>

- Hathout, D. (2015). Sine-Generated Curves: Theoretical and Empirical Notes. *Advances in Pure Mathematics*, 05(11), 689–702. <https://doi.org/10.4236/apm.2015.511063>
- Haugen, V., Nøvdal, G., Natvik, L. J., Evensen, G., Berg, A. M., & Flornes, K. M. (2008). History matching using the ensemble Kalman filter on a North Sea field case. *SPE Journal*, 13(4), 382–391. <https://doi.org/10.2118/102430-PA>
- Hickin, E. J. (1986). Concave-Bank Benches in the Floodplains of Muskwa and Fort Nelson Rivers, British Columbia. *Canadian Geographer / Le Géographe Canadien*, 30(2), 111–122. <https://doi.org/10.1111/j.1541-0064.1986.tb01036.x>
- Hill, R. (1952). The elastic behaviour of a crystalline aggregate. *Proceedings of the Physical Society. Section A*, 65(5), 349–354. <https://doi.org/10.1088/0370-1298/65/5/307>
- Hirsch, L. M., & Schuette, J. F. (1999). Graph theory applications to continuity and ranking in geologic models. *Computers and Geosciences*, 25(2), 127–139.
- Hoffman, B. T., & Caers, J. (2004). History matching with the regional probability perturbation method—Applications to a North Sea reservoir. *Proceedings of the ECMOR IX, Cannes*.
- Hosseini, S. A., Lashgari, H., Choi, J. W., Nicot, J. P., Lu, J., & Hovorka, S. D. (2013). Static and dynamic reservoir modeling for geological CO₂ sequestration at Cranfield, Mississippi, U.S.A. *International Journal of Greenhouse Gas Control*, 18, 449–462. <https://doi.org/10.1016/j.ijggc.2012.11.009>
- Hovorka, S. D., Doughty, C., Benson, S. M., Pruess, K., & Knox, P. R. (2004). The impact of geological heterogeneity on CO₂ storage in brine formations: A case study from the Texas Gulf Coast. *Geological Society Special Publication*, 233, 147–163. <https://doi.org/10.1144/GSL.SP.2004.233.01.10>
- Hovorka, S. D., Meckel, T. A., & Treviño, R. H. (2013). Monitoring a large-volume injection at Cranfield, Mississippi-Project design and recommendations. *International Journal of Greenhouse Gas Control*, 18, 345–360. <https://doi.org/10.1016/j.ijggc.2013.03.021>
- Howard, A. D. (1983). Simulation model of meandering. *River Meandering*, 952–963.
- Howard, R. A. (1966). Information value theory. *IEEE Transactions on Systems, Science and Cybernetics*, SSC-2(1), 22–26.
- Hu, L. Y. (2000). Gradual deformation and iterative calibration of Gaussian-related stochastic models. *Mathematical Geology*, 32(1), 87–108. <https://doi.org/10.1023/A:1007506918588>
- Hu, L. Y. (2002). Combination of dependent realizations within the gradual deformation method. *Mathematical Geology*, 34(8), 953–963. <https://doi.org/10.1023/A:1021316707087>
- Hu, L. Y., Blanc, G., & Noetinger, B. (2001). Gradual deformation and iterative calibration of sequential stochastic simulations. *Mathematical Geology*, 33(4), 475–489. <https://doi.org/10.1023/a:1011088913233>
- Hu, L. Y., & Le Ravalec-Dupin, M. (2004). An improved gradual deformation method for reconciling random and gradient searches in stochastic optimizations. *Mathematical Geology*, 36(6), 703–719. <https://doi.org/10.1023/B:MATG.0000039542.73994.a2>
- Ikeda, S., Gary, P., & Kenji, S. (1981). Bend Theory of River Meanders. *Journal of Fluid Mechanics*, 112, 363–377.
- Issautier, B., Fillacier, S., Le, Y., Audigane, P., Chiaberge, C., & Viseur, S. (2013). Modelling of CO₂

- Injection in Fluvial Sedimentary Heterogeneous Reservoirs to assess the impact of geological heterogeneities on CO₂ Storage Capacity and Performance . *Energy Procedia*, 37, 5181–5190. <https://doi.org/10.1016/j.egypro.2013.06.434>
- Issautier, B., Viseur, S., Audigane, P., & le Nindre, Y. M. (2014). Impacts of fluvial reservoir heterogeneity on connectivity: Implications in estimating geological storage capacity for CO₂. *International Journal of Greenhouse Gas Control*, 20, 333–349. <https://doi.org/10.1016/j.ijggc.2013.11.009>
- Jackson, M. D., & Muggeridge, A. H. (2000). Effect of discontinuous shales on reservoir performance during horizontal waterflooding. *SPE Journal*, 5(4), 446–455. <https://doi.org/10.2118/69751-PA>
- Jackson, R. G. (1976). Depositional model of point bars in the lower Wabash River. *J. Sediment. Petrol.*, 46, 579–594.
- Johansen, K., & Stenby, E. . (2005). Statistical Methods for History Matching. *Graduate Schools Year Book*, 103.
- Journal, A. G. (1983). Nonparametric estimation of spatial distributions. *Journal of the International Association for Mathematical Geology*, 15(3), 445–468. <https://doi.org/10.1007/BF01031292>
- Kadingdi, F. A., Ayawah, P. E., Azure, J. W., Bruno, K. A., Kaba, A. G., & Frimpong, S. (2022). Stacked Generalization for Improved Prediction of Ground Vibration from Blasting in Open-Pit Mine Operations. *Mining, Metallurgy and Exploration*, 1–13.
- Kashib, Tarun, & Srinivasan, S. (2006). A probabilistic approach to integrating dynamic data in reservoir models. *Journal of Petroleum Science and Engineering*, 50(3–4), 241–257. <https://doi.org/10.1016/j.petrol.2005.11.002>
- Kashib, Taurun, & Srinivasan, S. (2003). Iterative Integration of Dynamic Data in Reservoir Models. *Proceedings of SPE Annual Technical Conference and Exhibition*, 1–12.
- Kestin, J., Khalifa, E. and Correia, J. (1981). Tables of the Dynamic and Kinematic Viscosity of Aqueous NaCl Solutions in the Temperature Range 20–150°C and Pressure Range 0.1–35 MPa. *Journal of Physical and Chemical Reference Data*, 10(1), 71–87.
- Kim, S., & Hosseini, S. A. (2014). Above-zone pressure monitoring and geomechanical analyses for a field-scale CO₂ injection project in Cranfield, MS. *Greenhouse Gases: Science and Technology*, 4(1), 81–98. <https://doi.org/10.1002/ghg.1388>
- Kruskal, J. (1964). *Multidimensional scaling by optimizing goodness of fit to a nonmetric hypothesis. Psychometrika* 29, 1–27. [doi:10.1007/BF02289565](https://doi.org/10.1007/BF02289565).
- Kumar, Devesh, & Srinivasan, S. (2018). Ensemble-based history matching and uncertainty quantification for reservoirs exhibiting complex non-Gaussian characteristics. *Proceedings - SPE Annual Technical Conference and Exhibition, 2018-Sept.* <https://doi.org/10.2118/191648-ms>
- Kumar, Devesh, & Srinivasan, S. (2019). Ensemble-Based Assimilation of Nonlinearly Related Dynamic Data in Reservoir Models Exhibiting Non-Gaussian Characteristics. *Mathematical Geosciences*, 51(1), 75–107. <https://doi.org/10.1007/s11004-018-9762-x>
- Kumar, Dhananjay. (2006). A Tutorial on Gassmann Fluid Substitution : Formulation, Algorithm and Matlab Code. *Geohorizons*, January, 4–12. http://www.spgindia.org/geohorizon/jan_2006/dhananjay_paper.pdf
- Labrecque, P.A., Jensen, J. L., Hubbard, S. M., & Nielsen, H. (2011). Sedimentology and Stratigraphic

- Architecture of a Point-bar Deposit, Lower Cretaceous McMurray Formation, Alberta, Canada. *Bulletin of Canadian Petroleum Geology*, 59, 147–171.
- Labrecque, Philip A., Hubbard, S. M., Jensen, J. L., & Nielsen, H. (2011). Sedimentology and stratigraphic architecture of a point bar deposit, Lower Cretaceous McMurray Formation, Alberta, Canada. *Bulletin of Canadian Petroleum Geology*, 59 (2), 147–171.
- Labrecque, Phillip A., Jensen, J. L., & Hubbard, S. M. (2011). Cyclicity in Lower Cretaceous point bar deposits with implications for reservoir characterization, Athabasca Oil Sands, Alberta, Canada. *Sedimentary Geology*, 242(1–4), 18–33. <https://doi.org/10.1016/j.sedgeo.2011.06.011>
- Langbein, W. B., & Leopold, L. B. (1966). River meanders -- Theory of minimum variance. *U.S. Geological Survey Professional Paper 422-H*, 1–15. <https://doi.org/10.3133/PP422H>
- Le Ravalec-Dupin, M., & Nøttinger, B. (2002). Optimization with the gradual deformation method. *Mathematical Geology*, 34(2), 125–142. <https://doi.org/10.1023/A:1014408117518>
- Lee, E. T. Y. (1989). Choosing nodes in parametric curve interpolation. *Computer-Aided Design*, 21(6), 363–370. [https://doi.org/10.1016/0010-4485\(89\)90003-1](https://doi.org/10.1016/0010-4485(89)90003-1)
- Leopold, L. B., & Langbein, W. B. (1966). River Meanders. *Scientific American*, 214, 60–70.
- Leopold, L. B., & Wolman, M. G. (1960). River meanders. *Geol. Soc. Am. Bull.*, 71, 789–794.
- Li, H., & Srinivasan, S. (2015). Modeling Point Bars Using a Grid Transformation Scheme Heterogeneities in Point bars. *SPE Annual Technical Conference and Exhibition, September*, 28–30.
- Li, L. (2017). *A Bayesian Approach to Causal and Evidential Analysis for Uncertainty Quantification throughout the Reservoir Forecasting Process*. Stanford University.
- Li, Y.-K., & Nghiem, L. X. (1986). Phase Equilibria of Oil, Gas and Water/Brine Mixtures. *The Canadian Journal of Chemical Engineering*, 64(3), 486–496. <https://doi.org/10.1002/cjce.5450640319>
- Li, Y., & Wu, S. (2013). Hierarchical nested simulation approach in reservoir architecture modeling. *Petroleum Exploration and Development*, 40(5), 676–681. [https://doi.org/10.1016/S1876-3804\(13\)60091-9](https://doi.org/10.1016/S1876-3804(13)60091-9)
- Lloyd, S. P. (1982). "Least Squares Quantization in PCM." *IEEE Transactions on Information Theory*. 28, 129–137.
- Lu, J., Kordi, M., Hovorka, S. D., Meckel, T. A., & Christopher, C. A. (2013a). Reservoir characterization and complications for trapping mechanisms at Cranfield CO₂ injection site. *International Journal of Greenhouse Gas Control*. <https://doi.org/10.1016/j.ijggc.2012.10.007>
- Lu, J., Kordi, M., Hovorka, S. D., Meckel, T. A., & Christopher, C. A. (2013b). Reservoir characterization and complications for trapping mechanisms at Cranfield CO₂ injection site. *International Journal of Greenhouse Gas Control*, 18, 361–374. <https://doi.org/10.1016/j.ijggc.2012.10.007>
- Lu, Jiemin, Kharaka, Y. K., Thordsen, J. J., Horita, J., Karamalidis, A., Griffith, C., Hakala, J. A., Ambats, G., Cole, D. R., Phelps, T. J., Manning, M. A., Cook, P. J., & Hovorka, S. D. (2012). CO₂-rock-brine interactions in Lower Tuscaloosa Formation at Cranfield CO₂ sequestration site, Mississippi, U.S.A. *Chemical Geology*, 291, 269–277. <https://doi.org/10.1016/j.chemgeo.2011.10.020>
- Lu, Jiemin, Milliken, K., Reed, R. M., & Hovorka, S. (2011). Diagenesis and sealing capacity of the

- middle Tuscaloosa mudstone at the Cranfield carbon dioxide injection site, Mississippi, U.S.A. *Environmental Geosciences*, 18(1), 35–53. <https://doi.org/10.1306/eg.09091010015>
- Mantilla, C. A., Oruganti, Y. D., Bryant, S. L., & Srinivasan, S. (2009). Real-time assessment of CO₂ migration direction during geologic storage. *Energy Procedia*, 1(1), 2227–2234. <https://doi.org/10.1016/j.egypro.2009.01.290>
- Mantilla, C. A., Srinivasan, S., Cross, E. A., & Bryant, S. L. (2009). Inexpensive assessment of plume migration during CO₂ sequestration. *SPE International Conference on CO₂ Capture, Storage, and Utilization 2009*, 252–261. <https://doi.org/10.2118/126693-ms>
- Mantilla, C. A., Srinivasan, S., & Nguyen, Q. P. (2011). Updating Geologic Models using Ensemble Kalman Filter for Water Coning Control. *Engineering*, 03(05), 538–548. <https://doi.org/10.4236/eng.2011.35063>
- Mavko, G., Mukerji, T., & Dvorkin, J. (1998). *The rock physics handbook: Tools for seismic analysis in porous media* (2nd ed.). Cambridge Univ. Press.
- McCain, W. D. (1990). *The Properties of petroleum fluids* (2nd ed.). PennWell Books.
- McMahon, W. J., & Davies, N. S. (2018). The shortage of geological evidence for pre-vegetation meandering rivers. In *Fluvial Meanders and Their Sedimentary Products in the Rock Record* (Issue November). <https://doi.org/10.1002/9781119424437.ch5>
- Min, B., Nwachukwu, A., Srinivasan, S., & Wheeler, M. F. (2016). Selection of Geologic Models Based on Pareto-Optimality Using Surface Deformation and CO₂ Injection Data for the in Salah Gas Sequestration Project. *SPE Annual Technical Conference and Exhibition, Dubai, UAE*. <https://doi.org/https://doi.org/10.2118/181569-MS>
- Mito, S., & Xue, Z. (2011). Post-injection monitoring of stored CO₂ at the Nagaoka pilot site: 5 years time-lapse well logging results. *Energy Procedia*, 4, 3284–3289.
- Movshovitz-Hadar, N., & Shmukler, A. (2000). *River Meandering and a Mathematical Model of this Phenomenon*. 25, 1–23. http://physicaplus.org.il/zope/home/en/1124811264/1141060775rivers_en
- Murphy, W., Reischer, A., & Hsu, K. (1993). Modulus decomposition of compressional and shear velocities in sand bodies. *Geophysics*, 58, 227–239.
- Musial, G., Franco, R. L. and J., & Reynaud, J.-Y. (2013). Modeling of a Tide-influenced Point-bar Heterogeneity Distribution and Impacts on Steam-assisted Gravity Drainage Production: Example from Steepbank River, McMurray Formation, Canada. *AAPG Studies in Geology*, 64, 545 – 564.
- Nakayasu, M., Goda, T., Tanaka, K., & Sato, K. (2016). *Evaluating the Value of Single-Point Data in Heterogeneous Reservoirs With the Expectation-Maximization Algorithm*. 1–10.
- Nanson, G. C. (1980). Point Bar and Floodplain Formation of the Meandering Beatton River, Northeastern British Columbia, Canada. *Sedimentology*, 27, 3–29.
- Nanson, G. C., & Croke, J. C. (1992). A genetic classification of floodplains. *Geomorphology*, 4, 459–486.
- Nardin, Thomas R., Howard R. Feldman, and B. J. C. (2013). Stratigraphic architecture of a large-scale point-bar complex in the McMurray Formation: Syncrude’s Mildred Lake Mine, Alberta, Canada. *AAPG Studies in Geology*, 64, 273 – 311.
- Nazeer, A., Abbasi, S. A., & Solangi, S. H. (2016). Sedimentary facies interpretation of Gamma Ray (GR) log as basic well logs in Central and Lower Indus Basin of Pakistan. *Geodesy and*

- Geodynamics*, 7(6), 432–443. <https://doi.org/10.1016/j.geog.2016.06.006>
- Niu, B., Bao, Z., Yu, D., Zhang, C., Long, M., Su, J., Gao, X., Zhang, L., Zang, D., Li, M., & Li, Y. (2021). Hierarchical modeling method based on multilevel architecture surface restriction and its application in point-bar internal architecture of a complex meandering river. *Journal of Petroleum Science and Engineering*, 205(April), 108808. <https://doi.org/10.1016/j.petrol.2021.108808>
- Nwachukwu, A., Min, B., & Srinivasan, S. (2017). Model selection for CO₂ sequestration using surface deformation and injection data. *International Journal of Greenhouse Gas Control*, 56, 67–92. <https://doi.org/10.1016/j.ijggc.2016.11.019>
- Odundun, O., & Nton, M. (2011). Facies Interpretation from Well Logs: Applied to SMEKS Field, Offshore Western Niger Delta. *American Association of Petroleum Geologists*, 25.
- Oliver, D. S., & Chen, Y. (2011). Recent progress on reservoir history matching: A review. *Computational Geosciences*, 15(1), 185–221. <https://doi.org/10.1007/s10596-010-9194-2>
- Pearson, K. (1901). On Lines and Planes of Closest Fit to Systems of Points in Space. *Philosophical Magazine*, 2(11), 559–572.
- Peng, Y., and Robinson, B. (1976). A New Two-Constant Equation of State. *Industrial & Engineering Chemistry Fundamental*, 15(1), 59–64.
- Pickering, S., & Bickel, J. . (2006). *The value of seismic information*. *Oil and Gas Financial Journal*. 3(5), 26–33.
- Pitlick, J., & Cress, R. (2002). Downstream changes in the channel geometry of a large gravel bed river. *Water Resources Research*, 38(10), 34–1.
- Portier, S., & Rochelle, C. (2005). Modelling CO₂ solubility in pure water and NaCl-type waters from 0 to 300 C and from 1 to 300 bar: Application to the Utsira Formation at Sleipner. *Chemical Geology*, 217(3–4), 187–199.
- Pranter, M. J., Ellison, A. I., Cole, R. D., & Patterson, P. E. (2007). Analysis and modeling of intermediate-scale reservoir heterogeneity based on a fluvial point-bar outcrop analog, Williams Fork Formation, Piceance Basin, Colorado. *AAPG Bulletin*, 91(7), 1025–1051. <https://doi.org/10.1306/02010706102>
- Pratt, J., Raiffa, H., & Schlaiffer, R. (1995). *Introduction to Statistical Decision Theory*. The MIT Press, Cambridge, Massachusetts.
- Pyrzcz, M. J., Boisvert, J. B., & Deutsch, C. V. (2008). A library of training images for fluvial and deepwater reservoirs and associated code. *Computers and Geosciences*, 34(5), 542–560. <https://doi.org/10.1016/j.cageo.2007.05.015>
- Pyrzcz, M. J., & Deutsch, C. V. (2004). Stochastic modeling of inclined heterolithic stratification with the bank retreat model. *Proceedings of the 2004 Canadian Society of Petroleum Geologists, Canadian Well Logging Society and Canadian Heavy Oil Association Joint Convention (ICE 2004), Calgary, Canada Vol(8)*.
- Pyrzcz, M. J., Boisvert, J. . ., & Deutsch, C. V. (2009). *Computers & Geosciences ALLUVSIM: A program for event-based stochastic modeling of fluvial depositional systems* \$. 35, 1671–1685. <https://doi.org/10.1016/j.cageo.2008.09.012>
- Pyrzcz, Michael J., Catuneanu, O., & Deutsch, C. V. (2005). Stochastic surface-based modeling of turbidite lobes. *American Association of Petroleum Geologists Bulletin*, 89(2), 177–191.

<https://doi.org/10.1306/09220403112>

- Pyrzcz, Michael J. (2001). *Bank Retreat Meandering Fluvial Process-based Model*. 1–12.
- Pyrzcz, Michael J., & Deutsch, C. V. (2004). Stochastic Simulation of Inclined Heterolithic Stratification with Streamline-based Stochastic Models. *Center for Computational Geostatistics Annual Report Papers*, 1–14. [papers2://publication/uuid/4BADF3C6-381A-499D-A4C5-DD63447E3CAE](https://doi.org/10.1306/09220403112)
- Raiffa, H. (1968). *Decision Analysis Introductory Lectures on Choices under Uncertainty*. Addison-Wesley Publishing Company, Massachusetts.
- Ramirez, A., Newmark, R., & Daily, W. (2003). Monitoring carbon dioxide floods using electrical resistance tomography (ERT): sensitivity studies. *Journal of Environmental and Engineering Geophysics*, 8(3), 187–208.
- Raymer, L. L., Hunt, E. R., & Gardner, J. S. (1980). An improved sonic transit time-to-porosity transform. *Trans. Soc. Prof. Well Log Analysts 21st Ann. Logging Symp. Sbar, M. L., 2000, Exploration Risk*.
- Remy, N. (2004). *Geostatistical Earth Modeling Software: User's Manual*. 1–87. [papers2://publication/uuid/D72A1F6E-10B2-4C84-864E-7840DE1414BA](https://doi.org/10.1306/09220403112)
- Reuss, A. (1929). Berechnung der Fleissgrenzen von Mischkristallen auf Grund der Plastizitätsbedingung für Einkristalle. *Zeitschrift Für Angewandte Mathematik Aus Mechanik*, 9, 19–58.
- Richardson, J. G., Harris, D. G., Rossen, R. H., & Van Hee, G. (1978). The effect of small, discontinuous shales on oil recovery. *Journal of Petroleum Technology*, 20, 1531–1537.
- Rousseeuw, P. J. (1987). Silhouettes: a graphical aid to the interpretation and validation of cluster analysis. *Journal of Computational and Applied Mathematics*, 20, 53–65. [https://doi.org/https://doi.org/10.1016/0377-0427\(87\)90125-7](https://doi.org/10.1016/0377-0427(87)90125-7)
- Rowe, M., & Chou, S. (1970). No Title. *Journal of Physical and Chemical Reference Data*, 15(1), 61–66.
- Ruij, J., Caumon, G., & Viseur, S. (2016). Modeling Channel Forms and Related Sedimentary Objects Using a Boundary Representation Based on Non-uniform Rational B-Splines. *Mathematical Geosciences*, 48(3), 259–284. <https://doi.org/10.1007/s11004-015-9629-3>
- Sato, K. (2011). International Journal of Greenhouse Gas Control Value of information analysis for adequate monitoring of carbon dioxide storage in geological reservoirs under uncertainty. *International Journal of Greenhouse Gas Control*, 5(5), 1294–1302. <https://doi.org/10.1016/j.ijggc.2011.07.010>
- Schmidt-Hattenberger, C., Bergmann, P., Kiebling, D., Kruger, K., Rucker, C., Schutt, H., & Group, K. (2011). Application of a vertical electrical resistivity array (VERA) for monitoring CO₂ migration at the Ketzin Site: first performance evaluation. *Energy Procedia*, 4, 3363–3370.
- Schniger, A., Nowak, W., & Hendricks Franssen, H. J. (2012). Parameter estimation by ensemble Kalman filters with transformed data: Approach and application to hydraulic tomography. *Water Resources Research*, 48(4), 1–18. <https://doi.org/10.1029/2011WR010462>
- Sharifi, M., Kelkar, M., Bahar, A., & Slettebo, T. (2014). Dynamic ranking of multiple realizations by use of the fast-marching method. *Society of Petroleum Engineers*, 19(6), 1069–1082.
- Shmaryan, L. E., & Deutsch, C. V. (1999). Object-based modeling of fluvial/deepwater reservoirs with fast data conditioning: Methodology and case studies. *Proceedings - SPE Annual Technical Conference and Exhibition, OMEGA(1)*, 877–886. <https://doi.org/10.2118/56821-ms>

- Shu, X., Hu, Y., Jin, B., Dong, R., Zhou, H., & Wang, J. (2015). Modeling Method of Point Bar Internal Architecture of Meandering River Reservoir Based on Meander Migration Process Inversion Algorithm and Virtual Geo-surfaces Automatic Fitting Technology. *SPE Annual Technical Conference and Exhibition*. <https://doi.org/10.2118/175013-MS>
- Singh, M. (2019). *Quantitative Inversion of Microseismic Data: Bayesian Model Selection Using Fast Proxies for Fracturing and Wave Propagation*. The Pennsylvania State University.
- Smith, T. M., Sondergeld, C. H., & Rai, C. S. (2003). Gassmann fluid substitutions: A tutorial. *Geophysics*, 68(2), 430–440. <https://doi.org/10.1190/1.1567211>
- Spencer, J. W., Cates, M. E., & Thompson, D. D. (1994). Frame moduli of unconsolidated sands and sandstones. *Geophysics*, 59, 1352–1361.
- Srinivasan, S., & Mantilla, C. (2012). *Uncertainty Quantification and Feedback Control Using a Model Selection Approach Applied to a Polymer Flooding Process* (17th ed.).
- Stephen, K. D., Clark, J. D., & Gardiner, A. R. (2001). Outcrop-based stochastic modelling of turbidite amalgamation and its effects on hydrocarbon recovery. *Petroleum Geoscience*, 7(2), 163–172. <https://doi.org/10.1144/petgeo.7.2.163>
- Stewart, J., Dunn, P., Lyttle, C., Campion, K., Oyerinde, A., & Fischer, B. (2008). Improving performance prediction in deep-water reservoirs: Learning from outcrop analogues, conceptual models and flow simulation. *International Petroleum Technology Conference, IPTC 2008*, 4, 2735–2743. <https://doi.org/10.2523/iptc-12892-ms>
- Su, Y., Wang, J. Y., & Gates, I. D. (2013). SAGD well orientation in point bar oil sand deposit affects performance. *Engineering Geology*, 157, 79–92. <https://doi.org/10.1016/j.enggeo.2013.01.019>
- Sun, T., Meakin, P., & Jossang, T. (1996). = (*Uso*). 32(9), 2937–2954.
- Tahmasebi, P. (2017). Structural adjustment for accurate conditioning in large-scale subsurface systems. *Advances in Water Resources*, 101, 60–74. <https://doi.org/10.1016/j.advwatres.2017.01.009>
- Tao, Q., Bryant, S. L., & Meckel, T. A. (2013). Modeling above-zone measurements of pressure and temperature for monitoring CCS sites. *International Journal of Greenhouse Gas Control*, 18, 523–530. <https://doi.org/10.1016/j.ijggc.2012.08.011>
- Tavakoli, R., Srinivasan, S., & Wheeler, M. F. (2014). Rapid updating of stochastic models by use of an ensemble-filter approach. *SPE Journal*, 19(3), 500–513. <https://doi.org/10.2118/163673-PA>
- Thomas, R.G., Smith, D.G., Wood, J.M., Visser, J., Calverley-Range, E.A. and Koster, E. H. (1987). Inclined heterolithic stratification-terminology, description, interpretation and significance. *Sedimentary Geology*, 53, 123–179.
- Thompson, A. (1986). Secondary Flows and the Pool Riffle Unit: A Case Study of the Processes of Meander Development. *Earth Surface Processes and Landforms*, 11, 631–641.
- Thompson, D. W. (1917). *On Growth and Form*. Cambridge University Press, Cambridge. 793.
- Torgerson, W. S. (1958). Theory and methods of scaling. *Oxford, England: Wiley*.
- Trainor-Guitton, W. J., Ramirez, A., Yang, X., Mansoor, K., Sun, Y., & Carroll, S. (2013). Value of information methodology for assessing the ability of electrical resistivity to detect CO₂/brine leakage into a shallow aquifer. *International Journal of Greenhouse Gas Control*, 18, 101–113. <https://doi.org/10.1016/j.ijggc.2013.06.018>

- van Leeuwen, P. J., & Evensen, G. (1996). Data assimilation and inverse methods in terms of a probabilistic formulation. *Monthly Weather Review*, *124*, 2898–2913.
- Vasco, D. W., Alfi, M., Hosseini, S. A., Zhang, R., Daley, T., Ajo-Franklin, J. B., & Hovorka, S. D. (2019). The Seismic Response to Injected Carbon Dioxide: Comparing Observations to Estimates Based Upon Fluid Flow Modeling. *Journal of Geophysical Research: Solid Earth*, *124*(7), 6880–6907. <https://doi.org/10.1029/2018JB016429>
- Viseur, S., Shtuka, A., & Mallet, J. L. (2001). *Stochastic Object-Based Simulation of Channels Constrained By High Resolution Seismic Data*. 1–11.
- Voigt, W. (1928). *Lehrbuch der Kristallphysik*. Teubner Verlag, Leipzig.
- Wang, Z. (2001). Fundamentals of seismic rock physics. *Geophysics*, *66*(2), 398–412. <https://doi.org/10.1190/1.1444931>
- Wang, Z., Wang, H., & Cates, M. E. (2001). Effective elastic properties of solid clays. *Geophysical*, *66*(2), 428–440.
- Weber, K. J. (1982). Influence of common sedimentary structures on fluid flow in reservoir models. *Journal of Petroleum Technol-Ogy*, *34*, 665–672.
- Welton, N. J., Ades, A. E., Caldwell, D. ., & Peters, T. J. (2008). Research prioritization based on expected value of partial perfect information: a case-study on interventions to increase uptake of breast cancer screening. *Journal of the Royal Statistical Society: Series A (Statistics in Society)*, *171*(4), 807–841.
- Werren, E. G., Shew, R. D., Adams, E. R., & Stancliffe, R. J. (1990). Meander-belt reservoir geology, mid-dip Tuscaloosa, Little Creek field, Mississippi. In *Sandstone Petroleum Reservoirs*. Springer, New York, NY.
- Willie, M. R. J., Gregory, A. R., & Gardner, L. W. (1956). Elastic wave velocities in heterogeneous and porous media. *Geophysics*, *23*, 41–70.
- Willis, B. J., & Tang, H. (2010). Three-dimensional connectivity of point-bar deposits. *Journal of Sedimentary Research*, *80*(5–6), 440–454. <https://doi.org/10.2110/jsr.2010.046>
- Willis, B. J., & White, C. D. (2000). Quantitative outcrop data for flowsimulation. *Journal of Sedimentary Research*, *70*, 788–802.
- Wilson, B. W., & Nanz, R. H. (1959). Sand conditions as indicated by the self-potential Log. In *EPRM Memorandum Report*.
- Wyllie, M. R. J., Gregory, A. R., & Gardner, L. W. (1958). An experimental investigation of factors affecting elastic wave velocities in porous media. *Geophysics*, *23*, 459–493.
- Yang, C., Romanak, K., Hovorka, S., Holt, R. M., Lindner, J., & Trevino, R. (2013). Near-surface monitoring of large-volume CO₂ injection at Cranfield: Early field test of SECARB phase III. *SPE Journal*, *18*(3), 486–494. <https://doi.org/10.2118/163075-PA>
- Yao, L., Dimitrakopoulos, R., & Gamache, M. (2020). High-Order Sequential Simulation via Statistical Learning in Reproducing Kernel Hilbert Space. *Mathematical Geosciences*, *52*(5), 693–723. <https://doi.org/10.1007/s11004-019-09843-3>
- Yao, L., Dimitrakopoulos, R., & Gamache, M. (2021). Learning high-order spatial statistics at multiple scales: A kernel-based stochastic simulation algorithm and its implementation. *Computers and Geosciences*, *149*(January), 104702. <https://doi.org/10.1016/j.cageo.2021.104702>

- Yin, Y. (2013). A New Stochastic Modeling of 3-D Mud Drapes Inside Point Bar Sands in Meandering River Deposits. *Natural Resources Research*, 22(4), 311–320. <https://doi.org/10.1007/s11053-013-9219-3>
- Yin, Z., Feng, T., & Macbeth, C. (2019). Fast assimilation of frequently acquired 4D seismic data for reservoir history matching. *Computers and Geosciences*, 128, 30–40.
- Yokota, F., & Thompson, K. . (2004). Value of information analysis in environmental health risk management decisions: past, present, and future. *Risk Analysis*, 24(3), 635–650.
- Zhang, R., Ghosh, R., Sen, M. K., & Srinivasan, S. (2013a). Time-lapse surface seismic inversion with thin bed resolution for monitoring CO₂ sequestration: A case study from Cranfield, Mississippi. *International Journal of Greenhouse Gas Control*, 18(July 2008), 430–438. <https://doi.org/10.1016/j.ijggc.2012.08.015>
- Zhang, R., Ghosh, R., Sen, M. K., & Srinivasan, S. (2013b). Time-lapse surface seismic inversion with thin bed resolution for monitoring CO₂ sequestration: A case study from Cranfield, Mississippi. *International Journal of Greenhouse Gas Control*, 18(July 2008), 430–438. <https://doi.org/10.1016/j.ijggc.2012.08.015>
- Zhang, R., Sen, M. K., & Srinivasan, S. (2014). Time-lapse pre-stack seismic inversion with thin bed resolution for CO₂ sequestration from Cranfield, Mississippi. *International Journal of Greenhouse Gas Control*, 20, 223–229.
- Zhang, R., Song, X., Fomel, S., & Sen, M. K. (2013). Time-lapse seismic registration and inversion for CO₂ sequestration study at Cranfield Part II : Pre-stack Analysis. *SEG International Exposition and Annual Meeting*. <https://doi.org/10.1190/segam2013-0309.1>
- Zhang, R., Song, X., Fomel, S., Sen, M. K., & Sanjay, S. (2013a). Time-lapse seismic data registration and inversion for CO₂ sequestration study at Cranfield. *Geophysics*, 78(6), B329–B338.
- Zhang, R., Song, X., Fomel, S., Sen, M. K., & Srinivasan, S. (2013b). *Time-lapse seismic registration and inversion for CO₂ sequestration study at Cranfield Part II : Pre- stack Analysis SEG Houston 2013 Annual Meeting SEG Houston 2013 Annual Meeting*. 5015–5020.
- Zhang, Z., Yin, Z., & Yan, X. (2018). A workflow for building surface-based reservoir models using NURBS curves, coons patches, unstructured tetrahedral meshes and open-source libraries. *Computers and Geosciences*, 121(September), 12–22. <https://doi.org/10.1016/j.cageo.2018.09.001>
- Zhou, H., Gómez-Hernández, J. J., Hendricks Franssen, H. J., & Li, L. (2011). An approach to handling non-Gaussianity of parameters and state variables in ensemble Kalman filtering. *Advances in Water Resources*, 34(7), 844–864. <https://doi.org/10.1016/j.advwatres.2011.04.014>
- Zhu, H., & Journel, A. G. (1993). Formatting and Integrating Soft Data: Stochastic Imaging via the Markov-Bayes Algorithm. In Soares A. (eds) *Geostatistics Tróia '92. Quantitative Geology and Geostatistics*. vol 5, Springer, Dordrecht. https://doi.org/https://doi.org/10.1007/978-94-011-1739-5_1
- Zhu, X., & McMechan, G. A. (1990). *Direct estimation of the bulk modulus of the frame in fluid saturated elastic medium by Biot theory: 60th Ann. Internat. Mtg., Soc. Expl. Geophys., Expanded Abstracts Abstracts*. 787–790.

Vita

Ismael Dawuda was born in Assakae-Takoradi in the Western Region of Ghana, West Africa. He holds a BSc. Geological Engineering degree from the University of Mines and Technology (UMaT), Tarkwa-Ghana. Ismael pursued an MSc Petroleum Engineering program at the African University of Science and Technology, Abuja-Nigeria. He completed the master's program in December 2014. Ismael returned to UMaT and served as an Assistant Lecturer at the Petroleum Engineering Department where he taught Introduction to Petroleum, Petroleum Geology, and Formation Evaluation and Well Logging. Ismael begun his PhD program in Petroleum Engineering at Penn State University in January 2018. While at Penn State, he served as a Graduate Teaching Assistant for Drilling and Completion, Reservoir Engineering, as well as Rock and Fluid Properties. He is the recipient of the highly competitive Computers and Geoscience Research Scholarship—jointly awarded by the International Association for Mathematical Geosciences, and the Elsevier Journal for early career scientists with substantial research contribution to the field of Computational Geosciences and Geoinformatics.